
Anatomy of the Axon:

Dissecting the role of microtubule plus-end tracking proteins in axons of hippocampal neurons

ISBN: 978-90-393-7095-7

On the cover:

Interpretation of Rembrandt van Rijn's iconic oil painting *The Anatomy Lesson of Dr. Nicolaes Tulp* (1632). Instead of a human subject, a neuron is being dissected under the watchful eye of members of the Hoogenraad & Akhmanova labs circa 2018. The doctoral candidate takes on the role of Dr. Nicolaes Tulp.

The year in which this thesis is published, 2019, marks the 350th anniversary of Rembrandt's passing. It is therefore declared Year of Rembrandt.

Cover photography: Jasper Landman (Bob & Fzbl Photography)
Design and layout: Dieudonné van de Willige



© 2019; CC-BY-NC-ND.
Printed in The Netherlands.

Anatomy of the Axon:

Dissecting the role of microtubule plus-end tracking proteins in axons of hippocampal neurons

Anatomie van de Axon:

Ontleding van de rol van microtubulus-plus-eind-bindende eiwitten in axonen van hippocampale neuronen

(met een samenvatting in het Nederlands)

Proefschrift

ter verkrijging van de graad van doctor aan de Universiteit Utrecht
op gezag van de rector magnificus, prof.dr. H.R.B.M. Kummeling,
ingevolge het besluit van het college voor promoties in het openbaar te
verdedigen op woensdag 22 mei 2019 des middags te 2.30 uur

door

Dieudonné van de Willige

geboren op 24 oktober 1990 te Antwerpen, België

Promotoren: Prof. dr. C.C. Hoogenraad
Prof. dr. A. Akhmanova

Voor Hans & Miranda

Index

	Preface	7
	List of non-standard abbreviations	9
1	Microtubule plus-end tracking proteins in neuronal development <i>Cellular & Molecular Life Sciences, 2016</i>	10
2	Dynein regulator NDEL1 controls polarized cargo transport at the axon initial segment <i>Neuron, 2016</i>	56
3	Cytolinker Gas2L1 regulates axon branching and outgrowth via microtubule-dependent actin stabilization <i>Submitted manuscript</i>	104
4	Exploring the roles of newly identified plus-end tracking proteins in neuronal development <i>Collection of preliminary data</i>	150
5	General discussion	206
&	Appendix:	218
	CV & List of publications	220
	Non-expert summary in English and Dutch	224
	Acknowledgements	236

Preface

The complexity of the human brain has fascinated scientists since the late 19th century. According to estimations made in recent years, the male adult brain contains approximately 86 billion neurons [1, 2]. Perhaps more fascinating than the sheer number of nerve cells – there are over ten times as many neurons in a single brain as there are people on earth – is the assumption that each of those neurons is shaped uniquely. For neurons, form and function are tightly linked. A neuron’s morphology directly underlies its ability to participate in neural networks by forming connections with other neurons. Fortunately for the field of molecular neuroscience, the majority of these morphologies are established according to a common framework.

Multipolar neurons, the most prevalent type of neurons in the vertebrate central nervous system and the cells on which the work in this thesis is based, are divided into two distinct subcellular compartments. The somatodendritic compartment encompasses the soma or cell body, which contains the nucleus, and multiple dendrites, which are thick, branched and relatively short processes extending from the soma. Dendrites act as receivers of chemically encoded information. The second neuronal subcompartment, the axon, is the focus of this thesis. Axons transmit information by propagating action potentials, resulting in neurotransmitter release at terminals along the axon. Multipolar neurons typically extend one axon, which is much longer and thinner than dendrites. The axon is the first neurite to mature in dissociated neuron cultures. It forms a complex branched arbour that reaches impressive combined lengths of millimetres.

The cytoskeleton plays a crucial role in establishing neuronal morphology and polarity. It facilitates vesicle and organelle transport, allowing for the delivery of nutrients and macromolecules to build and maintain the neuronal processes, and offers structural support. The work in this thesis provides insight into the role and regulation of cytoskeletal processes during axon maturation, with a special focus on microtubules (MTs) and the proteins that bind to and regulate MTs from growing MT plus-ends (called +TIPs). Specifically, at the start of the work that resulted in this thesis, our goal was to identify new roles for +TIPs in neurodevelopment.

Chapter 1 features a review that familiarizes the reader with the various morphological changes associated with establishing neuronal polarity. It details the role that MTs play in this process and presents a discussion of what +TIPs had been implicated in neurodevelopment at the time of publishing.

In **Chapter 2**, we zoom in on a region located in the proximal axon. The so-called axon initial segment (AIS) is a gatekeeper of neuronal polarity. One of its functions is to sort cargo that enters from the soma: vesicles that are destined for dendrites reverse out of the axon, while cargo destined for the axon proceeds past the AIS. This chapter clears up some of the molecular mechanisms behind cargo filtering at the AIS. It describes how the MT-based motor protein dynein drives the reversal of mis-sorted vesicles, and how its regulator NDEL1 localizes to the AIS cortex to locally stimulate dynein activity. LIS1, a second dynein regulator that can also associate with the MT plus-end, is also shown to participate in vesicle filtering.

Chapter 3 features Gas2L1, a less well characterized +TIP that mediates crosstalk between the actin and MT cytoskeletons. We find that Gas2L1 promotes axon branching and balances axon outgrowth during neurodevelopment. In doing so, Gas2L1 functions as an actin stabilizer, but it utilizes a regulatory mechanism that places this function under direct control of MTs. We describe how Gas2L1 is inhibited via an intramolecular interaction, and how its autoinhibition is relieved by simultaneous binding of both MTs and actin filaments.

A number of other promising findings are presented in **Chapter 4**. This chapter hosts a collection of preliminary data. In addition to more insights into Gas2L1, we identify the +TIP NCKAP5L as a putative novel regulator of axon formation. Furthermore, we describe a link between MT plus-end dynamics and phosphorylation of the axonal MT-associated protein tau, which is associated with Alzheimer's disease. We reflect on the suggested role of a family of plus-end tracking tau kinases in this process. Surprisingly, these kinases appear to be native to the axon initial segment, raising questions about their function in healthy neurons.

Finally, we place these chapters in the context of recent literature in a summarizing discussion in **Chapter 5**.

References

1. Azevedo, F.A., et al., Equal numbers of neuronal and nonneuronal cells make the human brain an isometrically scaled-up primate brain. *J Comp Neurol*, 2009. 513(5): p. 532-41.
2. von Bartheld, C.S., J. Bahney, and S. Herculano-Houzel, The search for true numbers of neurons and glial cells in the human brain: A review of 150 years of cell counting. *J Comp Neurol*, 2016. 524(18): p. 3865-3895.

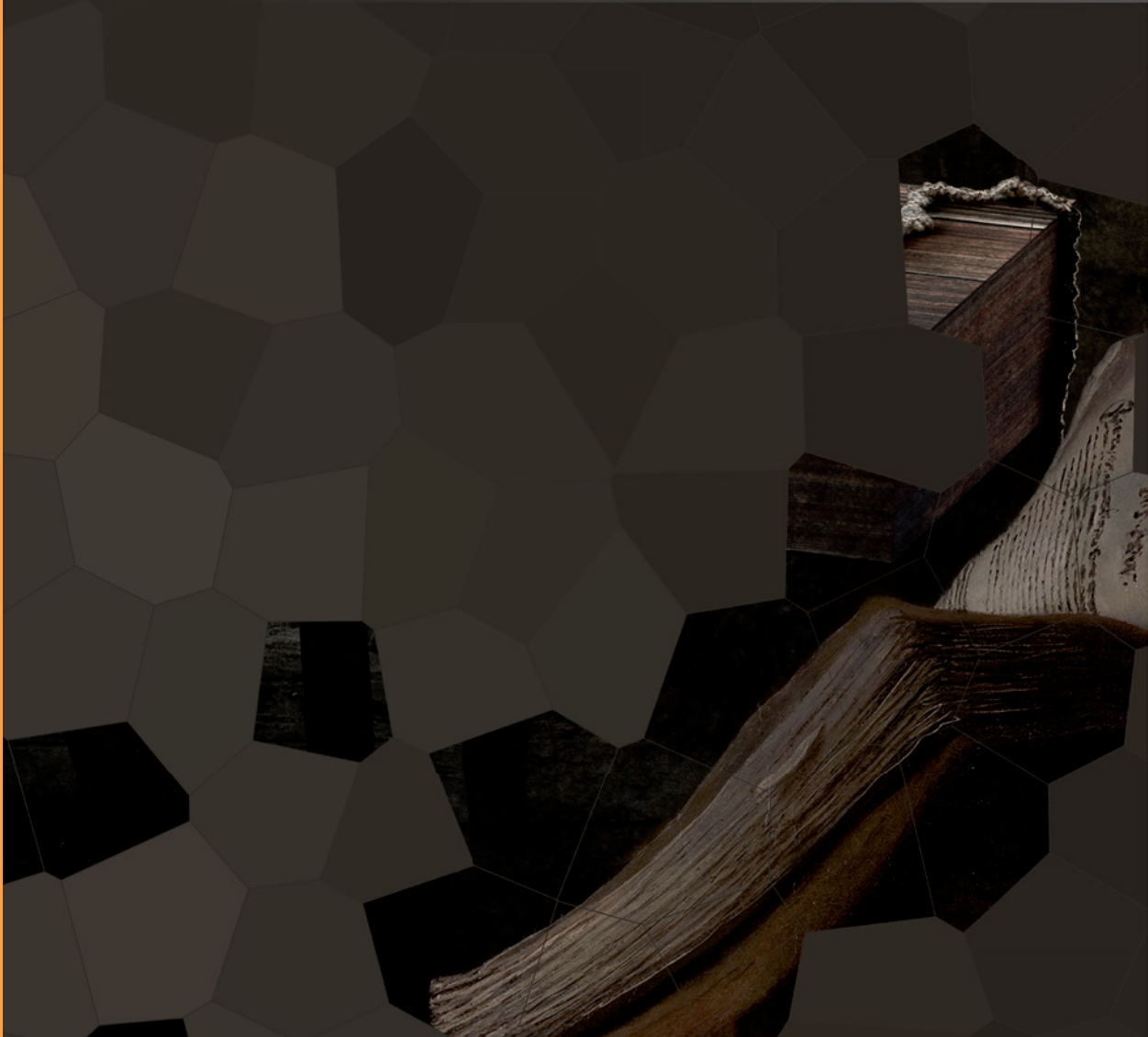
List of non-standard abbreviations throughout this thesis

Abbreviation	Full name	Classification
ABD	Actin-binding domain	Dom
Abi	Abelson interacting protein	P
Abl	Abelson kinase	Kin
ACF7	Actin crosslinking factor 7	+
AD	Alzheimer's Disease	D
AIS	Axon initial segment	Struc
AnkG	AnkyrinG	AIS +
AP	Adaptor protein	P
APC	Adenomatosis Polyposis Coli	+
AT8	Ser202/Thr205 phosphorylation sites on tau protein	
BDNF	Brain-derived neurotrophic factor	p
CAMSAP	Calmodulin-regulated spectrin-associated protein	p
CAP-Gly	Cytoskeletal-associated protein glycine-rich	Dom
cdk	Cyclin-dependent kinase	Kin
CDK5RAP2	CDK5 Regulatory Subunit Associated Protein 2	+
CEP/CP	Centrosomal protein	P
CFEOM1	Congenital fibrosis of the extraocular muscles type 1	D
CH	Calponin homology	Dom
CLASP	Cytoplasmic linker protein-associated protein	+
CLIP	Cytoplasmic linker protein	+
CNS	Central nervous system	
DIV	Days-in-vitro	
DRG	Dorsal root ganglia	
EB	End-binding protein	+
EFA-6	Exchange factor for Arf6	P
EM	Electron microscopy	T
ER	Endoplasmic reticulum	Struc
FRAP	Fluorescence recovery after photobleaching	T
GAR	Growth arrest-specific 2 protein-related region	Dom
Gas2L1/2	Growth arrest-specific 2-like 1/2	+
GSK3β	Glycogen synthase kinase 3 beta	Kin
HMN7B	Hereditary motor neuropathy 7B	D
IFT	Intraflagellar transport	Struc
IP3R	Inositol 1,4,5-triphosphate receptor	P
Jasp	Jasplakinolide	R
KIF1A	Kinesin-like protein KIF1A	Moto
LatB	Latrunculin B	R
LIS1	Lisencephaly-1 Protein	Moto +
MACF1/2	Microtubule-actin crosslinking factor 1/2	+
MAP	Microtubule-associated protein	P
MCAK	Mitotic centromere-associated kinesin	P
MT	Microtubule	Struc
MTA	Microtubule-targeting agent	R
NAV	Neuron Navigator	+
NCKAP5L	NCK Associated Protein 5 Like	+
NDE1	Nuclear distribution element 1	Moto
NDEL1	Nuclear distribution-like element 1	AIS Moto
NF-186	Neurofascin-186	AIS
NMDA	N-Methyl-D-aspartate	
PAEZ	Pre-axonal exclusion zone	Struc
PCM1	Pericentriolar material 1	P
PHF	Paired helical filament	Struc
PI3K	Phosphoinositide 3-kinase	Kin
PKC	Protein kinase C	Kin
SCA11	Spinocerebellar ataxia type 11	D
SOCE	Store operated calcium entry	Struc
STIM1	Stromal interaction molecule 1	+
SVs	Synaptic vesicles	Struc
+TIP	Microtubule plus-end tracking protein	+
TANC2	Tetratricopeptide Repeat, Ankyrin Repeat And Coiled-Coil Containing 2	Moto
TDP-43	Transactive response DNA binding protein of 43 kDa	P
TfR	Transferrin receptor	P
TOG	Tumor overexpressed gene	Dom
TRIM46	Tripartite Motif Containing 46	AIS
TRIO	Trio Rho Guanine Nucleotide Exchange Factor	+
TTBK1/2	Tau-tubulin kinase 1/2	+ Kin
VAPA/B	VAMP Associated Protein A/B	P

Legend*	
Microtubule plus-end tracking protein	+
Protein native to the axon initial segment	AIS
Kinase	Kin
Motor protein (or regulator thereof)	Moto
Other type of protein	P
Protein domain	Dom
Intracellular structure/mechanism	Struc
Technique	T
Disease	D
Reagent	R

* in context of this thesis; classifications are non-exhaustive

1



Microtubule plus-end tracking proteins in neuronal development

Dieudonné van de Willige¹, Casper C. Hoogenraad¹ & Anna Akhmanova¹

Cellular and Molecular Life Sciences (2016)

73:2053–2077

doi: 10.1007/s00018-016-2168-3

¹ Cell Biology, Faculty of Science, Utrecht University,
Padualaan 8, 3584 CH Utrecht, The Netherlands

Abstract

1

Regulation of the microtubule cytoskeleton is of pivotal importance for neuronal development and function. One such regulatory mechanism centers on microtubule plus-end tracking proteins (+TIPs): structurally and functionally diverse regulatory factors, which can form complex macromolecular assemblies at the growing microtubule plus-ends. +TIPs modulate important properties of microtubules including their dynamics and their ability to control cell polarity, membrane transport and signaling. Several neurodevelopmental and neurodegenerative diseases are associated with mutations in +TIPs or with misregulation of these proteins. In this review, we focus on the role and regulation of +TIPs in neuronal development and associated disorders.

Introduction

Microtubules (MTs) are one of the major types of filaments that constitute the eukaryotic cytoskeleton. Over the years, MTs have emerged as key players in cellular processes such as vesicle and organelle transport, DNA segregation during mitosis, cell migration and maintenance of cell polarity. Neurons are among the most complex and polarized cells, whose distinct morphology allows them to establish intercellular connections and propagate chemical and electrical signals across the nervous system. Mature neurons typically extend multiple processes, one of which (the axon) serves as a transmitter whereas others (the dendrites) act as receivers of input from other neurons. MTs are important for numerous functions in nerve cells (reviewed in [1-3]), such as long-range transport of cargo and neuron-specific processes like growth cone guidance. Indeed, MTs are indispensable for neurodevelopment, and many neurological diseases stem from defects in the MT cytoskeleton or its regulation.

Evidence for the existence of MTs was first obtained from electron microscopy (EM) data in the 1950s (reviewed in [4]). Prior to the development of EM, fibrillar structures had already been described as part of the mitotic spindle and cytoplasm. However, interpretative differences and technical limitations of early microscopy made it challenging to identify unity among observations [4]. It therefore wasn't until 1963 that MTs were acknowledged as distinct structures and named by Slautterback, Ledbetter and Porter [5, 6]. Today, we know that MTs are hollow tubes with a diameter of approximately 25 nm. MTs are typically assembled from 13 laterally associating protofilaments, which in turn consist of α , β -tubulin dimers aligned in a head-to-tail fashion. As a consequence of tubulin dimer polarity, MTs possess polarity throughout, which results in distinct ends of the polymer: the minus- and the plus-end, exposing α - and β -tubulin, respectively. MTs alternate between rapid phases of growth and shrinkage: a behavior termed 'dynamic instability' [7]. A transition from shrinkage to growth is called a rescue, whereas the opposite transition is referred to as a catastrophe.

Dynamic instability allows MTs to be swiftly remodeled in response to environmental cues. The MT cytoskeleton is suitable for rapidly sensing and responding to changes in the intracellular environment. To this end, the MT

cytoskeleton acts in concert with a large number of proteins (MAPs for MT-associated proteins) that either influence MTs themselves or relay signals from the MT cytoskeleton to other parts of the cell. MAPs are known to regulate MT behavior such as stability, assembly, bundling and targeting by associating with specific parts of the MT lattice or by interacting with the soluble tubulin pool. Well-characterized neuronal MAPs include MAP2 and tau, which maintain a polarized, mutually exclusive distribution and decorate MT bundles in dendrites and axons, respectively. Both proteins stabilize MTs and are able to induce MT bundling (reviewed in [8]). Abnormal phosphorylation of tau triggers its dissociation from MTs and causes tau to aggregate, resulting in the formation of potentially toxic tau deposits (neurofibrillary tangles) found in the brains of patients suffering from Alzheimer's disease (AD) and other tauopathies. This process is accompanied by degradation of the axonal MT cytoskeleton, suggesting a model in which dissociation of tau results in MT instability. It should be noted, however, that the precise hierarchy of events during the onset of AD remains unclear. Additional roles for tau are still emerging and may shed new light on the biology of tauopathies (reviewed in [9]). Among these is the regulation of the subcellular distribution of MAPs that specifically bind to the growing MT plus-end [10], the subclass of MAPs that this review will focus on.

MT dynamics are most pronounced at the plus-end. Although growth events have been observed at the MT minus-end [11], in cells minus-ends are often anchored or stabilized, restricting their dynamic behavior [12]. At the growing plus-end, freshly polymerized MT stretches contain GTP-loaded β -tubulin as opposed to the GDP-bound subunits present in the MT lattice, resulting in a so-called GTP cap. Moreover, the structures of polymerizing and depolymerizing MT plus-ends are different [13]. The unique chemical environment of the polymerizing MT plus-end grants it its own interactome within the realm of MAPs, consisting of MT plus-end tracking proteins (+TIPs; reviewed in [14-16]). +TIPs display a large structural and functional variation between individual proteins. However, a common theme sets them apart from other MAPs: +TIPs associate with the polymerizing MT plus-end, where they act as powerful regulators of MT dynamics and MT interactions with other structures.

In this review, we use the neuronal MT cytoskeleton to illustrate the role of +TIPs in the development of one of the most polarized and complex cell types. Before

discussing plus-end tracking mechanisms and highlighting the roles and regulation of various +TIPs in neurons, we touch upon the function of the MT cytoskeleton in the developing and mature nervous system. Moreover, we highlight the role of +TIPs in neurodegenerative and neurodevelopmental diseases. We conclude this review with an outlook on the future of neuronal +TIP research and briefly discuss the drug target potential of these pivotal proteins.

Microtubules in neurons

Neurons are derived from progenitor cells located in the ventricular zone deep inside the brain, necessitating young neurons to migrate large distances into remote regions. During their journey, neurons undergo dramatic changes in morphology and establish complex polarity. Even mature neurons must remain plastic as connections between neurons, synapses, are continuously rewired in response to stimuli. This intricate development relies heavily on both the MT and the actin cytoskeleton, on their crosstalk and on their accessory proteins. For a detailed analysis of the role of the cytoskeleton and in particular MTs during neuronal development, we refer the reader to a number of excellent reviews [1-3, 17]. Here, we briefly highlight some of the main events involving MTs during the maturation of multipolar neurons. It should be noted that the development of neurons extending a single process, unipolar neurons, is considerably different [18].

Microtubules during neurite formation and axon outgrowth

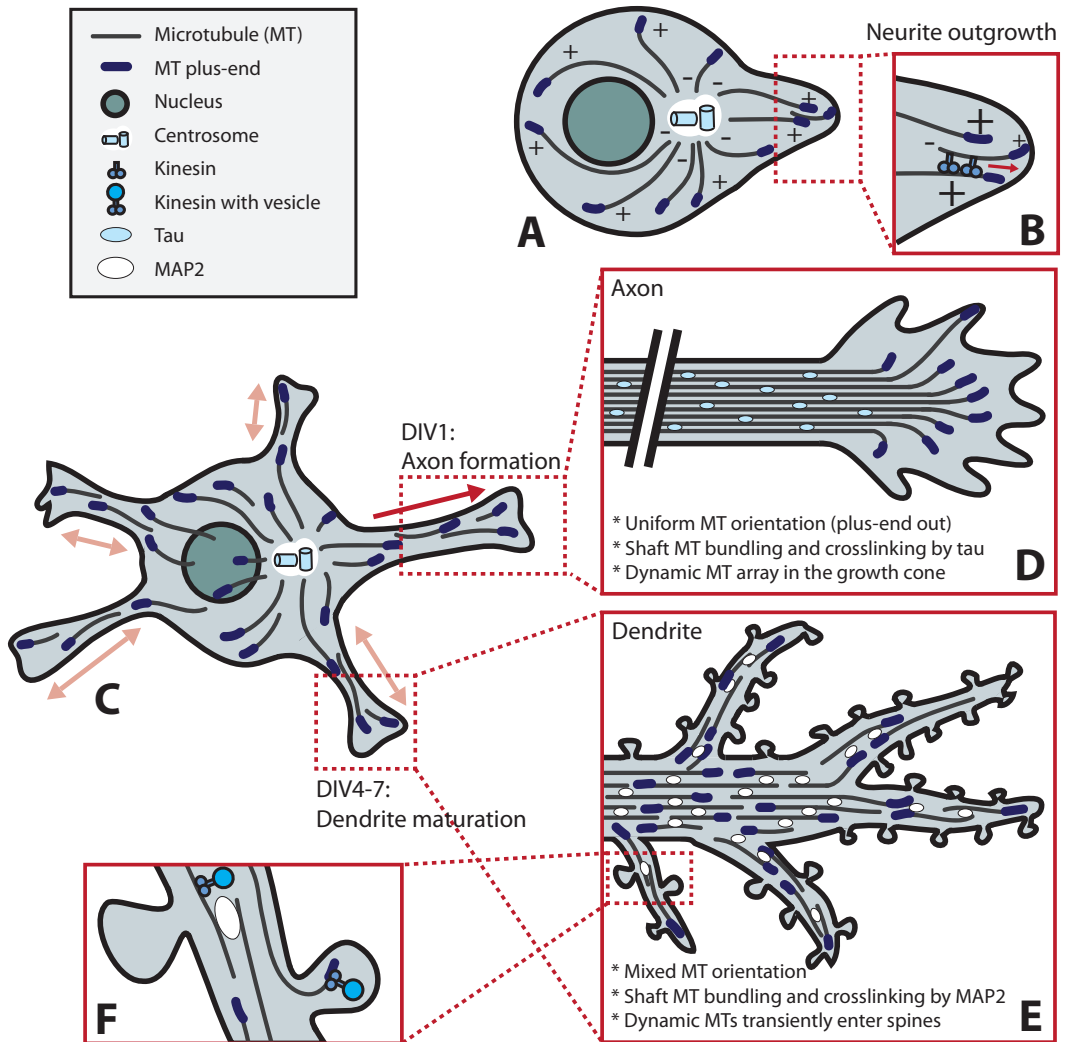
Neurons start out as spherical, unpolarized cells with a MT organization similar to that commonly found in mammalian cells (Fig. 1a). In young neurons, MTs mainly nucleate from the centrosome, with MT minus-ends pointing inward and plus-ends oriented towards the cell periphery [19]. Upon differentiation, neurons undergo symmetry breaking. During this event, the neuron extends multiple processes that start as small buds on the membrane and elongate to form thin protrusions [20]. These early protrusions, termed neurites, mature into axons and dendrites when the neuron polarizes. It has been proposed that neurite formation is powered, at least in part, by MT sliding. One model suggested that MAP2c (microtubule-associated protein 2c) induces stable MT bundles, which translocate to the membrane where

they exert a dynein-dependent force to trigger protrusion formation [21]. Another model proposed that the motor protein kinesin-1 powers the displacement of MTs along other MTs, exerting a mechanical force on the membrane which results in neurite extension [22] (Fig. 1b).

Shortly after neurite extension, the axon is formed (Fig. 1c). This event is preceded by local stabilization of MTs in the pre-axonal neurite [23]. As the newly formed axon starts to elongate, it relies on stable MT tracks for the transport of proteins and organelles necessary for the formation of new axonal segments [24]. The direction of axon outgrowth is determined by the growth cone, which probes the extracellular environment to allow non-random establishment of synaptic connections. Amidst the actin, which drives invasion of the extracellular matrix (reviewed in [25]), an array of MTs controls the direction in which the growth cone advances (Fig. 1d; [26]). The MT array assumes a looped conformation in pausing growth cones [27], while active growth cones maintain a dynamic MT array. These MTs probe the growth cone cortex and respond to guidance signals by being stabilized or destabilized, prompting the growth cone to turn towards or away from the guidance cue, respectively [24, 28]. As the axon matures further, it branches to

> **Figure 1. Microtubule organization and function during neurodevelopment**

Cultured dissociated neurons start out as spherical, unpolarized cells with MTs oriented with their plus-ends towards the plasma membrane (**a**). Upon symmetry breaking, neurite extension is thought to be facilitated by motor proteins, which were proposed to push MTs and thus exert a force on the membrane to form protrusions (**b**). Young neurons possess multiple neurites and maintain mainly plus-end out MT orientation (**c**). While remaining neurites cycle between phases of growth and shrinkage, one neurite rapidly extends to form the axon (**d**). In this neurite, MTs become stabilized and MT bundles are decorated with the axon-specific MAP tau, while MTs remain oriented plus-end out. The rate of advance and the directionality of axon outgrowth is controlled by the growth cone, a specialized structure at the tip of the axon that contains a dynamic array of MTs. Local stabilization of a MT in one of the filopodia of the growth cone prompts the growth cone to turn in that direction. Later in development, the remaining neurites differentiate into dendrites (**e**). Dendrites acquire unique antiparallel MT bundles decorated by MAP2, presumably contributing to selective cargo trafficking. The post-synapse is present at the tips of dendritic spines. Targeting of dynamic MTs to spines triggers morphological changes and alters synaptic strength (**f**), possibly by allowing the delivery of specific cargo to the spine or activating signaling processes.



allow higher interconnectivity. Branch formation is accomplished by splaying of tau-decorated MT bundles at branching sites. Here, dynamic MTs invade actin-rich areas close to the membrane to form a collateral branch [29]. Thus, while dynamic MTs play only a minor role in neurite outgrowth, they are crucial for axon polarization, pathfinding and branching.

Microtubules during dendrite maturation

Dendritic differentiation occurs later in development than axogenesis and prompts dramatic changes to the soon-to-be dendritic MT infrastructure. Prior to dendritogenesis, mammalian precursor neurites cycle between phases of growth and shrinkage and maintain ~80% plus-end out¹ MT directionality [30]. Perhaps the most striking feature of the dendritic MT cytoskeleton is the appearance of MTs with their minus-ends oriented towards the dendritic tips [31, 32] (Fig. 1e). However, it should be noted that the ratio between minus- and plus-end out MT orientations changes per neuron type and even differs between regions of the same dendrite. In invertebrates, as much as ninety percent of dendritic MTs are oriented minus-end out [33, 34]. Differences in MT orientations between axon and dendrites likely contribute to proper targeting of specific cargo by enabling transport by specific motor proteins. While dendrites branch more than axons, the behavior of MTs during this process has been studied less extensively. Specialized Golgi compartments called Golgi outposts were identified as potential sites of MT nucleation in centrosome-free *Drosophila* neurons [35], and were shown to localize to dendritic branch points [36]. Since axon branching depends on dynamic MTs arising from splayed bundles, it seems likely that dynamic MTs nucleated at Golgi outposts fulfill a similar role in dendritic branching [35].

Microtubules and synapses

The formation of synapses, connections between the axon of one neuron and the dendrite of another, is the final and ongoing step in neuronal maturation. Excitatory

¹With the terminology ‘plus-end out’, we designate MTs with their plus-end oriented towards the cell periphery, or towards dendritic or axonal tips. ‘Minus-end out’ indicates MTs of which the minus-end is oriented towards the cell periphery or process tips.

synapses are formed on dendritic spines, which are actin-rich protrusions on the dendrite that scaffold the post-synaptic density. The absence of MAP2-positive MTs in dendritic spines raised the belief that the MT cytoskeleton remained confined to the dendritic shaft [37]. However, visualization of the behavior of MTs and MT plus-ends revealed that dynamic MTs transiently invade dendritic spines by polymerizing from proximal sites [38-41]. MT-depolymerizing drugs such as nocodazole markedly reduce the number of spines while the number of dendrites remains unaffected [38]. Nocodazole also blocks the spine-inducing effect of the growth factor BDNF (brain-derived neurotrophic factor), while the MT stabilizing drug taxol enhances BDNF-induced spine formation [40]. Finally, depletion of end-binding protein 3 (EB3), a key scaffolding factor at the MT plus-end and regulator of MT dynamics discussed below, reduces the amount of spines [40]. These studies imply dynamic MTs as modulators of neuronal plasticity. +TIPs involved in synaptic remodeling may rely on dynamic MT plus-ends as a means of reaching spines targeted for remodeling [38]. Other candidate regulatory mechanisms may involve the facilitation of cargo delivery to the postsynaptic terminal [1] (Fig. 1f), though it remains to be elucidated exactly which events are at play.

Microtubule plus-end tracking proteins in neurons

MT behavior during neurodevelopment has been catalogued extensively. However, research has only just begun to uncover which factors control MT dynamics and how MTs are able to relay intricate signals in neurons. Many of the cellular processes and the molecular mechanisms that underlie them remain unknown to date.

Since +TIPs have emerged as potent MT regulators, they are excellent candidates to control MTs and relay their signals during neuronal development and homeostasis. Indeed, numerous +TIPs have already been linked to neurodevelopmental functions (Table I). New +TIPs are still discovered on a regular basis, and it is likely that additional roles for +TIPs in neurons will be uncovered in

(text continues after table I) >

Table I. Overview of +TIPs with confirmed functions and/or human disease significance in the nervous system.

+TIP (Aliases)	Mode(s) of MT plus-end association	Reported involvement in neuro-development	Human neurological disease association(s)	Refs
Amer2 (FAM123A)	SxIP motif	Neuronal migration		[188]
APC (DP2.5)	Autonomous; SxIP motif; Kinesin-dependent	Neuronal migration; Neurite outgrowth; Axon specification; Axon outgrowth; Axon branching; Growth cone steering; Synaptic maturation	Autism; Brain tumor-polyposis syndrome 2	[189-199]
APC2 (APCL)	SxIP motif	Neuronal migration; Axon branching; Growth cone steering	Sotos syndrome	[200-202]
CDK5RAP2 (Cep215)	SxIP motif	Neural progenitor cell division	Autosomal recessive primary microcephaly (ARPM)	[203-206]
CEP104 (KIAA0562)	SxIP motif		Joubert syndrome	[207]
ch-TOG (CKAP5)	Autonomous	Axon outgrowth		[128, 129]
CLASP1/2 (1: hOrbit1, KIAA0622; 2: hOrbit2, KIAA0627)	SxIP motif	Axon outgrowth; Growth cone steering; Dendritic branching; Synaptic maintenance; Synaptic activity		[90, 91, 93-96]
CLIP-115/170 (-115: CLIP2, WBSCR3, WBSCR4, KIAA0291; -170: CLIP1, CYLN1, Restin)	CAP-Gly domain	Axon formation; Axon outgrowth; Growth cone dynamics; Dendritic outgrowth; Dendritic branching	Williams Syndrome (CLIP-115); Autosomal recessive intellectual disability (CLIP-170)	[82, 83, 85, 208]
CTTNBP2 (CORTBP2, C7Orf8, KIAA1758)	SxIP motif	Dendritic branching; Dendritic spine formation; Dendritic spine maintenance; Synaptic signaling		[209-213]

Table I (continued).

+TIP (Aliases)	Mode(s) of MT plus-end association	Reported involvement in neuro-development	Human neurological disease association(s)	Refs
DDA3 (PSRC1, FP3214)	SxIP motif	Neurite outgrowth; Axon formation		[214]
EB1-3 (MAPRE1-3)	Autonomous	Neurite outgrowth; Axon formation; Dendritic branching; AIS maintenance; +TIP scaffolding* *note that due to their core function at the MT plus-end, it is difficult to separate EB roles in neurodevelopment from their scaffolding function		[64, 65, 67, 69, 215, 216]
FILIP1 (KIAA1275)	SxIP motif	Neuronal migration		[217]
iASPP (PPP1R13L, NKIP1, RAI)	SxIP motif	Neuronal fate after injury	Glioma; Stroke	[218-221]
KIF2C (MCAK, Kinesin-13)	SxIP motif; Plus-end directed motor activity		Glioma	[222]
KIF11 (Eg5, TRIP5, KNSL1)	SxIP motif	Neuronal migration; Neurite outgrowth; Axon outgrowth; Axon branching; Growth cone steering; Dendritic outgrowth; Cell surface receptor transport	Microcephaly with or without chorioretinopathy, lymphoedema, or mental retardation (MCLMR); Glioma	[223-231]
LIS1 (PAFAH1B1)	Via CLIP-170	Neural progenitor cell division; Neuronal migration; Neurite outgrowth; Axon outgrowth; Dendritic outgrowth; Dendritic branching; Synapse formation; Synaptic activity; Dynein-based transport	Lissencephaly; Subcortical band heterotopia (SBH)	[90, 91, 93-96]

Table I (continued).

+TIP (Aliases)	Mode(s) of MT plus-end association	Reported involvement in neuro-development	Human neurological disease association(s)	Refs
MACF1 (ACF7, Macrophin-1, ABP620, Trabeculin-alpha, KIAA1251)	SxIP motif	Neuronal migration; Axon outgrowth; Axon branching; Dendritic branching; Dendritic spine maturation	Spectraplaklinopathy type 1	[63, 99, 101, 144, 248, 249]
MACF2 (Dystonin, BPAG1, CATX15, Trabeculin-beta, KIAA0728)	SxIP motif	Axonal transport; Maintenance of axonal cytoskeleton integrity; Maintenance of Golgi integrity; ER stress level regulation; Autophagy	Dystonia; Hereditary sensory autonomic neuropathy	[104-109]
Neuron Navigators 1-3 (NAV1/2/3; Steerin-1/2/3; Unc53H1/2/3; -1: POMFIL3, KIAA1151, KIAA1213; -2: HELAD1, RAINB1, POMFIL2, KIAA1419; -3: POMFIL1, KIAA0938)	SxIP motif	Neuronal migration; Neurite outgrowth; Axon outgrowth	Neuroblastoma (NAV3)	[135, 250-258]
P140Cap (SNIP, SRCIN1, KIAA1684)	SxIP motif	Dendritic spine formation; Dendritic spine maintenance; Synaptic vesicle secretion		[38, 113, 115, 116, 259, 260]
p150glued (Dynactin subunit 1, DCTN1, p135, DAP-150)	CAP-Gly domain	Dynein-based transport	Perry syndrome; Hereditary Motor Neuropathy 7B (HMN7B); Amyotrophic lateral sclerosis (ALS)	[157, 159, 162, 163, 261, 262]
SLAIN1/2 (-1: C13orf32; -2: KIAA1458)	SxIP motif	Axon outgrowth		[128]

Table I (continued).

+TIP (Aliases)	Mode(s) of MT plus-end association	Reported involvement in neuro- development	Human neurological disease association(s)	Refs
STIM1 (GOK)	SxIP motif	Neural differentiation; Growth cone steering; Store-operated calcium entry	Amyotrophic lateral sclerosis (ALS); Neurogenic muscular atrophy; Huntington's Disease; Neuroblastoma; Brain damage after insult or injury	[118, 119, 263-269]
Syntabulin (Golsyn, KIAA1472)	SxIP motif	Axonal transport; Synaptic plasticity; Mitochondria trafficking		[270-273]
TACC3 (ERIC1)	Unclear	Neural progenitor cell division; Neuronal differentiation; Axon outgrowth		[274-277]
TRIO (ARHGEF23)	SxIP motif	Neuronal migration; Neurite outgrowth; Axon outgrowth; Growth cone steering		[258, 278- 285]
TTBK1 (KIAA1855)	SxIP motif		Alzheimer's Disease; Amyotrophic lateral sclerosis (ALS); Frontotemporal lobar degeneration (FTLD- TDP)	[176-178, 286]
TTBK2 (TTBK, KIAA0847)	SxIP motif	Ciliogenesis; GABA/osmolyte transport; Neuronal migration	Spinocerebellar ataxia type 11; Amyotrophic lateral sclerosis (ALS); Frontotemporal lobar degeneration (FTLD- TDP)	[167, 169, 172, 174, 178]

the future. Current knowledge suggests that, based on their mode of association with MTs, +TIPs can be divided into three categories: end-binding proteins (EBs), EB-dependent +TIPs and EB-independent +TIPs. It should be noted that even in the case of EB-independent +TIPs, there is crosstalk between these +TIPs and EBs albeit indirectly. Therefore, none of these categories can be regarded as fully independent.

End-binding proteins

EBs are at the core of the MT plus-end interactome. They are known to regulate MT behavior both autonomously and by providing a structural scaffold for other +TIPs [42-44]. EB plus-end tracking depends on an N-terminal calponin homology (CH) domain that grants MT affinity [45]. It has been shown that EB proteins associate with the MT plus-end by a CH-dependent nucleotide sensing mechanism [46, 47]. MT binding is regulated by a negatively charged C-terminal domain, which repels the negatively charged MT lattice and thereby contributes to specificity for the MT plus-end [48]. In addition, C-terminal coiled-coil and EB-homology domains mediate homo- and heterodimerization as well as interaction with other proteins including +TIPs [49, 50].

EBs mainly function as scaffolding proteins at the MT plus-end, where they form a hub for other +TIPs to associate with and thereby regulate local protein composition and MT dynamics. This is illustrated by the fact that EBs promote catastrophes when reconstituted with tubulin in biochemical preparations, while they reduce the number of catastrophes and promote continuous MT growth in cells. This suggests that EBs primarily act on other MT regulators in cells rather than autonomously [44]. Plus-end bound EBs rapidly exchange with the cytosolic pool, providing a rapidly remodeling platform for protein binding [43, 51]. Quantitative proteomic studies of non-neuronal cell lines have revealed that EBs are the most abundant plus-end binding proteins: the EB family outnumbers the second most abundant +TIPs by factors of approximately 7 to 30 in cultured fibroblasts [52, 53]. While technical limitations arising from sample heterogeneity have hampered large-scale quantitative proteomics studies in nerve cells [54], it is expected that EBs dominate neuronal MT plus-ends in a similar fashion as in cultured fibroblasts. The relatively high concentration of EBs compared to other +TIPs offers a simple explanation for how EB-decorated plus-ends are efficiently formed and maintained. Such a hub provides cells with an extra layer of control to regulate large numbers of

+TIPs with minimal changes to the MT cytoskeleton itself, making it easier to retain MT integrity and reliant functions alongside.

In mammalian cells, the EB family is represented by three members (EB1, EB2 and EB3), which all bind to MT plus ends but differ in their affinity for MT tips, phosphorylation and affinity for binding partners [44, 55-59]. EB1 and EB2 appear to be expressed ubiquitously, while EB3 is strongly expressed in muscle and brain tissue [60, 61]. During neurodevelopment, EB1 expression decreases while EB3 expression is upregulated [38]. Axon extension coincides with EB1 expression in neuroblastoma cells [62]. In *Drosophila*, depletion of EB1 impairs axon outgrowth and leads to the disorganization, but not loss, of MTs [63]. Other studies also point in the direction of a role for EB1 in axogenesis [64], and suggest a differential role of EB proteins in neurite formation. EB1 and EB3 have a positive role in neurite outgrowth, while EB2 has a negative effect [65], possibly because EB1 and EB3 have a higher affinity than EB2 for MT-stabilizing partners [56, 66]. EB3 has been specifically implicated in neuritogenesis in the context of actin-MT interactions [67], suggesting that the mechanisms underlying the importance of the EBs for controlling neuronal morphogenesis can be quite complex.

Apart from scaffolding other +TIPs, EBs may also aid the capture of MT plus-ends for regulatory purposes. For example, MTs are proposed to rely on EB3 and Drebrin to enter actin-rich spines. Drebrin interacts with the growing MT plus-end via an unconventional interaction with EB3 [67], and is enriched in spines by binding to F-actin [68]. Drebrin localization becomes enhanced in spines upon NMDA (N-Methyl-D-aspartate) receptor activity, whereupon Drebrin is believed to capture EB-decorated MT plus-ends near or in the spine neck and thereby guide dynamic MT entry into spines. Accordingly, Drebrin overexpression and increased amounts of F-actin upregulate the number of MT entries into spines [41].

Interestingly, another neuron-specific role for EB1/3 was reported that does not depend on plus-end tracking. EBs are enriched in the axon initial segment (AIS) of hippocampal neurons, where they contribute to AIS integrity and maintenance [69]. This possibly contributes to enhanced MT stability in the AIS [69], although the precise mechanism remains unclear.

EB-dependent +TIPs: CAP-Gly proteins

Most known EB-dependent +TIPs can be divided in two categories depending on

their mode of association with EB proteins. The first category consists of a minority of +TIPs that contain an evolutionarily conserved cytoskeletal-associated protein glycine-rich (CAP-Gly) domain, which associates with both EEY/F motifs in the C-terminus of EB proteins and tubulin [70-73].

An example of one such CAP-Gly domain-containing +TIP is p150glued: the largest out of eleven subunits of the dynactin complex. Dynactin is essential to nearly all functions of dynein, the most prominent minus-end directed motor protein [74]. Dynein plays a particularly important role in axons, wherein transport into the soma relies on minus-end directed transport due to the uniform plus-end out orientation of MTs. It is likely that multiple mechanisms contribute to dynein activation at different locations along the neuron [74]. At the MT plus-end specifically, one such model explains how retrograde transport is initiated when the dynamic MT plus-end loaded with p150glued and other dynein regulators encounters minus-end directed cargos ([75] and reviewed in [74]). While the role of dynactin in dynein plus-end targeting appears to differ between organisms [74], research suggests that dynactin accumulation at the MT plus-ends in axons of murine dorsal root ganglia (DRG) neurons contributes to long-range retrograde transport by recruiting dynein to vesicles [76]. It has been postulated that this function is exerted by a neuron-specific p150glued isoform, which reduces the frequency of catastrophes and thus increases MT stability [77].

Although p150glued binds to EBs directly, its affinity for MT plus ends appears not to be very high. In cells, p150glued is assisted in targeting the plus ends by another CAP-Gly domain containing protein, cytoplasmic linker protein of 170 kDa or CLIP-170 [76, 78]. Mammals also express a protein closely related to CLIP-170: the neuronally enriched CLIP-115 [79]. Both CLIPs are +TIPs, but differ by the structure of their C-termini. Only CLIP-170 contains zinc-binding domains and an EEY/F motif, which mediate the interactions with the CAP-Gly domain of p150glued and with the dynein regulator LIS1, as well as autoinhibition [78, 79]. Both CLIPs also promote MT rescue [80], although the underlying mechanism is still obscure, as it should involve depolymerizing MT ends or the MT lattice, where CLIPs are not enriched. Of note, CLIP plus-end tracking behavior is less prominent in neuronal compared to non-neuronal cells [81], which would be compatible with a function that is not directly related to growing MT tips. In addition to regulating dynactin recruitment, CLIPs are enriched in axonal growth cones, where they stabilize MTs

protruding into the actin-rich leading edge [82]. CLIPs are therefore necessary for axon formation and outgrowth as MT stabilization in the growth cone precedes engorgement and consolidation. CLIP-170 is involved in dendrite morphogenesis by regulating crosstalk between the actin cytoskeleton and dynamic MTs [83]. Given the importance of CLIPs for different processes in cultured neurons, the phenotypes of CLIP-115 and CLIP-170 knock-out mice are rather mild, though CLIP-115 knock-out animals do display behavioral phenotypes [84, 85]. The loss of CLIP-190, the *Drosophila* homologue of CLIP-170, causes no strong phenotype either [81]. This suggests that the neuronal function of CLIPs might be redundant with that of other MT regulators.

EB-dependent +TIPs: SxIP proteins

The largest subclass of EB-dependent +TIPs comprises proteins which utilize a short linear motif known as the SxIP motif (Serine/Threonine-any amino acid-Isoleucine/Leucine-Proline) to bind the EB homology domain ([42] and reviewed in [14]). SxIP motifs are generally embedded in unstructured amino acid stretches enriched in proline, serine and basic residues, resulting in a positive charge [42]. Further computational analysis revealed that the nine amino acids surrounding the SxIP motif cannot contain acidic amino acids, and that at least one basic amino acid is present in the four amino acids preceding the motif [56]. Since discussing all currently identified SxIP +TIPs is beyond the scope of this review, we here focus on a selection of prominent examples to illustrate the broad range of neurodevelopmental functions of these +TIPs. All currently known neurodevelopmental functions are listed per +TIP in Table I, along with their mode of association with the MT plus-end and the known neurological disease associations.

Among the most conserved SxIP proteins are CLASPs (cytoplasmic linker protein-associated proteins), the mammalian versions of which were discovered through their association with CLIPs [86]. Similar to CLIPs, there are two CLASP-encoding genes in mammals: *CLASP1*, which is expressed ubiquitously, and *CLASP2*, the products of which appear enriched in nervous tissue [86]. CLASPs utilize their SxIP motifs to bind EB1 and contain several additional TOG (tumor overexpressed gene) domains which can serve as tubulin-binding modules [87-89]. Different cell lines have revealed a function for CLASPs at the membrane, where they capture dynamic MT ends to promote MT rescue and pausing, and thus stabilize MTs [89,

90]. CLASP-mediated cortical MT stabilization is crucial to axon outgrowth and directionality and as such, CLASP was implicated in axon development in various organisms [90, 91]. Interestingly, CLASPs have affinity for both the MT plus-end and lattice, and differences in CLASP distribution and CLASP-MT associations inside the growth cone are able to direct axon growth status. CLASPs can be localized to the tips of growth cone filopodia, where they capture plus-ends of MTs to facilitate axon outgrowth. Conversely, in pausing growth cones, lattice-binding CLASP is present close to the end of the axon shaft to prevent MTs from protruding into the peripheral growth cone, thereby preventing outgrowth. The localization of CLASPs inside growth cones is regulated by kinases such as GSK3 β and Abelson kinase [90, 92-94]. In addition to axon growth status, the direction of axon outgrowth is regulated by CLASP localization. The kinase-controlled, asymmetric distribution of CLASPs to the filopodia of a growth cone determines the sites of MT capture and thereby dictates the direction in which the axon advances [94, 95]. Additional functions for CLASPs include a role in synaptic functioning likely via global control of neuronal morphology [95] and maintenance of the *Xenopus* growth cone lamellipodium [91]. Furthermore, CLASP2 mediates MT capture at the postsynaptic membrane to promote transport of acetylcholine receptors to neuromuscular junctions [96].

Morphological changes during neurodevelopment are the result of complex interplay between different components of the cytoskeleton. This is in part facilitated by the Microtubule-Actin Crosslinking Factor proteins MACF1 (ACF7) and MACF2 (Dystonin), known as spectraplakins. As spectraplakins nomenclature is complicated, we will here refer to MACF1/2. The reader is directed to Table I for a comprehensive list of alternative names for these proteins. Spectraplakins gain their name from membership of the spectrin family and their plakin repeats, which grant affinity for intermediate filaments [97]. Spectraplakins also contain CH domains to bind to actin, GAR (growth arrest-specific 2 protein-related region) domains to bind and stabilize MTs [98], and SxIP motifs to bind the MT plus-end via EBs. This places them at the heart of cytoskeletal crosstalk and renders them a popular subject for neurodevelopmental research. Indeed, homozygous MACF1 knockout mice are not viable, and mutant mice die from neuronal migration defects when MACF1 is depleted during development [99]. MACF1 is known to guide MTs along actin filaments and to mediate MT capture at actin-rich sites near the membrane [100], consistent with a role for MACF1 and its orthologs in growth cone microtubule

organization and axon extension [101]. In case of the *Drosophila* MACF1 ortholog Shot, this function was shown to depend on its SxIP motifs and interaction with EB1 [63]. MACF1 has also been implicated in formation of growth cone filopodia, although for Shot this function does not rely on its actin- or MT-binding domains [101].

The second mammalian spectraplaklin, MACF2 or dystonin, is best known for its role in the neurological disorder dystonia. MACF2 knockout mice develop dystonia and show repetitive muscle spasms [102], and mutations in MACF2 have been identified in patients with Hereditary Sensory Autonomic Neuropathy [103]. These pathologies are associated with the degeneration of sensory and autonomic nerves [102, 103]. Axons of MACF2 null mice degenerate as a result of MT fragmentation, which is believed to contribute to the dystonia phenotype independent of the neurofilament-binding functions of MACF2 [104]. MACF2 has also been implicated in retrograde axonal transport by interacting with p150glued [105]. This function may depend on MACF2's EB-dependent association with the MT plus-end, as overexpression of peptides which competitive block EB-SxIP interactions inhibit retrograde transport of endosomes [106]. Another important factor in dystonia may be the neuron's inability to regulate ER stress levels, Golgi integrity, MT acetylation and autophagy due to loss of a neuron-specific MACF2 isoform (BPAG1-a2) [107-109]. This particular isoform has an N-terminal transmembrane domain and does not localize to MTs [110], although it does affect MTs near the centrosome via an association with MAP1B [108] and retains the C-terminal SxIP motifs. The same isoform was shown to partially rescue phenotypes in a *dystonia musculorum* mouse model [111]. On the other hand, another neuron-specific MACF2 splice variant (BPAG1n3) exclusively binds MTs and may be involved in sustaining axonal MT integrity [104], suggesting distinct functions for different MACF2 isoforms. The same holds true for the many splice variants of MACF1, and more research is needed to elucidate the contribution of spectraplaklin plus-end tracking to their functions in both nerve cells and in other cell types.

+TIPs play important roles also in mature neurons, as neurons remain plastic throughout their lifespan and remodel synapses in response to both intra- and extracellular cues. One such +TIP with a function at the synapse is p140Cap, whose name is a combination of its molecular weight and 'Cas-associated protein' (Cap; Cas for Crk-associated substrate). p140Cap is regarded as a tumor suppressor

protein due to its function as an inhibitor of Src kinase, which is involved in cell migration and growth [112]. In addition to its potential to associate with MT plus-ends via an SxIP/EB3-mediated interaction, p140Cap binds actin fibers and localizes to actin-rich dendritic spines of hippocampal neurons [38, 112]. p140Cap knockout mice display impaired learning and memory functions, and spine defects have been observed in the absence of p140Cap both in cultured primary neurons and in knockout mice [38, 113]. Synaptosomes prepared from *p140Cap*^{-/-} mice reveal hyperactivation and hyperphosphorylation of Src kinase and its substrate cortactin, respectively, as well as reduced RhoA activity [113]. Research suggests that p140Cap forms a synaptic complex with and increases the interaction between Src kinase and Citron-N, a protein known to scaffold the actin remodeling machinery, and as such controls spine morphology [113]. EB3 appears to function upstream of the spine remodeling process as synaptic phenotypes of EB3 knockdown mimic those of p140Cap knockdown, and can be rescued by simultaneous overexpression of p140Cap or Citron-N [38, 113]. Notably, while overexpressed p140Cap tracks MT plus-ends in neurons, this is rarely the case for endogenous p140Cap. p140Cap's affinity for local binding partners in spines is likely sufficiently high to prevent cytoplasmic diffusion necessary for MT plus-end tracking behavior [38, 114]. In addition to its function at the postsynapse, p140Cap likely plays a role at the presynapse where it interacts with several proteins implicated in synaptic vesicle secretion [115, 116].

Another interesting SxIP-containing partner of EB1 is the Stromal interaction molecule 1 or STIM1 [117], a transmembrane ER protein which contains one SxIP motif and can thus link EB-decorated MT plus-ends to the ER membrane. STIM1 regulates store operated calcium entry (SOCE) in neurons and is necessary to resupply the ER with calcium by opening plasma membrane channels after calcium release during synaptic signaling [118, 119]. The function of the interaction of STIM1 with MT tips is not yet entirely clear. STIM1 participates in ER tubule extension by coupling growing MT plus-ends to the ER [117], and it is possible that such ER remodeling contributes to SOCE in certain cell types by bringing STIM1 in the vicinity of the plasma membrane. Interestingly, in HEK293T cells changes in MT dynamics affect STIM1's association with calcium channels [120], suggesting that in some cell types MT dynamics are important for calcium signaling, possibly via the action of +TIPs. It remains to be verified, however, what the exact contribution of

STIM1's plus-end tracking behavior is to SOCE in neurons. Part of the answer may come from the function of STIM2, a STIM1 homolog with 63% sequence identity but without conservation of the SxIP motif. STIM2 regulates SOCE instead of STIM1 in pyramidal neurons of the neocortex [121], suggesting that plus-end tracking is not required for STIM functioning during SOCE in neurons. However, remodeling of the ER was observed along MTs during SOCE [122]. As STIM1 was found to remodel the ER via its interaction with EB1 in HeLa cells [117], there is a possibility STIM1 may exert additional, potentially plus-end tracking-dependent functions in neurons. This is underlined by the finding that STIM1 participates in growth cone steering, and that this effect is only coupled to effects on SOCE for certain guidance cues [118].

To summarize, SxIP motif-containing proteins represent a large and heterogeneous group of EB-dependent +TIPs, which exert different functions at different stages of neurodevelopment. Although many roles have been identified (Table I), it is not always clear what the contribution of plus-end tracking behavior is to each of these functions.

Other +TIPs

While EB proteins are responsible for targeting a large variety of proteins to microtubule tips, several major classes of microtubule plus-end interacting factors target the growing MT plus-end via other mechanisms. These include the MT polymerase ch-TOG/XMAP215 and certain kinesin motor proteins, such as Kinesin-4, -8 and -13 family members (see below). In addition, for some MT- or tubulin-binding proteins, such as Doublecortin and stathmin, specific interaction with MT plus-ends was established or proposed based on *in vitro* reconstitution experiments [123, 124]. However, this was not demonstrated in cells, and is therefore not further discussed here.

ch-TOG/XMAP215 can track the growing plus-ends of MTs directly by recognizing the outmost MT tips [125, 126], or indirectly, via EB proteins. In mammalian cells, MT plus-end tracking of ch-TOG is facilitated by binding to SLAIN proteins, which themselves are EB-dependent, SxIP-containing +TIPs that have the ability to bind a number of other +TIPs [127]. Both SLAIN1/2 and ch-TOG are enriched in mammalian brain tissue, and promote MT growth by positioning the MT polymerase at the tip of the growing MT [128]. Like the majority of +TIPs implicated in maintaining MT cytoskeleton integrity, ch-TOG plays a role in axon outgrowth.

Depletion of ch-TOG increases catastrophe rates in all subcellular compartments of rat hippocampal neurons, while reducing MT growth rates [128]. Axon outgrowth defects are apparent in young neurons depleted of ch-TOG, as well as in those overexpressing a dominant negative SLAIN construct that prevents ch-TOG from accumulating at the MT plus-end [128]. In *Xenopus*, the ch-TOG homolog XMAP215 is necessary for MTs to resist axon retraction induced by contractile actin forces and thereby promotes persistent axon outgrowth [129]. Interestingly, depletion of XMAP215 results in increased rate of MT plus end displacement specifically in the growth cone but not in axons. This effect does not seem to depend on XMAP215's MT-polymerizing function, which relies on plus-end localization, but rather seems to be a result of an additional role for *Xenopus* XMAP215 in MT sliding [129].

The kinesin-4 family member KIF21A is also involved in axon development. In HeLa cells, KIF21A is part of a cortical MT-anchoring complex that includes CLASP, where KIF21A acts as a growth inhibitor to prevent further polymerization of MTs that reach the cell cortex [130]. Missense mutations in KIF21A cause Congenital Fibrosis of the Extraocular Muscles type 1 (CFEOM1), a disease characterized by the patients' inability to control eye movements due to defects in oculomotor nerve development [131]. These mutations were found to prevent KIF21A autoinhibition, promoting increased cortical MT growth inhibition via an EB-independent interaction of KIF21A with the MT plus-end [130, 132]. Mutant KIF21A results in growth cone and axon pathfinding defects in cultured neurons and knockin mice, suggesting that improper innervation of extraocular muscles in CFEOM1 is a result of misregulation of MT dynamics by KIF21A [130, 132].

Regulation of microtubule-+TIP interactions

It is clear that elaborate control of the MT cytoskeleton, which involves tight regulation of interactions between +TIPs and MTs, is of pivotal importance to neurons.

Since many +TIPs use the same mode of association with EBs, competitive binding between +TIPs from the same subclass is a major factor in the regulation

of interactions. This is illustrated by the use of SxIP-motif containing peptides to disrupt +TIP complexes and MT dynamics in literature (e.g. [133, 134]), and such competition was proposed between CLIP-115 and CLIP-170, for example [85]. However, competition between different subclasses has also been reported. For instance, the SxIP-motif containing Neuron Navigator (NAV) +TIPs have been shown to displace p150glued from MT plus-ends upon overexpression [135], although p150glued relies on CAP-Gly domains to associate with EBs. Small SxIP peptides can also abolish p150glued and CLIP binding to MT plus-ends in *in vitro* reconstitution assays, confirming that binding sites on EBs for different +TIPs of different subclasses overlap at least partly [133]. Additionally, it will be interesting to see whether +TIPs can provide indirect feedback to other +TIPs by impacting cytoskeleton dynamics or by affecting the conformation of EB proteins.

Not all dominant +TIP-EB interactions negatively impact the recruitment of other +TIPs. For instance, EB1 is sufficient to independently recruit both p150glued and CLIP-170 to the MT plus-end in reconstitution assays using purified proteins, but p150glued binds the plus-end tighter in the presence of CLIP-170 because of an additional interaction between the two +TIPs [133]. A similar mechanism is employed by SLAIN2, which likely uses interactions with multiple +TIPs to overcome the issue of competition [127]. Intuitively, multiplying the number of binding modules should also increase the affinity of +TIPs for the MT plus-end. This has been shown for both the repetition of SxIP motifs within individual proteins and for increases in the number of SxIP motifs via oligomerization [42].

Apart from effects arising from the presence of other +TIPs at the MT-plus end, modifications of MTs or +TIPs provide additional layers of control. At the MT level, post-translational tubulin modifications favor binding of certain +TIPs over others. For example, CAP-Gly +TIPs only associate with MT-plus ends containing tyrosinated α -tubulin [71, 136]. Presence of the C-terminal tyrosine on α -tubulin also promotes MT interaction with another +TIP, the SxIP-containing kinesin-13 KIF2C/MCAK (mitotic centromere-associated kinesin), which has a MT-destabilizing function [137]. MAPs present on the MT lattice may also contribute to regulation of +TIP binding: MAP1B is able to capture cytosolic EBs and immobilize them along MTs, effectively lowering the concentration of EBs at the plus-end of the MT and thereby fine-tuning axon outgrowth [138]. Likewise, MAP2 recruits EBs to the MT lattice in dendrites upon synaptic stimulation [139] and tau was recently reported

to bind to EB1. Tau expression levels may also regulate EB localization, as high levels of tau result in EB immobilization along the MT lattice [10].

At the +TIP level, phosphorylation is considered the classic mechanism to regulate binding. Phosphorylation of +TIPs results in unfavorable electrostatic interactions with negatively charged MTs and may promote +TIP accumulation at the MT plus-end rather than along the MT lattice, or abrogate binding altogether [15, 114]. Phosphorylation of +TIPs in the vicinity of SxIP motifs can also suppress binding to the negatively charged C-terminal part of EBs and thus the plus-end tracking [42]. Many +TIPs involved in axon outgrowth are substrates of GSK3 β [92, 140-142], a kinase involved in prominent signaling pathways such as the phosphoinositide 3-kinase (PI3K)/Akt pathway and Wnt signaling. In addition to the previously discussed role of CLASP as a GSK3 β substrate during axon outgrowth, GSK3 β exerts control on the +TIP APC during growth cone advance [140, 143]. Binding of the spectraplaklin +TIP MACF1 to MTs is also under control of GSK3 β , and the GSK3 β -MACF1 interaction plays a role in pyramidal neuron migration [142, 144]. Interestingly, both APC and MACF1 were suggested to regulate GSK3 β activity during Wnt signaling [145, 146], hinting at the existence of complex feedback loops between +TIPs and signaling pathways during neurodevelopment.

A second kinase with strong connections to +TIP regulation is the Abelson kinase (Abl). Together with its substrate, Abelson interacting protein (Abi), Abl orchestrates actin dynamics important for *Drosophila* axon guidance and synaptogenesis [90] and appears to link +TIPs to the actin remodeling machinery. The +TIP NAV2 can promote actin polymerization by interacting with Abi at sites targeted by pioneer MTs [147]. Abl also interacts with p140Cap and is required for p140Cap-mediated actin remodeling [148], although this interaction has not yet been explored in neurons. Interestingly, Abl controls axon guidance via CLASP, which is also under control of GSK3 β during the same process [90, 93]. Possibly, multiple signaling pathways and kinases act in parallel on the same +TIPs to allow additional levels of control.

Although phosphorylation remains the best-studied mechanism for regulation of MT-+TIP associations, other types of regulation have started to gain attention. For example, EB1 acetylation has been postulated to regulate binding of the SxIP motif-containing +TIP DDA3 during directional cell migration [149]. Intracellular calcium levels determine whether the MACF2 isoform BPAG1n4

localizes to the lattice or to the plus-end of MTs [150]. Finally, since individual EB proteins display different affinities for their binding partners [56, 151], their expression levels can also affect the composition of +TIP networks in way dependent on the cell type or developmental stage.

Microtubule plus-end tracking proteins in brain diseases

For certain neurological disorders, MT dynamics have been examined by live imaging of +TIPs. In case of multiple sclerosis, a neuroinflammatory condition associated with axonal transport defects and motor neuron degeneration, the number of EB3-positive microtubule plus-ends was found to increase and their directionality was altered in swollen axons of mouse models [152]. Microtubule plus-end dynamics were also investigated in *C. elegans* after axon damage, which can occur after spinal cord injury or stroke in humans. As expected, axon severing generated a large amount of dynamic MT plus-ends at the newly formed tip of the axon, but interestingly axon regrowth depended on the *C. elegans* EB homolog EBP-1 and could be inhibited by overexpression the MT catastrophe-promoting protein EFA-6 (Exchange Factor for Arf6) [153]. Consistently, axon injury or stress induced by the expression of expanded polyglutamine proteins led to increased microtubule dynamics, which had a neuroprotective role by delaying or counteracting neuron degeneration in *Drosophila* [154].

While such studies strongly imply that regulation of MT dynamics is important in the response to neurological damage and disease, the underlying mechanisms are still poorly understood. Due to their diverse range of neurodevelopmental functions, many +TIPs are involved in human neurological disorders (Table I), with mutations in certain +TIPs found to directly cause neurological disease. In this section, we highlight two +TIPs and associated diseases for which the role of plus-end tracking has been investigated at least to some extent: p150glued and tau-tubulin kinase 2 (TTBK2). In addition we consider TTBK1, the closest homolog of TTBK2.

P150glued in Perry syndrome and Hereditary Motor Neuropathy 7B

As described earlier in this review, p150glued is an essential component of the retrograde axonal transport machinery by regulating and positioning dynein at MT plus-ends. Mutations in the CAP-Gly domain of p150glued, which is required for p150glued binding to EBs and MTs [155, 156], cause two distinct neurological disorders: Perry syndrome and Hereditary Motor Neuropathy 7B (HMN7B). HMN7B affects motor neurons. Symptoms ensue in early adulthood and include muscle atrophy, vocal fold paralysis and breathing difficulties [157]. By contrast, Perry Syndrome (reviewed in [158]) mainly affects neurons in the substantia nigra but not motor neurons. This rare syndrome manifests itself around 46 years of age and is associated with parkinsonism, depression, hypoventilation and weight loss.

Interestingly, the p150glued mutations that give rise to these different conditions are in close proximity: G59S mutations cause HMN7B [157], and G71(R/E/A), T72P and Q74P mutations were identified in Perry syndrome patients [159]. Differences between these two diseases may in part be explained by the effect of these mutations on the stability of p150glued. In case of the HMN7B mutation, mutant p150glued aggregates and is incorporated into inclusion bodies [160, 161]. However, p150glued's global folding and stability is largely unaffected by Perry syndrome mutations [161]. This observation is reflected by the presence of dynactin aggregates in motor neurons of HMN7B patients [162], which are believed to contribute to cell death [160]. Such inclusions are less common in Perry syndrome patients [159]. All mutations disturb the interactions between p150glued and EB proteins or MTs [157, 159, 163], but functional differences between mutated forms of p150glued were also reported. The HMN7B mutation globally perturbs axonal transport by disturbing dynactin binding to dynein when mutant p150glued is incorporated in the dynactin complex. Conversely, Perry syndrome mutations do not affect global axonal transport, but G71R p150glued has as a dominant negative effect on the initiation of retrograde trafficking from distal axon tips [163]. This function directly depends on p150glued's interaction with EB proteins at the MT plus-end [76]. Another potentially disease-related mechanism is the MT catastrophe-suppressing function of p150glued, which is disturbed by the Perry syndrome mutation Q74P [77]. p150glued's ability to suppress catastrophes relies on its binding to MTs and free tubulin dimers, and is independent of EB proteins. p150glued isoforms harboring all domains necessary for these interactions are

primarily expressed in neurons, rendering the effect neuron-specific.

p150glued's involvement in Perry syndrome and HMN7B is an excellent example of how deficiencies in plus-end tracking can result in neurological disease. It underlines the importance of investigating the role of plus-end tracking for +TIPs implicated in disorders of the brain, yet surprisingly, p150glued remains the single best-studied case.

TTBK1/2 in spinocerebellar ataxia and Alzheimer's disease

Two other, closely related +TIPs firmly implicated in brain disease are tau-tubulin kinase 1 and 2 (TTBK1 and TTBK2). TTBK1/2 belong to the casein kinase 1 group and share 60% sequence identity, primarily between their N-terminal kinase domains (reviewed in [164]). Both TTBK proteins contain two SxIP motives in their C-terminal tail [56], which is only present in vertebrates [164].

TTBK2 was the first tau-tubulin kinase to be identified, phosphorylating MAP2 and α -casein in addition to tau and tubulin [165]. TTBK2 is expressed ubiquitously [166] and can phosphorylate tau at sites identified in paired helical filament tau, a hyperphosphorylated tau variant found in the brains of Alzheimer's disease (AD) patients [166]. Mutations in TTBK2, which yield a mutant protein truncated after the N-terminal kinase domain, cause spinocerebellar ataxia type 11 (SCA11) [167]: a rare neurodegenerative disease of which symptoms include pronunciation difficulties, involuntary eye movement and ataxia [168]. So far, the brain of one SCA11 patient has been examined and revealed the presence of tau deposits among other signs of pathological aging and cerebellar degeneration, raising the possibility that aberrant tau phosphorylation by mutant TTBK2 contributes to SCA11 pathology [167]. In addition, TTBK2 was more recently shown to be required for the formation of cilia by promoting the removal of the centriolar capping protein CEP110 to allow axoneme extension [169]. Diseases resulting from cilia defects, termed ciliopathies, often affect the brain (reviewed in [170]), and mice harboring a mutation that prematurely truncates TTBK2 lack certain neural cell types known to be lost in cilia-depleted animal models [169]. Since the SCA11-mutated form of TTBK2 is unable to initiate ciliogenesis and can interfere with the ciliary function of full-length TTBK2, TTBK2's function in cilia formation provides a second explanation for the symptoms of SCA11 [169]. However, the EB1-TTBK2 interaction plays no role in the recruitment of TTBK2 to the basal body or in the subsequent initiation

of ciliogenesis [171]. Recently, TTBK2 was found to phosphorylate the kinesin-13 family member KIF2A at the plus-end of MTs in an EB-dependent manner. This interaction regulates the binding and thereby depolymerization of MTs by KIF2A in HeLa cells [172]. The same study suggested that TTBK2 can exist in an auto-inhibited conformation, wherein the kinase domain is folded back onto the tail domain containing the SxIP motifs. Binding of EB would liberate the kinase domain and promote kinase activity, presenting an attractive mechanism for how TTBK kinase activity can be regulated at the plus-end of MTs [172]. Interestingly, overexpressed TTBK2 is also able to displace EB1 from the MT plus-end, and TTBK2 affinity to MTs itself appears to be regulated by its autophosphorylation, suggesting that TTBK2 has the potential to regulate +TIP-MT associations [56]. These studies clearly signal the importance of TTBK2's interaction with EBs and MT plus-ends. The direct relevance of plus-end tracking for neuronal functions of TTBK2 other than ciliogenesis has not been investigated. It is thus currently unclear whether the functions attributed to TTBK2, such as the earlier discussed pathological tau phosphorylation, a role in neuronal migration [172], regulation of the retrieval of synaptotagmin-1 during synaptic vesicle endocytosis [173] or the control of the activity of transport channels including BGT1, a betaine/ γ -amino-butyric acid (GABA) transporter [174], require TTBK2 plus-end tracking.

Full-length TTBK1 was only characterized in 2006 as a neuron-specific kinase with the ability to phosphorylate tau on sites associated with AD [175]. During AD, tau becomes hyperphosphorylated, causing it to detach from MTs and form non-soluble aggregates in the cytosol. Certain genetic variations of TTBK1 have been linked to lower risk of developing AD [176, 177], suggesting that TTBK1 and variations in its expression levels may play a role in Alzheimer pathology. Full-length TTBK1 co-localizes with EB1 and bundles MTs at high expression levels independent of its kinase activity [56], but the contribution of TTBK1 plus-end tracking and MT modulation has never been investigated in disease and function.

More recently, TTBK1 and TTBK2 were also shown to phosphorylate TDP-43 (transactive response DNA binding protein of 43 kDa) [178], the phosphorylation-driven aggregation of which is a hallmark of amyotrophic lateral sclerosis and frontotemporal lobar degeneration as well as numerous other neurodegenerative diseases [179]. Understanding the cell biology of these kinases both in health and disease, as well as mapping the full range of substrates of TTBKs will be a crucial step towards the identification of targets for therapeutic intervention.

Future outlook

As versatile regulators of the MT cytoskeleton, +TIPs play important roles in all aspects of neurodevelopment. It is therefore not surprising that +TIPs are involved in many neurological diseases (Table I). However, although more is known about how individual +TIPs affect MT behavior and integrity, in many cases this knowledge is yet to be extrapolated to neuronal MT networks and in some cases insight is lacking altogether.

It is crucial to develop such understanding as pharmacological intervention with +TIPs, and thereby specific subsets or properties of MTs, likely provides a more elegant and refined approach to therapy development than the use of MT targeting agents that globally impact MT dynamics. The influence of low doses of MT-targeting drugs on neurons has been studied extensively and was found to impact nearly all processes in developing and mature neurons. For example, treatment with 15-75 nM of the MT destabilizer nocodazole impairs the formation (but not outgrowth) of neurites in young dissociated neurons [23]. At 200 nM, nocodazole was also reported to inhibit primary dendrite formation [83] and has the ability to transform mature, mushroom-headed spines of dendrites into filopodia [38]. These morphological spine changes are paired with decreased synaptic response [38]. The MT stabilizing drug taxol, on the other hand, is known to induce the formation of multiple axons in young dissociated neurons at concentrations as low as 3 nM [23], and nanomolar concentrations of both MT stabilizing and destabilizing drugs affect axon pathfinding [28]. The above effects on neurons were mostly found to be a result of altered MT dynamics, rather than drug-specific effects on other cellular processes. It is therefore reasonable to assume that treatment with other MT-targeting agents results in similar effects on neuronal development and functioning.

MT-targeting agents do provide evidence that drugs altering MT dynamics may be successful in treating brain diseases. For example, the MT stabilizing, blood-brain-barrier penetrant drug epothilone D shows promise as a therapeutic agent in neurological disorders, as epothilone D treatment partially relieves pathology in Alzheimer's mouse models [180]. Recently, the closely related MT stabilizing agent epothilone B also proved to stimulate regeneration of axons after spinal cord injury in rats [181]. However, in contrast to the global effect of MT-targeting

drugs which can yield unintended side effects, individual +TIPs may be restricted to certain subcellular localizations or tissues, be expressed only at certain time points, or influence only limited aspects of MT behavior. Even when they are not involved in establishing pathogenesis, they can potentially be stimulated or inhibited to counteract MT-related disease mechanisms. Of note, it has recently been proposed that the neuroprotective peptide NAP possibly exerts its effects via EBs. NAP affects the brain-specific tubulin pool as well as MT stability and dynamics [182, 183], and has been described to have beneficial effects in tauopathy animal models [184-186]. NAP is believed to bind EB3 via an alternative SxIP motif, Ser-Ile-Pro, and EB silencing in PC12 cells obliterates the protective effect of NAP to zinc toxicity. Although the precise mechanism remains unclear, these data suggest that NAP's binding to EBs may contribute to its neuroprotective properties [187].

In summary, +TIPs may offer a more precise approach to interfere with pathological MT-related processes, rather than conventional MT-targeting agents currently used in the clinic. In order to truly establish their potential as therapeutic targets for treatment against neurological disorders, more research is needed into the functions and mechanisms of action of an ever-growing pool of +TIPs. New +TIPs are still being recognized on a large scale (e.g. [56]), rendering the field of +TIP research an exciting and promising one for years to come.

References

1. Hoogenraad, C.C. and F. Bradke, Control of neuronal polarity and plasticity--a renaissance for microtubules? *Trends Cell Biol*, 2009. 19(12): p. 669-76.
2. Conde, C. and A. Caceres, Microtubule assembly, organization and dynamics in axons and dendrites. *Nat Rev Neurosci*, 2009. 10(5): p. 319-332.
3. Kapitein, L.C. and C.C. Hoogenraad, Building the Neuronal Microtubule Cytoskeleton. *Neuron*, 2015. 87(3): p. 492-506.
4. Wells, W.A., Microtubules get a name. *J Cell Biol*, 2005. 168(6): p. 852-853.
5. Slautterback, D.B., CYTOPLASMIC MICROTUBULES. I. HYDRA. *J Cell Biol*, 1963. 18: p. 367-88.
6. Ledbetter, M.C. and K.R. Porter, A "MICROTUBULE" IN PLANT CELL FINE STRUCTURE. *J Cell Biol*, 1963. 19(1): p. 239-50.
7. Desai, A. and T.J. Mitchison, Microtubule polymerization dynamics. *Annu Rev Cell Dev Biol*, 1997. 13: p. 83-117.
8. Dehmelt, L. and S. Halpain, The MAP2/ Tau family of microtubule-associated proteins. *Genome Biology*, 2005. 6(1): p. 204-204.

9. Lee, G. and C.J. Leugers, chapter 8 - Tau and Tauopathies, in *Progress in Molecular Biology and Translational Science*, B.T. David, Editor. 2012, Academic Press. p. 263-293.
10. Sayas, C.L., et al., Tau regulates the localization and function of End-binding proteins 1 and 3 in developing neuronal cells. *J Neurochem*, 2015. 133(5): p. 653-67.
11. Jiang, K., et al., Microtubule minus-end stabilization by polymerization-driven CAMSAP deposition. *Dev Cell*, 2014. 28(3): p. 295-309.
12. Akhmanova, A. and C.C. Hoogenraad, Microtubule minus-end-targeting proteins. *Curr Biol*, 2015. 25(4): p. R162-71.
13. Nogales, E., Structural insights into microtubule function. *Annu Rev Biochem*, 2000. 69: p. 277-302.
14. Kumar, P. and T. Wittmann, +TIPs: SxIPping along microtubule ends. *Trends Cell Biol*, 2012. 22(8): p. 418-28.
15. Akhmanova, A. and M.O. Steinmetz, Tracking the ends: a dynamic protein network controls the fate of microtubule tips. *Nat Rev Mol Cell Biol*, 2008. 9(4): p. 309-22.
16. Akhmanova, A. and M.O. Steinmetz, Control of microtubule organization and dynamics: two ends in the limelight. *Nat Rev Mol Cell Biol*, 2015. 16(12): p. 711-26.
17. Poulain, F.E. and A. Sobel, The microtubule network and neuronal morphogenesis: Dynamic and coordinated orchestration through multiple players. *Mol Cell Neurosci*, 2010. 43(1): p. 15-32.
18. Sanchez-Soriano, N., et al., Are dendrites in *Drosophila* homologous to vertebrate dendrites? *Dev Biol*, 2005. 288(1): p. 126-38.
19. Kuijpers, M. and C.C. Hoogenraad, Centrosomes, microtubules and neuronal development. *Mol Cell Neurosci*, 2011. 48(4): p. 349-58.
20. Gotz, M. and W.B. Huttner, The cell biology of neurogenesis. *Nat Rev Mol Cell Biol*, 2005. 6(10): p. 777-88.
21. Dehmelt, L., et al., A microtubule-based, dynein-dependent force induces local cell protrusions: Implications for neurite initiation. *Brain Cell Biol*, 2006. 35(1): p. 39-56.
22. Lu, W., et al., Initial neurite outgrowth in *Drosophila* neurons is driven by kinesin-powered microtubule sliding. *Curr Biol*, 2013. 23(11): p. 1018-23.
23. Witte, H., D. Neukirchen, and F. Bradke, Microtubule stabilization specifies initial neuronal polarization. *J Cell Biol*, 2008. 180(3): p. 619-32.
24. Geraldo, S. and P.R. Gordon-Weeks, Cytoskeletal dynamics in growth-cone steering. *J Cell Sci*, 2009. 122(Pt 20): p. 3595-604.
25. Dent, E.W. and F.B. Gertler, Cytoskeletal dynamics and transport in growth cone motility and axon guidance. *Neuron*, 2003. 40(2): p. 209-27.
26. Tanaka, E., T. Ho, and M.W. Kirschner, The role of microtubule dynamics in growth cone motility and axonal growth. *J Cell Biol*, 1995. 128(1-2): p. 139-55.
27. Tanaka, E.M. and M.W. Kirschner, Microtubule behavior in the growth cones of living neurons during axon elongation. *J Cell Biol*, 1991. 115(2): p. 345-63.
28. Buck, K.B. and J.Q. Zheng, Growth cone turning induced by direct local modification of microtubule dynamics. *J Neurosci*, 2002. 22(21): p. 9358-67.
29. Dent, E.W. and K. Kalil, Axon branching requires interactions between dynamic microtubules and actin filaments. *J Neurosci*, 2001. 21(24): p. 9757-69.
30. Yau, K.W., et al., Dendrites In Vitro and In Vivo Contain Microtubules of Opposite Polarity and Axon Formation Correlates with Uniform Plus-End-Out Microtubule Orientation. *J Neurosci*, 2016. 36(4): p. 1071-85.

-
- 31.** Baas, P.W., et al., Polarity orientation of microtubules in hippocampal neurons: uniformity in the axon and nonuniformity in the dendrite. *Proc Natl Acad Sci U S A*, 1988. 85(21): p. 8335-9.
- 32.** Baas, P.W., M.M. Black, and G.A. Banker, Changes in microtubule polarity orientation during the development of hippocampal neurons in culture. *J Cell Biol*, 1989. 109(6 Pt 1): p. 3085-94.
- 33.** Stone, M.C., F. Roegiers, and M.M. Rolls, Microtubules have opposite orientation in axons and dendrites of *Drosophila* neurons. *Mol Biol Cell*, 2008. 19(10): p. 4122-9.
- 34.** Maniar, T.A., et al., UNC-33 (CRMP) and ankyrin organize microtubules and localize kinesin to polarize axon-dendrite sorting. *Nat Neurosci*, 2012. 15(1): p. 48-56.
- 35.** Ori-McKenney, K.M., L.Y. Jan, and Y.N. Jan, Golgi outposts shape dendrite morphology by functioning as sites of acentrosomal microtubule nucleation in neurons. *Neuron*, 2012. 76(5): p. 921-30.
- 36.** Ye, B., et al., Growing dendrites and axons differ in their reliance on the secretory pathway. *Cell*, 2007. 130(4): p. 717-29.
- 37.** Matus, A., Actin-based plasticity in dendritic spines. *Science*, 2000. 290(5492): p. 754-8.
- 38.** Jaworski, J., et al., Dynamic microtubules regulate dendritic spine morphology and synaptic plasticity. *Neuron*, 2009. 61(1): p. 85-100.
- 39.** Hu, X., et al., Activity-dependent dynamic microtubule invasion of dendritic spines. *J Neurosci*, 2008. 28(49): p. 13094-105.
- 40.** Gu, J., B.L. Firestein, and J.Q. Zheng, Microtubules in dendritic spine development. *J Neurosci*, 2008. 28(46): p. 12120-4.
- 41.** Merriam, E.B., et al., Synaptic regulation of microtubule dynamics in dendritic spines by calcium, F-actin, and drebrin. *J Neurosci*, 2013. 33(42): p. 16471-82.
- 42.** Honnappa, S., et al., An EB1-binding motif acts as a microtubule tip localization signal. *Cell*, 2009. 138(2): p. 366-76.
- 43.** Bieling, P., et al., Reconstitution of a microtubule plus-end tracking system in vitro. *Nature*, 2007. 450(7172): p. 1100-5.
- 44.** Komarova, Y., et al., Mammalian end binding proteins control persistent microtubule growth. *J Cell Biol*, 2009. 184(5): p. 691-706.
- 45.** Slep, K.C. and R.D. Vale, Structural basis of microtubule plus end tracking by XMAP215, CLIP-170, and EB1. *Mol Cell*, 2007. 27(6): p. 976-91.
- 46.** Maurer, S.P., et al., EBs recognize a nucleotide-dependent structural cap at growing microtubule ends. *Cell*, 2012. 149(2): p. 371-82.
- 47.** Zhang, R., et al., Mechanistic Origin of Microtubule Dynamic Instability and Its Modulation by EB Proteins. *Cell*, 2015. 162(4): p. 849-59.
- 48.** Buey, R.M., et al., Insights into EB1 structure and the role of its C-terminal domain for discriminating microtubule tips from the lattice. *Mol Biol Cell*, 2011. 22(16): p. 2912-23.
- 49.** De Groot, C.O., et al., Molecular insights into mammalian end-binding protein heterodimerization. *J Biol Chem*, 2010. 285(8): p. 5802-14.
- 50.** Slep, K.C., et al., Structural determinants for EB1-mediated recruitment of APC and spectraplakins to the microtubule plus end. *J Cell Biol*, 2005. 168(4): p. 587-98.
- 51.** Dragestein, K.A., et al., Dynamic behavior of GFP-CLIP-170 reveals fast protein turnover on microtubule plus ends. *J Cell Biol*, 2008. 180(4): p. 729-37.
- 52.** Nagaraj, N., et al., Deep proteome and transcriptome mapping of a human cancer cell line. *Mol Syst Biol*, 2011. 7: p. 548.
- 53.** Beck, M., et al., The quantitative proteome of a human cell line. *Mol Syst Biol*, 2011. 7: p. 549.

- 54.** Craft, G.E., A. Chen, and A.C. Nairn, Recent advances in quantitative neuroproteomics. *Methods*, 2013. 61(3): p. 186-218.
- 55.** Stepanova, T., et al., Visualization of microtubule growth in cultured neurons via the use of EB3-GFP (end-binding protein 3-green fluorescent protein). *J Neurosci*, 2003. 23(7): p. 2655-64.
- 56.** Jiang, K., et al., A Proteome-wide screen for mammalian SxIP motif-containing microtubule plus-end tracking proteins. *Curr Biol*, 2012. 22(19): p. 1800-7.
- 57.** Yue, J., et al., Microtubules regulate focal adhesion dynamics through MAP4K4. *Dev Cell*, 2014. 31(5): p. 572-85.
- 58.** Komarova, Y.A., et al., VE-cadherin signaling induces EB3 phosphorylation to suppress microtubule growth and assemble adherens junctions. *Mol Cell*, 2012. 48(6): p. 914-25.
- 59.** Ban, R., et al., Mitotic regulation of the stability of microtubule plus-end tracking protein EB3 by ubiquitin ligase SIAH-1 and Aurora mitotic kinases. *J Biol Chem*, 2009. 284(41): p. 28367-81.
- 60.** Nakagawa, H., et al., EB3, a novel member of the EB1 family preferentially expressed in the central nervous system, binds to a CNS-specific APC homologue. *Oncogene*, 2000. 19(2): p. 210-6.
- 61.** Su, L.K. and Y. Qi, Characterization of human MAPRE genes and their proteins. *Genomics*, 2001. 71(2): p. 142-9.
- 62.** Morrison, E.E., P.M. Moncur, and J.M. Askham, EB1 identifies sites of microtubule polymerisation during neurite development. *Brain Res Mol Brain Res*, 2002. 98(1-2): p. 145-52.
- 63.** Alves-Silva, J., et al., Spectraplakins promote microtubule-mediated axonal growth by functioning as structural microtubule-associated proteins and EB1-dependent +TIPs (tip interacting proteins). *J Neurosci*, 2012. 32(27): p. 9143-58.
- 64.** Jimenez-Mateos, E.M., et al., End binding protein-1 (EB1) complements microtubule-associated protein-1B during axonogenesis. *J Neurosci Res*, 2005. 80(3): p. 350-9.
- 65.** Arens, J., T.-T. Duong, and L. Dehmelt, A Morphometric Screen Identifies Specific Roles for Microtubule-Regulating Genes in Neuronal Development of P19 Stem Cells. *PLoS One*, 2013. 8(11): p. e79796.
- 66.** Laketa, V., et al., High-content microscopy identifies new neurite outgrowth regulators. *Mol Biol Cell*, 2007. 18(1): p. 242-52.
- 67.** Geraldo, S., et al., Targeting of the F-actin-binding protein drebrin by the microtubule plus-tip protein EB3 is required for neuritogenesis. *Nat Cell Biol*, 2008. 10(10): p. 1181-9.
- 68.** Kojima, N. and T. Shirao, Synaptic dysfunction and disruption of postsynaptic drebrin-actin complex: A study of neurological disorders accompanied by cognitive deficits. *Neuroscience Research*, 2007. 58(1): p. 1-5.
- 69.** Leterrier, C., et al., End-binding proteins EB3 and EB1 link microtubules to ankyrin G in the axon initial segment. *Proc Natl Acad Sci U S A*, 2011. 108(21): p. 8826-31.
- 70.** Bieling, P., et al., CLIP-170 tracks growing microtubule ends by dynamically recognizing composite EB1/tubulin-binding sites. *J Cell Biol*, 2008. 183(7): p. 1223-33.
- 71.** Weisbrich, A., et al., Structure-function relationship of CAP-Gly domains. *Nat Struct Mol Biol*, 2007. 14(10): p. 959-67.
- 72.** Mishima, M., et al., Structural basis for tubulin recognition by cytoplasmic linker protein 170 and its autoinhibition. *Proc Natl Acad Sci U S A*, 2007. 104(25): p. 10346-51.
- 73.** Honnappa, S., et al., Key interaction modes of dynamic +TIP networks. *Mol Cell*, 2006. 23(5): p. 663-71.

- 74.** Kardon, J.R. and R.D. Vale, Regulators of the cytoplasmic dynein motor. *Nat Rev Mol Cell Biol*, 2009. 10(12): p. 854-65.
- 75.** Vaughan, P.S., et al., A role for regulated binding of p150(Glued) to microtubule plus ends in organelle transport. *J Cell Biol*, 2002. 158(2): p. 305-19.
- 76.** Moughamian, A.J., et al., Ordered recruitment of dynactin to the microtubule plus-end is required for efficient initiation of retrograde axonal transport. *J Neurosci*, 2013. 33(32): p. 13190-203.
- 77.** Lazarus, J.E., et al., Dynactin subunit p150(Glued) is a neuron-specific anti-catastrophe factor. *PLoS Biol*, 2013. 11(7): p. e1001611.
- 78.** Lansbergen, G., et al., Conformational changes in CLIP-170 regulate its binding to microtubules and dynactin localization. *J Cell Biol*, 2004. 166(7): p. 1003-14.
- 79.** De Zeeuw, C.I., et al., CLIP-115, a Novel Brain-Specific Cytoplasmic Linker Protein, Mediates the Localization of Dendritic Lamellar Bodies. *Neuron*, 1997. 19(6): p. 1187-1199.
- 80.** Komarova, Y.A., et al., Cytoplasmic linker proteins promote microtubule rescue in vivo. *J Cell Biol*, 2002. 159(4): p. 589-99.
- 81.** Beaven, R., et al., Drosophila CLIP-190 and mammalian CLIP-170 display reduced microtubule plus end association in the nervous system. *Mol Biol Cell*, 2015. 26(8): p. 1491-1508.
- 82.** Neukirchen, D. and F. Bradke, Cytoplasmic linker proteins regulate neuronal polarization through microtubule and growth cone dynamics. *J Neurosci*, 2011. 31(4): p. 1528-38.
- 83.** Swiech, L., et al., CLIP-170 and IQGAP1 cooperatively regulate dendrite morphology. *J Neurosci*, 2011. 31(12): p. 4555-68.
- 84.** Akhmanova, A., et al., The microtubule plus-end-tracking protein CLIP-170 associates with the spermatid manchette and is essential for spermatogenesis. *Genes Dev*, 2005. 19(20): p. 2501-15.
- 85.** Hoogenraad, C.C., et al., Targeted mutation of Cyln2 in the Williams syndrome critical region links CLIP-115 haploinsufficiency to neurodevelopmental abnormalities in mice. *Nat Genet*, 2002. 32(1): p. 116-27.
- 86.** Akhmanova, A., et al., Clasps are CLIP-115 and -170 associating proteins involved in the regional regulation of microtubule dynamics in motile fibroblasts. *Cell*, 2001. 104(6): p. 923-35.
- 87.** Leano, J.B., S.L. Rogers, and K.C. Slep, A cryptic TOG domain with a distinct architecture underlies CLASP-dependent bipolar spindle formation. *Structure*, 2013. 21(6): p. 939-50.
- 88.** Al-Bassam, J. and F. Chang, Regulation of Microtubule Dynamics by TOG-domain proteins XMAP215/Dis1 and CLASP. *Trends Cell Biol*, 2011. 21(10): p. 604-614.
- 89.** Mimori-Kiyosue, Y., et al., CLASP1 and CLASP2 bind to EB1 and regulate microtubule plus-end dynamics at the cell cortex. *J Cell Biol*, 2005. 168(1): p. 141-53.
- 90.** Lee, H., et al., The microtubule plus end tracking protein Orbit/MAST/CLASP acts downstream of the tyrosine kinase Abl in mediating axon guidance. *Neuron*, 2004. 42(6): p. 913-26.
- 91.** Marx, A., et al., Xenopus cytoplasmic linker-associated protein 1 (XCLASP1) promotes axon elongation and advance of pioneer microtubules. *Mol Biol Cell*, 2013. 24(10): p. 1544-58.
- 92.** Watanabe, T., et al., Phosphorylation of CLASP2 by GSK-3beta regulates its interaction with IQGAP1, EB1 and microtubules. *J Cell Sci*, 2009. 122(Pt 16): p. 2969-79.
- 93.** Hur, E.M., et al., GSK3 controls axon growth via CLASP-mediated regulation of growth cone microtubules. *Genes Dev*, 2011. 25(18): p. 1968-81.
- 94.** Engel, U., et al., Abelson phosphorylation of CLASP2 modulates its association with microtubules and actin. *Cytoskeleton (Hoboken)*, 2014. 71(3): p. 195-209.

- 95.** Beffert, U., et al., Microtubule plus-end tracking protein CLASP2 regulates neuronal polarity and synaptic function. *J Neurosci*, 2012. 32(40): p. 13906-16.
- 96.** Schmidt, N., et al., Agrin regulates CLASP2-mediated capture of microtubules at the neuromuscular junction synaptic membrane. *J Cell Biol*, 2012. 198(3): p. 421-37.
- 97.** Suozzi, K.C., X. Wu, and E. Fuchs, Spectraplakins: master orchestrators of cytoskeletal dynamics. *J Cell Biol*, 2012. 197(4): p. 465-75.
- 98.** Sun, D., C.L. Leung, and R.K. Liem, Characterization of the microtubule binding domain of microtubule actin crosslinking factor (MACF): identification of a novel group of microtubule associated proteins. *J Cell Sci*, 2001. 114(Pt 1): p. 161-172.
- 99.** Goryunov, D., et al., Nervous-tissue-specific elimination of microtubule-actin crosslinking factor 1a results in multiple developmental defects in the mouse brain. *Mol Cell Neurosci*, 2010. 44(1): p. 1-14.
- 100.** Kodama, A., et al., ACF7: an essential integrator of microtubule dynamics. *Cell*, 2003. 115(3): p. 343-54.
- 101.** Sanchez-Soriano, N., et al., Mouse ACF7 and drosophila short stop modulate filopodia formation and microtubule organisation during neuronal growth. *J Cell Sci*, 2009. 122(Pt 14): p. 2534-42.
- 102.** Guo, L., et al., Gene targeting of BPAG1: abnormalities in mechanical strength and cell migration in stratified epithelia and neurologic degeneration. *Cell*, 1995. 81(2): p. 233-43.
- 103.** Edvardson, S., et al., Hereditary sensory autonomic neuropathy caused by a mutation in dystonin. *Ann Neurol*, 2012. 71(4): p. 569-72.
- 104.** Yang, Y., et al., Integrators of the cytoskeleton that stabilize microtubules. *Cell*, 1999. 98(2): p. 229-38.
- 105.** Liu, J.J., et al., BPAG1n4 is essential for retrograde axonal transport in sensory neurons. *J Cell Biol*, 2003. 163(2): p. 223-9.
- 106.** Kapur, M., et al., A SxIP motif interaction at the microtubule plus end is important for processive retrograde axonal transport. *Cell Mol Life Sci*, 2014. 71(20): p. 4043-54.
- 107.** Ryan, S.D., et al., Neuronal dystonin isoform 2 is a mediator of endoplasmic reticulum structure and function. *Mol Biol Cell*, 2012. 23(4): p. 553-66.
- 108.** Ryan, S.D., et al., Microtubule stability, Golgi organization, and transport flux require dystonin-a2-MAP1B interaction. *Journal of Cell Biology*, 2012. 196(6): p. 727-742.
- 109.** Ferrier, A., et al., Disruption in the autophagic process underlies the sensory neuropathy in dystonia musculorum mice. *Autophagy*, 2015. 11(7): p. 1025-1036.
- 110.** Young, K.G. and R. Kothary, Dystonin/Bpag1 is a necessary endoplasmic reticulum/nuclear envelope protein in sensory neurons. *Exp Cell Res*, 2008. 314(15): p. 2750-61.
- 111.** Ferrier, A., et al., Transgenic expression of neuronal dystonin isoform 2 partially rescues the disease phenotype of the Dystonia musculorum mouse model of hereditary sensory autonomic neuropathy VI. *Human Molecular Genetics*, 2014. 23(10): p. 2694-2710.
- 112.** Di Stefano, P., et al., p140Cap protein suppresses tumour cell properties, regulating Csk and Src kinase activity. *EMBO J*, 2007. 26(12): p. 2843-55.
- 113.** Repetto, D., et al., p140Cap regulates memory and synaptic plasticity through Src-mediated and citron-N-mediated actin reorganization. *J Neurosci*, 2014. 34(4): p. 1542-53.
- 114.** Akhmanova, A. and C.C. Hoogenraad, Microtubule plus-end-tracking proteins: mechanisms and functions. *Curr Opin Cell Biol*, 2005. 17(1): p. 47-54.

- 115.** Ito, H., et al., Characterization of a multidomain adaptor protein, p140Cap, as part of a pre-synaptic complex. *J Neurochem*, 2008. 107(1): p. 61-72.
- 116.** Chin, L.S., et al., SNIP, a novel SNAP-25-interacting protein implicated in regulated exocytosis. *J Biol Chem*, 2000. 275(2): p. 1191-200.
- 117.** Grigoriev, I., et al., STIM1 is a MT-plus-end-tracking protein involved in remodeling of the ER. *Curr Biol*, 2008. 18(3): p. 177-82.
- 118.** Mitchell, C.B., et al., STIM1 is necessary for store-operated calcium entry in turning growth cones. *J Neurochem*, 2012. 122(6): p. 1155-66.
- 119.** Hartmann, J., et al., STIM1 controls neuronal Ca²⁺(+) signaling, mGluR1-dependent synaptic transmission, and cerebellar motor behavior. *Neuron*, 2014. 82(3): p. 635-44.
- 120.** Galan, C., et al., The cytoskeleton plays a modulatory role in the association between STIM1 and the Ca²⁺ channel subunits Orai1 and TRPC1. *Biochem Pharmacol*, 2011. 82(4): p. 400-10.
- 121.** Berna-Erro, A., et al., STIM2 regulates capacitive Ca²⁺ entry in neurons and plays a key role in hypoxic neuronal cell death. *Sci Signal*, 2009. 2(93): p. ra67.
- 122.** Shen, W.W., M. Frieden, and N. Demarex, Remodelling of the endoplasmic reticulum during store-operated calcium entry. *Biol Cell*, 2011. 103(8): p. 365-80.
- 123.** Bechstedt, S. and G.J. Brouhard, Doublecortin recognizes the 13-protofilament microtubule cooperatively and tracks microtubule ends. *Dev Cell*, 2012. 23(1): p. 181-192.
- 124.** Gupta, K.K., et al., Mechanism for the catastrophe-promoting activity of the microtubule destabilizer Op18/stathmin. *Proc Natl Acad Sci U S A*, 2013. 110(51): p. 20449-54.
- 125.** Brouhard, G.J., et al., XMAP215 is a processive microtubule polymerase. *Cell*, 2008. 132(1): p. 79-88.
- 126.** Maurer, Sebastian P., et al., EB1 Accelerates Two Conformational Transitions Important for Microtubule Maturation and Dynamics. *Current Biology*, 2014. 24(4): p. 372-384.
- 127.** van der Vaart, B., et al., SLAIN2 links microtubule plus end-tracking proteins and controls microtubule growth in interphase. *J Cell Biol*, 2011. 193(6): p. 1083-99.
- 128.** van der Vaart, B., et al., Microtubule plus-end tracking proteins SLAIN1/2 and ch-TOG promote axonal development. *J Neurosci*, 2012. 32(42): p. 14722-8.
- 129.** Lowery, L.A., et al., Growth cone-specific functions of XMAP215 in restricting microtubule dynamics and promoting axonal outgrowth. *Neural Dev*, 2013. 8: p. 22.
- 130.** van der Vaart, B., et al., CFEOM1-associated kinesin KIF21A is a cortical microtubule growth inhibitor. *Dev Cell*, 2013. 27(2): p. 145-160.
- 131.** Yamada, K., et al., Heterozygous mutations of the kinesin KIF21A in congenital fibrosis of the extraocular muscles type 1 (CFEOM1). *Nat Genet*, 2003. 35(4): p. 318-21.
- 132.** Cheng, L., et al., Human CFEOM1 mutations attenuate KIF21A autoinhibition and cause oculomotor axon stalling. *Neuron*, 2014. 82(2): p. 334-49.
- 133.** Duellberg, C., et al., Reconstitution of a hierarchical +TIP interaction network controlling microtubule end tracking of dynein. *Nat Cell Biol*, 2014. 16(8): p. 804-11.
- 134.** Lesniewska, K., E. Warbrick, and H. Ohkura, Peptide aptamers define distinct EB1- and EB3-binding motifs and interfere with microtubule dynamics. *Mol Biol Cell*, 2014. 25(7): p. 1025-36.
- 135.** van Haren, J., et al., Mammalian Navigators are microtubule plus-end tracking proteins that can reorganize the cytoskeleton to induce neurite-like extensions. *Cell Motil Cytoskeleton*, 2009. 66(10): p. 824-38.

- 136.** Peris, L., et al., Tubulin tyrosination is a major factor affecting the recruitment of CAP-Gly proteins at microtubule plus ends. *J Cell Biol*, 2006. 174(6): p. 839-49.
- 137.** Peris, L., et al., Motor-dependent microtubule disassembly driven by tubulin tyrosination. *J Cell Biol*, 2009. 185(7): p. 1159-66.
- 138.** Tortosa, E., et al., MAP1B regulates microtubule dynamics by sequestering EB1/3 in the cytosol of developing neuronal cells. *EMBO J*, 2013. 32(9): p. 1293-306.
- 139.** Kapitein, L.C., et al., NMDA receptor activation suppresses microtubule growth and spine entry. *J Neurosci*, 2011. 31(22): p. 8194-209.
- 140.** Zumbrunn, J., et al., Binding of the adenomatous polyposis coli protein to microtubules increases microtubule stability and is regulated by GSK3 beta phosphorylation. *Curr Biol*, 2001. 11(1): p. 44-9.
- 141.** Kumar, P., et al., GSK3beta phosphorylation modulates CLASP-microtubule association and lamella microtubule attachment. *J Cell Biol*, 2009. 184(6): p. 895-908.
- 142.** Wu, X., et al., Skin stem cells orchestrate directional migration by regulating microtubule-ACF7 connections through GSK3beta. *Cell*, 2011. 144(3): p. 341-52.
- 143.** Asada, N. and K. Sanada, LKB1-mediated spatial control of GSK3beta and adenomatous polyposis coli contributes to centrosomal forward movement and neuronal migration in the developing neocortex. *J Neurosci*, 2010. 30(26): p. 8852-65.
- 144.** Ka, M., et al., MACF1 regulates the migration of pyramidal neurons via microtubule dynamics and GSK-3 signaling. *Dev Biol*, 2014. 395(1): p. 4-18.
- 145.** Valvezan, A.J., et al., Adenomatous polyposis coli (APC) regulates multiple signaling pathways by enhancing glycogen synthase kinase-3 (GSK-3) activity. *J Biol Chem*, 2012. 287(6): p. 3823-32.
- 146.** Chen, H.J., et al., The role of microtubule actin cross-linking factor 1 (MACF1) in the Wnt signaling pathway. *Genes Dev*, 2006. 20(14): p. 1933-45.
- 147.** Stringham, E.G. and K.L. Schmidt, Navigating the cell: UNC-53 and the navigators, a family of cytoskeletal regulators with multiple roles in cell migration, outgrowth and trafficking. *Cell Adh Migr*, 2009. 3(4): p. 342-6.
- 148.** Repetto, D., et al., Mapping of p140Cap phosphorylation sites: the EPLYA and EGLYA motifs have a key role in tyrosine phosphorylation and Csk binding, and are substrates of the Abl kinase. *PLoS One*, 2013. 8(1): p. e54931.
- 149.** Zhang, L., et al., DDA3 associates with microtubule plus ends and orchestrates microtubule dynamics and directional cell migration. *Sci Rep*, 2013. 3: p. 1681.
- 150.** Kapur, M., et al., Calcium tips the balance: a microtubule plus end to lattice binding switch operates in the carboxyl terminus of BPAG1n4. *EMBO Rep*, 2012. 13(11): p. 1021-9.
- 151.** Bjelic, S., et al., Interaction of mammalian end binding proteins with CAP-Gly domains of CLIP-170 and p150(glued). *J Struct Biol*, 2012. 177(1): p. 160-7.
- 152.** Sorbara, C.D., et al., Pervasive axonal transport deficits in multiple sclerosis models. *Neuron*, 2014. 84(6): p. 1183-90.
- 153.** Chen, L., et al., Axon regeneration pathways identified by systematic genetic screening in *C. elegans*. *Neuron*, 2011. 71(6): p. 1043-57.
- 154.** Chen, L., et al., Axon injury and stress trigger a microtubule-based neuroprotective pathway. *Proc Natl Acad Sci U S A*, 2012. 109(29): p. 11842-7.
- 155.** Waterman-Storer, C.M., S. Karki, and E.L. Holzbaur, The p150Glued component of the dynactin complex binds to both microtubules and the actin-related protein centractin (Arp-1). *Proc Natl Acad Sci U S A*, 1995. 92(5): p. 1634-1638.

- 156.** Askham, J.M., et al., Evidence that an interaction between EB1 and p150(Glued) is required for the formation and maintenance of a radial microtubule array anchored at the centrosome. *Mol Biol Cell*, 2002. 13(10): p. 3627-45.
- 157.** Puls, I., et al., Mutant dynactin in motor neuron disease. *Nat Genet*, 2003. 33(4): p. 455-6.
- 158.** Wider, C. and Z.K. Wszolek, Rapidly progressive familial parkinsonism with central hypoventilation, depression and weight loss (Perry syndrome)—A literature review. *Parkinsonism & Related Disorders*, 2008. 14(1): p. 1-7.
- 159.** Farrer, M.J., et al., DCTN1 mutations in Perry syndrome. *Nat Genet*, 2009. 41(2): p. 163-5.
- 160.** Levy, J.R., et al., A motor neuron disease-associated mutation in p150(Glued) perturbs dynactin function and induces protein aggregation. *J Cell Biol*, 2006. 172(5): p. 733-745.
- 161.** Ahmed, S., et al., Disease-associated mutations in the p150(Glued) subunit destabilize the CAP-gly domain. *Biochemistry*, 2010. 49(25): p. 5083-5.
- 162.** Puls, I., et al., Distal spinal and bulbar muscular atrophy caused by dynactin mutation. *Ann Neurol*, 2005. 57(5): p. 687-94.
- 163.** Moughamian, A.J. and E.L. Holzbaur, Dynactin is required for transport initiation from the distal axon. *Neuron*, 2012. 74(2): p. 331-43.
- 164.** Ikezu, S. and T. Ikezu, Tau-tubulin kinase. *Frontiers in Molecular Neuroscience*, 2014. 7: p. 33.
- 165.** Takahashi, M., et al., A novel tau-tubulin kinase from bovine brain. *FEBS Lett*, 1995. 372(1): p. 59-64.
- 166.** Tomizawa, K., et al., Tau-tubulin kinase phosphorylates tau at Ser-208 and Ser-210, sites found in paired helical filament-tau. *FEBS Lett*, 2001. 492(3): p. 221-7.
- 167.** Houlden, H., et al., Mutations in TTBK2, encoding a kinase implicated in tau phosphorylation, segregate with spinocerebellar ataxia type 11. *Nat Genet*, 2007. 39(12): p. 1434-6.
- 168.** Schöls, L., et al., Autosomal dominant cerebellar ataxias: clinical features, genetics, and pathogenesis. *The Lancet Neurology*, 2004. 3(5): p. 291-304.
- 169.** Goetz, S.C., K.F. Liem, Jr., and K.V. Anderson, The spinocerebellar ataxia-associated gene Tau tubulin kinase 2 controls the initiation of ciliogenesis. *Cell*, 2012. 151(4): p. 847-58.
- 170.** Waters, A.M. and P.L. Beales, Ciliopathies: an expanding disease spectrum. *Pediatric Nephrology (Berlin, Germany)*, 2011. 26(7): p. 1039-1056.
- 171.** Oda, T., et al., Binding to Cep164, but not EB1, is essential for centriolar localization of TTBK2 and its function in ciliogenesis. *Genes to Cells*, 2014. 19(12): p. 927-940.
- 172.** Watanabe, T., et al., TTBK2 with EB1/3 regulates microtubule dynamics in migrating cells through KIF2A phosphorylation. *J Cell Biol*, 2015. 210(5): p. 737-751.
- 173.** Zhang, N., et al., Phosphorylation of synaptic vesicle protein 2A at Thr84 by casein kinase 1 family kinases controls the specific retrieval of synaptotagmin-1. *Journal of Neuroscience*, 2015. 35(6): p. 2492-2507.
- 174.** Almilaji, A., et al., Upregulation of Na⁺/Cl⁻-coupled betaine/gamma-amino-butyric acid transporter BGT1 by Tau tubulin kinase 2. *Cell Physiol Biochem*, 2013. 32(2): p. 334-43.
- 175.** Sato, S., et al., Tau-tubulin kinase 1 (TTBK1), a neuron-specific tau kinase candidate, is involved in tau phosphorylation and aggregation. *J Neurochem*, 2006. 98(5): p. 1573-84.
- 176.** Yu, N.N., et al., Tau-tubulin kinase-1 gene variants are associated with Alzheimer's disease in Han Chinese. *Neurosci Lett*, 2011. 491(1): p. 83-6.
- 177.** Vazquez-Higuera, J.L., et al., Genetic variations in tau-tubulin kinase-1 are linked to Alzheimer's disease in a Spanish case-control

cohort. *Neurobiol Aging*, 2011. 32(3): p. 550 e5-9.

178. Liachko, N.F., et al., The tau tubulin kinases TTBK1/2 promote accumulation of pathological TDP-43. *PLoS Genet*, 2014. 10(12): p. e1004803.

179. Lee, E.B., V.M.Y. Lee, and J.Q. Trojanowski, Gains or losses: Molecular mechanisms of TDP43-mediated neurodegeneration. *Nature Reviews Neuroscience*, 2012. 13(1): p. 38-50.

180. Zhang, B., et al., The microtubule-stabilizing agent, epothilone D, reduces axonal dysfunction, neurotoxicity, cognitive deficits, and Alzheimer-like pathology in an interventional study with aged tau transgenic mice. *J Neurosci*, 2012. 32(11): p. 3601-11.

181. Ruschel, J., et al., Axonal regeneration. Systemic administration of epothilone B promotes axon regeneration after spinal cord injury. *Science*, 2015. 348(6232): p. 347-52.

182. Divinski, I., et al., Peptide neuroprotection through specific interaction with brain tubulin. *J Neurochem*, 2006. 98(3): p. 973-84.

183. Oz, S., Y. Ivashko-Pachima, and I. Gozes, The ADNP derived peptide, NAP modulates the tubulin pool: implication for neurotrophic and neuroprotective activities. *PLoS One*, 2012. 7(12): p. e51458.

184. Jouroukhin, Y., et al., NAP (davunetide) modifies disease progression in a mouse model of severe neurodegeneration: protection against impairments in axonal transport. *Neurobiol Dis*, 2013. 56: p. 79-94.

185. Matsuoka, Y., et al., Intranasal NAP administration reduces accumulation of amyloid peptide and tau hyperphosphorylation in a transgenic mouse model of Alzheimer's disease at early pathological stage. *J Mol Neurosci*, 2007. 31(2): p. 165-70.

186. Shiryaev, N., et al., NAP protects memory, increases soluble tau and reduces tau hyperphosphorylation in a tauopathy model.

Neurobiol Dis, 2009. 34(2): p. 381-8.

187. Oz, S., et al., The NAP motif of activity-dependent neuroprotective protein (ADNP) regulates dendritic spines through microtubule end binding proteins. *Mol Psychiatry*, 2014. 19(10): p. 1115-24.

188. Pfister, A.S., et al., Amer2 protein is a novel negative regulator of Wnt/beta-catenin signaling involved in neuroectodermal patterning. *J Biol Chem*, 2012. 287(3): p. 1734-41.

189. Preitner, N., et al., APC is an RNA-binding protein, and its interactome provides a link to neural development and microtubule assembly. *Cell*, 2014. 158(2): p. 368-82.

190. Purro, S.A., et al., Wnt regulates axon behavior through changes in microtubule growth directionality: a new role for adenomatous polyposis coli. *J Neurosci*, 2008. 28(34): p. 8644-54.

191. Koester, M.P., O. Muller, and G.E. Pollerberg, Adenomatous polyposis coli is differentially distributed in growth cones and modulates their steering. *J Neurosci*, 2007. 27(46): p. 12590-600.

192. Shi, S.H., et al., APC and GSK-3beta are involved in mPar3 targeting to the nascent axon and establishment of neuronal polarity. *Curr Biol*, 2004. 14(22): p. 2025-32.

193. Zhou, F.Q., et al., NGF-induced axon growth is mediated by localized inactivation of GSK-3beta and functions of the microtubule plus end binding protein APC. *Neuron*, 2004. 42(6): p. 897-912.

194. Votin, V., W.J. Nelson, and A.I. Barth, Neurite outgrowth involves adenomatous polyposis coli protein and beta-catenin. *J Cell Sci*, 2005. 118(Pt 24): p. 5699-708.

195. Mohn, J.L., et al., Adenomatous polyposis coli protein deletion leads to cognitive and autism-like disabilities. *Molecular Psychiatry*, 2014.

- 196.** Eom, T.Y., et al., Differential regulation of microtubule severing by APC underlies distinct patterns of projection neuron and interneuron migration. *Dev Cell*, 2014. 31(6): p. 677-689.
- 197.** Chen, Y., et al., Adenomatous polyposis coli regulates axon arborization and cytoskeleton organization via its n-terminus. *PLoS One*, 2011. 6(9).
- 198.** Rosenberg, M.M., et al., The postsynaptic APC multi-protein complex is required for localizing neuroligin and neuroligin to neuronal nicotinic synapses in vivo. *J Neurosci*, 2010. 30(33): p. 11073-11085.
- 199.** Hamilton, S.R., et al., The Molecular Basis of Turcot's Syndrome. *New England Journal of Medicine*, 1995. 332(13): p. 839-847.
- 200.** Almurieki, M., et al., Loss-of-function mutation in APC2 causes sotos syndrome features. *Cell Reports*, 2015. 10(9): p. 1585-1598.
- 201.** Shintani, T., et al., Directional neuronal migration is impaired in mice lacking adenomatous polyposis coli 2. *J Neurosci*, 2012. 32(19): p. 6468-84.
- 202.** Shintani, T., et al., APC2 plays an essential role in axonal projections through the regulation of microtubule stability. *Journal of Neuroscience*, 2009. 29(37): p. 11628-11640.
- 203.** Bond, J., et al., A centrosomal mechanism involving CDK5RAP2 and CENPJ controls brain size. *Nature Genetics*, 2005. 37(4): p. 353-355.
- 204.** Buchman, J.J., et al., Cdk5rap2 interacts with pericentrin to maintain the neural progenitor pool in the developing neocortex. *Neuron*, 2010. 66(3): p. 386-402.
- 205.** Hassan, M.J., et al., Previously described sequence variant in CDK5RAP2 gene in a Pakistani family with autosomal recessive primary microcephaly. *BMC Med Genet*, 2007. 8: p. 58.
- 206.** Lizarraga, S.B., et al., Cdk5rap2 regulates centrosome function and chromosome segregation in neuronal progenitors. *Development*, 2010. 137(11): p. 1907-17.
- 207.** Srour, M., et al., Joubert Syndrome in French Canadians and Identification of Mutations in CEP104. *The American Journal of Human Genetics*, 2015. 97(5): p. 744-753.
- 208.** Larti, F., et al., A defect in the CLIP1 gene (CLIP-170) can cause autosomal recessive intellectual disability. *European Journal of Human Genetics*, 2015. 23(3): p. 331-336.
- 209.** Cheung, J., et al., Identification of the human cortactin-binding protein-2 gene from the autism candidate region at 7q31. *Genomics*, 2001. 78(1-2): p. 7-11.
- 210.** Chen, Y.K., et al., CTTNBP2, but not CTTNBP2NL, regulates dendritic spinogenesis and synaptic distribution of the striatin-PP2A complex. *Mol Biol Cell*, 2012. 23(22): p. 4383-92.
- 211.** Chen, Y.K. and Y.P. Hsueh, Cortactin-binding protein 2 modulates the mobility of cortactin and regulates dendritic spine formation and maintenance. *J Neurosci*, 2012. 32(3): p. 1043-55.
- 212.** Shih, P.Y., et al., Cortactin-binding protein 2 increases microtubule stability and regulates dendritic arborization. *J Cell Sci*, 2014. 127(Pt 16): p. 3521-34.
- 213.** Iossifov, I., et al., De novo gene disruptions in children on the autistic spectrum. *Neuron*, 2012. 74(2): p. 285-99.
- 214.** Hsieh, P.C., et al., DDA3 stabilizes microtubules and suppresses neurite formation. *J Cell Sci*, 2012. 125(Pt 14): p. 3402-11.
- 215.** Sweet, E.S., et al., PSD-95 alters microtubule dynamics via an association with EB3. *J Neurosci*, 2011. 31(3): p. 1038-47.
- 216.** Laht, P., et al., B-plexins control microtubule dynamics and dendrite morphology of hippocampal neurons. *Experimental Cell Research*, 2014. 326(1): p. 174-184.
- 217.** Nagano, T., et al., Filamin A-interacting protein (FILIP) regulates cortical cell migration out of the ventricular zone. *Nat Cell Biol*, 2002. 4(7): p. 495-501.

- 218.** Wilson, A.M., et al., Inhibitor of apoptosis-stimulating protein of p53 (iASPP) is required for neuronal survival after axonal injury. *PLoS One*, 2014. 9(4): p. e94175.
- 219.** Li, G., et al., RNA interference-mediated silencing of iASPP induces cell proliferation inhibition and G0/G1 cell cycle arrest in U251 human glioblastoma cells. *Mol Cell Biochem*, 2011. 350(1-2): p. 193-200.
- 220.** Liu, X., et al., MicroRNA-124-mediated regulation of inhibitory member of apoptosis-stimulating protein of p53 family in experimental stroke. *Stroke*, 2013. 44(7): p. 1973-80.
- 221.** Zhao, W.H., S.Q. Wu, and Y.D. Zhang, Downregulation of miR-124 promotes the growth and invasiveness of glioblastoma cells involving upregulation of PPP1R13L. *Int J Mol Med*, 2013. 32(1): p. 101-7.
- 222.** Bie, L., et al., Kinesin family member 2C (KIF2C/MCAK) is a novel marker for prognosis in human gliomas. *Clin Neurol Neurosurg*, 2012. 114(4): p. 356-60.
- 223.** Falnikar, A., S. Tole, and P.W. Baas, Kinesin-5, a mitotic microtubule-associated motor protein, modulates neuronal migration. *Mol Biol Cell*, 2011. 22(9): p. 1561-1574.
- 224.** Haque, S.A., et al., Monastrol, a Prototype Anti-Cancer Drug That Inhibits a Mitotic Kinesin, Induces Rapid Bursts of Axonal Outgrowth from Cultured Postmitotic Neurons. *Cell Motil Cytoskeleton*, 2004. 58(1): p. 10-16.
- 225.** Jones, G.E., et al., Microcephaly with or without chorioretinopathy, lymphoedema, or mental retardation (MCLMR): review of phenotype associated with KIF11 mutations. *Eur J Hum Genet*, 2014. 22(7): p. 881-7.
- 226.** Myers, K.A. and P.W. Baas, Kinesin-5 regulates the growth of the axon by acting as a brake on its microtubule array. *J Cell Biol*, 2007. 178(6): p. 1081-1091.
- 227.** Nadar, V.C., et al., Kinesin-5 Is Essential for Growth-Cone Turning. *Current Biology*, 2008. 18(24): p. 1972-1977.
- 228.** Nadar, V.C., S. Lin, and P.W. Baas, Microtubule redistribution in growth cones elicited by focal inactivation of kinesin-5. *Journal of Neuroscience*, 2012. 32(17): p. 5783-5794.
- 229.** Ostergaard, P., et al., Mutations in KIF11 cause autosomal-dominant microcephaly variably associated with congenital lymphedema and chorioretinopathy. *American Journal of Human Genetics*, 2012. 90(2): p. 356-362.
- 230.** Venere, M., et al., The mitotic kinesin KIF11 is a driver of invasion, proliferation, and self-renewal in glioblastoma. *Science Translational Medicine*, 2015. 7(304).
- 231.** Yoon, S.Y., et al., Monastrol, a selective inhibitor of the mitotic kinesin Eg5, induces a distinctive growth profile of dendrites and axons in primary cortical neuron cultures. *Cell Motil Cytoskeleton*, 2005. 60(4): p. 181-190.
- 232.** Tsai, J.W., et al., LIS1 RNA interference blocks neural stem cell division, morphogenesis, and motility at multiple stages. *J Cell Biol*, 2005. 170(6): p. 935-45.
- 233.** Gambello, M.J., et al., Multiple dose-dependent effects of Lis1 on cerebral cortical development. *J Neurosci*, 2003. 23(5): p. 1719-29.
- 234.** Youn, Y.H., et al., Distinct dose-dependent cortical neuronal migration and neurite extension defects in Lis1 and Ndel1 mutant mice. *J Neurosci*, 2009. 29(49): p. 15520-30.
- 235.** Coquelle, F.M., et al., LIS1, CLIP-170's Key to the Dynein/Dynactin Pathway. *Mol Cell Biol*, 2002. 22(9): p. 3089-3102.
- 236.** Hirotsune, S., et al., Graded reduction of Pafah1b1 (Lis1) activity results in neuronal migration defects and early embryonic lethality. *Nat Genet*, 1998. 19(4): p. 333-9.
- 237.** Greenwood, J.S., et al., Seizures, enhanced excitation, and increased vesicle number in Lis1 mutant mice. *Ann Neurol*, 2009. 66(5): p. 644-53.

- 238.** Jones, D.L. and S.C. Baraban, Inhibitory inputs to hippocampal interneurons are reorganized in Lis1 mutant mice. *J Neurophysiol*, 2009. 102(2): p. 648-58.
- 239.** Hunt, R.F., et al., LIS1 deficiency promotes dysfunctional synaptic integration of granule cells generated in the developing and adult dentate gyrus. *J Neurosci*, 2012. 32(37): p. 12862-75.
- 240.** Kawabata, I., et al., LIS1-dependent retrograde translocation of excitatory synapses in developing interneuron dendrites. *Nat Commun*, 2012. 3: p. 722.
- 241.** Zheng, Y., et al., Dynein is required for polarized dendritic transport and uniform microtubule orientation in axons. *Nat Cell Biol*, 2008. 10(10): p. 1172-80.
- 242.** Grabham, P.W., et al., Cytoplasmic dynein and LIS1 are required for microtubule advance during growth cone remodeling and fast axonal outgrowth. *J Neurosci*, 2007. 27(21): p. 5823-34.
- 243.** Sudarov, A., et al., Lis1 controls dynamics of neuronal filopodia and spines to impact synaptogenesis and social behaviour. *EMBO Mol Med*, 2013. 5(4): p. 591-607.
- 244.** Fleck, M.W., et al., Hippocampal abnormalities and enhanced excitability in a murine model of human lissencephaly. *J Neurosci*, 2000. 20(7): p. 2439-50.
- 245.** Reiner, O., et al., Isolation of a Miller-Dieker lissencephaly gene containing G protein beta-subunit-like repeats. *Nature*, 1993. 364(6439): p. 717-21.
- 246.** Dobyns, W.B., et al., Lissencephaly. A human brain malformation associated with deletion of the LIS1 gene located at chromosome 17p13. *JAMA*, 1993. 270(23): p. 2838-42.
- 247.** Pilz, D.T., et al., Subcortical band heterotopia in rare affected males can be caused by missense mutations in DCX (XLIS) or LIS1. *Hum Mol Genet*, 1999. 8(9): p. 1757-60.
- 248.** Ka, M. and W.Y. Kim, Microtubule-Actin Crosslinking Factor 1 Is Required for Dendritic Arborization and Axon Outgrowth in the Developing Brain. *Molecular Neurobiology*, 2015.
- 249.** Jorgensen, L.H., et al., Duplication in the microtubule-actin cross-linking factor 1 gene causes a novel neuromuscular condition. *Sci Rep*, 2014. 4: p. 5180.
- 250.** Hekimi, S. and D. Kershaw, Axonal guidance defects in a *Caenorhabditis elegans* mutant reveal cell-extrinsic determinants of neuronal morphology. *J Neurosci*, 1993. 13(10): p. 4254-71.
- 251.** Coy, J.F., et al., Pore membrane and/or filament interacting like protein 1 (POMFIL1) is predominantly expressed in the nervous system and encodes different protein isoforms. *Gene*, 2002. 290(1-2): p. 73-94.
- 252.** Peeters, P.J., et al., Sensory deficits in mice hypomorphic for a mammalian homologue of unc-53. *Developmental Brain Research*, 2004. 150(2): p. 89-101.
- 253.** Muley, P.D., et al., The atRA-responsive gene neuron navigator 2 functions in neurite outgrowth and axonal elongation. *Dev Neurobiol*, 2008. 68(13): p. 1441-53.
- 254.** Martinez-Lopez, M.J., et al., Mouse neuron navigator 1, a novel microtubule-associated protein involved in neuronal migration. *Mol Cell Neurosci*, 2005. 28(4): p. 599-612.
- 255.** McNeill, E.M., et al., Nav2 hypomorphic mutant mice are ataxic and exhibit abnormalities in cerebellar development. *Dev Biol*, 2011. 353(2): p. 331-43.
- 256.** Marzinke, M.A., et al., 14-3-3epsilon and NAV2 interact to regulate neurite outgrowth and axon elongation. *Arch Biochem Biophys*, 2013. 540(1-2): p. 94-100.

- 257.** Carlsson, E., et al., Neuron navigator 3 alterations in nervous system tumors associate with tumor malignancy grade and prognosis. *Genes Chromosomes Cancer*, 2013. 52(2): p. 191-201.
- 258.** Van Haren, J., et al., Dynamic microtubules catalyze formation of navigator-TRIO complexes to regulate neurite extension. *Current Biology*, 2014. 24(15): p. 1778-1785.
- 259.** Tomasoni, R., et al., SNAP-25 regulates spine formation through postsynaptic binding to p140Cap. *Nature Communications*, 2013. 4: p. 1-13.
- 260.** Yang, Y., et al., Endophilin A1 regulates dendritic spine morphogenesis and stability through interaction with p140Cap. *Cell Research*, 2015. 25(4): p. 496-516.
- 261.** Munch, C., et al., Point mutations of the p150 subunit of dynactin (DCTN1) gene in ALS. *Neurology*, 2004. 63(4): p. 724-6.
- 262.** Kwinter, D.M., et al., Dynactin regulates bidirectional transport of dense-core vesicles in the axon and dendrites of cultured hippocampal neurons. *Neuroscience*, 2009. 162(4): p. 1001-10.
- 263.** Bell, N., et al., Store-operated Ca(2+) entry in proliferating and retinoic acid-differentiated N- and S-type neuroblastoma cells. *Biochim Biophys Acta*, 2013. 1833(3): p. 643-51.
- 264.** Shim, S., J.Q. Zheng, and G.L. Ming, A critical role for STIM1 in filopodial calcium entry and axon guidance. *Mol Brain*, 2013. 6: p. 51.
- 265.** Zhang, M., et al., The role of store-operated calcium channels in early brain injury after subarachnoid hemorrhage. *Journal of Xi'an Jiaotong University (Medical Sciences)*, 2013. 34(6): p. 710-716.
- 266.** Li, Y., et al., High expression of STIM1 in the early stages of diffuse axonal injury. *Brain Research*, 2013. 1495: p. 95-102.
- 267.** Hao, B., et al., Role of STIM1 in survival and neural differentiation of mouse embryonic stem cells independent of Orai1-mediated Ca2+ entry. *Stem Cell Res*, 2014. 12(2): p. 452-66.
- 268.** Kawamata, H., et al., Abnormal intracellular calcium signaling and SNARE-dependent exocytosis contributes to SOD1G93A astrocyte-mediated toxicity in amyotrophic lateral sclerosis. *J Neurosci*, 2014. 34(6): p. 2331-48.
- 269.** Vigont, V.A., et al., STIM1 Protein Activates Store-Operated Calcium Channels in Cellular Model of Huntington's Disease. *Acta Naturae*, 2014. 6(4): p. 40-7.
- 270.** Su, Q., et al., Syntabulin is a microtubule-associated protein implicated in syntaxin transport in neurons. *Nat Cell Biol*, 2004. 6(10): p. 941-53.
- 271.** Cai, Q., C. Gerwin, and Z.H. Sheng, Syntabulin-mediated anterograde transport of mitochondria along neuronal processes. *J Cell Biol*, 2005. 170(6): p. 959-69.
- 272.** Cai, Q., P.Y. Pan, and Z.H. Sheng, Syntabulin-kinesin-1 family member 5B-mediated axonal transport contributes to activity-dependent presynaptic assembly. *J Neurosci*, 2007. 27(27): p. 7284-96.
- 273.** Ma, H., et al., KIF5B motor adaptor syntabulin maintains synaptic transmission in sympathetic neurons. *J Neurosci*, 2009. 29(41): p. 13019-29.
- 274.** Yang, Y.T., C.L. Wang, and L. Van Aelst, DOCK7 interacts with TACC3 to regulate interkinetic nuclear migration and cortical neurogenesis. *Nature Neuroscience*, 2012. 15(9): p. 1201-1210.
- 275.** Xie, Z., et al., Cep120 and TACCs control interkinetic nuclear migration and the neural progenitor pool. *Neuron*, 2007. 56(1): p. 79-93.
- 276.** Wurdak, H., et al., A small molecule accelerates neuronal differentiation in the adult rat. *Proc Natl Acad Sci U S A*, 2010. 107(38): p. 16542-16547.

-
- 277.** Nwagbara, B.U., et al., TACC3 is a microtubule plus end-tracking protein that promotes axon elongation and also regulates microtubule plus end dynamics in multiple embryonic cell types. *Mol Biol Cell*, 2014. 25(21): p. 3350-3362.
- 278.** DeGeer, J., et al., Tyrosine phosphorylation of the Rho guanine nucleotide exchange factor Trio regulates netrin-1/DCC-mediated cortical axon outgrowth. *Mol Cell Biol*, 2013. 33(4): p. 739-51.
- 279.** O'Brien, S.P., et al., Skeletal muscle deformity and neuronal disorder in Trio exchange factor-deficient mouse embryos. *Proc Natl Acad Sci U S A*, 2000. 97(22): p. 12074-8.
- 280.** Newsome, T.P., et al., Trio combines with dock to regulate Pak activity during photoreceptor axon pathfinding in *Drosophila*. *Cell*, 2000. 101(3): p. 283-94.
- 281.** Bateman, J., H. Shu, and D. Van Vactor, The guanine nucleotide exchange factor trio mediates axonal development in the *Drosophila* embryo. *Neuron*, 2000. 26(1): p. 93-106.
- 282.** Liebl, E.C., et al., Dosage-sensitive, reciprocal genetic interactions between the Abl tyrosine kinase and the putative GEF trio reveal trio's role in axon pathfinding. *Neuron*, 2000. 26(1): p. 107-18.
- 283.** Awasaki, T., et al., The *Drosophila* trio plays an essential role in patterning of axons by regulating their directional extension. *Neuron*, 2000. 26(1): p. 119-31.
- 284.** Briancon-Marjollet, A., et al., Trio mediates netrin-1-induced Rac1 activation in axon outgrowth and guidance. *Mol Cell Biol*, 2008. 28(7): p. 2314-23.
- 285.** Peng, Y.J., et al., Trio is a key guanine nucleotide exchange factor coordinating regulation of the migration and morphogenesis of granule cells in the developing cerebellum. *J Biol Chem*, 2010. 285(32): p. 24834-44.
- 286.** Lund, H., et al., Tau-tubulin kinase 1 expression, phosphorylation and co-localization with phospho-Ser422 tau in the Alzheimer's disease brain. *Brain Pathol*, 2013. 23(4): p. 378-89.

2



Dynein regulator NDEL1 controls polarized cargo transport at the axon initial segment

Marijn Kuijpers*¹, Dieudonné van de Willige*¹, Amélie Freal¹, Anaël Chazeau¹, Mariella A. Franker¹, Jasper Hofenk¹, Ricardo J. Cordeiro Rodrigues¹, Lukas C. Kapitein¹, Anna Akhmanova¹, Dick Jaarsma² & Casper C. Hoogenraad¹

* Co-first author

Neuron (2016)

89:461–471

doi: 10.1016/j.neuron.2016.01.022

¹ Cell Biology, Faculty of Science, Utrecht University, Padualaan 8, 3584 CH Utrecht, The Netherlands

² Department of Neuroscience, Erasmus Medical Center, 3015 CE Rotterdam, the Netherlands

Abstract

2

The development and homeostasis of neurons relies heavily on the selective targeting of vesicles into axon and dendrites. Microtubule-based motor proteins play an important role in polarized transport; however, the sorting mechanism to exclude dendritic cargo from the axon is unclear. We show that the dynein regulator NDEL1 controls somatodendritic cargo transport at the axon initial segment (AIS). NDEL1 localizes to the AIS via an interaction with the scaffold protein Ankyrin-G. Depletion of NDEL1 or its binding partner LIS1 results in both cell-wide and local defects, including the non-polarized trafficking of dendritic cargo through the AIS. We propose a model in which LIS1 is a critical mediator of local NDEL1-based dynein activation at the AIS. By localizing to the AIS, NDEL1 facilitates the reversal of somatodendritic cargos in the proximal axon.

Introduction

Due to their distinct functions, axons and dendrites differ in their molecular organization and require specific building blocks and cellular materials. The axon initial segment (AIS) is a specialized compartment in the proximal axon that plays a critical role in separating the somatodendritic and axonal compartments, and in maintaining the molecular and functional polarity of the neuron [1]. The AIS forms a diffusion barrier for membrane proteins at the cell surface and regulates selective intracellular cargo traffic between the soma and the axon [2]. Vesicles containing somatodendritic cargo enter the axon but very rarely move beyond the AIS, whereas cargoes transporting axonal proteins proceed through the AIS into more distal parts [3, 4]. However, the molecular processes that control selective transport at the AIS remain unclear.

There is strong evidence that cytoskeleton-based motor proteins drive selective transport to sort cargo into axons and dendrites. One model suggests that filamentous actin in the AIS may contribute to selective transport by halting somatodendritic vesicles and serving as a substrate for myosin-mediated vesicle transport [5, 6]. Another model proposes that targeting of polarized cargo is determined by a distinct microtubule (MT) organization in axons and dendrites, in combination with the coordinated regulation of MT-based motor proteins [7]. In this way, the unidirectional axonal microtubule organization facilitates MT plus-end directed kinesin movements, resulting in axonal targeting [8, 9]. In contrast, MT minus-end-directed dynein drives retrograde axonal transport. Its function as key retrograde axonal motor raises the question whether dynein also plays a role in preventing somatodendritic cargo from entering the axon. However, whether dynein-mediated somatodendritic vesicle sorting plays a role at the AIS is unexplored.

In this study, we demonstrate that dynein and its regulator Nuclear distribution element like 1 (NDEL1) control cargo sorting at the AIS. Our data show that NDEL1 is concentrated in the AIS via interaction with the AIS scaffold protein Ankyrin-G (AnkG) and that depletion of NDEL1 or its binding partner LIS1 leads to the entry of dendritic cargo into the proximal axon. We propose a model in which LIS1 is a critical mediator of NDEL1-based dynein activation at the AIS, and in which

AIS-bound NDEL1 facilitates the local direction reversal of somatodendritic vesicles. These results suggest a new mechanism for selective vesicle filtering at the AIS and reveal a critical role for NDEL1 as a gatekeeper of somatodendritic transport cargos.

Results

2

Dynein regulators NDEL1 and LIS1 localize to the AIS

To determine whether dynein plays a role in somatodendritic cargo transport at the AIS, we screened the subcellular distribution of dynein components, dynactin and other dynein regulators in developing and mature neurons. Most dynein and dynactin antibodies showed diffuse cytoplasmic staining throughout the axon shaft, with a higher intensity in the growth cones (Figure S1 and data not shown). The NDEL1 antibody we used in this study is specific for NDEL1, as it does not recognize the NDEL1 homolog NDE1 (Figure 1A). Consistent with previous studies [10, 11], NDEL1 expression increased as neurons developed (Figure 1B). Immunocytochemistry of neurons at day in vitro 1 (DIV1) showed that NDEL1 was predominantly present around the centrosome as labeled by pericentrin and the pericentriolar marker PCM1 (Figure 1C,D,F and S1A). We found that NDEL1 staining was lost from the pericentriolar region at later stages of neuronal development (Figure 1E). Remarkably, however, in DIV3 neurons NDEL1 showed a preferential localization in the proximal part of the axon (Figure 1G). Furthermore, the axonal NDEL1 staining pattern overlapped with AnkG staining, which outlines the AIS (Figure S2A). Super-resolved images also indicated a strong degree of co-localization of both endogenous and overexpressed NDEL1 with AnkG at the AIS membrane (Figure 1H,I). To analyze the redistribution of NDEL1 during axogenesis and AIS formation, stage 3 neurons were fixed at DIV2 and stained for tau, AnkG and NDEL1. At this stage, only 10% of tau-positive axons were positive for NDEL1, indicating that NDEL1 distribution to the AIS occurred after axon specification. In contrast, AIS localization of NDEL1 was observed in 100% of AnkG positive axons (Figure 1J,K), suggesting that AnkG and NDEL1 localize to the AIS around the same time. Interestingly, LIS1, a binding partner of NDEL1 [10, 11], is expressed throughout the neuron and is enriched at the growth cone but also showed a preferential localization in the proximal part of the axon in ~60% of neurons (Figure 1L and S1B,C).

The homolog of NDEL1, NDE1, is predominantly present at early embryogenesis in proliferating neuronal progenitors and migrating neurons [12]. We could detect endogenous NDE1 expression in cortical neuron extracts, but no specific staining was found at the AIS or elsewhere in hippocampal neurons (Figure 1B and data not shown). However, low-level expression of GFP-tagged NDE1 yielded AIS localization (Figure S2C), suggesting that exogenous NDE1 interacts with the AIS. However, whether this interaction is physiologically relevant remains unclear. Finally, to determine whether NDEL1 localized at the AIS of neurons of the adult central nervous system (CNS), we performed immunohistochemistry of NDEL1 and AnkG on brain sections of adult mice. NDEL1 co-distributed with AnkG throughout the CNS and is present at the AIS of all neuronal types examined (Figure S2D-H). Together, these data indicate that NDEL1 shifts its localization from a pericentriolar region to the AIS during neuron differentiation. Consistent with previous immunohistochemistry data, both NDEL1 and LIS1 are present at the AIS in more mature neurons [11].

NDEL1 interacts with the neuron-specific isoform of AnkG

To better understand the role of NDEL1 and LIS1 at the AIS, we searched for binding partners by performing pull-down assays combined with mass spectrometry. Bio-GFP-LIS1, NDE1 and NDEL1 bound to several components of dynein and dynactin (Figure 2A), confirming the previously identified interactions with the dynein complex [10, 11]. In addition, we identified novel potential NDEL1 binding partners, including α -actinin, AnkG, β IV-spectrin and synaptopodin. These proteins were all described to be abundantly present at the AIS [13]. We also found these proteins highly enriched in the NDE1 but not in the LIS1 pull-down fraction (Figure 2A). Mass spectrometry results were confirmed by Western blotting and GFP pull-down experiments (Figure 2D,E), demonstrating that both NDE1 and NDEL1 associate with components of the AIS.

AnkG is essential for AIS assembly and required for clustering of most other AIS components [1]. The two largest AnkG isoforms, AnkG-270 and AnkG-480, are neuron-specific and contain serine-rich and tail domains that contribute to restriction of AnkG at the AIS [14]. To identify the region through which AnkG interacts with NDEL1, we made truncated AnkG-270-GFP constructs encoding either the serine-rich and tail domains or an AnkG variant lacking these domains

(Figure 2B). Pull-down experiments showed that NDEL1 only co-precipitates with AnkG fragments that contain the neuron specific serine-rich and tail domains (Figure 2F). We next generated several NDEL1 truncations, including the N-terminal domain (NDEL1-N) that binds to dynein and LIS1 [15], and the C-terminal domain (NDEL1-C) (Figure 2C). AnkG only co-precipitated with GFP-NDEL1 constructs that contained the C-terminal fragment (Figure 2G). When expressed in neurons, the NDEL1 N terminus showed a diffuse expression pattern throughout the neuron, while the NDEL1 C-terminal domain localized to the AIS (Figure 2H). Together, these data show that the C terminus of NDEL1 interacts with the neuron-specific isoform of AnkG.

AnkG is required for AIS localization of NDEL1

To determine the turnover of NDEL1 in the AIS, we performed fluorescence recovery after photobleaching (FRAP) analysis of GFP-NDEL1 compared to GFP-AnkG and

> Figure 1. NDEL1 shifts from a pericentriolar to an axon initial segment localization.

(A) Lysates of HEK293 cells transfected with GFP, GFP-NDE1 or -NDEL1 constructs, probed by the indicated antibodies on western blot.

(B) Western blot of DIV1-21 cortical neuron lysates probed by the indicated antibodies.

(C-E) DIV0, 1 or 3 cultured hippocampal neurons stained for centrosome marker pericentrin (red) and NDEL1 (green). Arrowheads indicate NDEL1 localization.

(F) Soma of a DIV1 neuron stained for pericentrin (blue), NDEL1 (green) and pericentriolar material 1 (PCM1, red).

(G) DIV3 neuron stained for NDEL1 (green) and axonal marker tau (red).

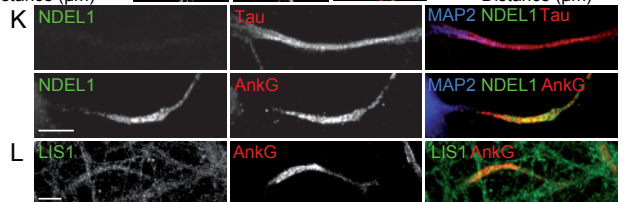
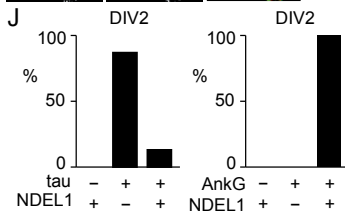
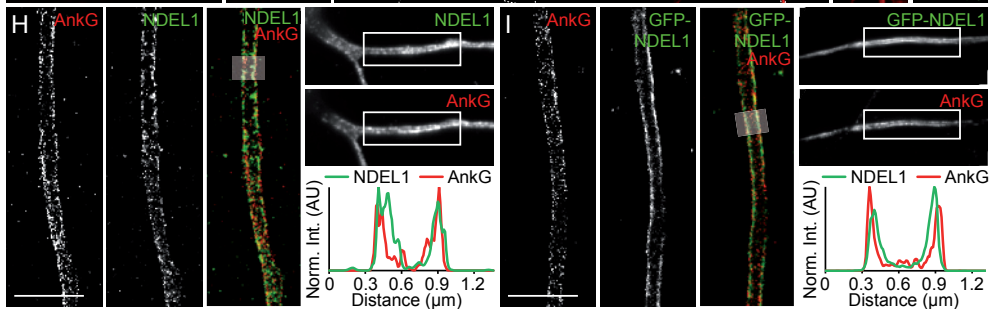
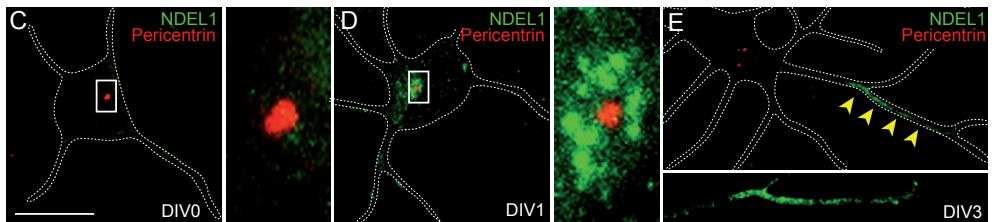
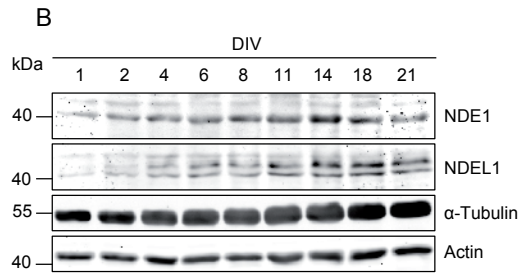
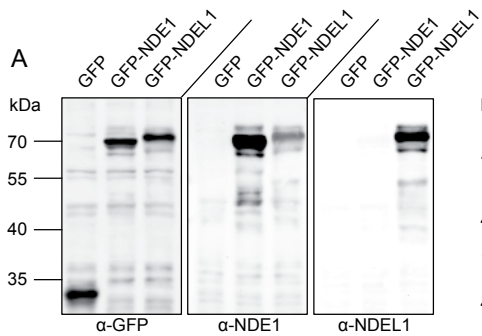
(H, I) dSTORM (direct stochastic optical reconstruction microscopy) images and line scans of DIV5 neurons, stained for AnkG (red) and NDEL1 (green) (H) or GFP-NDEL1 (green) (I). Left: dSTORM reconstructions, top right: widefield images (white boxes indicate super-resolved area), bottom right: line scans of fluorescence intensity along the transparent white line indicated in the dSTORM reconstruction image.

(J) Percentage of axons positive for NDEL1 and tau (left) or AnkG (right) at DIV2. 50-100 neurons were analyzed.

(K) Axons of DIV1 neurons stained for MAP2 (blue), NDEL1 (green) and tau or AnkG (red).

(L) A DIV11 neuron with endogenous LIS1 enrichment (green) in the AIS (marked by AnkG, red).

Neurons are outlined by dashes. Insets show magnification of boxed areas. Scale bars: 20 μm (C), 3 μm (F, H, I), 5 μm (G, K, L).



GFP-tau in axons of DIV11 neurons (Figure 2I). GFP-tau fluorescence recovered rapidly in axons and reached a maximal recovery of ~95% within 10 min. However, GFP-NDEL1 fluorescence had a much slower recovery reaching a maximum of ~20-25% and behaved similar to that of GFP-AnkG (Figure 2J), indicating that at the AIS a large fraction of NDEL1 molecules is immobile (Figure 2J,K). In contrast, FRAP analysis of GFP-LIS1 showed fast recovery at the AIS, suggesting that LIS1 is not stably bound to the AIS (Figure 2L). NDEL1 staining disappeared from the AIS after knockdown of AnkG (Figure S3C-E) and was slightly reduced in LIS1-depleted cells (Figure S3A,B), indicating that recruitment of NDEL1 to the AIS depends on AnkG and to some extent on LIS1. Upon drug-induced disruption of the MT or actin cytoskeleton, both AnkG and NDEL1 were still present at the AIS, suggesting that their localization is not largely dependent on the underlying cytoskeleton (Figure S3F,G). Taken together, these data show that both AnkG and NDEL1 are stably present at the AIS and that AnkG and LIS1 are required for the AIS localization of NDEL1.

> Figure 2. NDEL1 stably localizes to the AIS by binding to AnkG.

(A) Binding partners of bio-GFP-LIS1, -NDE1 and -NDEL1 from rat brain extracts identified by mass spectrometry. For proteins marked with *, only human peptides were identified. The orange box highlights novel potential binding partners.

(B, C) Overview of AnkG (B) and NDEL1 (C) truncations.

(D, E) Western blot analysis of biotin (D) and GFP (E) pull-downs from extracts of HEK293 transfected with the indicated constructs, probed for GFP and endogenous AnkG and β -IV-spectrin (D) or GFP and HA (E).

(F, G) Binding domain analysis by GFP pull-down using HEK293 lysates transfected with GFP-AnkG truncations and HA-NDEL1 (F) or with GFP-NDEL1 truncations and HA-AnkG.

(H) Neurons transfected with GFP-tagged NDEL1 N- or C-terminus and stained for AnkG (red) antibody. Arrows indicate AISs. Scale bar: 10 μ m

(I) Images showing GFP-tau, -AnkG or -NDEL1 recovery after photobleaching in the AIS of DIV7 neurons.

(J) Quantification of GFP fluorescence recovery in photobleached axons as in (I).

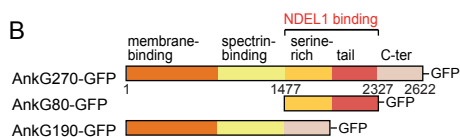
(K) Quantification of the mobile and immobile fractions of GFP-tau, -AnkG and -NDEL1. 10 cells were analyzed per condition.

(L) Quantification of GFP-LIS1 and -NDEL1 fluorescence recovery as in (J). 10 cells were analyzed per condition.

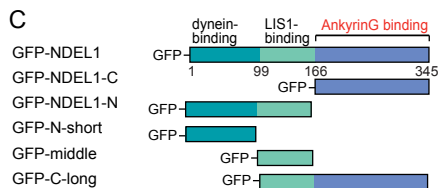
A

protein	accession	Unique peptides		
		LIS1	NDE1	NDEL1
Lissencephaly 1 (LIS1)	P63004	28	25	23
nuclear distribution gene E homolog 1 (NDE1)*	Q9NXR1	20	24	14
nuclear distribution gene E-like homolog 1 (NDEL1)	Q78PB6	13	6	22
Dynein 1 heavy chain (HC)	P38650	79	175	176
Dynein 1 intermediate chain 1 (IC1)	G3V792	0	13	17
Dynein 1 intermediate chain 2 (IC2)	Q32871	4	11	13
Dynein 1 light intermediate chain 1 (LIC1)	G3V7G0	0	13	17
Dynein 1 light intermediate chain 2 (LIC2)	Q82598	4	12	13
Dynein Roadblock light chain 1 (LRB1)	P62628	0	2	3
Dynein LC8 light chain 1 (LL1)	P63170	0	2	3
Dynein LC8 light chain 2 (LL2)	Q78F75	0	3	2
Dynactin 1 (p150)	D4A8U7	0	5	3
Dynactin 2 (p50 dynamitin)	Q6AVH5	0	4	0
F-actin-capping protein subunit beta	Q5XI32	2	9	8
Actinin, Alpha 2	D3ZCV0	6	33	35
Beta-IV Spectrin	F1LSL8	0	18	20
AnkyrinG	F1LNM3	0	17	15
Synaptopodin	Q9Z327	0	13	8

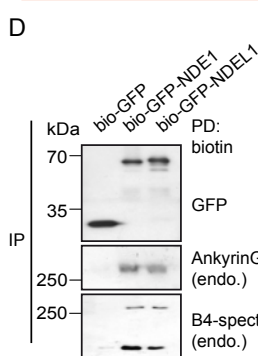
B



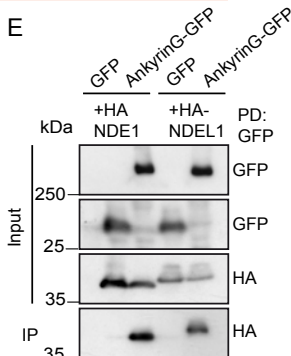
C



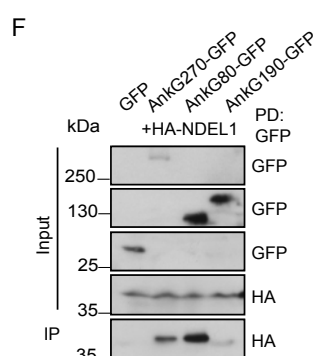
D



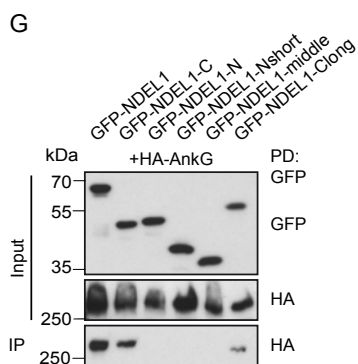
E



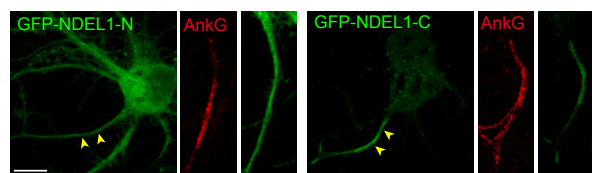
F



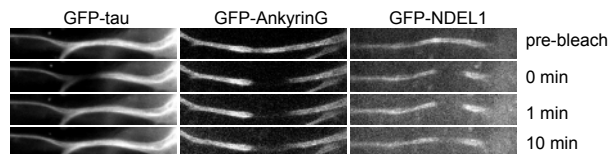
G



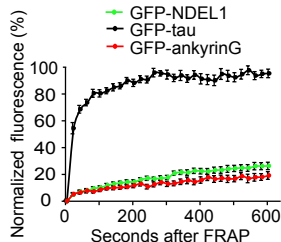
H



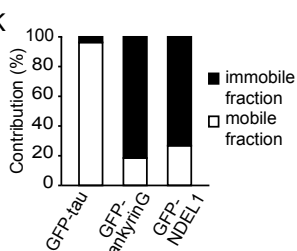
I



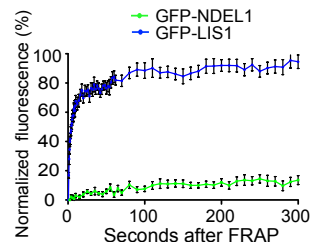
J



K



L



To test the role of NDEL1 at the AIS, we generated two independent shRNAs against NDEL1 [16, 17] and performed knockdown experiments in hippocampal neurons. Efficiency of shRNA knockdown was verified by immunostaining of endogenous NDEL1 (Figure 3A,B). In addition, we used the CRISPR/Cas9 system [18] to silence NDEL1 expression in hippocampal neurons (Figure S4A,C). In contrast to the loss of NDEL1 staining after AnkG knockdown (Figure S3C,E), NDEL1 knockdown or silencing did not affect the levels of AnkG at the AIS (Figure 3B, S4B). We next determined whether NDEL1 influences the localization of other dynein/dynactin components in the AIS. Both NDEL1 overexpression and depletion did not affect the diffuse cytoplasmic staining of the light intermediate chain of dynein, the p150 subunit of dynactin, or LIS1 at the AIS (Figure S3H,I). In addition, inhibition of the dynein/dynactin complex by overexpressing GFP-p150-cc1 did not affect NDEL1 localization (Figure S3J). These data suggest that NDEL1 is not required for AIS integrity or dynein/dynactin localization in the proximal axon, and that its AIS localization does not depend on dynein/dynactin activity.

NDEL1 depletion causes axon enlargement

Homozygous NDEL1 knockout mice die at early embryonic stages, while brain-specific mutants show severe cortical neuronal migration defects [16, 19, 20]. Analyses of mature neurons in conditional NDEL1 knockout mice revealed defects in axon and dendrite morphology and aberrant axonal enlargement at the AIS [21]. We analyzed the morphological defects in cultured neurons. Consistent with the *in vivo* data, NDEL1 depletion caused a decrease in axonal and dendritic length (Figure 3D-F) and resulted in increased axonal diameter both at the AIS (Figure 3G, S4A,D) and more distally (Figure 3H, S4D). We further analyzed the axonal enlargement and found that shRNA-mediated depletion of LIS1 (Figure 3A,C) or expression of dominant-negative dynactin (p150-cc1) also increased AIS thickness (Figure S5A,B), suggesting that regulation of dynein activity is required for normal axon morphology. The axonal phenotype of NDEL1 depletion was rescued by co-expressing full length NDEL1, (Figure S5C,D). In contrast, NDEL1 N- and C-terminal fragments were not able to restore normal axon diameter (Figure S5C,D). Instead, NDEL1 co-expression reduced axonal enlargement of NDEL1-depleted neurons, compatible with functional redundancy between NDEL1 and LIS1 (Figure S5E). LIS1 overexpression did not attenuate axonal enlargement in NDEL1-depleted neurons, suggesting

that NDEL1 is required for LIS1 function in maintaining axon caliber (Figure S5E). Similarly, axonal enlargement induced by LIS1 depletion could not be rescued by NDEL1 or NDE1 (Figure S5F). Finally, we determined the axon diameter of AnkG-depleted neurons, where NDEL1 is still present yet no longer concentrated in the AIS. As reported previously [22, 23], axons of AnkG knockdown neurons only showed a mild and local increase of axon diameter due to dendrite-like characteristics of the proximal axon (Figure 3H), which did not resemble the morphology of axons of NDEL1-depleted neurons (Figure S5K). Using a complimentary approach, we overexpressed the NDEL1 C terminus to displace endogenous NDEL1 from the AIS and found no differences in axon caliber (Figure S5I). In conclusion, NDEL1 is required for maintenance of axon caliber, but this function is most likely independent of its accumulation at the AIS.

Altered cytoskeleton organization in NDEL1-depleted axons

What mechanisms could explain the axonal enlargement in NDEL1-depleted neurons? We examined the effect of NDEL1 knockdown on axonal MT dynamics and organization, neurofilaments and actin. Consistent with previous data [24], neurofilament content was reduced when NDEL1 was depleted or dynein function was inhibited (Figure S6A). F-actin appeared unaffected in the proximal axon (Figure S6B,C), although periodic ring-like structures were disrupted (Figure S6D). While NDEL1-depleted neurons did not differ from control neurons in the amount of dynamic MTs (Figure S6E), the direction of MT plus-end growth (Figure S6F) or the localization of non-centrosomal MT minus-ends (Figure S6G), the overall MT organization was disrupted. At sites of focal axonal swellings, MT bundles splayed and some MTs buckled (Figure S6H). Live imaging revealed that MTs in the proximal axon deformed in NDEL1 knockdown neurons (Figure S6I,J), and FRAP experiments confirmed that MTs at the AIS of NDEL1-depleted neurons were less stable (Figure S6K). These MT organization alterations may be explained by mechanical stress, as was for example reported after axonal stretch injury [25]. Recently, dynein was proposed to counteract forces resulting from retrograde actin flow. As a result, dynein inhibition caused “en-masse” displacement of MTs towards the cell body and compacted axons [26]. To test whether NDEL1 depletion resulted in similar

(text continues after Figure 3) >

> **Figure 3. NDEL1 is required for axon morphology and polarized cargo trafficking.**

(A) Quantification of NDEL1 and LIS1 levels in the AIS (NDEL1) or soma (LIS1) of knockdown (KD) neurons. 9-14 images were analyzed per condition.

(B) AISs of DIV7 neurons co-expressing β -gal (β gal, not shown) and control (empty pSuper) or NDEL1-shRNA, stained for NDEL1 (red) and AnkG (green).

(C) Neurons transfected with GFP and control or LIS1-shRNA stained for LIS1 (red).

(D, E) Quantification of total axonal (D) and dendritic length (E) in control and NDEL1 knockdown neurons. 8 to 20 cells were analyzed per condition.

(F, G) DIV7 neurons transfected with control or NDEL1-shRNAs and β -gal (F) or MARCKS-GFP (G) to visualize morphology. In F: Red arrows indicate the AIS, brackets indicate the soma. In G: AnkG staining (red) indicates the AIS.

(H) Quantification of axon diameter of DIV8 neurons co-transfected with β -gal, Tfr-GFP and control, NDEL1- or AnkG-shRNA, measured at the indicated distances from the soma. 10 cells were analyzed per condition.

(I) Quantification of Tfr-GFP fluorescence intensity in neurons as described for (H), measured as the average intensity of various axonal segments (A, indicated distances) and normalized to dendrites (D). 10 cells were analyzed per condition.

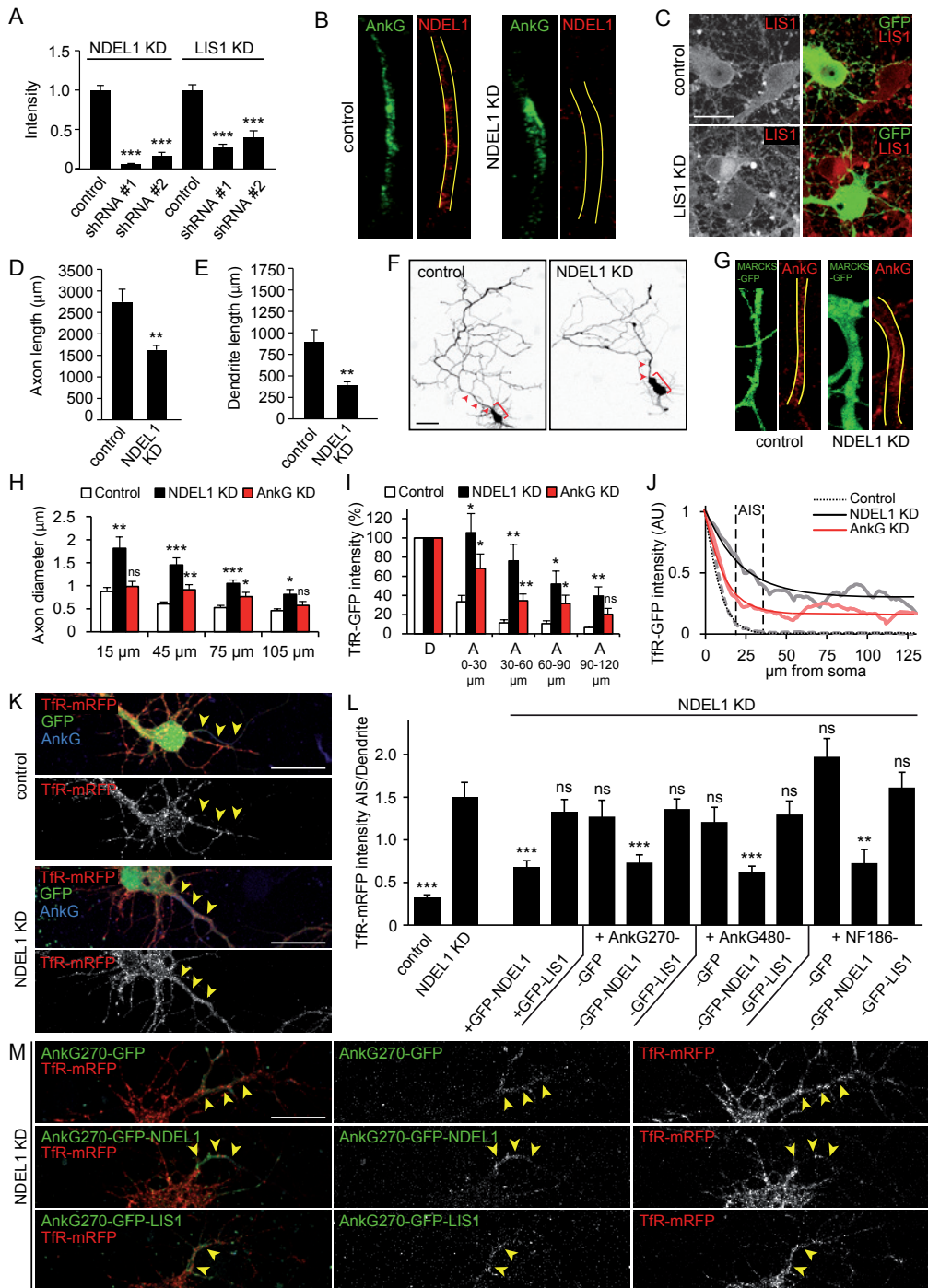
(J) Smoothened Tfr-GFP fluorescence intensity plots along axons of a single representative control, NDEL1 KD and AnkG KD neuron as described in (H). Values were normalized to the highest in the dataset. Dotted lines indicate the position of AnkG staining in control and NDEL1 KD neurons.

(K) DIV7 control neurons (top) or NDEL1 depleted neurons (bottom) co-transfected with Tfr-mRFP and GFP (fill), and stained for AnkG (blue). Yellow arrowheads indicate the AIS.

(L) Quantification of the ratio of Tfr-mRFP fluorescence intensity (AIS/dendrites) of neurons in the specified conditions. 15-20 neurons were analyzed per condition. P-values were calculated compared to the NDEL1 KD condition.

(M) DIV7 neurons depleted of endogenous NDEL1 and co-transfected with Tfr-mRFP and indicated AnkG270-GFP-fusions. Yellow arrowheads indicate the AIS.

Data are presented as means \pm SEM, * $P < 0.05$, ** $P < 0.01$, *** $P < 0.001$. Scale bars: 20 μ m (C), 50 μ m (F), 30 μ m (K,M).



translocations, we tracked the movement of photoactivated patches of MTs in the proximal axon. Indeed, MTs of NDEL1 knockdown neurons relocated toward the soma at a rate of 0.95 $\mu\text{m}/\text{hour}$, as opposed to the relatively static MTs of control neurons (Figure S6L). These data, paired with the decrease in axon length (Figure 3D), suggest that the axonal enlargement observed in NDEL1-depleted neurons may result from axonal compaction as a consequence of force imbalances.

AIS-localized NDEL1 is required for the polarized distribution of somatodendritic cargo

Because of NDEL1's specific localization at the AIS and its ability to regulate dynein, we hypothesized that NDEL1 could be involved in cargo sorting at the AIS. We therefore first examined the polarized distribution of the transferrin receptor (TfR), a recycling transmembrane protein strictly localized to the somatodendritic region. In control cells, TfR-GFP was excluded from the axon starting at the AIS (Figure 3I-L, S4E-F). However, after depletion of NDEL1, TfR appeared in the axon (Figure 3I-L, S4E,F,) and in some cases accumulated at the AIS (Figure 4A). Consistently, the observed mistargeting of TfR was rescued by co-expressing NDEL1 or NDE1 but not LIS1 (Figure S7B). In these experiments, some neurons showed non-polarized TfR trafficking without axon enlargement and vice versa (Figure S5G,H), suggesting that there is no causative relation between axon enlargement and trafficking defects. In addition, TfR transport was non-selective upon both LIS1 depletion and dynein inhibition (Figure 4A-C, S7C,D). Together, these data demonstrate that NDEL1, LIS1 and dynein are required for the polarized distribution of TfR vesicles.

We also assessed the behavior of mitochondria and Rab3-positive synaptic vesicle precursors, as well as the distribution of the somatodendritic coxsackie and adenovirus receptor (CAR) and AMPA receptor subunits GluR1 and GluR2, and confirmed a more general role for NDEL1 in selective cargo trafficking (Figure S7E-O) consistent with previous studies. Finally, to test the importance of NDEL1's localization at the AIS, we first examined TfR trafficking in AnkG-depleted neurons. Albeit less efficiently than in NDEL1 knockdown neurons, we found that TfR vesicles entered the axon (Figure 3I,J). Additionally, we displaced endogenous NDEL1 from the AIS by overexpressing the NDEL1 C terminus. In neurons overexpressing NDEL1-C, TfR vesicles moderately entered the AIS, while axons did not enlarge (Figure S5I,J). Lastly, we fused full-length NDEL1 to AIS-immobilized proteins and used these

chimeric proteins to rescue polarized TfR trafficking in the absence of endogenous NDEL1. We found that both fusions of NDEL1 to AnkG or neurofascin-186 (NF-186), a transmembrane AIS protein, prevented axonal entry of TfR (Figure 3L,M). By contrast, AIS-targeted fusions of LIS1 or GFP to NF186 or AnkG were not able to rescue this phenotype (Figure 3L,M). Our data suggest that NDEL1 localization to the AIS contributes to efficient local somatodendritic cargo reversal.

NDEL1 reverses the direction of somatodendritic vesicles at the AIS

We next tested how NDEL1 depletion affects axonal and dendritic vesicle transport dynamics at the AIS using live cell imaging. In control neurons, TfR vesicles that entered the axon paused (~34%), reversed direction (~55%) or proceeded through the AIS (~11%) (Figure 4E-G). In NDEL1 knockdown neurons, ~50% of TfR vesicles paused, while only ~5% reversed direction and ~45% of vesicles proceeded through the AIS into more distal parts of the axon (Figure 4F,G). By contrast, TfR movement in dendrites was unaffected (Figure 4H). Similar results were obtained by overexpression of p150-cc1 (Figure 4G). Importantly, transport of axonal vesicles labeled by NgCAM-GFP was not affected by NDEL1 knockdown and p150-cc1 expression (Figure 4D, 4I-L). Together, these results show that dynein and NDEL1 reverse the direction of somatodendritic vesicles.

Dynein drives retrograde transport at the proximal axon

Previous work suggested a role for Myosin motors in the retrograde transport of cargo at the AIS [3, 5, 6]. To compare the transport capacity of dynein and myosin at the AIS, we used an inducible cargo trafficking assay in which we trigger the binding of specific motor proteins to peroxisomes during live-cell recordings [9, 27] (Figure S8A). Coupling of dynein to peroxisomes via BICDN markedly increased the number of peroxisomes moving out of the AIS toward the soma (Figure S8B-D), consistent with dynein-mediated retrograde transport towards MT minus-ends in axons. However, very little cargo motility was observed upon recruitment of Myosin motors (Figure S8B-D), indicating that Myosin-V/VI is able to halt but not displace cargos in the proximal axon. These results support the view that dynein can drive retrograde cargo movement and that NDEL1 may serve as positive regulator of dynein activity at the AIS.

Discussion

AnkG anchoring of NDEL1 filters intracellular transport at AIS

The AIS is believed to be involved in the regulation of axon-dendrite polarity by controlling intracellular transport [2]. Here we show that NDEL1 specifically localizes to the proximal axon via its C-terminal interaction with AnkG. The highly conserved N terminus of NDEL1 binds to LIS1 and is critical for dynein activity [28, 29], providing a direct link between a core AIS scaffold and dynein regulation. NDEL1 is stably present at the AIS and may transiently activate dynein on cargos

2

> Figure 4. NDEL1 affects somatodendritic vesicle behavior at the AIS .

(A-C) DIV10 neurons co-transfected with TfR-GFP and control (A), NDEL1-shRNAs (B) or HA-p150-cc1 (C), and stained for dendrite specific marker MAP2 (red). Yellow arrowheads indicate the AIS.

(D) Images (top) and quantification of NgCAM-GFP fluorescence intensity (bottom) in the AIS and dendrites of DIV8 neurons, transfected with NgCAM-GFP, β -gal (blue) and control, NDEL1-shRNA or HA-p150-cc1 and stained for AnkG (red).

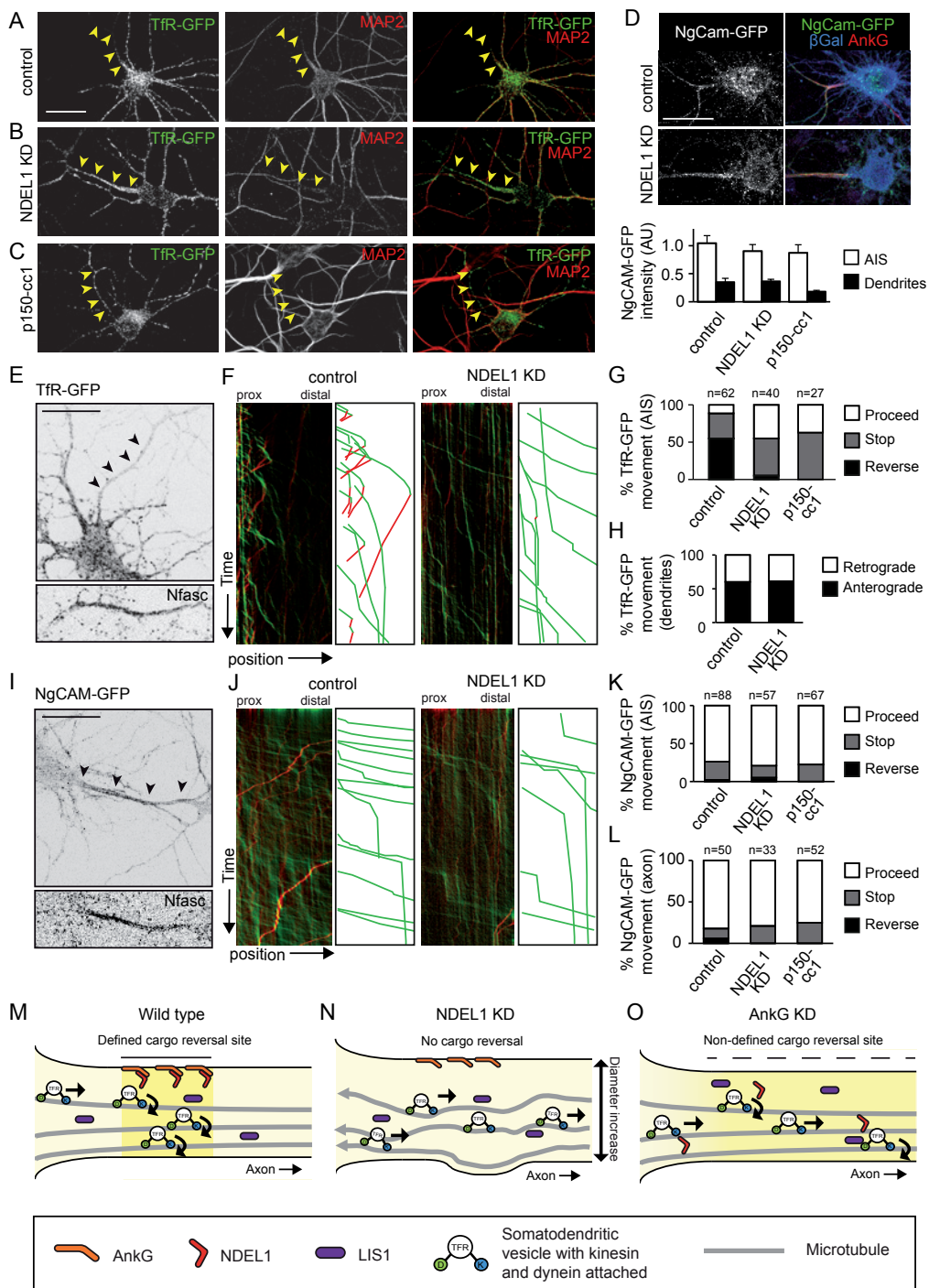
(E, F) Kymographs illustrating the behavior of TfR-GFP vesicles in the AIS of live DIV7 neurons, co-transfected with TfR-GFP and control (E, F) or NDEL1-shRNA (F). AISs were highlighted by neurofascin (Nfasc) staining. Anterograde traces are color-coded in green, retrograde traces are red.

(G, H) Quantification of vesicle TfR vesicle dynamics in the AIS (G) and dendrites (H) of neurons as described for (E, F), as well as DIV7 neurons co-transfected with TfR-GFP and HA-p150-cc1 (G). The number of events is shown above the graph.

(I-L) Live cell imaging analysis of the behavior of NgCAM-GFP vesicles in control, NDEL1 KD and HA-p150-cc1 overexpressing neurons as described for (E-H). In (I), a DIV7 neuron co-transfected with NgCAM-GFP and control vector. Kymographs show the behavior of NgCAM-GFP vesicles in control and NDEL1 knockdown neurons (J). Quantification of axonal vesicle dynamics inside the AIS is shown in (K). The behavior of vesicles exiting the AIS into the axon is quantified up until leaving the field of view in (L).

(M-O) Schematic depiction of somatodendritic vesicle behavior and microtubule architecture in control (M), NDEL1 KD (N) and AnkG KD neurons (O).

Scale bars: 30 μ m (A, D), 20 μ m (E, I). Data are presented as means \pm SEM, *P<0.05, **P<0.01, ***P<0.001.



that enter the proximal axon. An accumulation of regulatory proteins at the AIS might efficiently control intracellular transport, by making it possible to precisely modulate the activity of dynein-attached cargos during axonal entry. We speculate that NDEL1 is a limiting factor for dynein activity in the proximal axon and that high local concentration of NDEL1 facilitates rapid activation of dynein motors. This allows for quick switches of transport direction in a precisely defined axonal region (Figure 4M). Accordingly, loss of NDEL1 causes somatodendritic cargo to be retained at the AIS or to proceed into the axon (Figure 4N). NDEL1 redistribution caused by loss of AnkG results in moderate entry of somatodendritic cargo into axons, most likely because cargo reversals are not prevented by loss of dynein function but now occur in a larger, less-defined axonal region (Figure 4O). Thus, the link between AnkG and NDEL1 has important implications for filtering intracellular transport through the AIS.

Model for controlling NDEL1-mediated dynein activity at the AIS

Several observations have suggested that transport vesicles maintain a stable population of distinct motors. In such a model, regulatory proteins such as NDEL1 modulate the activities of specific motors present on cargo. We envision that kinesin motors driving dendritic vesicles into the axon are halted at the AIS, possibly by myosin motors. When dynein is locally activated, the cargo moves towards the MT minus-end back to the soma. Consistent with this model, NDEL1 has been shown to act as an upstream dynein-regulator to enhance efficient minus-end directed transport [10, 11, 30]. However, it remains unclear how AnkG-anchored NDEL1 activates dynein on dendritic cargo vesicles, either by directly contacting vesicles during axonal entry or by transiently recruiting regulatory factors that modulate dynein activity. In both scenarios, LIS1 is likely an important co-regulator of dynein activity at the AIS. Since LIS1 interacts with both NDEL1 and dynein [10, 11] and is enriched but not stably bound to the AIS, we suggest a model in which cytoplasmic LIS1 shuttles between AnkG-NDEL1 at the membrane and dynein on dendritic cargo vesicles. In this scenario, NDEL1 may activate LIS1 molecules by conformational rearrangement or other regulatory mechanisms. Given the fast exchange of LIS1 at the AIS, this creates a pool of activated LIS1 molecules that may intercept dynein on dendritic cargo vesicles and subsequently promote dynein motor activity. This model also implies that dynein motors bound to dendritic vesicles are particularly

sensitive to specific co-factors, which may be part of a general mechanism to assign individual dyneins for specific modes of cargo regulation [31]. Future studies are required to systematically test the combined regulatory actions of NDEL1 and LIS1 on cargo-specific dynein.

Materials and methods

Antibodies and reagents

The following antibodies were used: rat-anti-NDEL1 (clones 4-9-C and 5-3-D), mouse- and rabbit-anti-LIS1, rabbit-anti- β IV-spectrin, rabbit-anti-LIC1/2. Details of other reagents are in the Supplemental Materials and Methods.

DNA constructs

The NDEL1 and NDE1 expression constructs and their deletion mutants were generated from mouse NDEL1 cDNA (IMAGE clone 2646029) and human NDE1 cDNA (IMAGE clone 2820974). The following rat shRNA sequences were used: NDEL1-shRNA#1 (5'-GCTAGGATATCAGCACTAA-3'), NDEL1-shRNA#2 (5'-GCAGGTCTCAGTGTAGAA-3'), LIS1-shRNA#1 (5'-CAATTAAGGTGTGGGATTA-3'), LIS1-shRNA#2 (5'-GAGTTGTGCTGATGACAAG-3') and AnkG-shRNA (5'-GAGTTGTGCTGATGACAAG-3').

Primary hippocampal neuron cultures and transfection

Primary hippocampal cultures were prepared from embryonic day 18 (E18) rat brains. Cells were plated on coverslips coated with poly-L-lysine (35 μ g/ml) and laminin (5 μ g/ml) at a density of 100,000 or 50,000/well (12-well plate). Cultures were grown in Neurobasal medium (NB) supplemented with B27, 0.5 mM glutamine, 12.5 μ M glutamate and penicillin/streptomycin. Hippocampal neurons were transfected using Lipofectamine 2000.

Live-cell imaging and Fluorescence Recovery After Photobleaching (FRAP)

Live cell imaging and TIRFM was performed on a Nikon Eclipse TE2000E microscope with CoolSNAP and QuantEM cameras (Roper Scientific). Neurons were maintained at 37°C with 5% CO₂ (Tokai Hit). The FRAP experiments were performed using the ILas2 system (Roper Scientific). For details see Supplemental Materials and Methods.

Acknowledgements

We thank Dr. H. Arai for the NDEL1 and NDE1 antibodies, Dr. M.N. Rasband for the β IV-Spectrin antibody and the HA-NF186-EGFP construct, Dr. O. Reiner for the LIS1 antibody, Dr. R. Vallee for the LIC1/2 antibodies, Dr. K. Rhee for the GFP-PCNTB-myc construct, Dr. Lippincott-Schwartz and Dr. Patterson for the PA-GFP construct and Dr. J. Demmers and Ing. K. Bezstarosti for help with mass spectrometry analyses. We are grateful to Dr. P.J.J. Mangeol, Dr. B. Prevo and Dr. E.J.G. Peterman for the kymography plugin. This work was supported by Netherlands Organization for Scientific Research (NWO-ALW-VICI, A.A., C.C.H.), the Netherlands Organization for Health Research and Development (ZonMW-TOP, C.C.H.), the European Science Foundation (EURYI, C.C.H.) and EMBO Young Investigators Program (YIP, C.C.H.).

2

Competing interests statement

The authors declare no competing financial interests.

Author contributions

M.K. and D.v.d.W. cloned DNA constructs, designed and performed biochemical and imaging experiments and wrote the manuscript, A.F. performed CRISPR-Cas9 experiments and cloned constructs, A.C. performed live imaging and dSTORM experiments under supervision of L.C.K, R.J.C.R. and J.H. cloned shRNA constructs and performed antibody staining experiments; M.A.F. performed the rapalog-inducible cargo trafficking assay; L.C.K and A.A. gave advice throughout the project and edited the manuscript; D.J. performed the immunohistochemistry on brain sections; C.C.H. supervised the research, coordinated the study and wrote the manuscript.

References

1. Rasband, M.N., The axon initial segment and the maintenance of neuronal polarity. *Nat Rev Neurosci*, 2010. 11(8): p. 552-62.
2. Leterrier, C. and B. Dargent, No Pasaran! Role of the axon initial segment in the regulation of protein transport and the maintenance of axonal identity. *Semin Cell Dev Biol*, 2013.
3. Al-Bassam, S., et al., Differential trafficking of transport vesicles contributes to the localization of dendritic proteins. *Cell Rep*, 2012. 2(1): p. 89-100.
4. Petersen, J.D., S. Kaech, and G. Banker, Selective microtubule-based transport of dendritic membrane proteins arises in concert with axon specification. *J Neurosci*, 2014. 34(12): p. 4135-47.
5. Lewis, T.L., Jr., et al., Myosin-dependent targeting of transmembrane proteins to neuronal dendrites. *Nat Neurosci*, 2009. 12(5): p. 568-76.
6. Watanabe, K., et al., Networks of polarized actin filaments in the axon initial segment provide a mechanism for sorting axonal and dendritic proteins. *Cell Rep*, 2012. 2(6): p. 1546-53.
7. Kapitein, L.C. and C.C. Hoogenraad, Which way to go? Cytoskeletal organization and polarized transport in neurons. *Mol Cell Neurosci*, 2011. 46(1): p. 9-20.
8. Nakata, T. and N. Hirokawa, Microtubules provide directional cues for polarized axonal transport through interaction with kinesin motor head. *J Cell Biol*, 2003. 162(6): p. 1045-55.
9. Kapitein, L.C., et al., Mixed microtubules steer dynein-driven cargo transport into dendrites. *Curr Biol*, 2010. 20(4): p. 290-9.
10. Niethammer, M., et al., NUDEL is a novel Cdk5 substrate that associates with LIS1 and cytoplasmic dynein. *Neuron*, 2000. 28(3): p. 697-711.
11. Sasaki, S., et al., A LIS1/NUDEL/cytoplasmic dynein heavy chain complex in the developing and adult nervous system. *Neuron*, 2000. 28(3): p. 681-96.
12. Feng, Y., et al., LIS1 regulates CNS lamination by interacting with mNudE, a central component of the centrosome. *Neuron*, 2000. 28(3): p. 665-79.
13. Sanchez-Ponce, D., et al., Colocalization of alpha-actinin and synaptopodin in the pyramidal cell axon initial segment. *Cereb Cortex*, 2012. 22(7): p. 1648-61.
14. Zhang, X. and V. Bennett, Restriction of 480/270-kD ankyrin G to axon proximal segments requires multiple ankyrin G-specific domains. *J Cell Biol*, 1998. 142(6): p. 1571-81.
15. Segal, M., et al., Ndel1-derived peptides modulate bidirectional transport of injected beads in the squid giant axon. *Biol Open*, 2012. 1(3): p. 220-31.
16. Shu, T., et al., Ndel1 operates in a common pathway with LIS1 and cytoplasmic dynein to regulate cortical neuronal positioning. *Neuron*, 2004. 44(2): p. 263-77.
17. Raaijmakers, J.A., M.E. Tanenbaum, and R.H. Medema, Systematic dissection of dynein regulators in mitosis. *J Cell Biol*, 2013. 201(2): p. 201-15.
18. Incontro, S., et al., Efficient, complete deletion of synaptic proteins using CRISPR. *Neuron*, 2014. 83(5): p. 1051-7.
19. Sasaki, S., et al., Complete loss of Ndel1 results in neuronal migration defects and early embryonic lethality. *Mol Cell Biol*, 2005. 25(17): p. 7812-27.
20. Youn, Y.H., et al., Distinct dose-dependent cortical neuronal migration and

- neurite extension defects in Lis1 and Ndel1 mutant mice. *J Neurosci*, 2009. 29(49): p. 15520-30.
- 21.** Hippenmeyer, S., et al., Genetic mosaic dissection of Lis1 and Ndel1 in neuronal migration. *Neuron*, 2010. 68(4): p. 695-709.
- 22.** Hedstrom, K.L., Y. Ogawa, and M.N. Rasband, AnkyrinG is required for maintenance of the axon initial segment and neuronal polarity. *J Cell Biol*, 2008. 183(4): p. 635-40.
- 23.** Sobotzik, J.M., et al., AnkyrinG is required to maintain axo-dendritic polarity in vivo. *Proc Natl Acad Sci U S A*, 2009. 106(41): p. 17564-9.
- 24.** Nguyen, M.D., et al., A NUDEL-dependent mechanism of neurofilament assembly regulates the integrity of CNS neurons. *Nat Cell Biol*, 2004. 6(7): p. 595-608.
- 25.** Tang-Schomer, M.D., et al., Partial interruption of axonal transport due to microtubule breakage accounts for the formation of periodic varicosities after traumatic axonal injury. *Exp Neurol*, 2012. 233(1): p. 364-72.
- 26.** Roossien, D.H., P. Lamoureux, and K.E. Miller, Cytoplasmic dynein pushes the cytoskeletal meshwork forward during axonal elongation. *J Cell Sci*, 2014. 127(Pt 16): p. 3593-602.
- 27.** Kapitein, L.C., et al., Myosin-V opposes microtubule-based cargo transport and drives directional motility on cortical actin. *Curr Biol*, 2013. 23(9): p. 828-34.
- 28.** Derewenda, U., et al., The structure of the coiled-coil domain of Ndel1 and the basis of its interaction with Lis1, the causal protein of Miller-Dieker lissencephaly. *Structure*, 2007. 15(11): p. 1467-81.
- 29.** Wang, S. and Y. Zheng, Identification of a novel dynein binding domain in nudel essential for spindle pole organization in *Xenopus* egg extract. *J Biol Chem*, 2011. 286(1): p. 587-93.
- 30.** McKenney, R.J., et al., LIS1 and NudE induce a persistent dynein force-producing state. *Cell*, 2010. 141(2): p. 304-14.
- 31.** Vallee, R.B., R.J. McKenney, and K.M. Ori-Mckenney, Multiple modes of cytoplasmic dynein regulation. *Nat Cell Biol*, 2012. 14(3): p. 224-30.

> **Figure S1, related to Figure 1. Dynein and dynactin antibodies show a diffuse cytoplasmic pattern while NDEL1 localizes to the centrosome (young neurons) or AIS (old neurons), the latter sometimes with LIS1.**

(A) Representative images of hippocampal neurons (DIV1) stained with indicated antibodies (red) and transfected with GFP-pericentrin (PCNT) or stained for pericentrin (green) to show the centrosome. The lower panel shows enlarged regions of the cells, as indicated by the white squares.

(B, C) Analysis of antibody stainings at the AIS of DIV3 (B) or DIV21 (C) hippocampal neurons. Fluorescence intensity plots provide a comparison of immunosignal strength of AnkG (AIS, green) and the indicated antibody (red).

Scale bars: 6 μm (A), 10 μm (B, C).

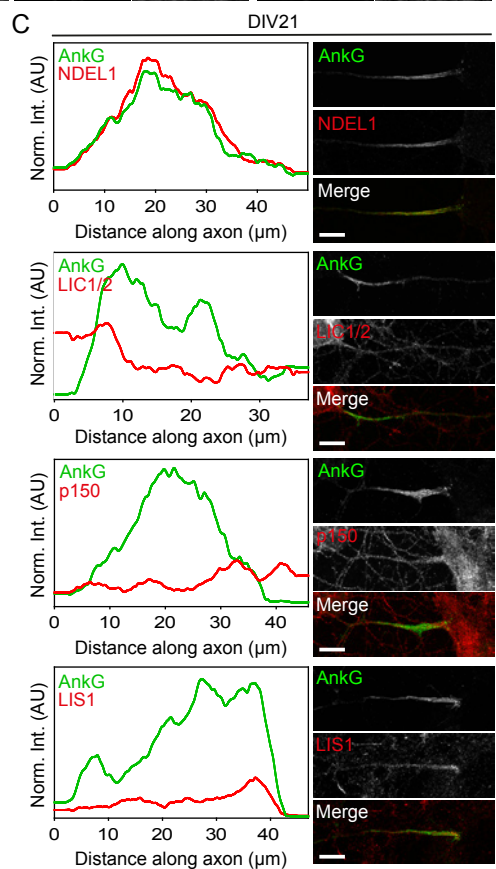
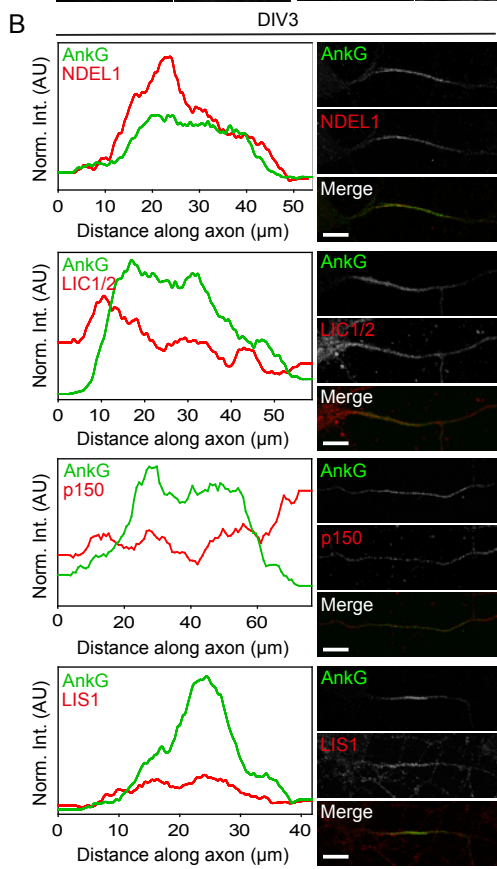
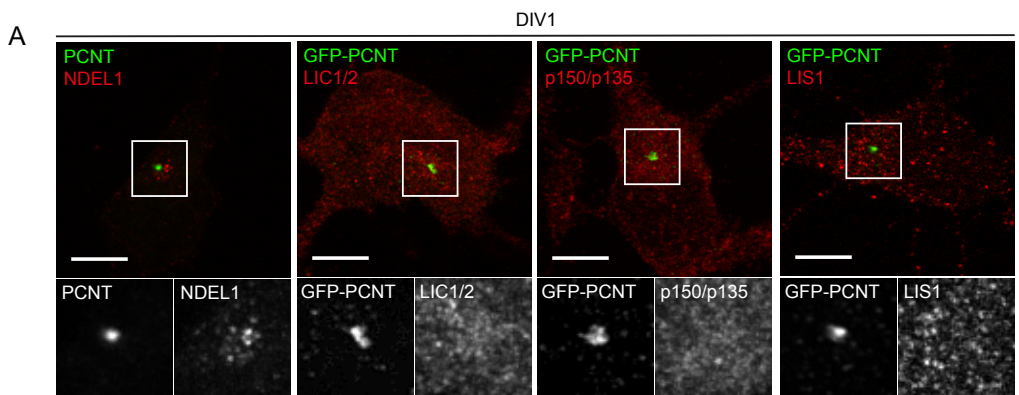


> Figure S2, related to Figure 1. NDEL1 localizes to the AIS of cultured neurons and in all brain regions of adult mice.

(A) Hippocampal neurons at DIV3 stained for NDEL1 (green) and axon initial segment marker AnkG (red). Scale bar: 5 μ m.

(B, C) Representative images of axons of neurons transfected at DIV1 for 2 days with GFP-NDEL1 (B) or GFP-NDE1 (C) and stained for AnkG (red).

(D) Double labeling confocal immunofluorescence of NDEL1 (green) and AnkG (red) in the mouse hippocampus, showing co-distribution of NDEL1 and AnkG in adult CA1 pyramidal neurons. The left image provides an overview of hippocampal NDEL1 immunostaining, illustrating the preferential AIS localization in other hippocampal subfields and the dentate gyrus (DG). Scale bars: 250 μ m (left), 25 μ m (right). Or, stratum oriens; Py, stratum pyramidale; cc, cerebral cortex.

(E, F) Triple labeling of NDEL1 (green), AnkG (red) and neurofilament-M (NF-M) (blue) in the cerebral cortex (E) and striatum (F). Note NDEL1 co-distribution with AnkG in the AIS and the low level of NDEL1 immunostaining in nodes of Ranvier that are also outlined by AnkG labeling (arrows). Ic, internal capsule. Scale bars: 25 μ m (E, left), 5 μ m (E, right), 50 μ m (F, left), 10 μ m (F, right).

(G, H) Labeling of NDEL1 (red) in the cerebellar cortex showing intense staining of the AIS of molecular layer (ml) interneurons (arrowheads) and Purkinje cells (arrows), and in Golgi cells in the cerebellar granule cell layer (gl) outlined by GFP signal in a GlyT2-EGFP transgenic mouse.

Scale bars: 25 μ m (G), 10 μ m (H).

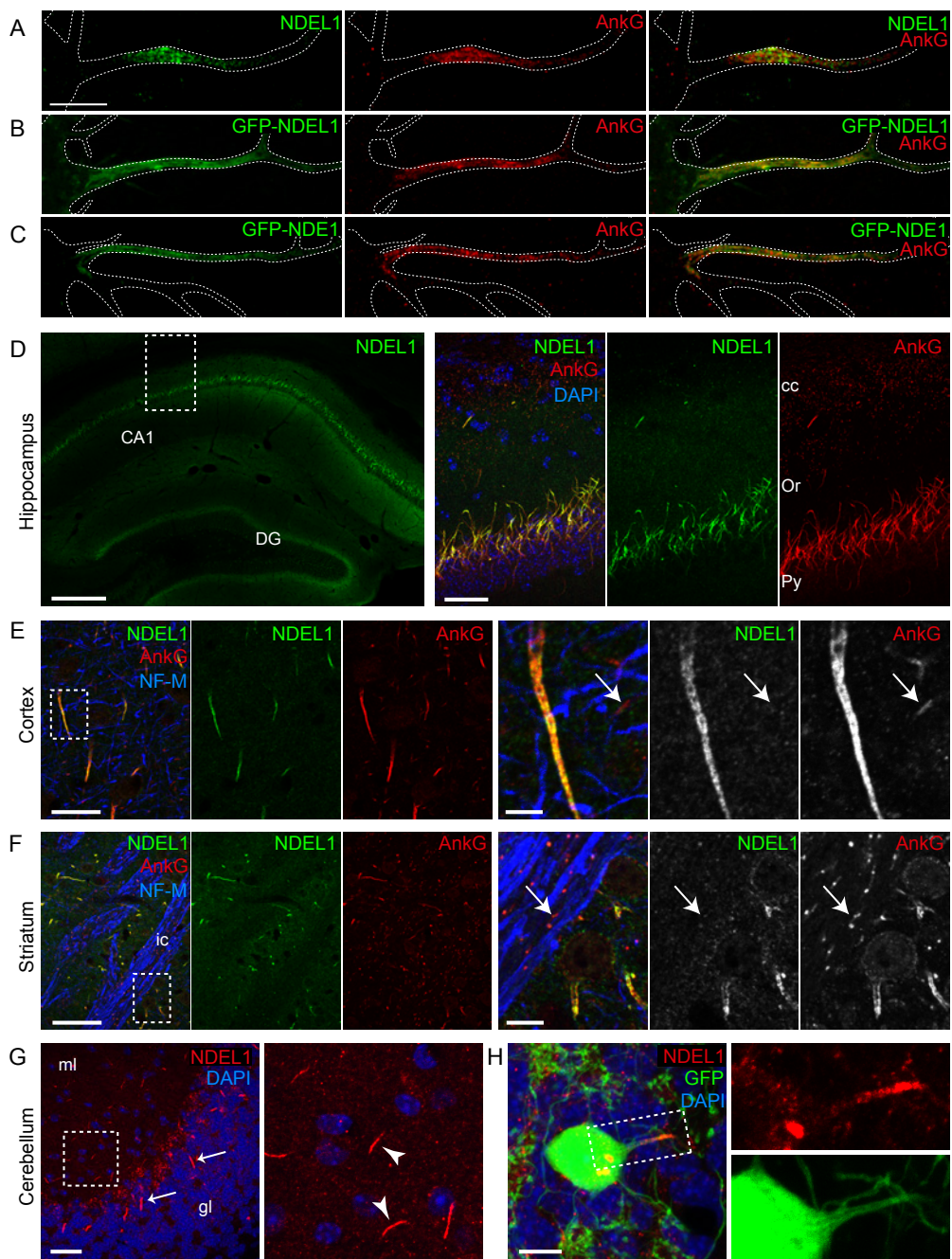


> Figure S3, related to Figure 2. NDEL1 localization to the AIS is dependent on AnkG and LIS1.

(A) Arrowheads mark the AISs of a DIV8 hippocampal neuron transfected with β -galactosidase (not shown) and LIS1-shRNA, and stained for endogenous NDEL1 (green) and AnkG (red).

(B) Quantification of the fluorescence intensity ratio of endogenous NDEL1/AnkG staining in the AIS of DIV8 neurons transfected with β -galactosidase and empty pSuper (control), NDEL1-shRNA, LIS1-shRNA or HA-LIS1. 8 cells were analyzed for the NDEL1 KD condition; 15 cells were analyzed for other conditions.

(C) Representative images of primary neurons (DIV10) transfected with empty pSuper (control) or AnkG-shRNA and β -galactosidase (red), and stained for NDEL1 (green) and AnkG (blue).

(D, E) Quantification of AnkG (D) and NDEL1 levels (E) in AISs of neurons expressing AnkG-shRNA for 4 days. 11 (control) and 13 (NDEL1 KD) cells were analyzed.

(F, G) Images of neurons treated with nocodazole (F) or latrunculin (G) fixed at DIV5 and labeled with antibodies against NDEL1 (green), neuron specific tubulin or actin (red) and AnkG (blue). Arrowheads indicate the AnkG-labeled AIS and insets show AnkG labeling.

(H) Images of AISs of hippocampal neurons transfected with GFP or GFP-NDEL1 (green). Neurons are stained with antibodies against AnkG to highlight the AIS (blue, left panel) and dynein light intermediate chain (LIC1/2), p150 or LIS1 (right panel).

(I) Images of AIS of DIV11 neurons transfected with empty pSuper (control) or NDEL1-shRNAs and stained with antibodies against AnkG or β IV-spectrin to highlight the AIS (left panel) and dynein light intermediate chain (LIC1/2), p150 or LIS1 (right panel).

(J) Representative images of neurons transfected with GFP or GFP-p150-cc1 (green) and labeled with anti-NDEL1 (red) and anti-AnkG antibodies (blue). Yellow arrowheads indicate the AIS.

Data are presented as means \pm SEM, ***P<0.001. Scale bars: 20 μ m (A, C), 10 μ m (J).

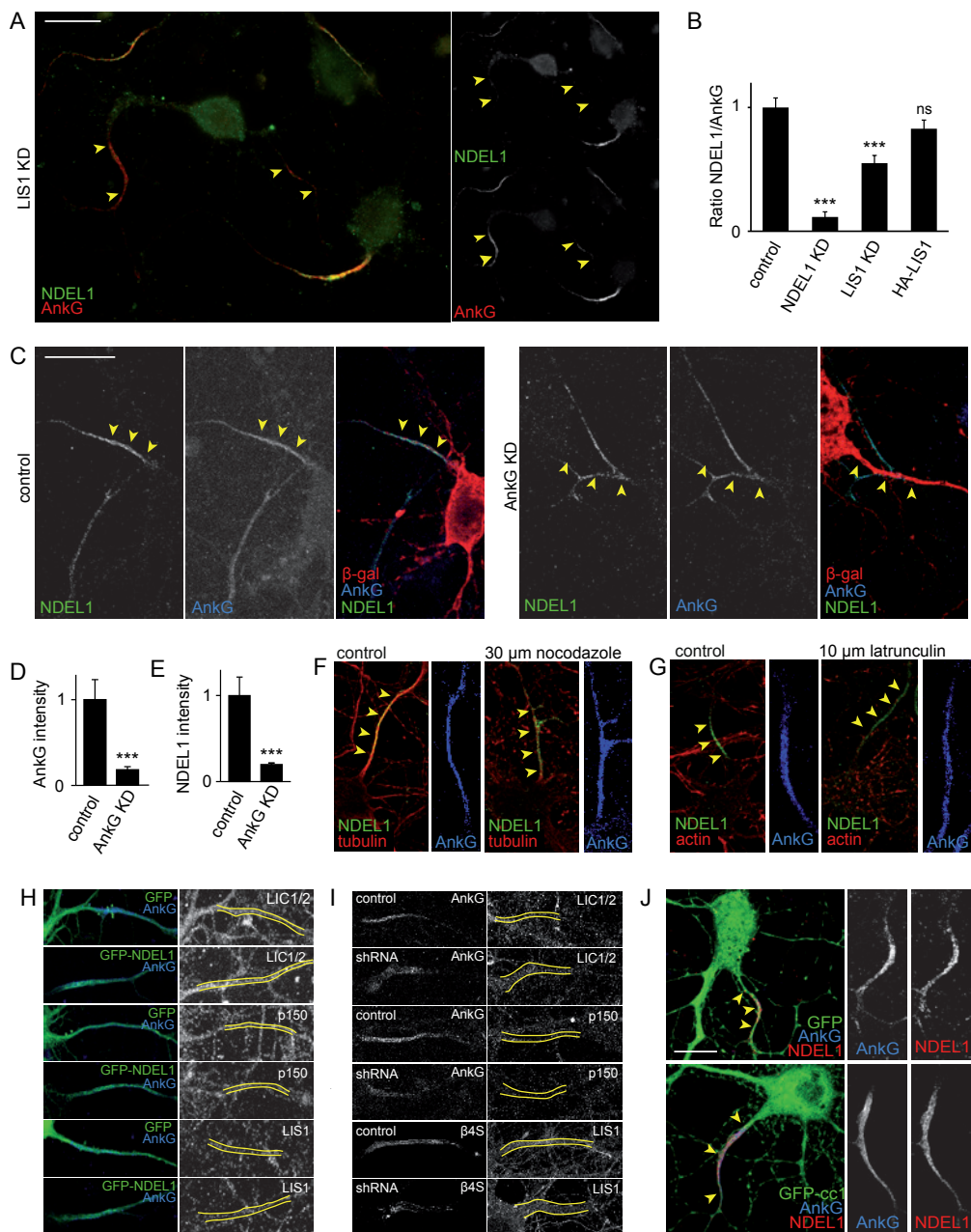


> Figure S4, related to Figure 3. NDEL1 down-regulation by CRISPR-Cas9 alters axon morphology and somatodendritic vesicle sorting at the AIS.

(A) Representative images of AISs of DIV7 primary neurons co-expressing GFP (not shown) and control or CRISPR_NDEL1 for 6 days and stained for endogenous NDEL1 and AnkG to show the efficiency of NDEL1 down-regulation at the AIS.

(B) Representative images of AISs of DIV7 hippocampal neurons co-expressing GFP and control or CRISPR_NDEL1 for 6 days and stained for endogenous AnkG to highlight the AIS.

(C) Quantification of NDEL1 levels in the AIS of DIV7 neurons co-transfected with GFP and control or CRISPR_NDEL1 for 6 days, normalized to NDEL1 levels in surrounding non-transfected neurons. At least 10 neurons were quantified for each condition.

(D) Quantification of AIS diameter (left) and axon diameter (right) in control and CRISPR_NDEL1 neurons. At least 80 neurons were analyzed for each condition.

(E) Quantification of TfR-GFP intensity ratio (axons/dendrites) in neurons co-transfected with TfR-GFP and control or CRISPR_NDEL1 (16 and 17 cells were analyzed, respectively).

(F) Representative images of cultured hippocampal neurons (DIV7) co-transfected with TfR-GFP and control or CRISPR_NDEL1 for 6 days, and stained with antibodies against dendrite specific marker MAP2 (red) and AIS marker AnkG (blue). Arrowheads mark the AIS.

Data are presented as means \pm SEM, *** $P < 0.001$. Scale bars: 2 μm (A, B), 10 μm (F).

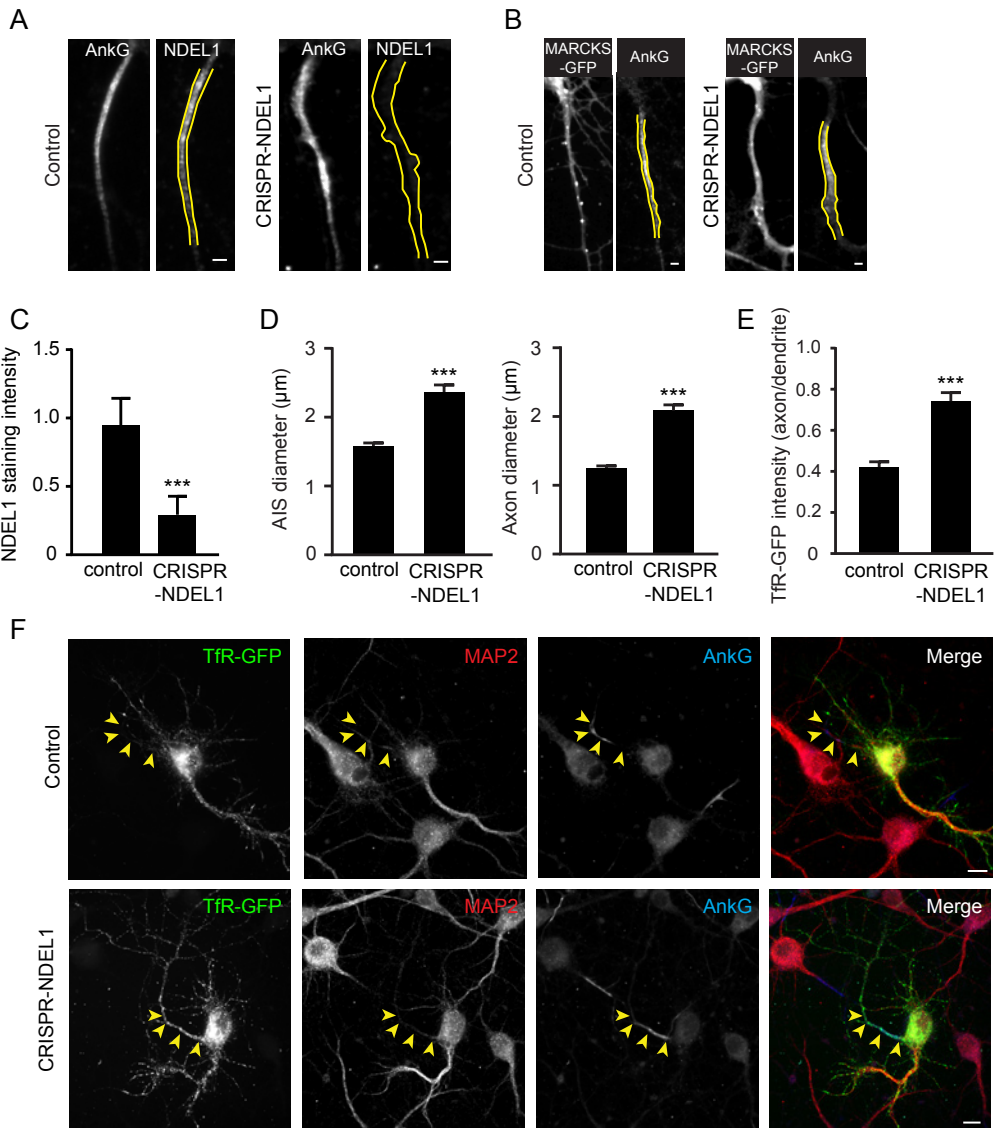


> Figure S5, related to Figure 3. Axon enlargement is induced by NDEL1-shRNA, LIS1-shRNA or p150-cc1 overexpression and does not correlate with somatodendritic vesicle entry into the axon.

(A) Representative images of AISs of hippocampal neurons (DIV7) co-transfected with empty pSuper (control), NDEL1-shRNA, LIS1-shRNA or HA-p150-CC1 and MARCKS-GFP (green) to visualize morphology. Neurons are labeled with anti-AnkG antibody (red) to highlight the AIS.

(B) Quantification of axonal diameter, measured at the AIS of neurons in the indicated conditions. 15–20 cells were analyzed per condition.

(C) Representative images of AISs of hippocampal neurons (DIV7) co-transfected with empty pSuper (control) or NDEL1-shRNA and indicated NDEL1 constructs. MARCKS-RFP (red) was used to visualize morphology. Neurons are labeled with anti-AnkG antibody (blue) to highlight the AIS.

(D) Quantification of axonal diameter of neurons in the indicated conditions, measured at the AIS.

(E, F) Quantification of axonal diameter of DIV8 neurons, measured in the AIS of neurons transfected with empty pSuper (control) or NDEL1-shRNA co-transfected with the indicated constructs (E), or LIS1-shRNA co-transfected with the indicated constructs (F). 10 neurons were analyzed for each condition in (E). 16–20 neurons were analyzed per condition in (F).

(G) Scatter plot visualizing the relation between axonal caliber and TfR distribution in control, NDEL1 KD and NDEL1 KD rescue conditions with co-expressed NDE1 or NDEL1 (DIV8). A neuron with a TfR-mRFP AIS/dendrite fluorescence intensity ratio >1 is considered non-polarized; an axon with an AIS diameter $>1.5 \mu\text{m}$ is considered enlarged.

(H) Example of a DIV11 neuron with a severely enlarged axon while TfR vesicles are excluded from the AIS, here transfected with NDEL1 shRNA, HA-NDE1 (blue after anti-HA immunolabeling) and TfR-GFP (green and right). The AIS is marked by AnkG staining (red) and outlined in yellow.

(I, J) Quantification of AIS diameter (I) and TfR-mRFP intensity ratio (AIS/Dendrite, J) of DIV8 hippocampal neurons transfected with pSuper empty vector (control), NDEL1 shRNA (NDEL1 KD) or pSuper empty vector and GFP-NDEL1-C (NDEL1-C). 8–10 neurons were quantified per condition.

(K) Representative examples of axon morphology of control, NDEL1 KD and AnkG KD neurons. Red arrowheads indicate the axon.

Data are presented as means \pm SEM, * $P < 0.05$, ** $P < 0.01$, *** $P < 0.001$. Scale bars: 10 μm (H), 30 μm (K).

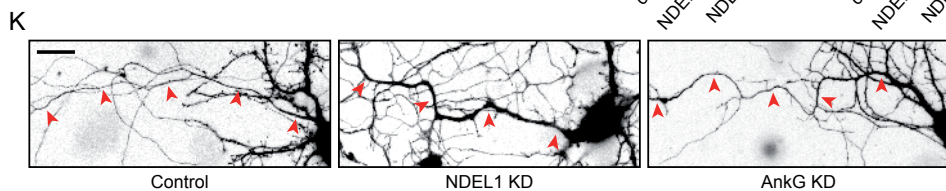
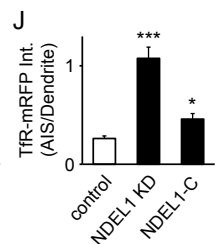
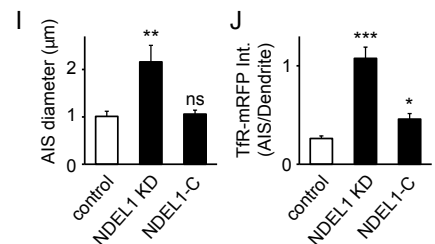
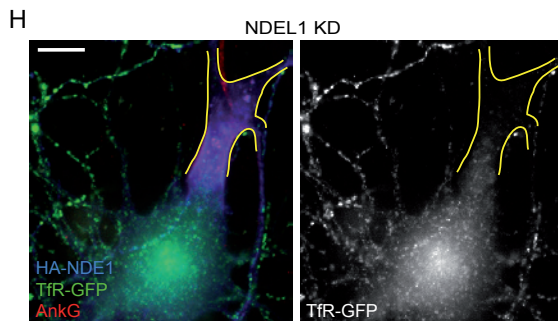
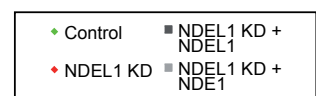
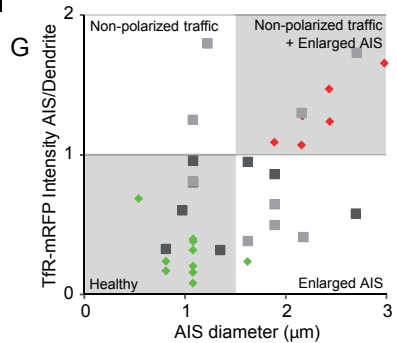
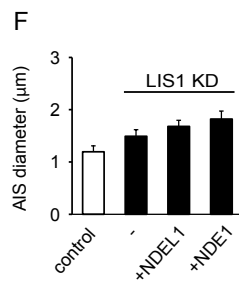
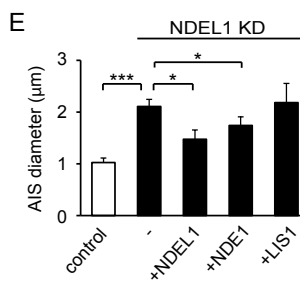
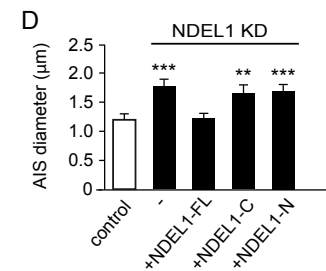
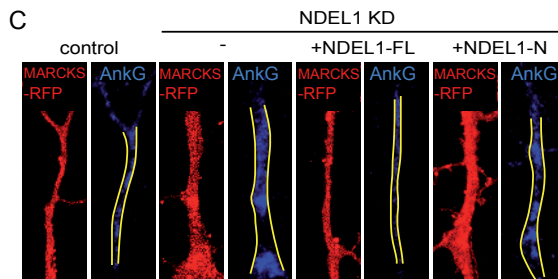
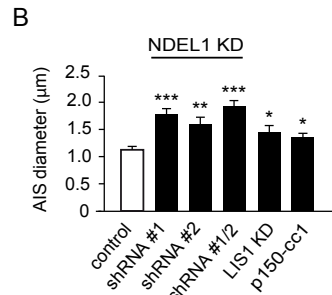
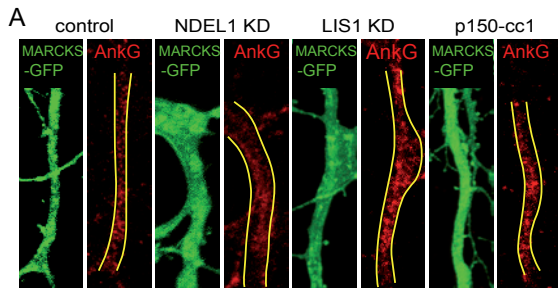


> Figure S6, related to Figure 3. NDEL1 is required for proper cytoskeleton organization.

(A) Semiquantitative analysis of the amount of neurofilament-L (left) and neurofilament-M (right) immunofluorescence signal after immunolabeling in the AIS of DIV8 hippocampal neurons. Categories – (none) to +++ (saturated) indicate the amount of neurofilaments in the AIS. 25 neurons were reviewed for each condition.

(B, C) Analysis of Phalloidin staining intensity in the proximal axon of control and NDEL1 KD neurons. For each condition, 10 cells were analyzed.

(D) Representative images of β 4-Spectrin actin ring organization in the AIS of DIV13 control and NDEL1 KD neurons. Boxed areas are magnified and show dSTORM reconstructions on the right.

(E) Quantification of the number of EB3 comets in the AIS of control and NDEL1 KD neurons. Neurons were labeled with anti-EB3 antibody and AIS were identified by AnkG staining (not shown). 10 neurons were analyzed for each condition. Representative images show AISs of neurons co-transfected with β -galactosidase (not shown) and empty pSuper (control) or NDEL1-shRNAs. Outlines indicate axon contours.

(F) Quantification of the direction of GFP-MT+TIP (GFP-MACF43) comets in the AIS of hippocampal neurons expressing empty pSuper (control) or NDEL1-shRNAs. Representative kymographs along axons illustrate behavior of GFP-MT+TIP in the AIS.

(G) Representative images of AISs of neurons co-expressing GFP and empty pSuper (control) or NDEL1-shRNAs, stained for CAMSAP2 (red) and AnkG (blue). Outlines indicate axon contours.

(H) Representative images of a DIV7 NDEL1 KD hippocampal neuron stained for neurofascin and tubulin (top, widefield images). Bottom left: dSTORM reconstruction of tubulin staining in the boxed areas. Bottom right: fluorescence intensity profile on dSTORM reconstructions of tubulin staining in the AIS of a control neuron (not shown, black) and a NDEL1 KD neuron (red, linescan along the transparent white line indicated in the image to the left).

(I) Representative frames of microtubule behavior in live DIV6-7 control and NDEL1 KD neurons. Neurons were transfected with β -Tubulin-GFP and empty pSuper (control) or NDEL1 shRNA. Microtubules in the proximal axon were classified as static, bending or buckling based on nine hour timelapse movies recorded with a live imaging setup.

(J) Quantification of the behavior of microtubules in live neurons, categorized as in (I). 11 and 16 neurons were analyzed for control and NDEL1 KD conditions, respectively.

(K) Fluorescence recovery plots showing the mean rates of β -Tubulin-GFP recovery in photobleached AISs of DIV7 control neurons (black) and NDEL1 KD neurons (red). Fluorescence intensity was normalized to the baseline intensity before bleaching.

(L) Analysis of en-masse microtubule displacement in live DIV4 control and NDEL1 KD neurons, transfected with RFP (red, 'Fill') and PA-GFP- α -Tubulin (green). A small rectangular region of PA-GFP- α -Tubulin was photoactivated in the proximal axon and tracked on a live imaging setup for 3 hours or until the signal was lost. Displacement of the region boundary nearest to the soma (dashed line) was measured relative to the cell body. The quantification (right) only includes neurons of which the photoactivated region moved uniformly; 21 and 10 neurons were analyzed in control and NDEL1 neurons, respectively.

Scale bars: 2 μ m (D, H, I), 5 μ m (L). Data are presented as means \pm SEM.

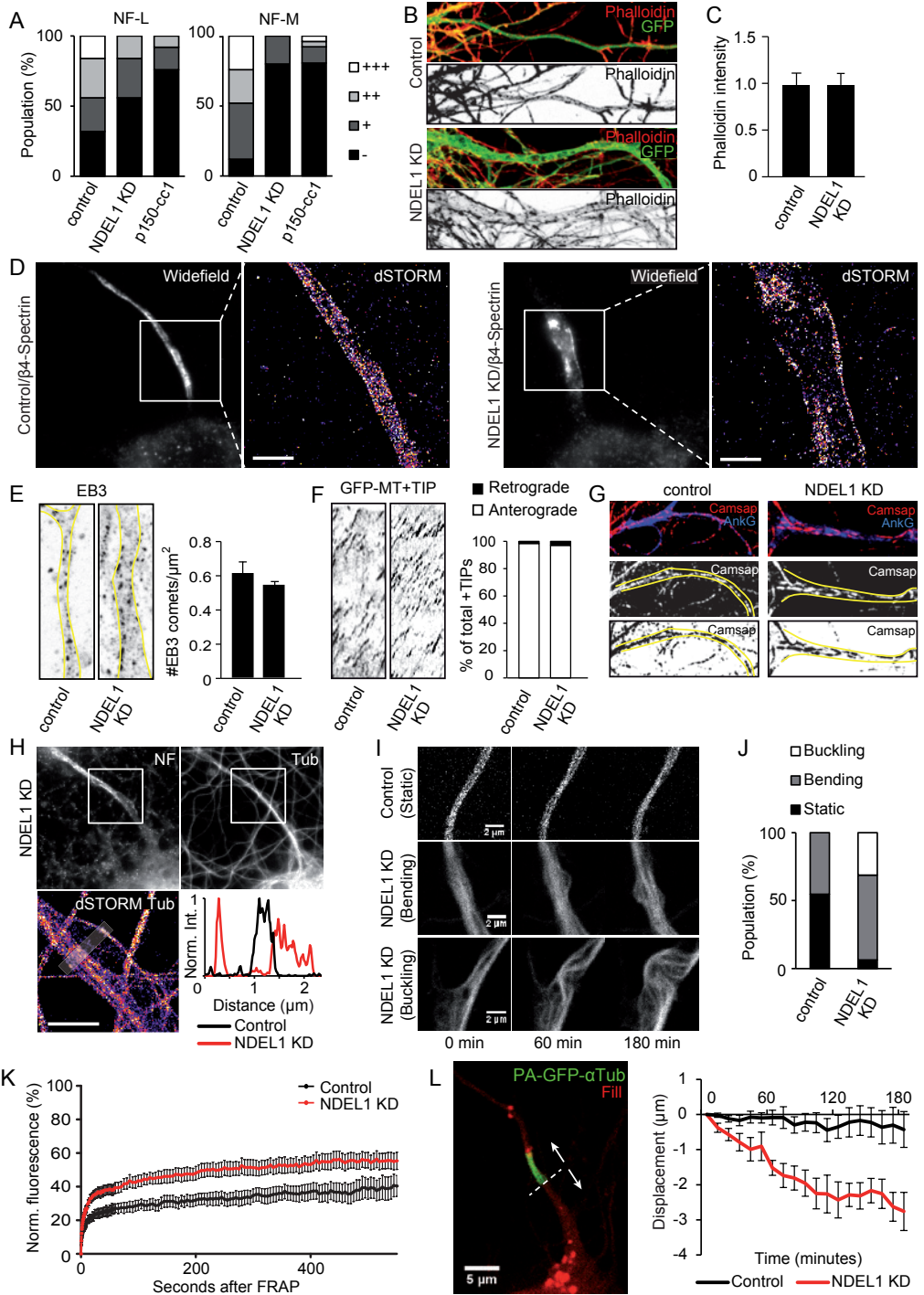


> Figure S7, related to Figure 4. NDEL1 is required for sorting of various cargoes, which also involves LIS1 and dynein .

(A) Tfr-mRFP distributions near and inside the AIS (dashed lines) of representative fixed DIV8 hippocampal neurons stained for AnkG and transfected with GFP, Tfr-mRFP and empty pSuper (control) or NDEL1-shRNA.

(B) Tfr-GFP fluorescence intensity ratios (AIS/dendrites) of fixed DIV8 hippocampal neurons transfected with Tfr-GFP and empty pSuper (control), NDEL1-shRNA, or NDEL1-shRNA and rescued with overexpressed GFP-NDEL1, -NDEL1 or -LIS1. 10 neurons were analyzed per condition.

(C) Quantification of the AIS/dendrite ratio of Tfr-GFP fluorescence intensity in control, NDEL1 KD and HA-p150-cc1 expressing neurons. 8-10 cells were analyzed per condition.

(D) Quantification of the AIS/dendrite ratio of Tfr-GFP fluorescence intensity in control, NDEL1 KD and LIS1 KD neurons. 7-10 cells were analyzed per condition.

(E) Panels show representative images of neurons transfected with empty pSuper (control) or NDEL1-shRNAs and GFP as a fill, fixed and stained with mitochondrial marker cytochrome-c (red) and AnkG as AIS marker (blue).

(F) Quantification of cytochrome-c intensity in the AIS of control and NDEL1 KD neurons. 17 cells were analyzed per condition.

(G, H) Hippocampal neurons were co-transfected with RFP-mito and empty pSuper (control) or NDEL1-shRNAs and live-cell imaging was used to visualize mitochondrial motility in the AIS. The AIS was highlighted by neurofascin (Nfasc) staining. Arrowheads indicate RFP-mito-labeled mitochondria in a representative AIS and the kymograph shows the motility of mitochondria. Quantification of mitochondrial transport in the AIS is shown in (H). 15 (control) and 23 (NDEL1 KD) cells were analyzed.

(I) Representative images of neurons transfected with empty pSuper (control) or NDEL1-shRNAs, fixed and stained with antibodies against rab3 and beta4-spectrin to label the AIS (not shown). Insets show magnification of the AIS (boxed areas).

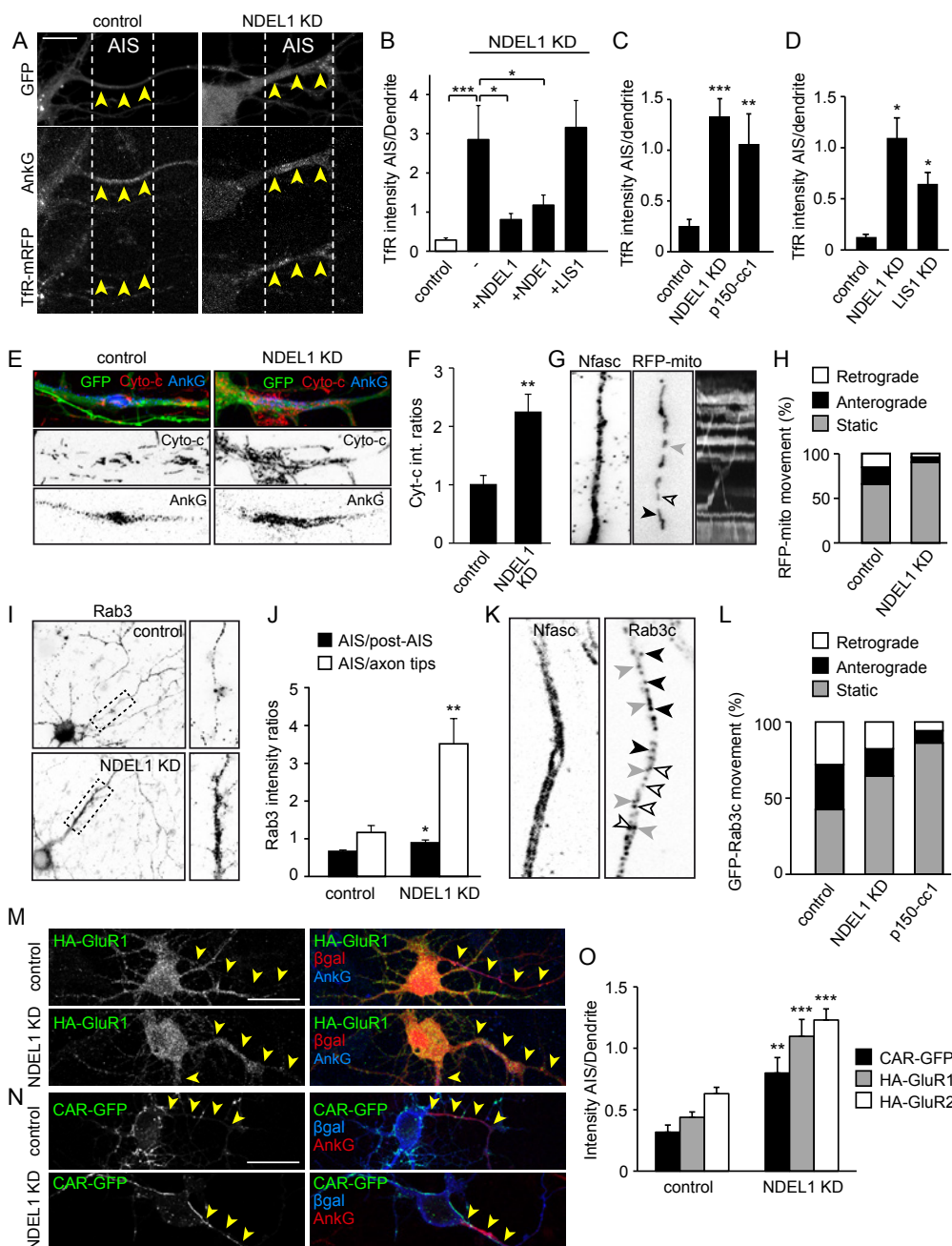
(J) Quantification of the intensity of rab3 staining in the AIS of control neurons and neurons expressing NDEL1-shRNAs. The intensity is either normalized to a region just after the AIS (as indicated by beta4-spectrin staining, 31 or 32 cells were analyzed for each condition) or to the distal axon (5 or 9 cells were analyzed for each condition).

(K, L) Hippocampal neurons were co-transfected with GFP-rab3c and empty pSuper (control, n=26), NDEL1-shRNAs (n=33) or RFP-p150-cc1 (n=5) and live-cell imaging was used to visualize synaptic vesicle transport in the AIS. The AIS was highlighted by neurofascin (Nfasc) staining. Arrowheads indicate rab3c-labeled vesicles in a representative AIS (K). Quantification of rab3c vesicle transport in the AIS is shown in (L). White, black and grey arrowheads indicate respectively retrograde moving, anterograde moving or static cargo.

(M, N) Representative images of DIV7 neurons in control conditions (top) or depleted of NDEL1 (bottom), co-transfected with RFP (red) and HA-GluR1 (M, green) or CAR-GFP (N, green) and stained for AnkG (blue). Yellow arrowheads indicate the AIS.

(O) Quantification of the ratio of fluorescence intensity (AIS/dendrites) in control and NDEL1 knockdown neurons transfected with CAR-GFP (black bars), HA-GluR1 (grey bars) or HA-GluR2 (white bars). 17-20 neurons were analyzed per condition.

Scale bars: 10 μ m (A), 30 μ m (M, N). Data are presented as means \pm SEM, *P<0.05, **P<0.01, ***P<0.001



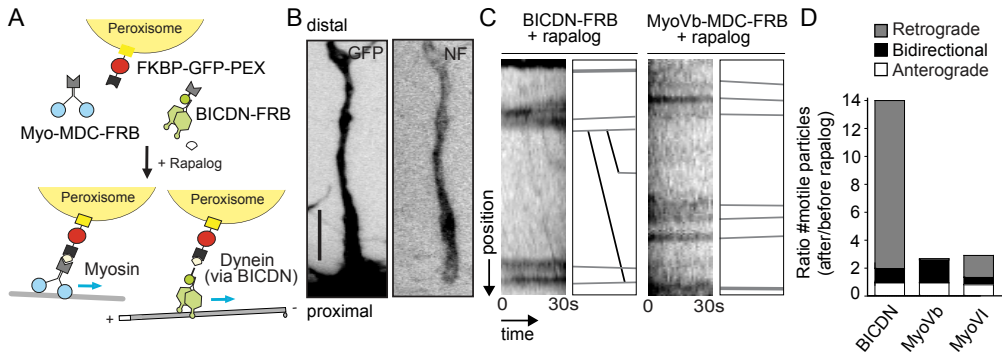


Figure S8, related to Figure 4. Dynein drives retrograde movement of cargo at the proximal axon.

(A) Schematic representation of the inducible FKBP-FRB heterodimerization system. Fusion construct FKBP-mRFP-PEX contains a peroxisome targeting sequence and is incorporated into the membrane. Myosin or dynein motor proteins, the latter via adaptor protein BICDN, are recruited to peroxisomes upon addition of rapalog heterodimerizer to assess the directionality of transport by each individual motor type.

(B) Dissociated hippocampal neurons were transfected with GFP, FKBP-mRFP-PEX and BICDN-FRB or myoVb-MDC-FRB or myoVI-MDC-FRB at DIV6 and imaged at DIV8. AISs were visualized by staining of extracellular neurofascin prior to imaging. Representative images of GFP fill (left panel) and extracellular neurofascin staining (right panel) of the proximal axon. Scale bar: 10 μ m.

(C) Representative kymographs showing motion of peroxisomes induced by BICDN or myosin Vb after addition of rapalog. Kymograph dimensions are 24 μ m x 30 seconds.

(D) Graph showing retrograde, anterograde and bidirectional movements of peroxisomes coupled to either BICDN, truncated myosin V or truncated myosin VI. Values shown are the ratio of motile peroxisomes after/before rapalog addition, i.e. after coupling to the motor proteins compared to before coupling. Movements were analyzed from kymographs drawn along the first 20-30 μ m of the axon (n = 64-90; 51-64 and 63-85 particles for BICDN, myoVb and MyoVI respectively).

Supplementary materials & methods

Animals

All animal experiments were performed in compliance with the guidelines for the welfare of experimental animals issued by the Federal Government of The Netherlands. All animal experiments were approved by the Animal Ethical Review Committee (DEC) of Utrecht University.

Antibodies and reagents

The following antibodies were used for immunocytochemistry: rat-anti-NDEL1 and rat anti-NDE1 (clones 4-9-C/5-3-D and clone 1-11-B, respectively, generous gift from H. Arai [1]), mouse-anti-LIS1 and rabbit-anti-LIS1 (generous gift from O. Reiner [2, 3]), rabbit-anti- β IV-spectrin (generous gift from M. N. Rasband [4]) and rabbit-anti-LIC1/2 (generous gift from R.B. Vallee [5]). The following antibodies were obtained from commercial sources: rabbit-anti-pericentrin (Covance), goat-anti-PCM1 (Santa Cruz), mouse-anti-tau-1 (Chemicon), mouse-anti-MAP2 (Sigma), mouse-anti-Ankyrin-G (Zymed), mouse-anti-neurofascin (extracellular, Neuromab), rabbit-anti-tubulin (Covance), rabbit-anti- α -tubulin (Sigma) directly coupled to Alexa Fluor 647 (in-house), mouse-anti-p150 (Santa cruz), rabbit anti-CAMSAP2 (Proteintech), rabbit-anti-HA (Santa Cruz Biotechnology), , rat-anti-HA (Roche), rabbit-anti- β -galactosidase (MP Biomedicals), chicken-anti- β -galactosidase (Aves lab), rabbit-anti-neurofilament L (Cell Signaling), chicken anti-neurofilament M (Millipore), rabbit-anti-neurofilament M (Abcam), rabbit-anti-GFP (MBL), mouse-anti-rab3 (BD Biosciences), mouse-anti-cytochrome c (BD Biosciences), Alexa 568 phalloidin, Alexa Fluor 405-, Alexa Fluor 488-, Alexa Fluor 598-, Alexa Fluor 594-, and Alexa Fluor 647-conjugated secondary antibodies (Invitrogen and Life Technologies). The following antibodies were used for Western blot analysis: mouse-anti-p150 (Santa cruz), mouse-anti-IC74 (Santa cruz), rabbit-anti-GFP (Abcam); rat-anti-NDE1 and NDEL1 clone 1-11-B and 5-3-D, rabbit-anti-HA (Santa Cruz); mouse-anti-HA (Covance), mouse-anti-actin (Chemicon), rabbit-anti- α Tubulin (Abcam), HRP conjugated secondary antibodies (Dako), IRDye 680LT- and IRDye 800CW-conjugated secondary antibodies (LI-COR Biosciences). Nocodazole was obtained from Sigma and latrunculin from Bioconnect.

Expression constructs, shRNA and gRNA

The following mammalian expression plasmids have been described previously: FKBP-GFP-PEX, MyoV-MDC-FRB, MyoVI-MDC-FRB and BICDN-FRB [6, 7], protein-biotin ligase BirA [8], pGW1-GFP and p β actin-HA- β -galactosidase [6], pSuper vector [9], bio-GFP [10], Tfr-GFP [11], NgCAM-GFP ([12], Addgene plasmid 45061), MARCKS-GFP [13], GFP-tau [14], GFP-MACF43 [15], GFP-rab3c [16], mito-dsRed and GFP-p150-cc1 [16]. GFP-PCNT-myc was generated by subcloning p3xFLAG-CMV10-GFP-PCNTB-myc [17] into a pGW2-expression vector. All other constructs were created using PCR based strategy. Mouse NDEL1 cDNA (IMAGE clone 2646029) and human NDE1 cDNA (IMAGE clone 2820974) were used to create the NDEL1 and NDE1 construct in pEGFP-C2

(Clontech). These constructs were used to generate all other NDEL1/NDE1 and NDEL1 truncation constructs and subcloned into HA-tagged GW1, bio-GFP or pEGFP-C2 expression vectors. Mouse LIS1 cDNA was obtained by RT-PCR from total mouse brain RNA and subsequently cloned into bio-GFP or HA-tagged vector. NDEL constructs used for rescue experiments in Figure 3 were based on an shRNA-resistant (shRes) NDEL1 construct where the sequence GCTAGGATATCAGCACTAA was mutated to GCGCGAATCAGTGCCTTA by PCR. NDEL1 and LIS1 fusions used in Figure 3 were created from GFP-NDEL shRes or GFP-LIS1 fragments generated by PCR and used to replace GFP in *Agel*/*NotI* sites of AnkG480-GFP (pCAGGS) or AnkG270-GFP (CMV). AnkG480-GFP (pCAGGS) and AnkG270-GFP (CMV) were generated by subcloning the cDNA sequences of the mouse 480AnkG and 270AnkG (WEBIN ID number HG915716 and HG915715, respectively) into pEGFP-N1 (Clontech) in the *KpnI* and *Agel* restriction cloning sites. These two restriction sites were deleted from the synthesized cDNA without altering the protein sequences. In order to increase expression level of the 480AnkG-GFP construct, the promoter was replaced by the promoter of the pCAGGS (BCCM/LMBP) which was inserted in the *Asel* and *EcoRI* restriction sites. HA-NF186-GFP-NDEL/LIS and HA-NF186-GFP were created by replacing RFP of HA-NF186-RFP-FKBP at *Agel*/*Ascl* sites with GFP, GFP-NDEL (shRes) or GFP-LIS1 fragments with a C-terminal stop codon introduced by PCR. HA-NF186-mRFP-FKBP was made by subcloning HA-NF186-EGFP (kind gift from Dr. M. N. Rasband) into PEX-RFP-FKBP [6, 7]. Full-length and truncated AnkG constructs used for pulldown experiments and FRAP were generated by PCR using Ankyrin-G-GFP [18] as template and cloned into HA- and GFP-tagged pGW2-expression vectors. mRFP-p150-cc1 and HA-p150-cc1 were generated using GFP-p150-cc1 and subcloned into pGW2-mRFP or pGW1-HA expression vectors. MARCKS-tagRFP was generated by inserting tagRFP-T (gift from Dr. R. Tsien) into the *BamHI* and *XbaI* sites of MARCKS-GFP. GW2-mRFP was created by inserting mRFP into *HindIII*/*Ascl* sites of a GW2 backbone. TfR-mRFP was generated by PCR on TfR-GFP and insertion of the fragment into a β actin-mRFP-N vector. PA-GFP- α -Tubulin was created by replacing YFP of YFP- α -Tubulin (Clontech) with PA-GFP (kind gift from Dr. Patterson and Dr. Lippincott-Schwartz [19]). GW2- β -Tubulin-EGFP or β actin- β -Tubulin-EGFP was created by PCR based on cDNA of β -tubulin2C from the human ORFeome collection (<http://horfdb.dfci.harvard.edu/>) after which the fragment was inserted into *NheI*/*XbaI* sites of a GW2-HA or *NheI*/*NotI* sites of a β actin expression vector, respectively. The following rat shRNA sequences were used: NDEL1-shRNA#1 (5'-GCTAGGATATCAGCACTAA-3'), NDEL1-shRNA#2 (5'-GCAGGTCTCAGTGTAGAA-3'), LIS1-shRNA#1 (5'-CAATTAAGGTGTGGGATTA-3'), LIS1-shRNA#2 (5'-GAGTTGTGCTGATGACAAG-3') and AnkG-shRNA (5'-GAGTTGTGCTGATGACAAG-3'). shRNAs were designed based on previously published sequences [20-22]. Unless stated otherwise, NDEL1-shRNA #1 was used for NDEL1 knockdown experiments. The design of NDEL1 gRNA was performed on the 5' end of the protein-coding region using the online tool <http://crispr.mit.edu/>. The primers used were: forward (5' to 3') caccg CTAGCTCATCCGAGCTTCTGG and reverse (5' to 3') aaac CCAGGAAGCTCGGGATGAGCTAG c. The uppercase character represents the gRNA. These primers were inserted into pSpCas9(BB)-2A-Puro (Addgene, PX459) at the *BbSI* site. The cloning was verified by subsequent sequencing. Empty pSpCas9(BB)-2A-Puro was used as a control.

Hippocampal neuron cultures, transfection and immunohistochemistry

Primary hippocampal cultures were prepared from embryonic day 18 (E18) rat brains [16]. Cells were plated on coverslips coated with poly-L-lysine (35 µg/ml) and laminin (5 µg/ml) at a density of 100,000 or 50,000/well (12-well plates). Hippocampal cultures were grown in Neurobasal medium (NB) supplemented with B27, 0.5 mM glutamine, 12.5 µM glutamate and penicillin/streptomycin. Hippocampal neurons were transfected using Lipofectamine 2000 (Invitrogen). DNA (1.8 µg/well in 12 well plate) was mixed with 3.3 µl Lipofectamine 2000 in 200 µl NB, incubated for 30 min, and then added to the neurons in NB at 37°C in 5% CO₂ for 45 min. Next, neurons were washed with NB and transferred back to conditioned medium and maintained at 37°C in 5% CO₂. For latrunculin and nocodazole experiments, 30 µM nocodazole or 10 µM latrunculin was added to the culture medium 2 hours before fixing.

For immunocytochemistry, neurons were fixed with 4% paraformaldehyde/4% sucrose in PBS at room temperature or with methanol/1 mM EGTA at -20°C followed by 4%PFA/4% sucrose at room temperature, washed three times in PBS for 10 min and incubated with the indicated primary antibodies in GDB buffer (0.2% BSA, 0.8 M NaCl, 0.5% Triton X-100, 30 mM phosphate buffer, pH 7.4) overnight at 4°C. Neurons were then washed three times in PBS for 30 min, incubated with secondary antibodies in GDB for 1hr at room temperature and washed three times in PBS for 30 min. Coverslips were mounted using Vectashield mounting medium (Vector laboratories). For live labeling of the AIS, an antibody recognizing an extracellular epitope of neurofascin was used. Neurons were incubated with primary antibody in fresh NB for 10 minutes, washed twice with NB and incubated with a secondary Alexa-conjugated antibody for 10 minutes. Confocal images were acquired using a LSM700 confocal microscope (Zeiss) with a 20x (dry), 40x or 63x oil objective.

To visualize NDEL1 in mouse brain tissue we used the brains from a 3 month old non-transgenic C57Bl6 and GlyT2-GFP transgenic mice [23] perfused transcardially with 4% paraformaldehyde. Brains were sectioned at 40 µm with a freezing microtome, and sections were processed double- and triple-labeling NDEL1 (labeled with Mab5-3-D) with Ankyrin G or Neurofilament-M. Images were collected with a Zeiss LSM700 confocal laser scanning microscope.

Western blotting

HEK293T cells were cultured in DMEM/Hams-F10 (50/50%) medium containing 10% FCS and 1% penicillin/streptomycin and were transfected using Max Pei (Polysciences). Cells were lysed 24 h later on ice, in sample buffer containing DTT. Primary cortical neurons were cultured as described for hippocampal neuron cultures, except they were plated at a density of 640,000 cells per well (6-well plate) without coverslips. Cortical neuron lysates were prepared at the appropriate DIVs by scraping cells directly in sample buffer containing DTT and protease inhibitors (Roche) at room temperature. After scraping, samples were directly put on ice.

Samples were loaded equally and ran on 10% SDS-PAGE gels, transferred to nitrocellulose membranes using a semi-dry blotting setup and blocked for at least 1 hour in 2%

bovine serum albumin in PBS/0.02% Tween 20. Primary antibodies were diluted in the blocking solution and applied overnight at 4°C. Membranes were washed 3 times in PBS/0.02% Tween 20 and incubated with secondary IRDye 680LT or IRDye 800LT antibodies (LI-COR Biosciences) for 45 minutes at room temperature. Membranes were then washed 3 more times in PBS/0.02% Tween 20 and scanned on an Odyssey Infrared Imaging system (LI-COR Biosciences).

Biotin-streptavidin/GFP pull-down and mass spectrometry

HEK293T cells were cultured in DMEM/Hams-F10 (50/50%) medium containing 10% FCS and 1% penicillin/streptomycin and were transfected using Max Pei (Polysciences). Cells were lysed 24h later in 20 mM Tris-HCl pH 8.0, 150 mM KCl, 1% Triton X-100, and protease inhibitors (Roche). Cell lysates were centrifuged at 13,000 rpm for 15 min and the supernatants were incubated with Dynabeads M-280 streptavidin (Dyna; Invitrogen) or GFP-trap magnetic beads (Chromotek) for 30 min. Beads were separated using a magnet (Dyna; Invitrogen) and washed in lysis buffer. Brains were obtained from adult female rats and homogenized in 10x volume/weight in the same lysis buffer. Brain lysates were centrifuged at 16,000 g for 15 min at 4°C and the supernatant was incubated with the Dynabeads containing bio-GFP-constructs for 2 hrs at 4°C and washed three times with lysis buffer. For protein elution, the beads were boiled in NuPAGE LDS 4 sample buffer (Invitrogen), separated, and supernatants were run on a 4-12% NuPAGE Bis-Tris gel (Invitrogen). Gels were stained with the Colloidal Blue staining kit (Invitrogen) and mass spectrometry was performed as described previously [8]. Proteins present in the negative controls (pull-down assays with bio-GFP alone) were regarded as background.

For Western blot analysis, samples were eluted in SDS sample buffer, equally loaded onto SDS-PAGE gels and subjected to western blotting on polyvinylidene difluoride membrane. Blots were blocked with 5% non-fat milk and 0.05% Tween 20 in PBS for 1 hour at RT and incubated with primary antibodies at 4°C overnight. Blots were washed with 0.05% Tween 20 in PBS three times for 10 min at room temperature and incubated with either anti-rabbit or anti-mouse IgG antibody conjugated to horseradish peroxidase (conjugated to horseradish peroxidase (HRP; Dako). Blots were developed with enhanced chemiluminescent Western blotting substrate (Pierce).

dSTORM imaging

For NDEL1/GFP-NDEL1 and AnkG co-staining, hippocampal neurons were fixed for 5 minutes with methanol (100%) containing 1mM EGTA at -20°C followed by 5 minutes 4% PFA in PBS at room temperature. For β 4-Spectrin staining, neurons were fixed for 15 minutes with 4% PFA in PBS. For α -tubulin staining, neurons were live stained for neurofascin as described in the section 'Hippocampal neuron cultures, transfection and immunohistochemistry'. Neurons were then extracted for 1.5 minutes with 0.25% glutaraldehyde + 0.3% Triton X-100 + 5mM MgCl₂ + 150mM NaCl + 5mM glucose in PEM80 buffer at 37°C (80mM PIPES, 1mM EGTA, 4mM MgCl₂, pH 6.9). Extraction was followed by a 10 minute fixation using 4% PFA in PBS at 37°C. For all conditions

cells were further permeabilized for 7 minutes using 0.25% Triton X-100 in PBS, washed and incubated for 30 minutes in blocking solution (2% BSA + 0.2% gelatin, 10mM glycine + 50mM NH_4Cl in PBS, pH 7.4). Neurons were incubated with primary and secondary antibodies in the blocking solution for 1h30 and 1h, respectively. Rat-anti-NDEL1 was used followed by goat anti-rat coupled to A488. Rabbit-anti-GFP was used followed by goat anti-rabbit-A488. Mouse-anti-AnkG was used followed by goat-anti-mouse-A647. Rabbit-anti- β 4-Spectrin was used followed by goat anti-rabbit coupled to A647. For α -tubulin-A647, antibodies against α -tubulin were directly coupled to Alexa647. Stained neurons were post-fixed for 10 minutes using 2% PFA in PBS. Imaging was performed using 5mM MEA, 5% w/v glucose, 700 $\mu\text{g}/\text{ml}$ glucose oxidase, 40 $\mu\text{g}/\text{ml}$ catalase in PBS. dSTORM microscopy was performed on an inverted microscope with Perfect Focus System (Nikon Eclipse Ti, Nikon) equipped with a Apo TIRF 100x NA 1.49 oil objective, a 2.5x Optovar (to achieve an effective pixel size of 64 nm), and a DU-897D EMCCD camera (Andor) which were all controlled using Micro-Manager software [24].

Alexa-Fluor-647 and A488 imaging was performed by continuous oblique laser illumination with a 640 nm diode laser and a 491 nm DPSS laser, respectively. For both A647 and A488 the sample was also illuminated with a 405 nm diode laser. Between 7000 and 15000 frames were recorded per acquisition with exposure times of 20-30ms for A647 and 30ms for A488. Single molecule localization was performed as previously described [25]. A particle table with molecule coordinates and errors was used to reconstruct a super resolution image. A 20 nm pixel size was used for all image display. 20 nm pixel size was used for α -tubulin linescans (Figure S6H), while 10 nm pixel size was used for NDEL1 and AnkG linescans (Figure 1H,I). For two color imaging, chromatic corrections obtained from images with multichromatic 100 nm-beads (Tetraspeck, Invitrogen) were applied to the A647 particle table. For sample drift during acquisition, a correction algorithm was applied [26].

Live cell imaging

Live cell imaging of GFP-MACF43 (GFP-MT+TIP), TfR-GFP, NgCAM-GFP, β -Tubulin-GFP and GFP-rab3c was performed on a spinning disk microscope; an inverted research microscope Nikon Eclipse Ti-E (Nikon) with perfect focus system (PFS) (Nikon), equipped with Plan Apo VC 100x N.A.1.40 oil objective (Nikon), CSU-X1-A1 Spinning Disk (Yokogawa) and Photometrics Evolve 512 EMCCD camera (Roper Scientific). During imaging, cells were maintained at 37°C and 5% CO_2 in a stage top incubator (INUBG2E-ZILCS, Tokai Hit).

Live cell imaging of mitochondria motility was performed on a Nikon Eclipse TE2000E (Nikon) equipped with Nikon CFI Apo TIRF 100x 1.49 N.A. oil objective (Nikon), CoolSNAP HQ2 CCD camera (Roper Scientific) and incubation chamber (INUG2-ZILCS-H2; Tokai Hit) mounted on a motorized stage (Prior).

Inducible cargo trafficking assay

The inducible cargo trafficking assay was performed to probe the transport directionality of specific motor protein groups when coupled to endogenous peroxisomes [6, 7]. Dissociated hippocampal neurons were transfected with FKBP-mRFP-PEX, containing a peroxisome targeting sequence, and BICDN-FRB or myoVb-MDC-FRB or myoVI-MDC-FRB at DIV6 and imaged after 2 days. To induce specific binding of FRB and FKBP constructs, cell-permeabilizable heterodimerizer rapalog (AP21967, Clontech/Ariad Pharmaceuticals) was added to the cell medium during acquisition. The axon initial segment (AIS) was stained extracellularly with pan-neurofascin (extracellular) (Neuromab) prior to imaging. Individual neurons were imaged at 1 fps using an epi-fluorescence microscope: an inverted research microscope Nikon Eclipse Ti-E (Nikon) with perfect focus system (PFS) (Nikon), equipped with Plan Fluor 40x/1.30 Oil objective (Nikon), and Photometrics CoolSNAP HQ2 CCD camera (Roper Scientific). MicroManager and FIJI software were used to acquire and process images.

Photobleaching and photoactivation experiments

For quantitative fluorescence recovery after photobleaching (FRAP) experiments, neurons were transfected as described before, and imaged on an inverted research microscope Nikon Eclipse Ti-E (Nikon) with perfect focus system (PFS) (Nikon), equipped with Nikon CFI Apo TIRF 100x 1.49 N.A. oil objective (Nikon), CoolSNAP HQ2 CCD camera (Roper Scientific) and controlled by MetaMorph 7.7 software (Molecular Devices). The FRAP experiments were performed using the ILas2 system (Roper Scientific). Coverslips (24 mm) were mounted in metal rings and maintained at 37°C and 5% CO₂ in a stage top incubator INUBG2E-ZILCS (Tokai Hit). For FRAP experiments in Figure S3B, A 3x3 μm ROI on the proximal axon was photobleached with high laser power. For FRAP experiments in Figure S3D and S6K, constant FRAP duration was used to determine FRAP regions. FRAP regions were chosen in the middle of the AIS as marked by neurofascin live staining. Photoactivation of PA-GFP-α-Tubulin was performed on the FRAP setup and achieved by scanning the desired region 3 times at 10% laser power with a Vortran Stradus 405 nm (100 mW) laser.

Image analysis and quantification

Confocal images were processed using maximum intensity projections. For all of the analysis, background subtraction of the image was applied. Image processing, kymographs, and various quantifications were performed using ImageJ, MatLab software, GraphPad Prism software or SynD [27]. Images were prepared for publication using Adobe Photoshop or ImageJ. Statistical analysis was performed using nonparametric Mann–Whitney U test in SPSS software or using t-tests. P<0.05 was considered significant.

Analysis of FRAP experiments. To analyze the recovery of fluorescence, the bleached area was selected and background subtracted frame-by-frame by subtracting the intensity of an empty,

non-bleached area. Recovery R was then calculated as

$$R = (I(t) - I(\text{directly after bleaching})) / (I(\text{before bleaching}) - I(\text{directly after bleaching}))$$

with I denoting total intensity. After normalization, the final recovery (R_{final}) for each individual trace was determined as the level at the end of the recording. The immobile fraction was then calculated as 1-R_{final}.

Quantification of endogenous antibody staining in neurons. To determine intensities from endogenous staining in an image (acquired with an LSM700 confocal microscope and a 63x objective or a Nikon Eclipse 80i upright microscope and a 60x objective), ImageJ was used to measure average intensity of signal in the cell body, axon or dendrites. To control for background signals we measured the intensity near the axon, dendrite or cell body (same ROI size) and subtracted the random fluorescence intensity in these images. Intensities were averaged over multiple cells and normalized. ImageJ plugin ComDet was used to quantify the number of EB3 comets (<https://github.com/ekatruxha/ComDet>).

Quantification and analysis of vesicle and mitochondria mobility. Neurons were stained for neurofascin to highlight the AIS. For vesicle motility in the AIS, movies (4-5 frames/sec) were used to manually quantify the direction of moving vesicles. Only vesicles that were observed to enter the AIS during the movie and could be tracked throughout were taken into account. For Rab3c motility, the first 20 frames (5 frames/sec) of each movie were used to manually quantify the number and direction of moving vesicles. For mitochondria mobility, 5 minute movies were used to manually quantify the number and direction of moving mitochondria. For kymographs in Figure 4, anterograde and retrograde movements were separated using an ImageJ plugin (see <http://www.nat.vu.nl/~erwinp/downloads.html>).

Analysis of morphology. For the morphometric analysis of axon and dendrite morphology, we used β -galactosidase or GFP as an unbiased cell fill. Analysis of neuron morphology was performed using SynD [27].

Analysis of inducible cargo trafficking assay. Neurons were imaged at 1fps before and after addition of rapalog. % of retrograde, anterograde and bidirectional were calculated from kymographs drawn along the first 20-30 μ m of the axon (as identified by extracellular NF staining). FIJI plugin multiple kymograph was used to draw kymographs (http://www.embl.de/eamnet/html/body_kymograph.html). Values calculated were the ratio of motile peroxisomes after/before rapalog addition, i.e. after coupling to the motor proteins compared to before coupling. Movements were analyzed from kymographs drawn along the first 20-30 μ m of the axon (n = 64-90; 51-64 and 63-85 particles for BICDN, myoVb and MyoVI respectively).

Supplementary references

1. Yamaguchi, N., et al., Expression of NUDEL in manchette and its implication in spermatogenesis. *FEBS Lett*, 2004. 566(1-3): p. 71-6.
2. Sapir, T., et al., LIS1 is a microtubule-associated phosphoprotein. *Eur J Biochem*, 1999. 265(1): p. 181-8.
3. Sapir, T., M. Elbaum, and O. Reiner, Reduction of microtubule catastrophe events by LIS1, platelet-activating factor acetylhydrolase subunit. *EMBO J*, 1997. 16(23): p. 6977-84.
4. Ogawa, Y., et al., Spectrins and ankyrinB constitute a specialized paranodal cytoskeleton. *J Neurosci*, 2006. 26(19): p. 5230-9.
5. Tynan, S.H., et al., Light intermediate chain 1 defines a functional subfraction of cytoplasmic dynein which binds to pericentrin. *J Biol Chem*, 2000. 275(42): p. 32763-8.
6. Kapitein, L.C., et al., Mixed microtubules steer dynein-driven cargo transport into dendrites. *Curr Biol*, 2010. 20(4): p. 290-9.
7. Kapitein, L.C., et al., Myosin-V opposes microtubule-based cargo transport and drives directional motility on cortical actin. *Curr Biol*, 2013. 23(9): p. 828-34.
8. Lansbergen, G., et al., CLASPs attach microtubule plus ends to the cell cortex through a complex with LLSbeta. *Dev Cell*, 2006. 11(1): p. 21-32.
9. Brummelkamp, T.R., R. Bernards, and R. Agami, A system for stable expression of short interfering RNAs in mammalian cells. *Science*, 2002. 296(5567): p. 550-3.
10. Jaworski, J., et al., Dynamic microtubules regulate dendritic spine morphology and synaptic plasticity. *Neuron*, 2009. 61(1): p. 85-100.
11. Burack, M.A., M.A. Silverman, and G. Banker, The role of selective transport in neuronal protein sorting. *Neuron*, 2000. 26(2): p. 465-72.
12. Sampo, B., et al., Two distinct mechanisms target membrane proteins to the axonal surface. *Neuron*, 2003. 37(4): p. 611-24.
13. De Paola, V., S. Arber, and P. Caroni, AMPA receptors regulate dynamic equilibrium of presynaptic terminals in mature hippocampal networks. *Nat Neurosci*, 2003. 6(5): p. 491-500.
14. Lu, M. and K.S. Kosik, Competition for microtubule-binding with dual expression of tau missense and splice isoforms. *Mol Biol Cell*, 2001. 12(1): p. 171-84.
15. Honnappa, S., et al., An EB1-binding motif acts as a microtubule tip localization signal. *Cell*, 2009. 138(2): p. 366-76.
16. van Spronsen, M., et al., TRAK/Milton motor-adaptor proteins steer mitochondrial trafficking to axons and dendrites. *Neuron*, 2013. 77(3): p. 485-502.
17. Lee, K. and K. Rhee, PLK1 phosphorylation of pericentrin initiates centrosome maturation at the onset of mitosis. *J Cell Biol*, 2011. 195(7): p. 1093-101.
18. Zhang, X. and V. Bennett, Restriction of 480/270-kD ankyrin G to axon proximal segments requires multiple ankyrin G-specific domains. *J Cell Biol*, 1998. 142(6): p. 1571-81.
19. Patterson, G.H. and J. Lippincott-Schwartz, A photoactivatable GFP for selective photolabeling of proteins and cells. *Science*, 2002. 297(5588): p. 1873-7.
20. Hedstrom, K.L., et al., Neurofascin assembles a specialized extracellular matrix at the axon initial segment. *J Cell Biol*, 2007. 178(5): p. 875-86.
21. Raaijmakers, J.A., M.E. Tanenbaum, and R.H. Medema, Systematic dissection of dynein regulators in mitosis. *J Cell Biol*, 2013. 201(2): p. 201-15.

- 22.** Shu, T., et al., Ndel1 operates in a common pathway with LIS1 and cytoplasmic dynein to regulate cortical neuronal positioning. *Neuron*, 2004. 44(2): p. 263-77.
- 23.** Zeilhofer, H.U., et al., Glycinergic neurons expressing enhanced green fluorescent protein in bacterial artificial chromosome transgenic mice. *J Comp Neurol*, 2005. 482(2): p. 123-41.
- 24.** Edelstein, A., et al., Computer control of microscopes using microManager. *Curr Protoc Mol Biol*, 2010. Chapter 14: p. Unit14 20.
- 25.** Yau, K.W., et al., Microtubule minus-end binding protein CAMSAP2 controls axon specification and dendrite development. *Neuron*, 2014. 82(5): p. 1058-73.
- 26.** Mlodzianoski, M.J., et al., Sample drift correction in 3D fluorescence photoactivation localization microscopy. *Opt Express*, 2011. 19(16): p. 15009-19.
- 27.** Schmitz, S.K., et al., Automated analysis of neuronal morphology, synapse number and synaptic recruitment. *J Neurosci Methods*, 2011. 195(2): p. 185-93.



3

Cytolinker Gas2L1 regulates axon branching and outgrowth via microtubule-dependent actin stabilization

Dieudonné van de Willige*¹, Celine Alkemade*^{2,3}, Jessica J.A. Hummel*¹,
Olga I. Kahn¹, Marileen Dogterom², Gijsje H. Koenderink^{3#},
Casper C. Hoogenraad^{1#} & Anna Akhmanova^{1#}

* Co-first author

Co-corresponding author

Submitted manuscript (2019)

¹ Cell Biology, Department of Biology, Faculty of Science, Utrecht University, Padualaan 8, 3584 CH Utrecht, the Netherlands.

² Department of Bionanoscience, Kavli Institute of Nanoscience, Delft University of Technology, van der Maasweg 9, 2629 HZ Delft, the Netherlands.

³ AMOLF, Living Matter Department, Science Park 104, 1098 XG Amsterdam, The Netherlands.

Abstract

Crosstalk between the actin and microtubule cytoskeletons underlies cellular morphogenesis. Interactions between actin filaments and microtubules are particularly important for establishing the complex polarized morphology of neurons. Here, we characterised the neuronal function of Growth Arrest Specific 2-like 1 (Gas2L1), a protein that can directly bind to actin, microtubules and microtubule plus-end-tracking End Binding proteins. We found that Gas2L1 promotes axon branching, but restricts axon elongation in cultured hippocampal neurons. Using pull-down experiments and *in vitro* reconstitution assays, in which purified Gas2L1 was combined with actin and dynamic microtubules, we demonstrated that Gas2L1 is autoinhibited. This autoinhibition is relieved by simultaneous binding to actin filaments and microtubules. In neurons, Gas2L1 primarily localizes to the actin cytoskeleton and functions as an actin stabilizer. The ability of Gas2L1 to interact with microtubules directs its actin-stabilizing activity to the axon. We propose that Gas2L1 acts as an actin regulator, the function of which is spatially modulated by microtubules.

Introduction

The cytoskeleton is a key player in cellular morphogenesis, as it provides cells with structural support and acts as a scaffold for organelle positioning. An example of a process where cytoskeletal filaments play intricate roles is neuronal development. Neurons have complex morphologies that allow them to form elaborate networks and propagate signals in the brain. Developing neurons undergo extensive cell shape changes, which are coordinated by guidance cues relayed to the actin and microtubule (MT) cytoskeletons (reviewed in [1]).

In particular, the crosstalk between MTs and actin plays an essential role during axon maturation (reviewed in [2-4]). At the tips of axonal processes, specialized structures called growth cones determine the direction and rate of axon advance. Growth cones contain a central dynamic MT array which probes the actin-rich periphery. Axon outgrowth is preceded by MT stabilization in filopodia at the tip of the growth cone, and conversely, repellent cues restrict peripheral MT entry. In a similar process, axon branching is believed to start with the formation of an actin patch along the axon, either *de novo* or as a remnant of a pausing growth cone (reviewed in [5, 6]). At the site of branch formation, newly generated dynamic MT plus ends are stabilized on the actin patch to initiate a new branch.

Actin-MT crosslinking proteins, also referred to as cytolinkers, are obvious candidates to regulate cytoskeletal crosstalk during axon development (reviewed in [7]). Most studies in this context have focussed on spectraplakins, a family of large proteins, which directly bind both to actin filaments and MT shafts and indirectly associate with growing MT plus ends through End Binding (EB) proteins [8-11]. The actin-MT crosslinking abilities of ACF7 (a spectraplakin otherwise known as MACF1) and its *Drosophila* ortholog Short Stop (Shot) are necessary for axon extension [12, 13]. Other MT plus end-associated proteins, such as CLASP and APC, participate in regulating axon outgrowth, possibly also by coordinating actin-MT coupling [14, 15].

Gas2L1 (Growth Arrest Specific 2-like 1) is a much smaller cytolinker with a domain composition similar to ACF7, but its role is less well understood. Like ACF7, Gas2L1 contains an N-terminal actin-binding calponin homology (CH) domain, a MT lattice-binding Gas2-related (GAR) domain and a C-terminal SxIP motif, which

mediates the interaction with MT plus-ends via EB proteins [16-18]. The actin-MT crosslinking abilities of Gas2L1 and its *Drosophila* ortholog Pigs (Pickled eggs) have been previously demonstrated in cells [18, 19]. So far, Gas2L1 was shown to regulate the distance between centrioles in cycling cells [20], and Pigs was identified as a cytoskeletal target of Notch signalling, which participates in *Drosophila* wing muscle development and oogenesis [21]. However, Gas2L1 has not been studied in the context of neuronal development, although Gas2L1 mRNA is abundant in mammalian brain tissue [16]. Here, we reveal that Gas2L1 participates in regulating axon outgrowth and branching in developing mammalian neurons. By combining data obtained in primary rat hippocampal neurons, *in vitro* reconstitution assays and biochemical experiments, we show that Gas2L1 is autoinhibited and requires the simultaneous binding of both actin filaments and MTs to fully relieve this autoinhibition. Our data suggest that Gas2L1 locally regulates the actin cytoskeleton during axon maturation by stabilizing actin in response to MT binding. Gas2L1 hereby promotes axon branching while tempering axon extension.

> Figure 1 - Gas2L1 balances axon outgrowth and branching in developing neurons.

(A) qPCR experiments showing the decrease in Gas2L1 (G2L1) mRNA levels upon DIV0-DIV3 shRNA treatment of primary rat hippocampal neurons (A; n=3). Electroporated neurons were subjected to 48 hour puromycin selection prior to mRNA isolation.

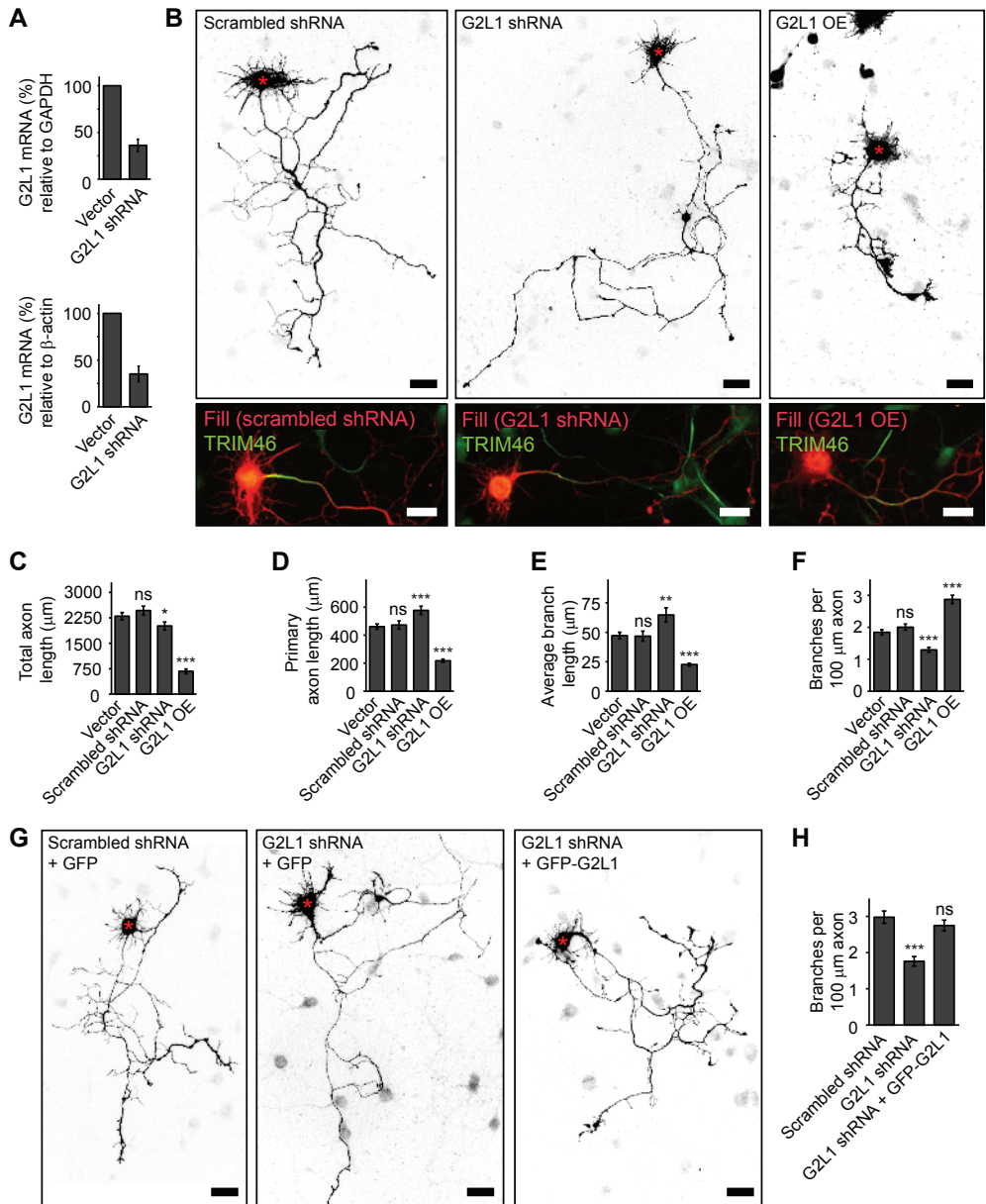
(B) Silhouettes (from β -galactosidase fill, top panels) of DIV3 neurons treated with scrambled or G2L1 shRNA and co-expressing HA- β -galactosidase, or overexpressing HA-G2L1 and HA- β -galactosidase for three days. Red asterisks indicate the position of the soma. Bottom panels show fill (red) combined with TRIM46 staining (green) of the neurons shown in the panels above.

(C-F) Quantifications of total axon length (C), primary axon length (D), average (non-primary) branch length (E) and the number of branches per 100 μ m axon (F) for DIV3 neurons treated as described in (B). Vector = empty shRNA vector co-expressing HA- β -galactosidase. n=50 neurons per condition from 3 independent experiments.

(G, H) Rescue experiments showing the number of branches per 100 μ m axon in neurons co-expressing scrambled or G2L1 shRNA with GFP, or G2L1 shRNA with GFP-G2L1, and HA- β -galactosidase from DIV0 to DIV3. Silhouettes (from β -galactosidase fill) are shown in (G). n=34-43 neurons per condition from 2 independent experiments.

Data information:

Scale bars: 30 μ m in (B, G). Data is displayed as means \pm SEM. Mann-Whitney test, ns: not significant, * p < 0.05, ** p < 0.01, *** p < 0.001.



Results

Gas2L1 affects axon branching and outgrowth in developing neurons

To determine whether Gas2L1 plays a role in neuronal development, we examined the effects of Gas2L1 depletion and overexpression on axon development in dissociated primary rat hippocampal neurons. Depletion resulted in a ~64% reduction of Gas2L1 mRNA as determined by qPCR, for which day-in-vitro (DIV) 0 neurons were electroporated with the empty vector or Gas2L1 shRNA-encoding plasmids and subjected to puromycin selection before mRNA isolation at DIV3 (Fig. 1A, Fig. S1A and B).

The depletion of Gas2L1 from DIV0 to DIV3 resulted in less complex axons (Fig. 1B) characterized by an increased axon branch length and reduced branch density (the number of branches per unit of axon length; Fig. 1C-F). We note that in this set of experiments, total axon length was slightly reduced, whereas other experiments showed no significant difference (Fig. S1E, Fig. 5G). The effects of Gas2L1 depletion on neuronal morphology could be rescued by co-expressing low levels of Gas2L1 (Fig. 1G and H, Fig. S1E-G), indicating that this phenotype is specific. Importantly, neuronal polarity was not affected by the loss of Gas2L1, as evidenced by staining of the axon initial segment marker TRIM46 (Fig. 1B) [22].

When Gas2L1 was overexpressed from DIV0 to DIV3, we observed a phenotype opposite to that of Gas2L1 depletion: the length of the primary axon and axonal branches was decreased, whereas the branch density was increased (Fig. 1C-F). Interestingly, axons of Gas2L1-overexpressing neurons thickened and frequently developed lamellipodia-like structures and excessive filopodia (Fig. S1C). We note that these features were beyond the level of detail included in our morphology analyses, which were based on axon tracings (Fig. S1D). Despite the obvious morphological defects, axons of Gas2L1-overexpressing neurons were still polarized, as TRIM46 staining appeared normal (Fig. 1B).

We conclude that Gas2L1 stimulates formation of new axon branches but restricts their elongation. The latter effect is different from that of ACF7, a structurally related cytolinker that promotes both axon outgrowth and branching [12, 13]. The ability of a protein to interact with both actin filaments and MTs can thus be associated with distinct neurodevelopmental functions.

Gas2L1 specifically localizes to actin-MT overlaps in *in vitro* reconstitution assays

To better understand how Gas2L1 mediates actin-MT crosstalk, we purified full-length Gas2L1, its actin-binding CH domain, and its MT-binding C-terminal fragment, which was termed Tail (Fig. 2A and S2A). We studied the behaviour of these proteins in an *in vitro* reconstitution assay, which included dynamic MTs and actin filaments stabilized with phalloidin [23]. We immobilized stable MT seeds on a glass surface, allowing dynamic MTs to grow in a solution containing tubulin dimers and unattached free-moving actin filaments (Fig. 2B).

As the first step, we tested the behaviour of Gas2L1 and mutants in the presence of dynamic MTs or stabilized actin filaments alone. Full-length Gas2L1 did not bind to single actin filaments in the absence of MTs (Fig. 2C), whereas the CH domain did (Fig. 2D, Fig. S2B). Similarly, in an assay with MTs alone, full-length Gas2L1 did not bind MTs (Fig. 2E). By contrast, the Tail mutant was able to bind MTs in the absence of actin filaments (Fig. 2F). Moreover, Gas2L1 did not track growing MT plus ends in the presence of EB3, whereas the Tail fragment did (Fig. S2C and S2D). These results indicate that under the tested conditions, individual domains of Gas2L1 are capable of binding actin filaments, the MT lattice and MT plus ends, but the full-length protein is not.

Surprisingly, when we added Gas2L1 to a composite assay with both MTs and low concentrations of actin filaments, we observed that Gas2L1 exclusively accumulated at the sites where actin filaments and MTs overlapped (Fig. 2G). Specific accumulation of Gas2L1 on actin-MT overlaps was especially obvious from events during which an actin filament gradually aligned with a growing MT: the appearance of the Gas2L1 signal along the MT coincided with the zippering of the unbound part of an actin filament along the MT (Fig. 2G). Similar zippering of actin filaments and MTs was observed previously with an engineered cytolinker containing a CH domain targeting actin and an SxIP motif targeting EB proteins [24]. In a composite assay where more actin filaments were available for binding, we observed MTs covered with multiple co-aligned actin filaments (Fig. 2H), whereas no MT-actin co-alignment occurred without Gas2L1 (Fig. S2H).

Time-lapse analysis of actin-MT-Gas2L1 bundles revealed that MTs inside these bundles remained dynamic (Fig. 2I and J). When a catastrophe occurred and the MT shrunk back, Gas2L1 did not remain bound to actin, but disappeared together with the MT (Fig. 2I and J), and the actin filaments that were initially co-

aligned with the MT dispersed (Supplementary movie 1, Fig. 2K). Once the MT repolymerized, the accumulation of Gas2L1 and actin along its shaft was restored (Fig. 2K). The addition of EB3 to the assay did not alter Gas2L1-induced MT-actin co-alignment and did not induce any enrichment of Gas2L1 at growing MT plus ends, in spite of the fact that EB3 was able to track MT plus ends in the same assay (Fig. S2E-G). These data confirm that Gas2L1 does not behave as a canonical plus end tracking protein although it does contain an EB-binding SxIP motif.

> Figure 2 - *In vitro* reconstitution of the interaction of Gas2L1 with actin filaments and MTs.

(A) Schematic depiction of the domain structure of Gas2L1 (G2L1) and Gas2L1 mutants used in this study.

(B) Schematic depiction of *in vitro* TIRF assays. Stable MT seeds are attached to the glass surface, from which dynamic MTs grow by addition of tubulin dimers (either with or without EB3 present). Actin filaments are free to move around. G2L1 links F-actin to MTs.

(C) *In vitro* reconstitution of full-length Gas2L1 in the presence of actin (0.5 μM) only.

(D) *In vitro* reconstitution of the Gas2L1 CH domain in the presence of actin (0.5 μM) only. The intensity range between the F-actin panels and Gas2L1/CH panels of (C) and (D) are equal.

(E) *In vitro* reconstitution of full-length Gas2L1 in the presence of MTs only.

(F) *In vitro* reconstitution of the Gas2L1 Tail domain in the presence of MTs only.

(G) *In vitro* reconstitution of full-length Gas2L1 in a composite assay with both actin (10 nM) and MTs. Gas2L1 only localizes at MT-actin overlaps. Gas2L1 accumulation (yellow arrows) occurs after an actin filament 'lands' and zippers (purple arrows) onto at a MT (blue arrows).

(H) *In vitro* reconstitution of full-length Gas2L1 in a composite assay as in (G), but with higher actin concentration (1 μM).

(I) Still frames showing the dynamics of a Gas2L1-F-actin-MT bundle, from a composite *in vitro* reconstitution assay as described in (H). The red line indicates the (stable) MT seed.

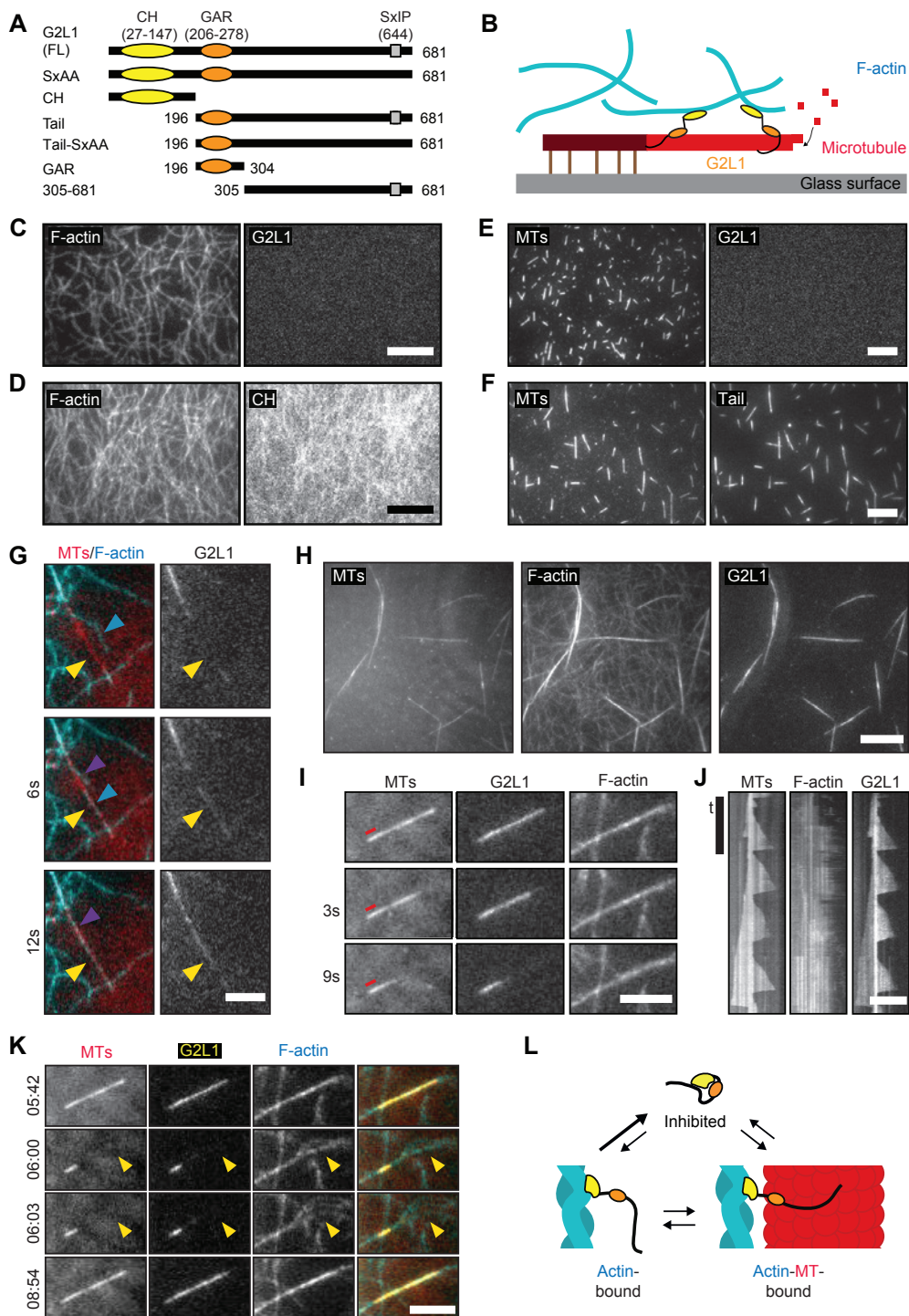
(J) Kymographs showing the dynamics of the Gas2L1-F-actin-MT bundle seen in (I).

(K) Still frames taken from Supplementary movie 1 at the indicated timestamps, showing the dispersion of actin filaments (yellow arrowheads) after Gas2L1 and the MT disappear from the Gas2L1-F-actin-MT-bundle and renewed actin bundling and Gas2L1 accumulation upon MT regrowth. Experimental conditions are as described for (H).

(L) Model of Gas2L1 autoinhibition.

Data information:

Scale bars: 10 μm (C-F, H, I), 5 μm (G, K). For (J), vertical scale bar: 3 min, horizontal scale bar 5 μm .



Our results confirm that Gas2L1 can crosslink actin filaments and MTs. However, while individual fragments of Gas2L1 are able to bind MTs or actin filaments, full-length Gas2L1 does not localize to either of these separate cytoskeletal components *in vitro*. Instead, Gas2L1 binds to MTs and actin filaments simultaneously, suggesting that the protein might be autoinhibited and that the interaction with both actin and MTs is required to relieve autoinhibition. Of note, Gas2L1 did not bind independently to MTs regardless of incubation time. However, over time Gas2L1 accumulated on slowly forming actin bundles (but never individual filaments) in the absence of MTs (Fig. S2I). Since there appears to be some interaction between Gas2L1 and actin in the absence of MTs, we propose that the binding of Gas2L1 to actin acts as the first step towards initiating actin-MT crosslinking (Fig. 2L).

Autoinhibition of Gas2L1 is a result of the interaction between the CH domain and MT-binding tail

If Gas2L1 is indeed autoinhibited, its MT-binding tail should directly compete with actin for binding its CH domain. A similar intramolecular interaction was reported for *Shot*: its N-terminal tandem CH domains interact with the C-terminal EF-hand/GAR region [25].

We mapped potential intramolecular interactions of Gas2L1 by testing whether its different deletion mutants (Fig. 2A) interacted with the CH domain in a pull-down assay. Gas2L1 fragments were tagged with an N-terminal AviTag fused to GFP (bioGFP), which was biotinylated by co-expressing the biotin ligase BirA. Streptavidin beads were used to bind biotinylated Gas2L1 fragments and incubated with HA-tagged CH domains, which in case of interaction were retained on the beads after washing and could be detected by Western blotting.

Full-length Gas2L1 and the MT-binding Tail fragment pulled down the CH domain, whereas the biotinylated GFP, used as a negative control, displayed no binding (Fig. 3A). Moreover, a Tail mutant harbouring a mutated SxIP motif (Tail-SxAA), which was previously shown to abolish Gas2L1-EB interaction [20], still bound the CH domain. When the Tail domain was split into smaller fragments, the binding to the CH domain was lost (Fig. 3A). These data show that the interaction of the CH domain of Gas2L1 with the MT-binding C-terminal part of the protein requires both the GAR domain and the unstructured region, and occurs independently from the

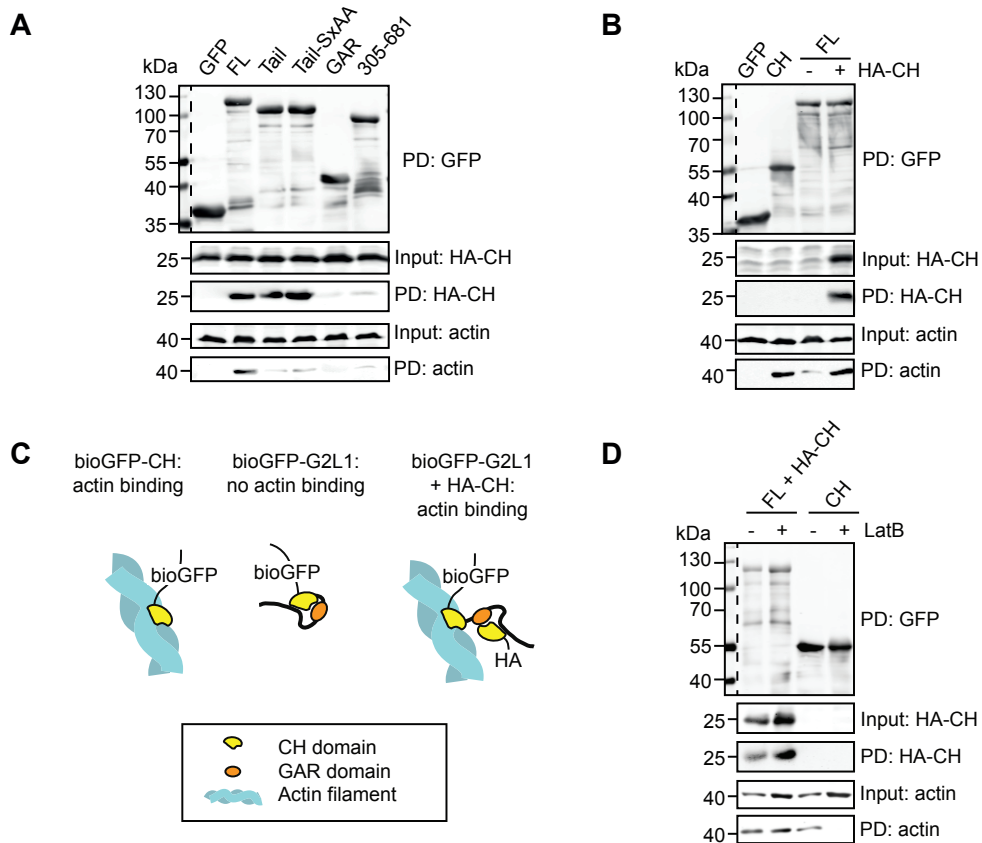


Figure 3 - Intramolecular interaction between Gas2L1 domains.

(A) Pull-down experiment showing the binding of Gas2L1's CH domain (HA-CH) to full length Gas2L1 (G2L1) and both Tail and Tail-SxAA mutants in HEK293 cell lysates, as well as co-precipitation of actin with full-length Gas2L1 bound to HA-CH.

(B) Pull-down experiment showing co-precipitation of actin with Gas2L1's CH domain in HEK293 cell lysates, and full-length Gas2L1 only when HA-CH is co-expressed.

(C) Model of increased co-precipitation of actin with Gas2L1 in the presence of HA-CH.

(D) Pull-down experiment showing the effect of Latrunculin B (LatB) on actin co-precipitation in HEK293 cell lysates. Cells were treated with 10 μ M LatB prior to harvesting, and 10 μ M LatB was added to the cell lysates for the duration of the experiment.

Data information:

Dotted lines separate marker lanes from sample lanes on the same blots (top panels). For bottom panel blots, markers were detected on the same blot, but in a different channel than the one used for signal detection that are shown here.

association with EB proteins.

Interestingly, consistent with the pattern of *in vitro* reconstitution experiments, the CH domain of Gas2L1 pulled down endogenous actin while full-length Gas2L1 did not (Fig. 3B). However, full-length Gas2L1 acquired the ability to pull down actin in the presence of a co-expressed CH domain (Fig. 3A and B). This was likely due to the additional CH domain competing with the tail part of the full-length Gas2L1 for binding to the CH domain located within the same molecule (Fig. 3C), confirming our model of Gas2L1 autoinhibition. Furthermore, the MT-binding Tail fragment did not pull down actin even though the CH domain co-precipitated (Fig. 3A). This reinforces the idea that the CH domain of Gas2L1 cannot bind to actin when it is associated with the tail part of the protein in the autoinhibited conformation. Lastly, the addition of 10 μ M Latrunculin B (LatB), which inhibits actin polymerization, abolished the interaction between actin and the CH domain (Fig. 3D). This reveals that our pull-down experiments reflect an interaction between Gas2L1 and actin filaments rather than actin monomers.

Taken together, we conclude that Gas2L1 is autoinhibited through a direct interaction between its CH domain and its MT-binding tail. Our *in vitro* reconstitution observations predict that this mechanism could promote the selective activity of the protein at actin-MT interfaces.

Gas2L1 localizes to neuronal F-actin and regulates axon development by influencing actin stability

Next, we turned back to primary hippocampal neurons to investigate how Gas2L1 affects their cytoskeleton. In NIH3T3 and COS7 cells, Gas2L1 was shown to localize predominantly to actin stress fibres [16, 18]. In neurons, which lack stress fibres, GFP-tagged Gas2L1 primarily co-localized with the total F-actin population (Fig. 4A). The localization of Gas2L1 to F-actin was also apparent in subcellular areas devoid of MTs. This observation reveals that in contrast to our *in vitro* experiments, Gas2L1 can localize to actin structures independently of MTs in neurons. This result further strengthens the idea that actin binding may be the first step towards stably relieving the autoinhibition of Gas2L1. Some Gas2L1 accumulation along MTs was also observed (Fig. 4B). Interestingly, axons of DIV3-4 neurons expressing high levels of Gas2L1 showed clear cytoskeletal abnormalities: MTs frequently buckled inside growth cones, which were enlarged due to what appeared to be increased amounts

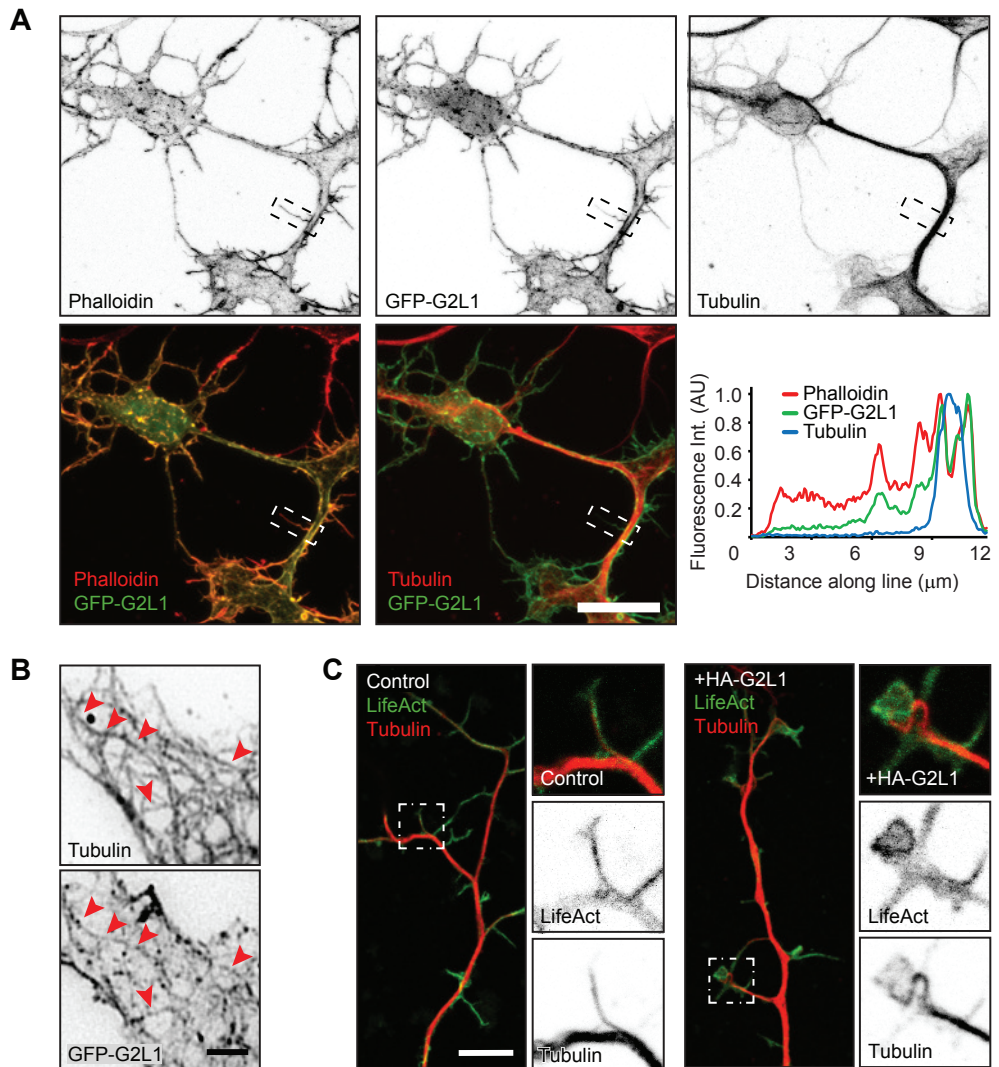


Figure 4 - Neuronal localization of Gas2L1 and effects of its overexpression.

(A) Localization of GFP-Gas2L1 (G2L1) in a DIV4 neuron stained for MTs (α -tubulin) and F-actin (Phalloidin), as well as merged images showing colocalization between GFP-Gas2L1 and Phalloidin or GFP-Gas2L1 and α -tubulin. The linescan shows colocalization along the boxed neurite.

(B) Close-up of GFP-Gas2L1 localization to MTs (tubulin staining). Red arrowheads point along MTs positive for GFP-Gas2L1.

(C) Cytoskeleton of DIV3 neurons electroporated at DIV0, co-expressing LifeAct-GFP and control empty vector (left) or HA-Gas2L1 (right) and stained for MTs (tubulin). Boxes indicate zoomed region.

Data information: Scale bars: 20 μm in (A), 3 μm in (B), 10 μm in (C).

of F-actin (Fig. 4C).

Given the dominant localization of Gas2L1 to F-actin, we then focused on actin-related effects of the protein. We noticed that Gas2L1 depletion and overexpression phenotypes during axon development line up with results published in various studies investigating the effect of mild changes of actin stability on this process [26-31]. Therefore, we tested the effect of low nanomolar doses of LatB on the primary hippocampal neurons in our culture system. DMSO, which was used as a vehicle, had no effects on axon morphology at the highest concentration used in these experiments (Fig. S5A-E). In contrast, 48-hours treatment with 10-100 nM LatB reduced branch density and induced branch elongation at DIV3 (Fig. 5A-E). Mild actin destabilization with LatB thus resembled the effects of Gas2L1 knockdown (summarized in Fig. 7A). However, primary axon length did not increase after LatB treatment (resulting in a net decrease of combined axon length as seen in Fig. 5B and C), whereas the depletion of Gas2L1 did induce lengthening of the primary axon (Fig. 1D). These data suggest that Gas2L1 could act by stabilizing actin and

> Figure 5 - Gas2L1 phenotypes reflect changes in actin stability.

(A) Silhouettes (from β -galactosidase fill) of DIV3 neurons, transfected at DIV1 and treated with the indicated doses of Latrunculin B for 48 hours.

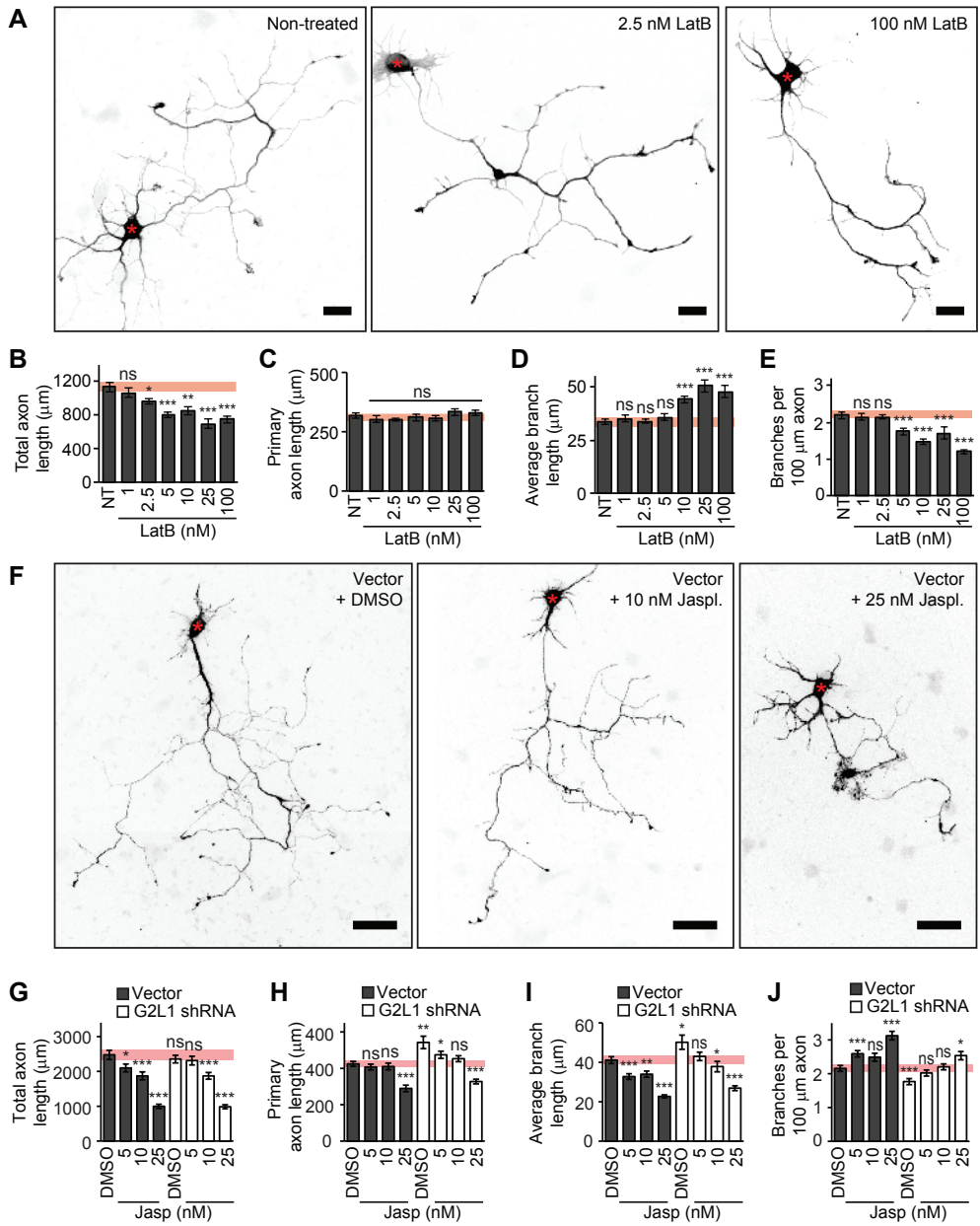
(B-E) Quantifications of total axon length (B), primary axon length (C), average axon branch length (D) and the number of branches per 100 μm axon (E) for neurons as described in (A). Pink bars show range of means \pm SEM of control conditions. NT=non-treated;n=37-40 neurons per condition from 3 independent experiments.

(F) Silhouettes (from β -galactosidase fill) of DIV4 neurons, transfected at DIV1 with empty shRNA vector (grey) or Gas2L1 shRNA (white) and coexpressing β -galactosidase. 24 hours after transfection, neurons were treated with the indicated doses of Jasplakinolide or DMSO (equivalent of 25 nM dose) for 48 hours.

(G-J) Quantifications of total axon length (G), primary axon length (H), average axon branch length (I) and the number of branches per 100 μm axon (J) for neurons as described in (F). Pink bars show range of means \pm SEM of control conditions. n=64-69 neurons per condition from 4 independent experiments.

Data information:

Scale bars: 20 μm in (A), 50 μm in (F). Data is displayed as means \pm SEM. Mann-Whitney test, ns: not significant, * $p < 0.05$, ** $p < 0.01$, *** $p < 0.001$. For Fig. G-J, all values were compared to those of DMSO control (vector) neurons.



display higher activity in the primary axon compared to elsewhere in the neuron, possibly due to presence of distinct actin filament populations.

F-actin stabilization by low nanomolar doses of jasplakinolide mimicked effects of Gas2L1 overexpression on axons of control vector-expressing DIV4 neurons treated for 48 hours (Fig. 5F-J, grey bars, and summarized in Fig. 7A). Moreover, at 25 nM of jasplakinolide, axons displayed thickening and lamellipodia- and filopodia-like protrusions akin to Gas2L1 overexpression (Fig. S1C and 5F). Importantly, 5-10 nM jasplakinolide was able to rescue the effects of Gas2L1 depletion on axon morphology (Fig. 5F-J, white bars). Taken together, these data suggest that Gas2L1 mediates axon branching and outgrowth by increasing F-actin stability. These findings are consistent with the observation that the *Drosophila* Gas2L-ortholog Pigs stabilizes F-actin when overexpressed [19].

3

MT behaviour appears unaffected in neurons depleted of Gas2L1

We next determined if and how MT-related effects contribute to the role of Gas2L1 in axon development. In line with reports in NIH3T3 cells [18], Gas2L1 overexpression caused the displacement of endogenous EB1 away from MT plus-ends and onto Gas2L1-decorated actin structures (Fig. 6A). We confirmed that this behaviour depended on the SxIP motif of Gas2L1, as mutating the SxIP motif to SxAA abolished EB1 displacement (Fig. S6A). These results are in agreement with our observation that Gas2L1 is not a plus-end tracking protein *in vitro*. However, Gas2L1 does not recruit EB3 *in vitro* (Fig. S2G), suggesting that Gas2L1-dependent EB recruitment may require additional factors or post-translational modifications absent in the assays using purified proteins. Taken together, our data indicate that EB3 does not appear to be bound to Gas2L1 on actin-MT bundles as is apparent from *in vitro* data (Fig. S2G), and it does not appear to load Gas2L1 onto MT plus-ends. The function of the EB-Gas2L1 interaction might be to augment the intrinsically weak MT affinity of Gas2L1.

Of note, the redistribution of EB proteins and detrimental effects on axon development induced by Gas2L1 overexpression show that, although overexpression experiments provide valuable insights into the functioning of the protein, endogenous Gas2L1 operates at low levels with more nuanced outcomes. To determine the contribution of Gas2L1 to MT regulation at endogenous levels, we looked for signs of MT disruption in neurons depleted of Gas2L1. In cultured

cell lines, overexpression of Gas2L1 or its tail fragments was reported to promote resistance to nocodazole-induced MT depolymerization and to decrease MT dynamics [16, 18]. We used a photoactivatable fusion of GFP- α -tubulin to measure the longevity of MTs in axon shafts and found that, while Gas2L1 overexpression could indeed increase MT lifetimes, there was no difference between control and Gas2L1-depleted neurons (Fig. 6B). Similarly, there was no change in the growth velocity of EB3-positive MT plus ends in growth cones upon Gas2L1 depletion (Fig. 6C). These results suggest that MT behaviour is relatively normal in Gas2L1 knockdown neurons.

MTs guide Gas2L1 activity in neurons

Interestingly, we found that while the Gas2L1 MT-binding Tail mutant could decorate all neuronal MTs, it was enriched on TRIM46-positive MTs in proximal axons (Fig. 6D). Given our *in vitro* findings which suggest a model of full release of Gas2L1 autoinhibition in the presence of actin and MTs, we wondered whether this increase in MT affinity could impact Gas2L1 activity locally. More specifically, we wondered whether the preferential interaction of the tail of Gas2L1 with MTs in the proximal axon could drive differential effects of Gas2L1 on actin stabilization.

Quantifications of the total amount of F-actin in proximal axons and non-axonal neurites (future dendrites; dendritic maturation occurs at later stages of development) revealed that overexpression of GFP-Gas2L1, GFP-Gas2L1-SxAA and GFP-CH increased F-actin levels compared to GFP overexpression (Fig. 6F and G, white bars). To determine whether the enhanced levels of F-actin also reflected enhanced actin stability, as suggested by drug-induced effects including rescue experiments (Fig. 5F-J), we treated neurons overexpressing Gas2L1 fusions with high concentrations of LatB to reveal stable F-actin populations (Fig. 6E, F and G, grey bars). Treatment of control GFP-expressing neurons with 10 μ M LatB for 30 minutes resulted in a near-complete loss of F-actin in all projections of control, GFP-expressing neurons. By contrast, some F-actin remained in the presence of overexpressed Gas2L1 fusions, although the patterns of stabilization were strikingly different between full-length Gas2L1 and mutants (Fig. 6E).

To quantify and illustrate the differences in actin stabilization compared to the localization of the various fusion proteins tested, we compared the polarity indices of the localization of each Gas2L1 fusion before treatment and of F-actin

distribution with or without LatB treatment (Fig. 6H). The polarity indices are derived from raw fluorescence intensities in axons and non-axonal neurites (see supplementary Materials & Methods for details) and range from 1 to -1 for purely axonal or purely non-axonal localizations, respectively. A value of 0 signifies no particular enrichment. Our analysis showed that the CH domain of Gas2L1 is enriched in non-axonal neurites, where it also stabilizes actin. By contrast, full-length Gas2L1 was evenly distributed between the axons and other neurites, and

> Figure 6 - MTs modulate the actin-stabilizing activity of Gas2L1.

(A) Endogenous EB1 re-localization upon overexpression of GFP-Gas2L1 (G2L1) in a DIV4 neuron. Boxes indicate zoomed regions of transfected (continuous outline) or untransfected neurons (dotted outline).

(B) Lifetime of photoactivated GFP- α Tubulin signal in axons of DIV3-4 neurons electroporated at DIV0 with RFP, paGFP- α Tubulin and control GW1-EV or Gas2L1 shRNA or HA-Gas2L1. $n=54-59$ axons per condition from 3 independent experiments.

(C) Growth velocity of anterograde MT comets near the axon terminus, as labelled with EB3-tagRFP-T in DIV3-4 neurons electroporated at DIV0 with pSuper empty vector (control) or Gas2L1 shRNA. $n=27-28$ neurons (664-714 comets) per condition from 2 independent experiments.

(D) Localization of GFP-Tail in DIV3 neurons co-expressing HA- β -galactosidase fill (blue) and stained for TRIM46 (red). Boxed region is enlarged to the right. Arrowheads indicate the axon.

(E) DIV3 neurons expressing GFP control, GFP-Gas2L1 or GFP-CH and treated with 10 μ M Latrunculin B for 30 minutes or non-treated, stained for F-actin (phalloidin) and the axon initial segment (TRIM46).

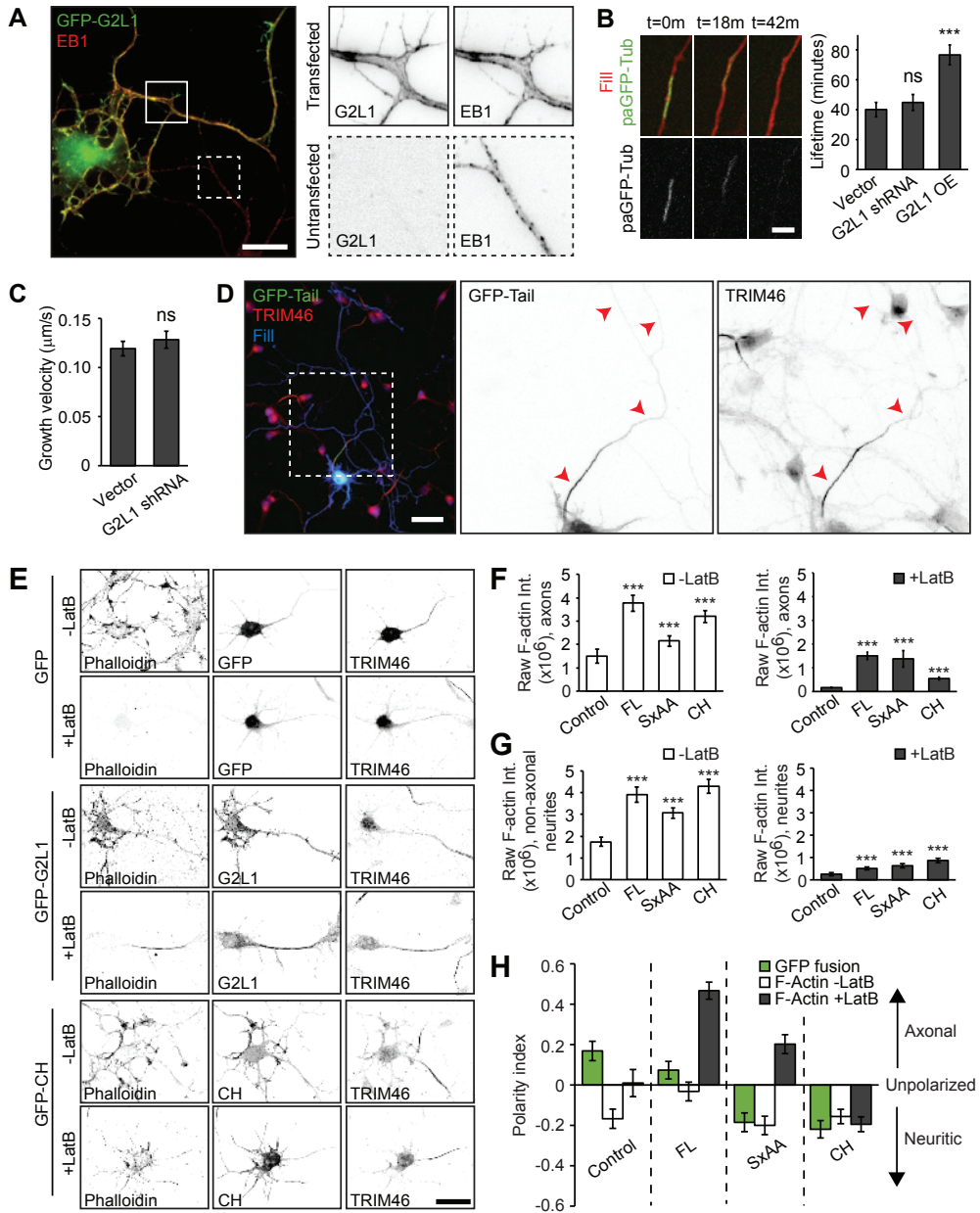
(F, G) Raw phalloidin staining intensities in axons (F) and non-axonal neurites (pre-dendrites) (G) of DIV3 neurons expressing the indicated GFP fusions and treated with 10 μ M Latrunculin B for 30 minutes (grey bars) or non-treated (white bars). $n=27-40$ cells per condition from 2 independent experiments.

(H) Polarity index representing localization of the indicated GFP fusions in non-treated neurons (green bars), and localization of F-actin as labelled by phalloidin in DIV3 neurons treated with 10 μ M Latrunculin B for 30 minutes (grey bars) or non-treated (white bars). $n=27-40$ cells per condition from 2 independent experiments. Positive values indicate axonal enrichment, negative values indicate neuritic enrichment and a value of 0 signifies no particular enrichment.

Data information:

Scale bars: 10 μ m in (A), 4 μ m in (B), 50 μ m in (D), 30 μ m in (E).

Data is displayed as means \pm SEM. Mann-Whitney test (B, F, G), unpaired t-test (C), ns: not significant, * $p < 0.05$, ** $p < 0.01$, *** $p < 0.001$.



selectively stabilized actin in the axon (Fig. 6H). This suggests that the MT-binding tail region promotes axonal localization of Gas2L1 in addition to the non-axonal neurite targeting of protein via the CH domain. Importantly, the pattern of actin stabilization by Gas2L1 mirrored the preference of the Gas2L1 tail for axonal MTs rather than the broad localization of the full-length protein to neuronal actin. The SxAA mutant displayed slightly less efficient axonal localization and actin stabilization (Fig. 6H), implying that the SxIP motif of Gas2L1 may function to enhance the affinity of the protein for axonal MTs.

One could argue that the tail region of Gas2L1 counteracts the strong preference of the CH domain of Gas2L1 for non-axonal neurites not through its MT affinity, but rather by directly enhancing the binding of Gas2L1 to some specific axonal populations of actin filaments. If this were the case, Gas2L1-Tail would likely exert a similar effect on other actin-binding domains. To test this possibility, we fused Gas2L1-Tail to the tandem actin-binding CH domains of α -actinin (ABD and ABD-Tail; Fig. S6B). Although the CH domains of Gas2L1 and α -actinin belong to different classes [32], ABD behaved very similarly to the CH domain of Gas2L1 – it preferentially localized to non-axonal neurites, where it also stabilized actin. ABD was unaffected by fusing it to Gas2L1-Tail (Fig. S6C-F), indicating that the tail of Gas2L1 has no direct effect on the specificity of actin binding. The localization of Gas2L1 thus appears to be an emergent property of the combination of its specific CH domain and MT-binding tail, which can interact with each other.

Discussion

In this study, we show that the cytolinker Gas2L1 regulates axon morphology by stabilizing F-actin. Interestingly, the actin-binding CH domain of Gas2L1 preferentially localizes to non-axonal neurites, but the presence of the MT-binding C-terminus in the full-length protein leads to equal distribution of Gas2L1 to F-actin in all neurites. In spite of its uniform localization, full-length Gas2L1 stabilizes F-actin more potently in the proximal axon, whereas the CH domain preferentially stabilizes F-actin in non-axonal neurites. These results suggest that the binding of Gas2L1 to MTs influences both the localization and activity of the protein in neurons. This finding is further reinforced by the fact that the Gas2L1 MT-binding tail fragment is enriched on

MTs in the proximal axon, which coincides with the region of the strongest F-actin stabilization by Gas2L1.

How can MTs regulate Gas2L1's activity towards F-actin? We propose that this property depends on the autoinhibition of Gas2L1. Our *in vitro* reconstitution experiments demonstrated that Gas2L1 efficiently localizes to actin-MT bundles, but not to individual actin filaments or MTs. This can be explained by the interaction between CH domain and MT-binding tail, which employs the same interfaces as those used for the actin and MT binding. The association of the Gas2L1 tail domain with MTs is expected to liberate the CH domain and to allow Gas2L1 to interact with actin filaments, placing the activity of the protein under direct control of the simultaneous presence of actin and MTs. Our results complement previous observations hinting towards an inhibitory relation between the CH and GAR domains of Gas2L proteins in other cell types [16, 19]. For example, Girdler and colleagues briefly mention observing that Pigs, the *Drosophila* Gas2L ortholog, stabilizes actin at MT interfaces [19]. Therefore, the regulatory mechanism we identified for Gas2L1 may be conserved in evolution. Furthermore, the CH and EF-hand/GAR domains of the *Drosophila* spectraplakine Shot also undergo an autoinhibitory interaction [25]. The direct regulation by actin and MTs might thus be a common mechanism in CH/GAR domain-containing cytolinkers.

Although autoinhibition of Gas2L1 is obvious from the biochemical and *in vitro* reconstitution experiments, it is less apparent in neurons. Purified Gas2L1 does not associate with individual actin filaments *in vitro* unless MTs are present, yet overexpressed Gas2L1 localizes to neuronal F-actin including the areas where MTs are excluded. This discrepancy may arise from the differential affinity of Gas2L1 for various types of actin, e.g. different organisation of actin filaments, their posttranslational modifications and the presence of actin-associated proteins. Evidence for the binding selectivity of Gas2L1 was already provided by previous studies [18, 19]. We note that over time, Gas2L1 does accumulate on actin bundles also in *in vitro* reconstitution experiments, whereas it does not bind MTs, suggesting that the association with actin is the first step towards releasing autoinhibition. Importantly, we find that Gas2L1 localization to neuronal F-actin is not sufficient to stabilize it. Instead, Gas2L1-mediated actin stabilization appears to depend on the MT binding by its C-terminus, suggesting that full relief of autoinhibition requires the presence of both actin and MTs even in neurons.

We show that the actin-stabilizing drug jasplakinolide is able to rescue axon morphology of Gas2L1-depleted neurons and mimics Gas2L1 overexpression when applied to control neurons. Conversely, actin destabilization via LatB induces morphological changes in line with Gas2L1 depletion: axon branches elongate in response to LatB as they do in Gas2L1-depleted neurons. Interestingly, the primary axon does not respond to low-dose LatB treatment but does become longer after Gas2L1 depletion (summarized in Fig. 7A). In line with this observation, axonal branches but not the primary axon are shortened after treatment with low doses of jasplakinolide (5-10 nM). It thus appears that the growth cones of primary axons are less sensitive to mild drug-mediated actin perturbations, possibly due to the presence of more robust regulatory machinery. We speculate that the reduced sensitivity of primary axons to low doses of LatB might be caused by the elevated activity of Gas2L1 in this neuronal compartment, which is caused by a higher affinity of the Gas2L1 C-terminus to MTs in the primary axon. However, we cannot exclude alternative explanations, such as the distinct drug response of specific actin subpopulations that could be present in the primary axon and axonal branches. Precedents for such distinct sensitivity have been described: for example, LatA has been suggested to specifically inhibit the function of the actin regulator β -thymosin and to thereby preferentially inhibit filopodia formation [33].

It is worth emphasizing that the dose of jasplakinolide needed to compensate the effects of neuronal Gas2L1 depletion is minimal (5-10 nM). Together with the dramatic changes induced by Gas2L1 overexpression, these findings suggest that the protein is extremely potent and that endogenous expression levels of Gas2L1 are low. This is in line with other studies investigating Gas2L-proteins [16, 19, 21]. Notably, at early development stages, Pines et al. reported phenotypes associated with cytoskeletal defects in Pigs null mutant flies without being able to detect the underlying cytoskeletal changes using conventional light microscopy [21]. The nuances of how Gas2L1 depletion affects the neuronal cytoskeleton are likely similarly subtle and challenging to identify.

Remarkably, key regions of Gas2L1 – the actin-binding CH domain, the MT-binding GAR domain and the EB-binding SxIP motif – are also found in the spectraplakine ACF7. Both Gas2L1 and ACF7 are actin-MT crosslinking proteins. However, depletion of ACF7 or its *Drosophila* counterpart Shot impairs axon outgrowth [12, 13, 34], whereas we find that Gas2L1 depletion promotes axon

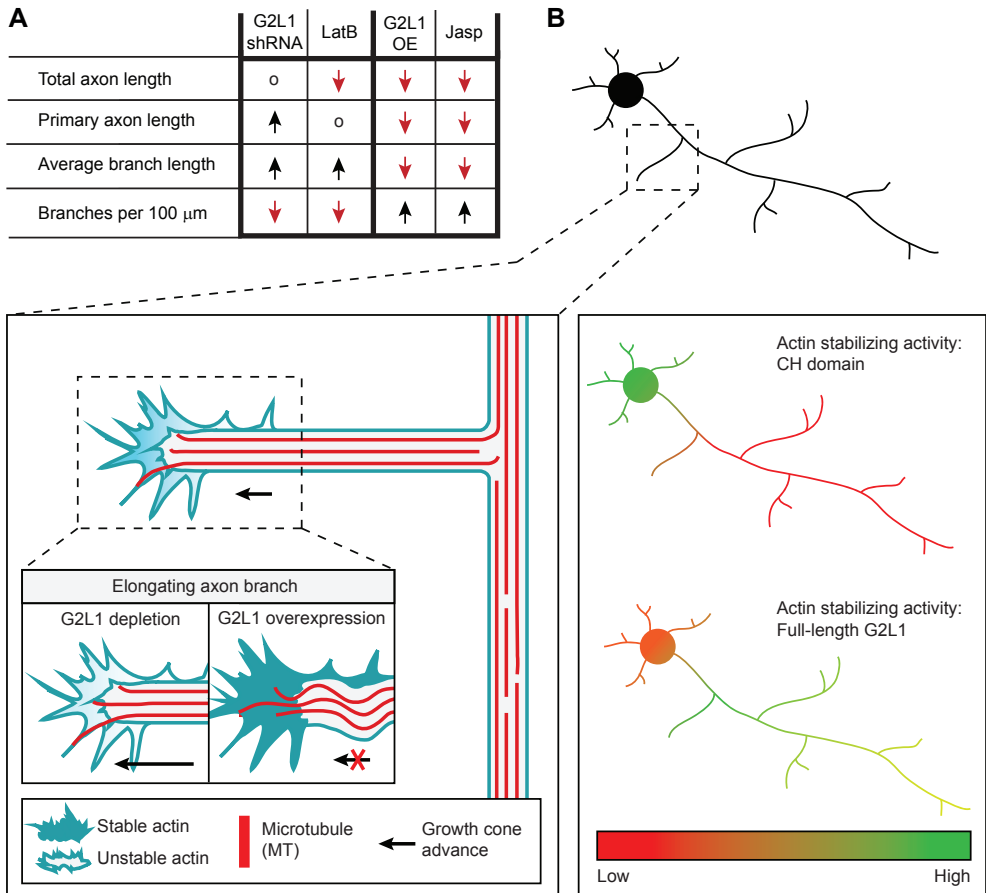


Figure 7 - Model of Gas2L1 activity during axon development.

(A) Summary of the effects of Gas2L1 shRNA-mediated depletion, Gas2L1 overexpression (G2L1 OE) and low nanomolar doses of jasplakinolide (jasp) and Latrunculin B (LatB) on axon development of DIV3-4 neurons. o = no effect; ↓ = lower values, ↑ = higher values.

(B) Proposed working model of the role of Gas2L1 during axon branching and outgrowth. MT binding by the tail of Gas2L1 promotes local actin binding and stabilization by the CH domain and shifts the actin-stabilizing activity of Gas2L1 towards the axon. In growth cones, where dynamic MTs probe the actin-rich periphery, Gas2L1 contributes to actin stability levels necessary for normal outgrowth. Reduced actin stability causes overextension of branches in the absence of Gas2L1. Axons of neurons overexpressing Gas2L1 have increased actin stability, resulting in shorter branches with higher F-actin levels and buckling MTs.

elongation. Actin-MT crosslinking proteins can thus exert opposite regulatory effects during neuronal development.

The difference between ACF7 and Gas2L1 may be explained by the observation that Gas2L1 is primarily an actin-localized protein, whereas ACF7 strongly interacts with MTs [35, 36]. Axon outgrowth requires dynamic MTs to invade the actin-rich growth cone periphery. MTs are disorganized and destabilized in growth cones lacking ACF7 [12, 13], and as such ACF7 is thought to guide MT entry into growth cones. We found that the behaviour of MTs in Gas2L1-depleted neurons appears normal, suggesting that Gas2L1 does not operate via this mechanism. Instead, we propose that Gas2L1 stabilizes the surrounding actin network in response to the invasion of MTs (Fig. 7B).

Although actin and actin-MT coupling are required for axon extension, a subpopulation of actin acts as a barrier for MT invasion in the growth cone and as a brake on outgrowth. The local actin network also produces a contractile, retrograde-oriented force that is counteracted by MTs during extension (reviewed in [37]). Actin reorganization can thereby positively and negatively affect axon elongation, and the net result is a matter of balance. By increasing actin stability, Gas2L1 could increase the MT-restricting function of growth cone actin and/or the level of contractility. This model explains axon overextension in the absence of Gas2L1, as well as the appearance of buckled MTs in the short axons of Gas2L1-overexpressing neurons (Fig. 7B). At endogenous levels, Gas2L1 likely contributes to a certain level of actin stability required for normal growth cone behaviour. Finally, in contrast to their opposing roles in axon extension, Gas2L1 and ACF7 share a function in axon branching [12]. This suggests that both ACF7-mediated MT guidance and actin stabilization via Gas2L1 are necessary for the initial steps of axon branch formation.

To summarize, we reveal the role for the cytolinker Gas2L1 in axon growth and branching, describe important clues about the underlying mechanism and provide insight into the functional diversity of factors involved in cytoskeletal cross-talk.

Materials and methods

Detailed Materials & Methods are included in the supplementary information. We here provide an overview of the most important experimental details.

Animals and primary neuron cultures

Animal experiments were approved by the Dutch Animal Experiments Committee (DEC) and conducted in agreement with guidelines of Utrecht University, Dutch law (Wet op de Dierproeven, 1996) and European regulations (Guideline 86/609/EEC). Primary dissociated hippocampal neuron cultures were derived from hippocampi of E18.5 mixed-sex pups of pregnant Wistar rats (Janvier) according to protocols for mechanic/enzymatic dissociation described previously [38].

DNA and shRNA constructs

All G2L1 expression constructs were N-terminal fusions generated from PCR-based strategies using GFP-G2L1 or GFP-G2L1-SxAA as templates, which were based on human G2L1 (GenBank Accession No NM_152236.1) and kindly provided by Dr. F.K.C. Au and Prof. Dr. R.Z. Qi (Hong Kong University of Science and Technology) [20]. The following targeting sequences were used for shRNA-mediated depletion: scrambled - GCGCGCTTTGTAGATTCCG; G2L1 shRNA (rat) - CGCCAATGACATTCGAAA.

qPCR

Experimental procedures are detailed in [39]. The following primer pairs were used: GAPDH 5'-TGCCCCATGTTTGTGATG and 3'-TGTGGTCATGAGCCCTTCC; β -actin 5'- AGGCCAACCGTGAAAAGATG and 3'-CCAGAGGCATACAGGGACAAC; G2L1 5'-ACATTCGAAACCTGGACGAG and 3'-TCAGCACCTCACAAAGATG.

Protein purification and *in vitro* reconstitution assays

N-terminal GFP-G2L1 fusions were purified from HEK293 cells using Strep(II)-streptactin affinity purification using protocols described in [40]. Lyophilized porcine brain tubulin was obtained from Cytoskeleton. Monomeric (G-)actin was purified from rabbit skeletal muscle acetone powder [41, 42]. 6xHis-tagged recombinant human mCherry-EB3 was expressed and purified as described before [43-45].

In vitro reconstitutions were performed in passivated glass flow cells using the MRB80-based “TIRF buffer” [23]. Actin filaments were pre-polymerized and later stabilized with phalloidin. After surface attachment of the MT seeds, the final mix of all proteins in TIRF buffer, was flowed in. Experiments were carried out at 30°C with protein concentrations of 30 nM for Gas2L1 (or its truncations), 20 µM tubulin, 133 nM mCherry-EB3 and 10-1000 nM of pre-polymerized F-actin. Data was collected using a triple-colour TIRF microscope, equipped with a FRAP system and objective heater.

Acknowledgements

3

qPCR experiments were performed with the kind help of M. de Wit and support of Prof. Dr. R.J. Pasterkamp. We are grateful to Dr. F.K.C. Au and Prof. Dr. R.Z. Qi for sharing Gas2L1 constructs and thank M. Vinkenoog-Kuit for actin purification.

This work was supported by the European Research Council (Synergy grant 609822 to M.D. and A.A. and ERC-consolidator grant 617050 to C.C.H.), the Netherlands Organization for Scientific Research (NWO-ALW-VICI 865.10.010 to C.C.H.) and the Netherlands Organization for Health Research and Development (ZonMW-TOP 912.16.058 to C.C.H.).

Competing interests statement

The authors declare no competing interests.

Author contributions

DW and JJA performed, designed and analysed biochemical and imaging experiments in cells. CA performed, designed and analysed *in vitro* reconstitution experiments. DW and OIK performed qPCR experiments collaboratively. MD, GHK, CCH and AA supervised the research and coordinated the study. DW, CA and AA wrote the manuscript.

References

1. Schelski, M. and F. Bradke, Neuronal polarization: From spatiotemporal signaling to cytoskeletal dynamics. *Mol Cell Neurosci*, 2017. 84: p. 11-28.
2. Coles, C.H. and F. Bradke, Coordinating neuronal actin-microtubule dynamics. *Curr Biol*, 2015. 25(15): p. R677-91.
3. Lewis, T.L., Jr., J. Courchet, and F. Polleux, Cell biology in neuroscience: Cellular and molecular mechanisms underlying axon formation, growth, and branching. *J Cell Biol*, 2013. 202(6): p. 837-48.
4. Pacheco, A. and G. Gallo, Actin filament-microtubule interactions in axon initiation and branching. *Brain Res Bull*, 2016. 126(Pt 3): p. 300-310.
5. Kalil, K. and E.W. Dent, Branch management: mechanisms of axon branching in the developing vertebrate CNS. *Nat Rev Neurosci*, 2014. 15(1): p. 7-18.
6. Gibson, D.A. and L. Ma, Developmental regulation of axon branching in the vertebrate nervous system. *Development*, 2011. 138(2): p. 183-95.
7. Dogterom, M. and G.H. Koenderink, Actin-microtubule crosstalk in cell biology. *Nat Rev Mol Cell Biol*, 2018.
8. Alves-Silva, J., et al., Spectraplakins promote microtubule-mediated axonal growth by functioning as structural microtubule-associated proteins and EB1-dependent +TIPs (tip interacting proteins). *J Neurosci*, 2012. 32(27): p. 9143-58.
9. Roper, K., S.L. Gregory, and N.H. Brown, The 'spectraplakins': cytoskeletal giants with characteristics of both spectrin and plakin families. *J Cell Sci*, 2002. 115(Pt 22): p. 4215-25.
10. Suozzi, K.C., X. Wu, and E. Fuchs, Spectraplakins: master orchestrators of cytoskeletal dynamics. *J Cell Biol*, 2012. 197(4): p. 465-75.
11. Voelzmann, A., et al., Drosophila Short stop as a paradigm for the role and regulation of spectraplakins. *Semin Cell Dev Biol*, 2017. 69: p. 40-57.
12. Kuijpers, M., et al., Dynein Regulator NDEL1 Controls Polarized Cargo Transport at the Axon Initial Segment. *Neuron*, 2016. 89(3): p. 461-71.
13. Sanchez-Soriano, N., et al., Mouse ACF7 and drosophila short stop modulate filopodia formation and microtubule organisation during neuronal growth. *J Cell Sci*, 2009. 122(Pt 14): p. 2534-42.
14. Engel, U., et al., Abelson phosphorylation of CLASP2 modulates its association with microtubules and actin. *Cytoskeleton (Hoboken)*, 2014. 71(3): p. 195-209.
15. Zhou, F.Q., et al., NGF-induced axon growth is mediated by localized inactivation of GSK-3beta and functions of the microtubule plus end binding protein APC. *Neuron*, 2004. 42(6): p. 897-912.
16. Goriounov, D., C.L. Leung, and R.K. Liem, Protein products of human Gas2-related genes on chromosomes 17 and 22 (hGAR17 and hGAR22) associate with both microfilaments and microtubules. *J Cell Sci*, 2003. 116(Pt 6): p. 1045-58.
17. Jiang, K., et al., A Proteome-wide screen for mammalian SxIP motif-containing microtubule plus-end tracking proteins. *Curr Biol*, 2012. 22(19): p. 1800-7.
18. Stroud, M.J., et al., GAS2-like proteins mediate communication between microtubules and actin through interactions with end-binding proteins. *J Cell Sci*, 2014. 127(Pt 12): p. 2672-82.

-
- 19.** Girdler, G.C., et al., The Gas2 family protein Pigs is a microtubule +TIP that affects cytoskeleton organisation. *J Cell Sci*, 2016. 129(1): p. 121-34.
- 20.** Au, F.K., et al., GAS2L1 Is a Centriole-Associated Protein Required for Centrosome Dynamics and Disjunction. *Dev Cell*, 2017. 40(1): p. 81-94.
- 21.** Pines, M.K., et al., The cytolinker Pigs is a direct target and a negative regulator of Notch signalling. *Development*, 2010. 137(6): p. 913-22.
- 22.** van Beuningen, S.F.B., et al., TRIM46 Controls Neuronal Polarity and Axon Specification by Driving the Formation of Parallel Microtubule Arrays. *Neuron*, 2015. 88(6): p. 1208-1226.
- 23.** Preciado Lopez, M., et al., In vitro reconstitution of dynamic microtubules interacting with actin filament networks. *Methods Enzymol*, 2014. 540: p. 301-20.
- 24.** Preciado Lopez, M., et al., Actin-microtubule coordination at growing microtubule ends. *Nat Commun*, 2014. 5: p. 4778.
- 25.** Applewhite, D.A., et al., The actin-microtubule cross-linking activity of *Drosophila* Short stop is regulated by intramolecular inhibition. *Mol Biol Cell*, 2013. 24(18): p. 2885-93.
- 26.** Bradke, F. and C.G. Dotti, The role of local actin instability in axon formation. *Science*, 1999. 283(5409): p. 1931-4.
- 27.** Chia, J.X., N. Efimova, and T.M. Svitkina, Neurite outgrowth is driven by actin polymerization even in the presence of actin polymerization inhibitors. *Mol Biol Cell*, 2016.
- 28.** Dent, E.W. and K. Kalil, Axon branching requires interactions between dynamic microtubules and actin filaments. *J Neurosci*, 2001. 21(24): p. 9757-69.
- 29.** Flynn, K.C., et al., ADF/cofilin-mediated actin retrograde flow directs neurite formation in the developing brain. *Neuron*, 2012. 76(6): p. 1091-107.
- 30.** Gallo, G., H.F. Yee, and P.C. Letourneau, Actin turnover is required to prevent axon retraction driven by endogenous actomyosin contractility. 2002. 158(7): p. 1219-28.
- 31.** Lu, W., et al., Initial neurite outgrowth in *Drosophila* neurons is driven by kinesin-powered microtubule sliding. *Curr Biol*, 2013. 23(11): p. 1018-23.
- 32.** Gimona, M., et al., Functional plasticity of CH domains. *FEBS Lett*, 2002. 513(1): p. 98-106.
- 33.** Yarmola, E.G., et al., Actin-latrunculin A structure and function. Differential modulation of actin-binding protein function by latrunculin A. *J Biol Chem*, 2000. 275(36): p. 28120-7.
- 34.** Lee, S., et al., short stop is allelic to kakapo, and encodes rod-like cytoskeletal-associated proteins required for axon extension. *J Neurosci*, 2000. 20(3): p. 1096-108.
- 35.** Ka, M., et al., MACF1 regulates the migration of pyramidal neurons via microtubule dynamics and GSK-3 signaling. *Dev Biol*, 2014. 395(1): p. 4-18.
- 36.** Kodama, A., et al., ACF7: an essential integrator of microtubule dynamics. *Cell*, 2003. 115(3): p. 343-54.
- 37.** Lowery, L.A. and D. Van Vactor, The trip of the tip: understanding the growth cone machinery. *Nat Rev Mol Cell Biol*, 2009. 10(5): p. 332-43.
- 38.** Kapitein, L.C., K.W. Yau, and C.C. Hoogenraad, Microtubule dynamics in dendritic spines. *Methods Cell Biol*, 2010. 97: p. 111-32.
- 39.** Kahn, O.I., et al., APC2 controls dendrite development by promoting microtubule dynamics. *Nat Commun*, 2018. 9(1): p. 2773.
- 40.** Aher, A., et al., CLASP Suppresses Microtubule Catastrophes through a Single TOG Domain. *Dev Cell*, 2018. 46(1): p. 40-58.e8.
- 41.** Gentry, B.S., et al., Multiple actin binding domains of Ena/VASP proteins determine actin network stiffening. *Eur Biophys J*, 2012. 41(11): p. 979-90.

- 42.** Pardee, J.D. and J.A. Spudich, Mechanism of K⁺-induced actin assembly. *J Cell Biol*, 1982. 93(3): p. 648-54.
- 43.** Honnappa, S., et al., An EB1-binding motif acts as a microtubule tip localization signal. *Cell*, 2009. 138(2): p. 366-76.
- 44.** Komarova, Y., et al., Mammalian end binding proteins control persistent microtubule growth. *J Cell Biol*, 2009. 184(5): p. 691-706.
- 45.** Montenegro Gouveia, S., et al., In vitro reconstitution of the functional interplay between MCAK and EB3 at microtubule plus ends. *Curr Biol*, 2010. 20(19): p. 1717-22.

> Figure S1 - Experimental details of neuronal phenotype validation.

(A, B) Representative melt curves of various samples amplified with Gas2L1 primers (A) and amplification curves of GAPDH or Gas2L1 cDNA amplified in control and shRNA samples (B) from qPCR experiments shown in Fig. 1A. cDNA samples of control (empty shRNA vector, in duplo) and Gas2L1-shRNA-expressing neurons (G2L1 shRNA, in duplo) show one peak in the melt curve (A), demonstrating specific amplification of Gas2L1 cDNA; negative water control (MQ instead of cDNA template) shows no amplification with Gas2L1-specific primers; negative RNA control (RNA instead of cDNA as template) reveals minor unspecific product that is not amplified and therefore not interfering in the presence of cDNA.

(C) Fine details of axon morphology of a DIV3 neuron overexpressing HA-Gas2L1 as described in Fig. 1B. Boxed regions (1 and 2) are enlarged below. Red asterisk indicates the soma.

(D) Example of axon tracings for morphology analysis, using the DIV3 neuron expressing scrambled shRNA as shown in Fig. 1B as a template. Boxed region is enlarged to the right. Blue tracing denotes the primary axon; the longest possible uninterrupted tracing from the soma to the tip of an axon branch. Red tracings denote non-primary branches and black circle marks the position of the soma.

(E-G) Rescue experiments showing the total axon length (E), primary axon length (F) and average axon branch length (G) in neurons co-expressing scrambled or Gas2L1 shRNA with GFP, or Gas2L1 shRNA with GFP-Gas2L1, and HA- β -galactosidase from DIV0 to DIV3. Data belongs to the experiment shown in Fig. 1G and H. n=34-43 neurons per condition from 2 independent experiments.

Data information:

Scale bars: 25 μ m in (C), 30 μ m in (D).

Data is displayed as means \pm SEM. Mann-Whitney test, ns: not significant, ***p<0.001.

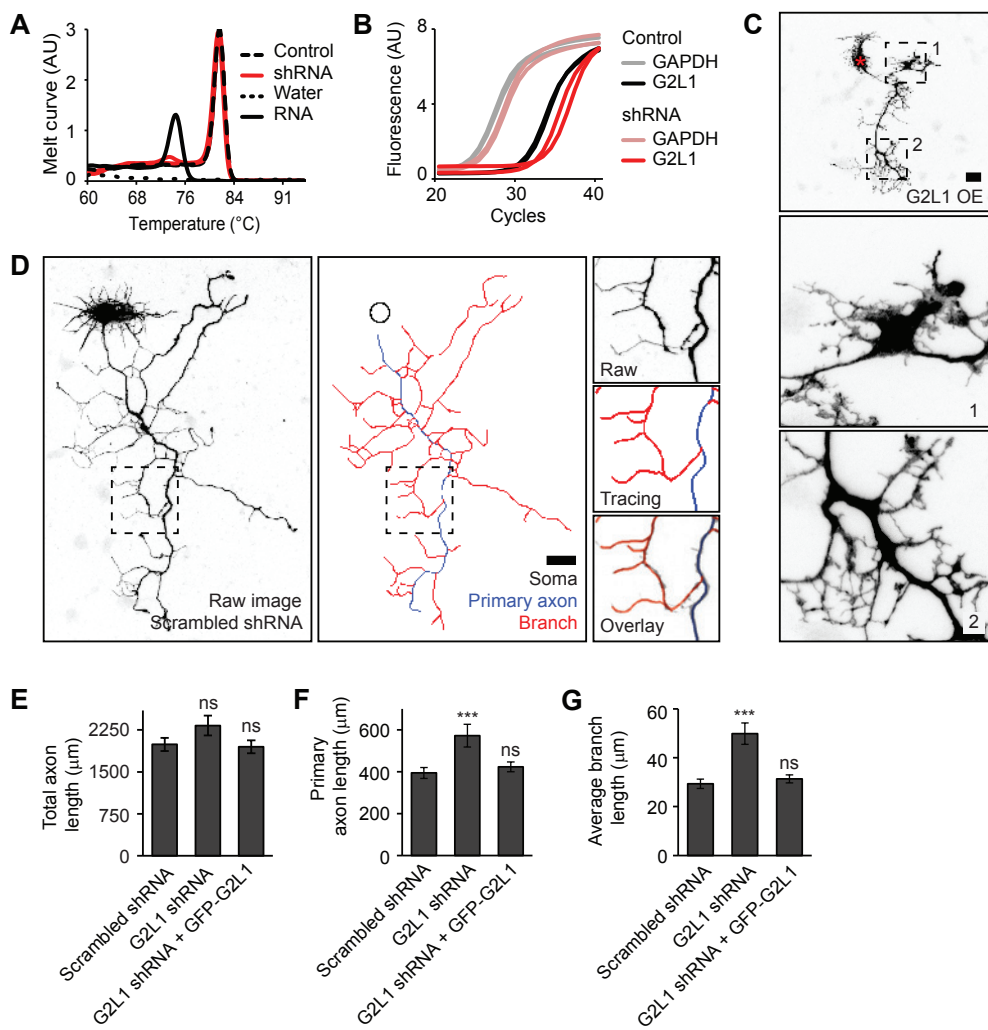


> **Figure S2 - *In vitro* reconstitution assays showing the influence of EB3 on the interaction of Gas2L1 with MTs and the relation between Gas2L1 and actin.**

(A) Coomassie-stained SDS-PAGE gels showing the purity of the purified Gas2L1 (G2L1) fusions used for *in vitro* reconstitutions. For GFP-CH, the additional band at 40 kDa was identified as co-purified actin by Western blotting.

(B) Intensity ratios of GFP signal over actin signal from Fig. 2C (orange) and 2D (green). “Empty” (dark red) is from the channel with only F-actin and no GFP-protein present. This analysis reveals that there is no GFP-Gas2L1 (orange) accumulated on F-actin, since it has nearly the same intensity ratio as the empty channel (dark red). We do observe GFP-CH (green) binding to F-actin. TIRF images were captured on the same day using identical microscope settings.

(C, D) Kymographs of Gas2L1 (C) and Tail (D) from an *in vitro* reconstitution assay with MTs and EB3. Only the Tail fragment behaves as a plus-end tracking protein.

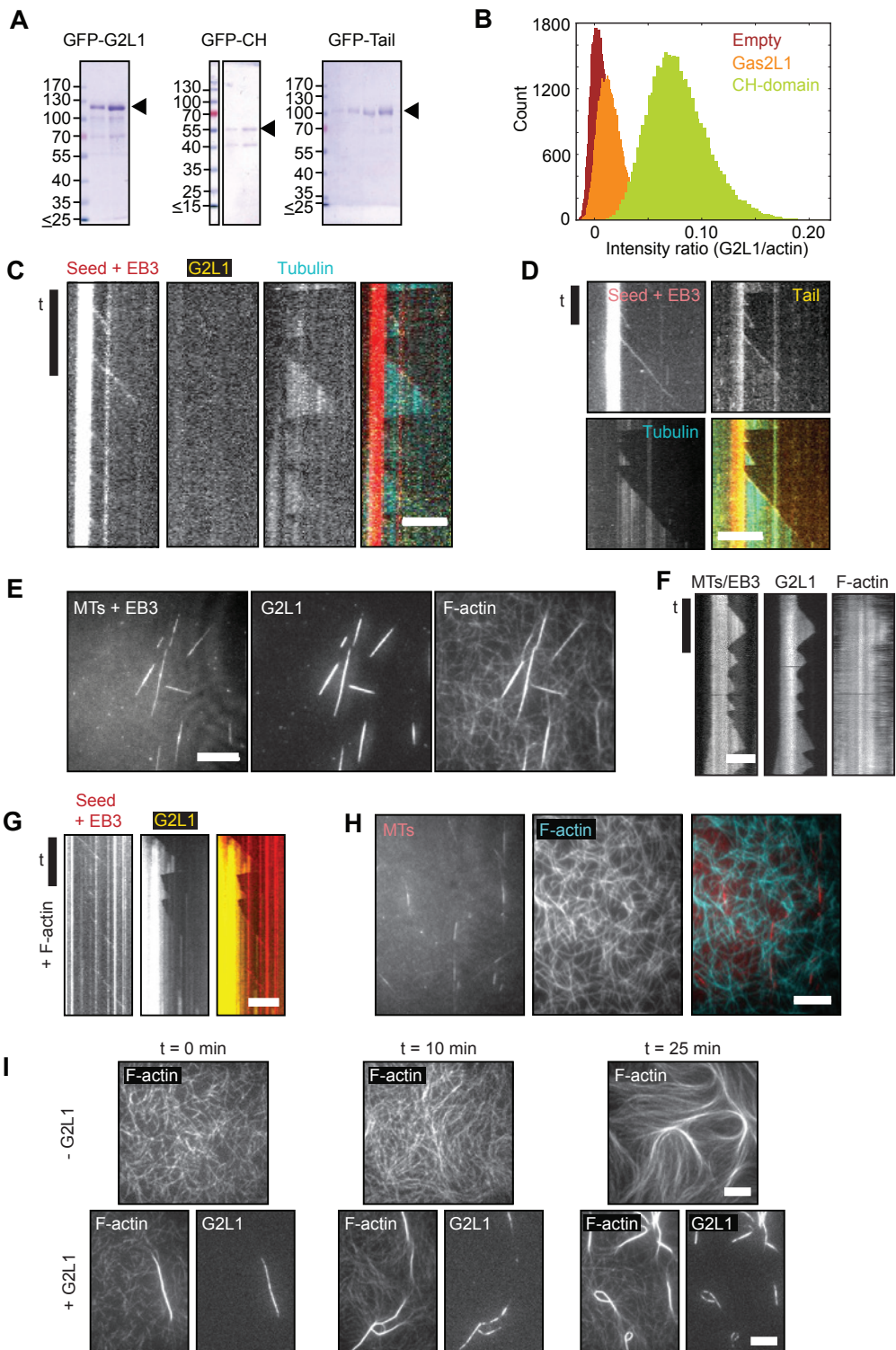
(E-G) TIRF images (E) and kymographs (F, G) showing specific Gas2L1 localization to MT-actin overlaps and absence of plus-end tracking in an *in vitro* reconstitution with Gas2L1, F-actin (1 μ M), MTs and EB3. These data indicate that EB3 does not influence the localization of Gas2L1 in this system, even when EB3 tracks growing MT plus ends (G).

(H) Control *in vitro* reconstitution experiment showing no alignment of F-actin (1 μ M) to MTs in the absence of Gas2L1.

(I) *In vitro* reconstitution experiments with F-actin (1 μ M) without Gas2L1 (top) or with Gas2L1 added (bottom) observed at different time intervals after mixing. Gas2L1 enhances actin bundling and localizes to these bundles. No actin bundles appear at 10 min after flushing in the F-actin mix in the absence of Gas2L1 (top, middle panel), while a few Gas2L1-decorated bundles can be observed right after flushing in the mix in the presence of Gas2L1 (left, bottom panels). Over time, the number of bundles increases, as a result of the densification of actin filaments due to the presence of methyl cellulose.

Data information:

Scale bars: 10 μ m except for (G). For (G), horizontal scale bar 5 μ m. All vertical (time) scale bar: 3 min, except for (H). For (H), vertical scale bar 5 min.



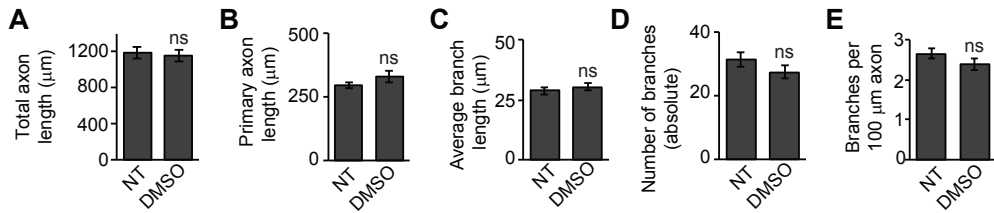


Figure S5 - DMSO does not affect axon morphology.

(A-E) Effect of DMSO (equivalent to DMSO concentration in 100 nM Latrunculin B condition shown in Fig. 4F-J) on axon morphology of DIV3 neurons, transfected at DIV1 and treated with DMSO (1:100) for 48 hours. NT=non-treated; n=20-25 neurons per condition from 2 independent experiments.

Data information:

Data is displayed as means \pm SEM. Mann-Whitney test, ns: not significant.

3

> Figure S6 - The MT-binding tail fragment does not influence localization of a different actin-binding domain.

(A) Endogenous EB1 localization upon overexpression of GFP-Gas2L1-SxAA (G2L1-SxAA) in a DIV3 neuron. Boxes indicate zoomed region of transfected neuron.

(B) Schematic overview of α -actinin mutants.

(C) Additional conditions included in the experiment shown in Fig. 6E: DIV3 neurons expressing GFP-ABD or GFP-ABD-Tail and treated with 10 μ M Latrunculin B for 30 minutes or non-treated, stained for F-actin (phalloidin) and the axon initial segment (TRIM46).

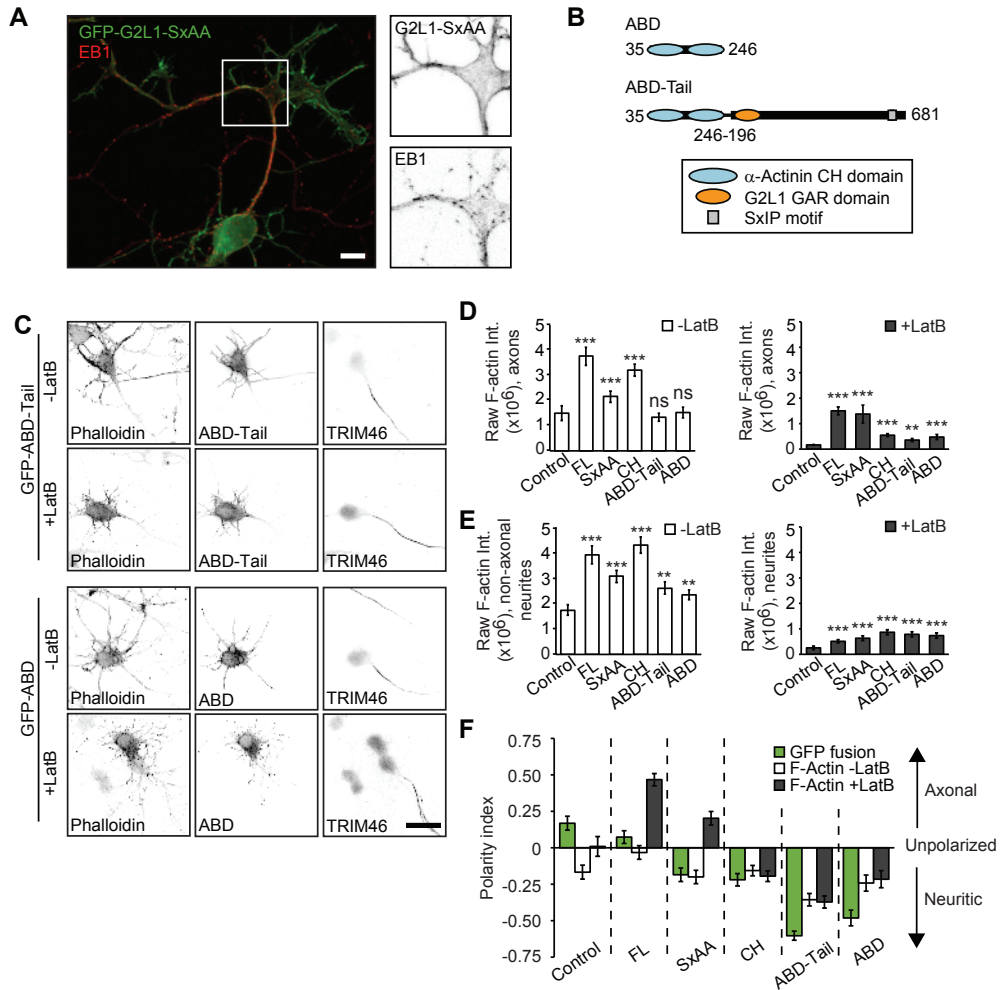
(D, E) Additional conditions included in the experiment shown partially in Fig. 6F and G: Raw phalloidin staining intensities in axons (D) and non-axonal neurites (pre-dendrites) (E) of DIV3 neurons expressing the indicated GFP fusions and treated with 10 μ M Latrunculin B for 30 minutes (grey bars) or non-treated (white bars). n=27-40 cells per condition from 2 independent experiments.

(F) Additional conditions included in the experiment shown partially in Fig. 6H: Polarity index representing localization of the indicated GFP fusions in non-treated neurons (green bars), and localization of F-actin as labelled by phalloidin in DIV3 neurons treated with 10 μ M Latrunculin B for 30 minutes (grey bars) or non-treated (white bars). n=27-40 cells per condition from 2 independent experiments. Positive values indicate axonal enrichment, negative values indicate neuritic enrichment and a value of 0 signifies no particular enrichment.

Data information:

Scale bars: 10 μ m in (A), 30 μ m in (C).

Data is displayed as means \pm SEM. Mann-Whitney test, ns: not significant, ** $p < 0.01$, *** $p < 0.001$.



Supplementary movie 1.

Timelapse showing the dynamics of a Gas2L1 (G2L1)-F-actin-MT bundle, as shown in Figures 2I-K. The MT shows dynamic instability, and Gas2L1 localizes specifically to the MT/actin overlaps. As soon as the MT undergoes a catastrophe, Gas2L1 disappears and the actin filaments that initially co-aligned with the MT disperse. When the MT regrows, Gas2L1 reappears and actin filaments again co-align with the MT. Actin concentration is 1 μ M.

Data information:

20 frames per second, 20 min timelapse. Scale bar: 2.5 μ m.

Supplementary movie 1 can be accessed via the following QR code:



Supplementary materials & methods

Animals, primary neuron cultures, electroporation and transfection

Animal experiments were approved by the Dutch Animal Experiments Committee (DEC) and conducted in agreement with guidelines of Utrecht University, Dutch law (Wet op de Dierproeven, 1996) and European regulations (Guideline 86/609/EEC). Neuron cultures were derived from hippocampi of E18.5 mixed-sex pups from pregnant Wistar rats (Janvier). Adult rats were at least ten weeks of age, not involved in previous experiments, provided with unrestricted access to food and water and kept with a companion, wood-chip bedding and paper tissue for cage enrichment. Animals were housed in an environment with a 12 hour light-dark cycle and a temperature of $22 \pm 1^\circ\text{C}$.

Primary hippocampal dissociated neuron cultures were prepared according to protocols for mechanical/enzymatic dissociation described previously [1]. Neurons were maintained at 37°C and 5% CO_2 .

In case of electroporation for imaging experiments, 200k neurons per condition were taken from the cell suspension directly after mechanical dissociation, spun down for 5 minutes at 200g and resuspended in home-made electroporation buffer (12.5 mM NaCl, 123 mM KCl, 20 mM KOH, 10 mM EGTA, 4.5 mM MgCl_2 , 20 mM PIPES, pH 7.2). Neurons in electroporation buffer were then mixed with 4 μg DNA per condition, transferred to cuvettes (Bio-Rad GenePulser, 0.2 cm gap) and electroporated using program O-003/'Rat hippocampal neurons' of a Lonza Nucleofector 2b machine. Electroporated neurons were plated in full medium (Neurobasal medium (Gibco) supplemented with 2% B27 (Gibco), 0.5 mM glutamine (Gibco), 15.6 μM glutamate (Sigma-Aldrich) and 1% penicillin-streptomycin (Gibco)) on 18 mm coverslips coated with poly-L-lysine (37.5 $\mu\text{g}/\text{ml}$, Sigma) and laminin (1.25 $\mu\text{g}/\text{ml}$, Roche). The procedure for electroporation for qPCR experiments was described previously [2].

For transfection, 100k neurons per well of a 12-well plate were directly plated in full medium onto 18 mm coverslips coated as described above, and transfected at the indicated times using Lipofectamine 2000 (Invitrogen). For one well of a 12-well plate, 1.8 μg DNA was mixed with 3.3 μl Lipofectamine in 200 μl Neurobasal medium and incubated for 30 minutes at room temperature. Meanwhile, conditioned full medium of neurons was transferred to a new plate, and transfection medium (neurobasal medium supplemented with 0.5 mM glutamine) was added. The DNA/lipofectamine mix was added to the neurons in transfection medium and incubated for 45 minutes at 37°C and 5% CO_2 . After transfection, neurons were rinsed by dipping coverslips in pre-warmed neurobasal medium and placed back into conditioned full medium.

DNA and shRNA constructs

The following DNA constructs were used in this study and described before: p β -actin-HA- β -Galactosidase [3], pCl-neo-BirA [4], EB3-tagRFP-T [5], and paGFP- α -Tubulin [6].

All Gas2L1 expression constructs were N-terminal fusions generated from PCR-based

strategies using GFP-Gas2L1 or GFP-Gas2L1-SxAA as templates, which were based on human Gas2L1 (GenBank Accession No NM_152236.1) and kindly provided by Dr. F.K.C. Au and Prof. Dr. R.Z. Qi (Hong Kong University of Science and Technology) [7]. The following backbones were used to create Gas2L1 plasmids: GW1-GFP/HA for neuronal expression, bioGFP and GW1-HA for pull-down experiments, and StrepII-EGFP for protein purification [8]. To create GW1-GFP/HA-ABD and GW1-GFP/HA-ABD-Tail, α -actinin CH domains were amplified from *Gallus gallus* cDNA (amino acids 35-246, NCBI ref. NM_204127.1) using a standard PCR based strategy. To obtain ABD-Tail, amino acids 35-246 of *Gallus gallus* α -actinin were fused to amino acids 196-681 of human Gas2L1 (NCBI ref. NM_152236.1) by overlap extension PCR. GW2-LifeAct-EGFP was obtained from Dr. M. Adrian and Dr. P. Schätzle (Utrecht University) and based on the LifeAct peptide sequence MGVDLIKKFESISKEE(5'-ATGGGTGTCGCAGATTTGATCAAGAAATTCGAAAGCATCTCAAAGGAAGAA), which was flanked by EGFP inserted into BamHI/XbaI sites of a GW2 backbone.

For shRNA-mediated depletion, shRNA sequences were inserted into HindIII and BglII sites of the pSuper backbone [9]. The following targeting sequences were used: scrambled - GCGCGCTTTGTAGGATTCG; Gas2L1 shRNA (rat) - CGCCCAATGACATTCGAAA. For use in qPCR experiments, we excised the puromycin resistance region from pSuper.puro and transplanted it into EcoRI/BamHI sites of pSuper-Gas2L1-shRNA.

Antibodies and reagents

The following antibodies, staining reagents and dilutions were used for immunofluorescence experiments: chicken-anti- β -galactosidase (1:2500, Aves Labs #BGL-1040); rabbit-anti-TRIM46 serum (1:500, described in [10]); mouse-anti- α -tubulin (1:1000, Sigma #T-5168, clone #B-5-1-2); mouse-anti-EB1 (1:100, BD Biosciences #610535); Alexa Fluor 594 Phalloidin (1:50, Thermo Fischer Scientific #A12381); goat-anti-chicken Alexa 488 (1:400, Thermo Fischer Scientific #A11039); goat-anti-rabbit Alexa 405 (1:400, Thermo Fischer Scientific #A31556); goat-anti-mouse Alexa 405 (1:400, Thermo Fischer Scientific #A31553), goat-anti-mouse Alexa 568 (1:400, Thermo Fischer Scientific #A11031).

The following antibodies, staining reagents and dilutions were used for Western blotting: rabbit-anti-GFP (1:10,000, Abcam #ab290); mouse-anti-HA (1:2000, Biolegend/Covance #mms-101p, clone #16B12); mouse-anti-actin (1:10,000, Chemicon #MAB1501R, clone #C4); goat-anti-mouse IRDye800CW (1:15,000, LI-COR #926-32210); goat-anti-rabbit IRDye680LT (1:20,000, LI-COR #926-68021).

The following reagents were used for drug treatments: DMSO (Sigma), Latrunculin B (Santa Cruz Biotechnology #SC-203318) and Jasplakinolide (Tocris/Biotechne #2792).

Immunofluorescence microscopy

For co-stainings with mouse-anti-EB1, neurons were fixed for 5 minutes at -20°C in 100% methanol supplemented with 1 mM EGTA, immediately followed by 5 minutes fixation room temperature in 4% paraformaldehyde/4% sucrose. In all other cases, neurons were fixed for 10 minutes at room temperature in 4% paraformaldehyde/4% sucrose.

After fixation, neurons were washed 2x in PBS. Primary antibodies were diluted in GDB buffer (0.1% BSA, 0.45M NaCl, 0.3% Triton X-100, 16.7mM phosphate buffer, pH 7.4) and incubated overnight at 4°C, followed by 3x 5 minutes washing in PSB and 1-2 hour incubation with secondary antibodies in GDB buffer at room temperature. Samples were mounted in Vectashield mounting medium (Vectorlabs).

Images of fixed cells were collected using 1) a Nikon Eclipse 80i upright widefield fluorescence microscope, equipped with a Photometrics CoolSNAP HQ2 CCD camera and Nikon NIS Br software, using one of the following oil objectives: Plan Apo VC 60x N.A. 1.40, Plan Fluor 40x N.A. 1.30 or Plan Fluor 20x N.A. 0.75; or 2) using a Carl Zeiss LSM 700 confocal laser scanning microscope running ZEN2011 software and using a Plan-Apochromat 63x/1.40 Oil DIC objective. For quantitative comparisons between conditions, imaging settings were kept identical for all acquired images.

Live cell imaging and photoactivation

Live cell imaging and photoactivation experiments were performed on an inverted Nikon Eclipse Ti-E confocal microscope equipped with a perfect focus system (Nikon), a CSU-X1-A1 Spinning Disc unit (Yokogawa), and a Photometrics Evolve 512 EMCCD camera (Roper Scientific) while using a Plan Apo VC 100x N.A.1.40 oil objective. Neurons were kept at 37°C and 5% CO₂ in a stage incubator (Tokai Hit) during imaging. Movies used to determine MT growth velocity were acquired at a framerate of 1 frame per second, and acquisitions lasted 3 minutes per movie.

For photoactivation experiments, we made use of an ILas FRAP unit (Roper Scientific) and a Vortran Stradus 405 nm (100 mW) laser. The photoactivation procedure of paGFP- α -Tubulin was previously described [6]. We co-transfected neurons with GW2-mRFP to label transfected neurons, and identified axons based on morphology. We placed the soma just outside the field of view, which spanned 34 μ m in total, and photoactivated axon regions of approximately 6-7 μ m wide in the center of the image. To prevent excessive photobleaching, frames were acquired at intervals varying between 6 and 15 minutes.

qPCR

qPCR experiments were performed with the kind help of M. de Wit and prof. dr. R.J. Pasterkamp (UMC Utrecht). Experimental procedures are detailed in [2]. To summarize, neurons were electroporated at DIV0 with empty pSuper-puro or pSuper-Gas2L1 shRNA-puro, and subjected to selection with 0.5 mg/ml puromycin for 48 hours prior to RNA isolation. We performed PCR reactions with the Fast Start DNA Master PLUS SYBR green I kit (Roche) and calculated Gas2L1 mRNA levels relative to those of GAPDH and β -actin using the $\Delta\Delta$ Ct method.

The following primer pairs were used: GAPDH 5'-TGCCCCATGTTTGTGATG and 3'-TGTGGTCATGAGCCCTTCC; β -actin 5'- AGGCCAACCGTGAAAAGATG and 3'-CCAGAGGCATACAGGGACAAC; Gas2L1 5'-ACATTCGAAACCTGGACGAG and 3'-TCAGCACCTCACAAAGATG.

Pull-down experiments and Western blotting

HEK293 cells were cultured in 50/50 DMEM/Ham's F10 medium (DMEM: Lonza or Biowest; Ham's F10: Lonza) supplemented with 10% FCS (Sigma) and 1% penicillin-streptomycin (Sigma), and routinely tested for mycoplasma.

HEK293 cells were co-transfected with pCI-Neo-BirA, bioGFP-tagged constructs and HA-tagged constructs using MaxPEI (Polysciences) in a ratio of 3:1 PEI:DNA. After 24-48h expression, cells were washed with ice-cold PBS supplemented with 0.5x protease inhibitor cocktail (Roche) and 5 mM MgCl₂. Next, cells were lysed in pull-down lysis buffer for 30 minutes on ice (50mM Tris-HCl pH 7.5, 233 mM NaCl, 0.5% Triton X-100, 5mM MgCl₂, protease inhibitors (Roche)). Lysates were then pre-cleared by centrifugation (15 minutes at 13.2 krpm, 4°C) and supernatants were incubated with pre-blocked magnetic bioGFP beads (Invitrogen Dynabeads M-280 Streptavidin; blocking by incubation with 20 mM Tris-HCl pH 7.5, 150mM KCl, 0.2µg/µl chicken egg albumin for 1 hour at 4°C) for 1.5-2 hours at 4°C. Lastly, beads were generously washed 5x in wash buffer (20mM Tris-HCl pH 7.5, 150mM KCl, 0.1% Triton X-100) and eluted by boiling 10 minutes at 95°C in 2x DTT+ sample buffer (20% glycerol, 4% SDS, 200 mM DTT, 100 mM TRIS-HCl pH 6.8, bromophenol blue).

For pull-down experiments in the presence of Latrunculin B, 10 µM Latrunculin B was added to HEK293 cells 30 minutes prior to lysis. Lysis buffers used during the experiment were additionally supplemented with 10 µM Latrunculin B.

Samples ran on 12-14% SDS PAGE gels and were transferred onto nitrocellulose membranes by semi-dry blotting at 16V for one hour. Membranes were blocked in 2% bovine serum albumin (BSA)/0.02% Tween20/PBS for 1 hour at room temperature, followed by overnight incubation with primary antibodies in 2%BSA/0.02% Tween20/PBS, 3x 5 minute washes with 0.02% Tween20/PBS and one hour of incubation with secondary antibody in 2%BSA/0.02% Tween20/PBS, followed by another 3 washing steps.

Membranes were scanned on an Odyssey Infrared Imaging system (LI-COR Biosciences) and, if required, re-incubated to detect and discriminate multiple signals on the same membrane.

Gas2L1 protein purification

Gas2L1 fusions were purified from HEK293 cells using Strep(II)-streptactin affinity purification. We expressed tandem StrepII-tagged GFP-Gas2L1 fusions for 24-48h in HEK293 cells cultured and transfected as described for pull-down experiments.

Prior to lysis, cells were washed once in ice-cold PBS supplemented with 0.5x protease inhibitors. Cells were lysed for 15 minutes on ice in purification lysis buffer (50 mM HEPES pH 7.4, 300 mM NaCl, 0.5% Triton X-100, 1x protease inhibitors), followed by centrifugation for 20 minutes at 13.2 krpm/4°C. Supernatants were incubated for 45 minutes in the presence of pre-washed StrepTactin Sepharose High Performance beads (GE Healthcare) at 4°C. Following incubation, beads were washed three times in ice-cold wash buffer (50 mM HEPES pH 7.4, 300 mM NaCl, 0.5 % Triton X-100). StrepII-GFP-Gas2L1 was then eluted in standard elution buffer (50 mM HEPES pH 7.4, 150 mM NaCl, 1 mM MgCl₂, 1 mM EGTA, 0.05 % Triton X-100, 1 mM DTT, 2.5

mM d-Desthiobiotin) by incubating beads with elution buffer for ten minutes on ice. To prevent aggregation, the elution buffer used to purify Gas2L1 truncation mutants was supplemented with 50 mM arginine, 50 mM glutamic acid and 10% glycerol. After incubation with elution buffers, supernatants were collected by centrifuging for 1 minute at 3000 rpm/4°C, and cleared a second time by centrifuging for 1 minute at 13.2k rpm/4°C. The remaining supernatant was aliquoted in single-use vials, snap frozen in liquid nitrogen and stored at -80°C.

The concentration and purity of purified Gas2L1 fusions was determined by Coomassie blue staining of SDS-PAGE gels. Set amounts of purified Gas2L1 ran alongside a range of standardized BSA concentrations (100 ng - 2000 ng). The resulting Gas2L1 band intensities were compared to the BSA concentration curve, and used to calculate the amount of protein in ng/ μ L from which molarity could be determined.

***In vitro* reconstitution assays**

Protein production and purification

Gas2L1 was purified as described above. Lyophilized porcine brain tubulins were obtained from Cytoskeleton (Denver, CO, USA), resuspended at 50-100 μ M in MRB80, snap-frozen and stored at -80°C until use. G-actin was purified from rabbit skeletal muscle acetone powder [11, 12] and stored at -80°C in G-buffer [13]. Before use, G-actin was thawed overnight at 4°C and spun for 15min at 149.000 x g to remove any aggregates, and stored at 4°C for no longer than 2 weeks. Alexa Fluor 647 (Molecular Probes, Life Technologies, Carlsbad, CA, USA) was used to produce labelled G-actin [11]. 6xHis-tagged recombinant human mCherry-EB3 was expressed and purified as described before [14-16].

Preparation of flow cells for in vitro assays

Glass coverslips and slides (Menzel-Gläsner, Braunschweig, Germany) were cleaned in basepiranha and stored at RT in milliQ for no longer than 5 days. Flow cell channels (10-15 μ L) were assembled by cutting parafilm in thin pieces, which were sandwiched between clean glass slides and coverslips [13]. Biotinylated glass surfaces were obtained by sequentially incubating the flow cell channels with the following solutions: 0.1 mg/ml PLL-PEG-Biotin (PLL(20)-g[3.5]-PEG(2)/PEG(3.4)-Biotin(20%), SuSos AG, Dübendorf, Switzerland) for 30-60min, 0.25 mg/ml streptavidin (Thermo Scientific Pierce Protein Biology Products, Rockford, IL, USA) for 10 min, 0.5 mg/ml κ -casein for 10min and 1% (w/v) Pluronic F-127 for 10min, all diluted in MRB80, with 40-70 μ L rinses with MRB80 in between steps.

TIRF assays

Stabilized microtubule seeds were prepared using the slowly hydrolysable GTP analogue guanylyl-(α,β)-methylene-diphosphonate (GMPCPP, Jena Biosciences, Jena, Germany), following the double-cycling as described in [13] and using 12% labelled tubulin, 18% biotinylated tubulin, and 70% unlabelled tubulin. Phalloidin-stabilized F-actin was first polymerized at 7.5 μ M G-actin

concentration (15% labelled and 85% unlabelled G-actin) in MRB80 (with 50 mM KCl, 0.2 mM Mg-ATP, 4 mM DTT) for 30-90 minutes at room temperature, before adding phalloidin in 1:1 molar ratio. Dynamic microtubules were nucleated from GMPCPP-stabilized microtubule seeds bound to the biotinylated surface of the glass flow cells. Any non-attached seeds were always rinsed with MRB80 before the actin filaments and/or the microtubule polymerization mix was added. Once the flow cell channel was prepared with microtubule seeds, the microtubule polymerization mix, including actin filaments, was added. The core reaction mix is MRB80 buffer based (pH 6.8 with KOH, 80 mM Pipes, 4 mM MgCl₂, 1 mM EGTA) and supplemented with 0.5 mg/ml κ-casein, 0.2% (v/v) methyl cellulose, 75 mM KCl, 1 mM GTP, 0.2 mM Mg-ATP and an oxygen scavenging system (4 mM dithiothreitol (DTT), 2 mM protocatechuic acid (PCA), and 100 nM protocatechuate-3,4-dioxygenase (PCD)).

The tubulin concentration was kept at 20 μM (6% labelled and 94% unlabelled tubulin), and the pre-polymerized F-actin (15% labelled and 85% unlabelled G-actin) was diluted to a final concentration of 10 nM – 1 μM. After mixing (before the addition of the F-actin), the final mixture was clarified at 149.000 x g for 5min and immediately added to the flow cell channel, which was finally sealed with vacuum grease to avoid solvent evaporation while imaging.

TIRF microscope (laser, power, timelapses, temperature)

Triple-colour TIRF microscopy experiments were performed on a Nikon Eclipse Ti-E inverted microscope (Nikon Corporation, Tokyo, Japan) equipped with an Apo TIRF 100 x 1.49 N.A. oil objective, a motorized stage, Perfect Focus System, a motorized TIRF illuminator (Roper Scientific, Tucson, AZ, USA) and a QuantEM:512SC EMCCD camera (Photometrics, Roper Scientific). For excitation, we used a 561 nm (50 mW) Jive (Cobolt, Solna, Sweden), a 488 nm (40mW) Calypso (Cobolt) diode-pumped solid-state laser, and a 635 nm (28 mW) Melles Griot laser (CVI Laser Optics & Melles Griot, Didam, Netherlands). Most of the imaging of dynamic microtubules was performed at 3s per frame with 50-100 ms exposure time at 8-18% laser power. The sample temperature was kept fixed with the use of a home-built objective heater/cooler to 30 ± 1°C.

Data analysis and image processing for biochemical assays and cell imaging experiments

All images were processed with ImageJ software and plugins described below. For display purposes, images shown in this publication had their dynamic ranges adjusted when necessary. Quantitative analyses were performed on raw data collected using the same microscope with identical settings throughout experiments.

For axon morphology analyses, β-galactosidase co-overexpression and staining was used to identify transfected neurons and to visualize morphology. We acquired composite images of the total axon by manually piecing together multiple acquisitions of the same neuron. TRIM46 staining was included to identify axons, which were traced and analysed using the NeuronJ plugin for ImageJ by Dr. E. Meijering [17]. We excluded neurons with multiple axons and neurons without TRIM46-positive neurites from our analyses. To avoid selection bias, neurons that satisfied these requirements were included on a first-come-first-served basis during image

acquisition. The number of independent experiments stated in figure legends reflects the number of experiments performed on independent neuron cultures, ie cultures derived from pups from a different mother animal. We would like to note that, as is expected of primary cultures, there was some morphological heterogeneity between individual neurons and also between neuron cultures.

To quantify MT growth velocity in growth cones, we co-transfected neurons with shRNA, EB3-tagRFPt and a GFP fill. Axons were identified on the basis of morphology, and growth cones could be located by observing the GFP signal. Kymographs were drawn along the shafts and growth cones, using a line thickness sufficient to cover the majority of EB traces as seen on a maximum intensity projection, and generated using the KymoResliceWide plugin for ImageJ by dr. E. Katrukha (Utrecht University, available on GitHub). The resulting kymographs were manually traced, and growth velocities obtained from individual traces were first used to calculate average velocity per neuron/kymograph before using the resulting values to calculate the average growth velocity in each condition.

For polarity index calculations, neurons were transfected with different GFP-Gas2L1 fusion constructs. TRIM46 staining was used to identify the axon initial segment and Phalloidin staining was used to visualize F-actin. Images were acquired with identical microscope settings for all coverslips within one experiment. Using ImageJ, a line of 3.18 μm width with a length of 12-32 μm was drawn in the axon initial segment. The same ROI was positioned in the nearest area where no cell was present to obtain background intensity, which was subtracted from the raw measurements. Intensities were measured at identical positions in both the green (GFP-Gas2L1 fusions) and red channels (Phalloidin). The same was done for two dendrites of the same neuron. Polarity indexes were then calculated using the formula $(I_a - I_d)/(I_a + I_d)$, in which I_a is the intensity in the axon and I_d is the average intensity of two dendrites.

Data analysis for *in vitro* assays

For the *in vitro* reconstitution assays, all image processing was performed in FIJI, including the construction of kymographs [18]. Kymographs were constructed using the plugin in ImageJ. For the intensity ratios, we used a custom-written program in Python. Briefly, we selected a region-of-interest and measured the intensity distributions of both the GFP-signal and the actin signal. The intensity ratios were calculated using the formula $(I_{\text{GFP}} - I_{\text{Camera noise}})/\langle I_{\text{actin}} \rangle$, where $I_{\text{Camera noise}}$ is the peak GFP-intensity measured in an empty channel, and $\langle I_{\text{actin}} \rangle$ is the mean actin intensity of the selected region.

Statistics

Statistical analysis was performed in GraphPad 5. Datasets were first tested for normality using Shapiro-Wilk tests. Datasets that did not satisfy the normality assumption were compared using Mann-Whitney U test, and datasets that did were compared using unpaired t-tests. Tests were two-tailed. Statistical tests used for each experiment are detailed in the figure legends.

1. Kapitein, L.C., K.W. Yau, and C.C. Hoogenraad, Microtubule dynamics in dendritic spines. *Methods Cell Biol*, 2010. 97: p. 111-32.
2. Kahn, O.I., et al., APC2 controls dendrite development by promoting microtubule dynamics. *Nat Commun*, 2018. 9(1): p. 2773.
3. Hoogenraad, C.C., et al., GRIP1 controls dendrite morphogenesis by regulating EphB receptor trafficking. *Nat Neurosci*, 2005. 8(7): p. 906-15.
4. Lansbergen, G., et al., CLASPs attach microtubule plus ends to the cell cortex through a complex with LL5beta. *Dev Cell*, 2006. 11(1): p. 21-32.
5. van der Vaart, B., et al., CFEOM1-associated kinesin KIF21A is a cortical microtubule growth inhibitor. *Dev Cell*, 2013. 27(2): p. 145-160.
6. Kuijpers, M., et al., Dynein Regulator NDEL1 Controls Polarized Cargo Transport at the Axon Initial Segment. *Neuron*, 2016. 89(3): p. 461-71.
7. Au, F.K., et al., GAS2L1 Is a Centriole-Associated Protein Required for Centrosome Dynamics and Disjunction. *Dev Cell*, 2017. 40(1): p. 81-94.
8. Aher, A., et al., CLASP Suppresses Microtubule Catastrophes through a Single TOG Domain. *Dev Cell*, 2018. 46(1): p. 40-58.e8.
9. Brummelkamp, T.R., R. Bernards, and R. Agami, A system for stable expression of short interfering RNAs in mammalian cells. *Science*, 2002. 296(5567): p. 550-3.
10. van Beuningen, S.F.B., et al., TRIM46 Controls Neuronal Polarity and Axon Specification by Driving the Formation of Parallel Microtubule Arrays. *Neuron*, 2015. 88(6): p. 1208-1226.
11. Gentry, B.S., et al., Multiple actin binding domains of Ena/VASP proteins determine actin network stiffening. *Eur Biophys J*, 2012. 41(11): p. 979-90.
12. Pardee, J.D. and J.A. Spudich, Mechanism of K+-induced actin assembly. *J Cell Biol*, 1982. 93(3): p. 648-54.
13. Preciado Lopez, M., et al., In vitro reconstitution of dynamic microtubules interacting with actin filament networks. *Methods Enzymol*, 2014. 540: p. 301-20.
14. Honnappa, S., et al., An EB1-binding motif acts as a microtubule tip localization signal. *Cell*, 2009. 138(2): p. 366-76.
15. Komarova, Y., et al., Mammalian end binding proteins control persistent microtubule growth. *J Cell Biol*, 2009. 184(5): p. 691-706.
16. Montenegro Gouveia, S., et al., In vitro reconstitution of the functional interplay between MCAK and EB3 at microtubule plus ends. *Curr Biol*, 2010. 20(19): p. 1717-22.
17. Meijering, E., et al., Design and validation of a tool for neurite tracing and analysis in fluorescence microscopy images. *Cytometry A*, 2004. 58(2): p. 167-76.
18. Schindelin, J., et al., Fiji: an open-source platform for biological-image analysis. *Nat Methods*, 2012. 9(7): p. 676-82.



4



Exploring the roles of newly identified plus-end tracking proteins in neuronal development

Dieudonné van de Willige¹, Jessica J.A. Hummel¹,
Eveline van Leeuwen¹, Merel A. Post¹, Robin R. Buijs¹, Riccardo Stucchi¹,
Olga I. Kahn¹, Casper C. Hoogenraad^{#1} & Anna Akhmanova^{#1}

Co-corresponding author

Collection of Preliminary Data

¹ Cell Biology, Faculty of Science, Utrecht University,
Padualaan 8, 3584 CH Utrecht, The Netherlands

Abstract

Microtubule plus-end tracking proteins (+TIPs) play key roles in all stages of neurodevelopment. Following the identification of approximately twenty new +TIPs, we evaluated which of these proteins are of potential interest to the neuronal cytoskeleton field. This chapter contains a collection of preliminary data.

Introduction

As reviewed in chapter 1, microtubule (MT) plus-end tracking proteins (+TIPs) are involved in all stages of neurodevelopment [1]. The most common mode of MT plus-end tracking depends on interaction with end-binding (EB) proteins via a so-called SxIP motif: a small, unstructured stretch of nine amino acids with the sequence [S/T]-x-[I/L]-P at its core [2]. In 2012, the number of known SxIP-+TIPs nearly doubled. By combining a proteome-wide computational screen for SxIP motifs with mass-spectrometry analysis of EB binding partners, Jiang et al. identified 20 additional +TIPs and confirmed their plus-end tracking abilities in non-neuronal cell lines [2].

Given the important roles of +TIPs in neurodevelopment, we systematically screened the localization of these novel +TIPs and their co-localization with endogenous EB1 in primary hippocampal neurons (Supplementary Table SI). We also performed a preliminary analysis of phenotypes induced by their depletion. Based on these observations and literature, we selected Gas2L1, NCKAP5L and TTBK1/2 for follow-up analysis. Although our understanding of Gas2L1 as described in Chapter 3 is currently the most advanced, the data presented in this chapter points towards interesting roles for NCKAP5L and TTBK proteins in neurodevelopment, and reveals additional insights into the functioning of Gas2L1.

Further insights into the function of Gas2L1

We identified the MT-actin crosslinker Gas2L1 (Gas2-related protein-like 1) as a MT-dependent actin stabilizer with a role in balancing axon branching and outgrowth. In Chapter 3, we show that Gas2L1 is autoinhibited via an intramolecular interaction between the N-terminal actin-binding calponin homology (CH) domain and the MT-binding tail, consisting of a Gas2-related (GAR) domain and a C-terminal SxIP motif. *In vitro*, Gas2L1 cannot bind individual actin filaments without simultaneously binding to a MT. In neurons, Gas2L1 localizes to actin independently, but appears to stabilize actin more effectively when it is bound to MTs. Moreover, the MT-binding tail of Gas2L1 steers the activity and localization of the protein towards axons. We propose that Gas2L1 selectively stabilizes actin in MT-rich regions of the cell and

that its activity is controlled by an autoinhibitory mechanism.

In neurons, the elongation of new axon branches starts when axonal actin patches are targeted by MTs (reviewed in [3]). We hypothesize that Gas2L1 allows only MT-targeted patches to develop by locally enhancing actin stability, while untargeted patches are left to dissolve. In the growth cone, where actin-MT crosstalk coordinates the direction and rate of axon outgrowth (reviewed in [4]), MT invasion of the actin-rich growth cone periphery directly affects local actin stability and thereby balances axon elongation.

In addition to our findings described in Chapter 3, we here reveal extra data supporting the idea that Gas2L1 is sensitive to its intracellular surroundings. We also further explored a potential role for the Gas2L1 SxIP motif, documented the effects of Gas2L1 overexpression in COS-7 cells, and developed tools that may aid future research into this intriguing cytoskeletal crosslinker.

Gas2L1 is sensitive to the local cellular environment

We first compared the behaviour of Gas2L1 in neurons to that of Gas2L1 in COS-7 cells. Similar to neurons, overexpressed Gas2L1 co-localized with both F-actin and MTs (Fig 1A), although co-localization with MTs was more readily identifiable in COS-7 cells. This may be due to the sparse MT network in these cells, which allowed for the observation of individual MTs.

Strikingly, Gas2L1 overexpression prompted the accumulation of endogenous EB1 exclusively on the MT lattice near the cell periphery (Fig 1B). We did not observe recruitment to F-actin. By contrast, Gas2L1 recruits EBs away from MTs and onto F-actin meshworks in neurons (Chapter 3), while Stroud et al. reported that Gas2L1 recruits EBs to actin stress fibres in NIH3T3 cells [5]. These are three distinct cell types, each with their own cytoskeletal features, which respond differently to Gas2L1 overexpression. These data strongly suggest that the mechanism by which Gas2L1 operates is sensitive to the local cellular environment. This claim is further underlined by the observation that Gas2L1 changes its localization relative to MTs in NIH3T3 cells plated on soft or hard substrates, which give rise to different types of actin networks [5].

In all cases described, EB recruitment was mediated by the SxIP motif. This included our experiments in COS-7 cells, wherein EBs maintained plus-end localization in the presence of an overexpressed Gas2L1 mutant that cannot bind

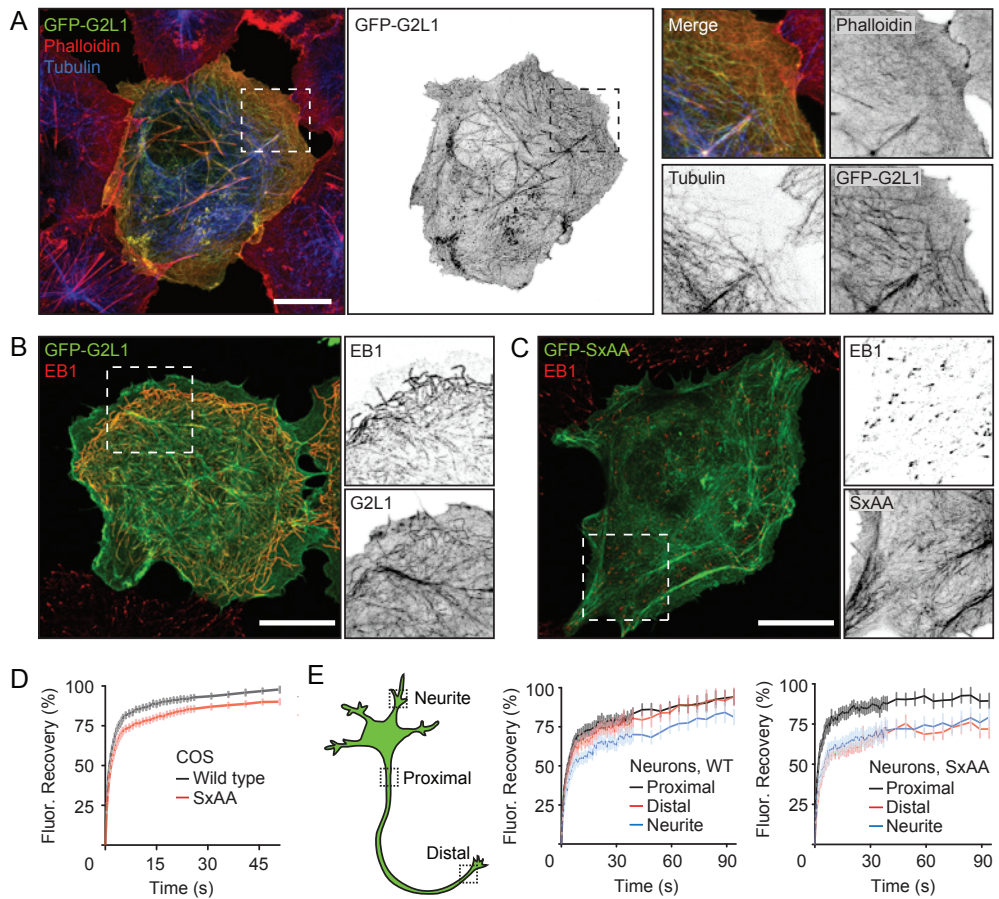


Figure 1. Gas2L1-EB interaction is controlled by local cellular environment.

(A) Localization of Gas2L1 (G2L1) in a COS-7 cell expressing GFP-Gas2L1 and stained for MTs (α -tubulin) and F-actin (Phalloidin). Boxed regions are enlarged to the right.

(B, C) Localization of endogenous EB1 in COS-7 cells overexpressing GFP-Gas2L1 (B) or GFP-Gas2L1-SxAA (C). Boxed regions are enlarged to the right.

(D) Curves showing FRAP of wild-type GFP-Gas2L1 (black line) and GFP-Gas2L1-SxAA (red line) in MT-rich peripheral regions of COS-7 cells. $n=30-42$ cells from 3 independent experiments.

(E) Curves showing FRAP of wild-type GFP-Gas2L1 (middle) or GFP-Gas2L1-SxAA (right) in various regions of DIV3-4 neurons. FRAP regions are schematically depicted in the scheme to the left. $n=19-25$ regions per condition from 3 independent experiments.

Scale bars: 20 μ m.

EBs (SxIP to SxAA, Fig 1C [6]). In Chapter 3, we describe that the SxIP motif is not required for Gas2L1 to crosslink actin and MTs or for its autoinhibition, and propose that the SxIP motif may enhance MT affinity. However, its precise role remains unclear. We therefore compared the turnover of wild-type Gas2L1 to that of EB-binding-deficient Gas2L1 mutant (Gas2L1-SxAA) by measuring fluorescence recovery after photobleaching (FRAP) in live cells.

In COS-7 cells, we chose to photobleach MT-rich regions near the cell periphery, where SxIP-dependent EB immobilization was most evident. Here, GFP-Gas2L1-SxAA fluorescence recovered less than that of GFP-Gas2L1 (Fig 1D), suggesting that part of the intracellular Gas2L1 pool depends on EB binding for its turnover.

We sought to repeat this observation in neurons. However, in contrast to the relatively homogenous cytoskeletons of COS-7 cells, neurons have distinct cytoskeletal organizations in different intracellular compartments. In dendrites, MTs are organized in bundles with mixed orientations, which are decorated by MAP2. Axonal MT bundles have uniform plus-end-out polarity and are decorated by tau. The somatodendritic and axonal compartments are separated by the axon initial segment (AIS) located in the proximal axon. Here, MT bundles are tethered to the membrane and decorated by a population of MT lattice-bound EBs. Both MAP2 and tau are excluded, and the MT-associated protein TRIM46 decorates AIS MTs instead. The AIS also hosts its own subset of spectrins which coordinate the actin cytoskeleton (reviewed in [7]).

We therefore photobleached Gas2L1 in three regions: in pre-dendrites/neurites, in the proximal axon and in the distal axon (Fig 1E). Interestingly, the turnover of wild-type Gas2L1 seemed different between axons and non-axonal neurites, confirming that Gas2L1 acts differently depending on its local surroundings. Differences in turnover were more pronounced for Gas2L1-SxAA, which mainly affected the behaviour of Gas2L1 in the distal axon. Here, the recovery of Gas2L1-SxAA was significantly lower than that of wild-type Gas2L1.

Our results suggest that Gas2L1 changes its binding kinetics depending on the type of cytoskeleton and/or local protein composition, and that part of this selectivity arises from binding to EBs in a context-specific manner.

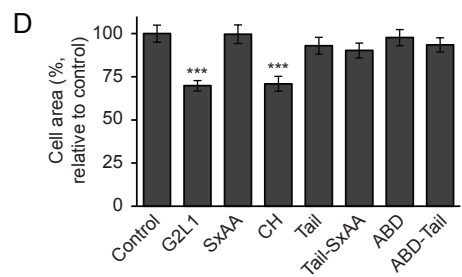
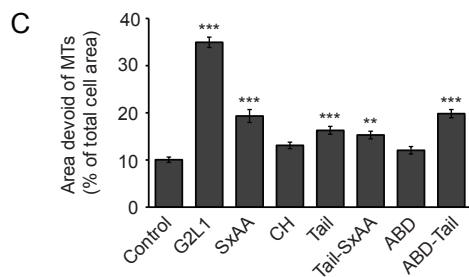
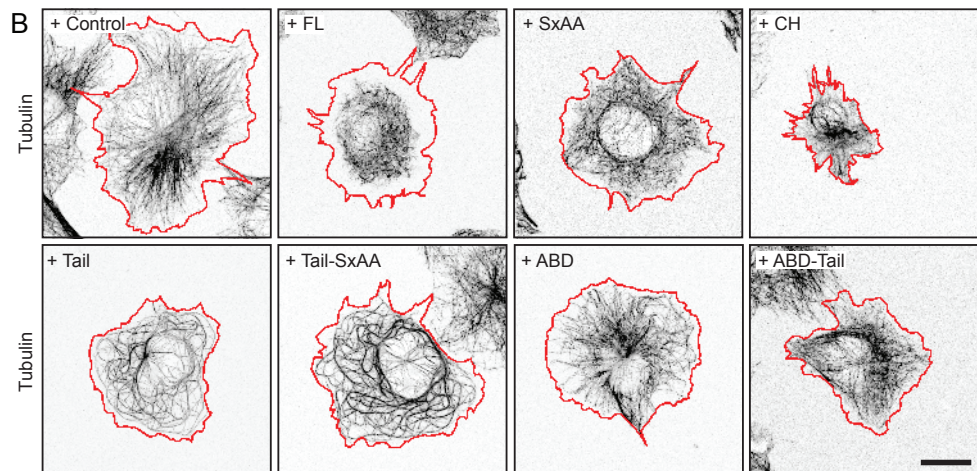
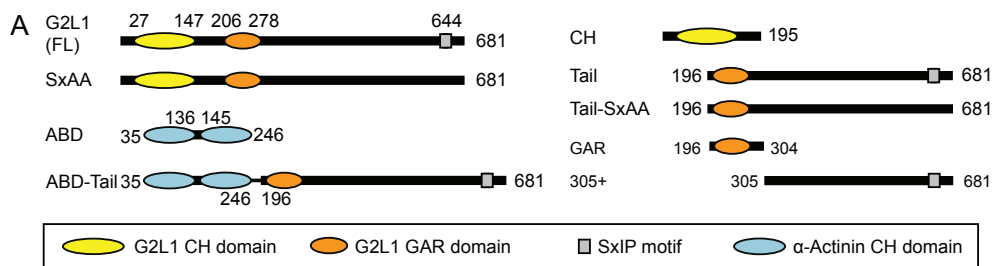


Figure 2. Gas2L1 restricts peripheral MT entry and reduces cell area.

(A) Schematic depiction of Gas2L1 (G2L1) and α -actinin mutants used in this study.

(B) Representative pictures of the MT cytoskeleton (labelled by α -tubulin staining) of COS-7 cells expressing the indicated HA-Gas2L1 and HA- α -actinin mutants. Red outlines mark the cell periphery.

(C, D) Quantification of cellular area devoid of MTs (C) and total cell area (D) of COS-7 cells overexpressing the indicated HA-Gas2L1 and HA- α -actinin mutants. $n=40$ cells per condition from 2 independent experiments.

One-way ANOVA with post-hoc Tukey's test (C) or Kruskal-Wallis with post-hoc Dunn's Multiple Comparison test (D). **, $p < 0.01$, ***, $p < 0.001$. Scale bars: 20 μm .

Gas2L1 restricts MT entry into the periphery of COS-7 cells

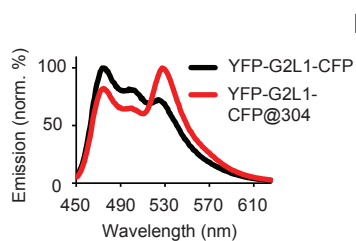
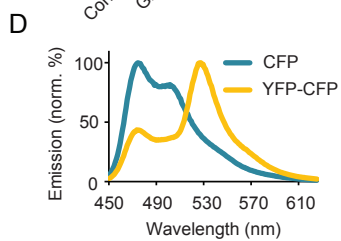
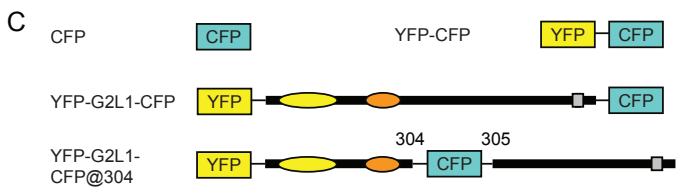
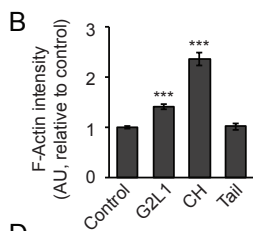
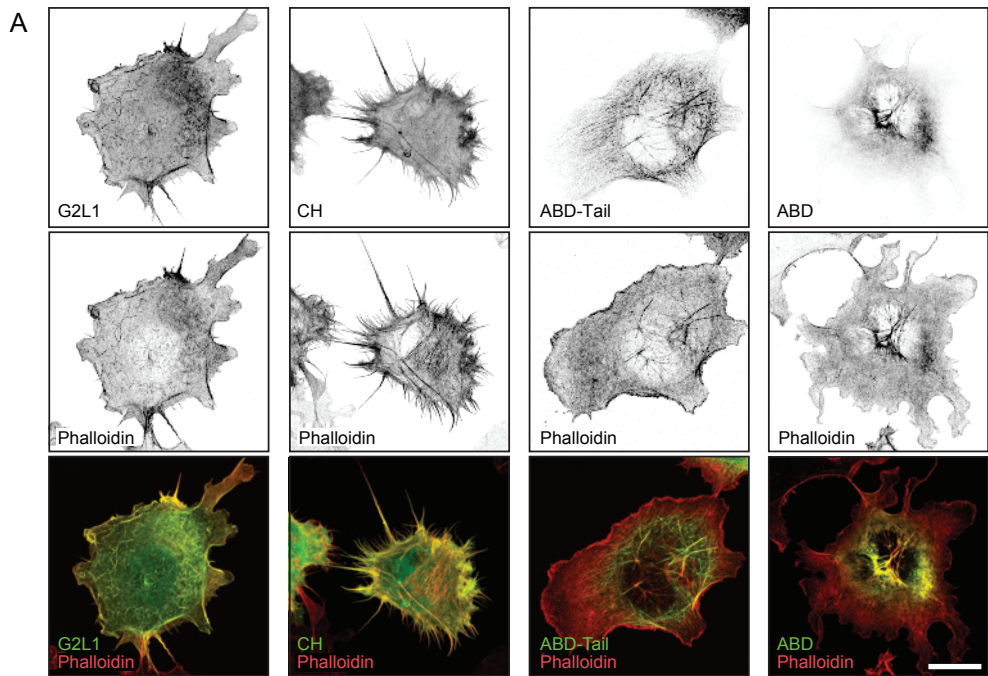
We aimed to gain additional insight into the behaviour of Gas2L1 and the role of its SxIP motif in COS-7 cells. Stroud et al. reported that Gas2L1 overexpression prevented MTs from entering the cell periphery, which was later suggested to be a general result of crosslinking actin filaments to MT plus-ends [5, 8]. We reproduced this finding and evaluated the ability of different Gas2L1 mutants (Fig 2A) to restrict peripheral MT entry and quantified the relative area of COS-7 cells devoid of MTs after overexpression of each mutant (Fig 2B, C). To this end, we calculated the total cell area from cell silhouettes visualized with CellTracker dyes, and the MT-rich area from endogenous alpha-tubulin staining. Furthermore, to study the contribution of Gas2L1's actin-binding CH domain, we also included the actin-binding domain of α -actinin, consisting of tandem CH domains, both independently (ABD) and fused to the MT-binding tail fragment of Gas2L1 (ABD-Tail, Fig 2A).

As expected, the peripheral MT-free area increased to ~35% of total cell size upon Gas2L1 overexpression, compared to ~10% in control COS-7 cells. Neither the Gas2L1 CH domain, nor the α -actinin ABD restricted MT entry, confirming that MT restriction is not solely actin-dependent. We observed a mild increase in MT-free areas with Gas2L1-Tail and Tail-SxAA. However, this could be attributed to their MT

> Figure 3. Gas2L1's CH domain induces filopodia formation and is in close proximity to the GAR domain.

- (A) Localization of GFP-Gas2L1 (G2L1) and GFP- α -actinin mutants in COS-7 cells stained for F-actin (phalloidin).
- (B) Quantification of phalloidin staining intensity in COS-7 cells transfected with HA control, HA-Gas2L1, HA-CH or HA-Tail and normalized to control levels. n=55-60 cells per condition from 3 independent experiments.
- (C) Schematic overview of FRET mutants used to obtain emission spectra in (D).
- (D) Emission spectra of the indicated FRET mutants upon CFP excitation ($\lambda=425$ nm), measured in HEK293 cell lysates.
- (E) Ratio of YFP/CFP emission peaks ($\lambda=527$ and 475 nm, respectively) obtained from spectra shown in (D). A higher ratio indicates more FRET and therefore closer proximity of CFP and YFP.

Kruskal-Wallis with post-hoc Dunn's Multiple Comparison test (B). ***; $p < 0.001$. Scale bars: 20 μ m.



E

	Em. 527nm/ Em. 475nm
CFP	0.39
YFP-CFP	2.31
YFP-G2L1-CFP	0.70
YFP-G2L1-CFP@304	1.22

bundling properties (Fig 2B), reaffirming that MT restriction is a result of actin-MT coupling. Gas2L1-SxAA could also restrict peripheral MT entry, but only in ~20% of the cell, confirming that this process is partly SxIP-dependent and that the SxIP motif of Gas2L1 may serve to enhance affinity for MTs. Finally, the ABD-Tail chimera was not as potent as wild-type Gas2L1, implying that differences in actin binding affect peripheral MT restriction.

Interestingly, COS-7 cells overexpressing wild-type Gas2L1 or the Gas2L1 CH domain were smaller than COS-7 cells in other conditions (Fig 2D). This observation suggests that the CH domain of Gas2L1 may alter cellular morphology by changing the composition and/or stability of the actin network.

The Gas2L1 CH domain can reorganize actin

COS-7 cells overexpressing Gas2L1-CH developed exaggerated filopodia-like protrusions and contained actin bundles in the center of the cell (Fig 3A). The intensity of F-actin staining with phalloidin increased accordingly (Fig 3B). Consistent with the model for Gas2L1 autoinhibition presented in Chapter 3, overexpression of full-length Gas2L1 had a less pronounced effect on actin reorganization, but still mildly increased total F-actin levels in COS-7 cells as it did in neurons (Fig 3A/B of this chapter and Fig 5F/G of chapter 3).

Remarkably, the CH domain did not localize to all F-actin in the cell: it mainly bound the fine peripheral actin meshwork, but remained largely excluded from the actin bundles concentrated near the center of the cell. By contrast, the actin-binding domain of α -actinin preferentially localized to central stress-fibre-like structures, reflecting the native localization of α -actinin to stress fibres. In line with the respective localizations of their actin-binding domains, full-length Gas2L1 could bind peripheral actin filaments, whereas ABD-Tail bound stress fibres and MTs in the inner cell region (Fig 3A). These results suggest that various CH domains have distinct actin binding preferences, and that the CH domain of Gas2L1 has higher affinity towards finely organized actin filaments.

Intramolecular proximity of the Gas2L1 CH and GAR domains

Finally, in Chapter 3 we describe an interaction between the CH domain and MT-binding tail fragment of Gas2L1, resulting in the autoinhibition of the protein. This model suggests the presence of a hinge region between the Gas2L1 N- and C-termini,

so the protein can fold on itself. We attempted to dissect the folding of Gas2L1 by designing FRET probes using YFP-CFP pairing. Normally, CFP excitation at 425 nm yields a corresponding emission peak at 475 nm. However, when YFP is in close proximity, CFP emission carries over in a distance-dependent manner, resulting in YFP excitation and emission at 527 nm instead. Determining the emission spectra of FRET probes excited at CFP wavelengths (425 nm) thereby provides information about the proximity of YFP and CFP by monitoring the ratio between emission peaks at 475 nm (CFP) and 527 nm (YFP).

We expressed YFP-Gas2L1-CFP or YFP-Gas2L1-CFP@304, containing an intramolecular CFP tag between the GAR domain and unstructured tail (Fig 3C), in HEK293 cells. We also included CFP and a YFP-CFP tandem as negative and positive controls, respectively, and confirmed that the localization of both Gas2L1 FRET probes was identical to that of GFP-Gas2L1 in COS-7 cells (data not shown). We lysed HEK293 cells in a lysis buffer designed to prevent protein aggregation, obtained emission spectra of all lysates excited at CFP wavelengths (Fig 3D) and calculated YFP/CFP peak ratios as a quantitative readout of YFP-CFP proximity (Fig 3E).

Lysates of non-transfected HEK293 cells showed no emission peaks at any wavelength (data not shown). CFP lysates featured a characteristic emission peak at 475 nm, which was shifted to 527 nm for YFP-CFP. This result illustrates that we were able to observe FRET using our approach (Fig 3D, E). Interestingly, YFP-Gas2L1-CFP showed minimal FRET, whereas YFP-Gas2L1-CFP@304 did reveal a prominent emission peak at 527 nm (Fig 3D, E). The YFP/CFP peak ratio did not change upon further dilution of the lysate (data not shown), confirming that the FRET signal of YFP-Gas2L1-CFP@304 arose from proximity of intramolecular YFP and CFP tags and not from high protein concentrations that enabled intermolecular FRET in the lysate.

Taken together, these data show that the N-terminus of Gas2L1 is in close proximity of the GAR domain in cell lysates. We assume that Gas2L1 indeed contains a hinge region between these two domains.

Gas2L1: future directions

As discussed in Chapter 3, an autoinhibitory mechanism controlled by the binding of actin filaments and MTs is naturally followed by the question of selectivity.

Which cytoskeletal subpopulations most potently bind to and thereby relieve the autoinhibition of Gas2L1? Evidence of the binding selectivity of Gas2L1 and its ortholog Pigs was provided previously [5, 9], but the specifics remain unclear.

Here, we show that the SxIP motif may be involved in sensing the local cellular environment. The pattern of SxIP-dependent EB recruitment in COS-7 cells is different from that in neurons. An EB-deficient binding mutant of Gas2L1 affects the protein's turnover in distal axons, but much less in proximal axons or non-axonal neurites. In Chapter 3, we speculate that the SxIP motif of Gas2L1 enhances MT binding affinity. This claim is further supported by additional results from this chapter, which show that the MT-restricting action of Gas2L1 in COS-7 cells partially depends on its SxIP motif.

Interestingly, the SxIP motif appears to be required for Gas2L1 to reduce the size of COS-7 cells. 'Compact' cells are usually associated with increased contractile forces. Apart from myosin activity, contractility levels depend on the properties of the cortical actin network, and cortical thickness depends on the length of actin filaments [10]. However, COS-7 cells lack endogenous myosin-IIa expression which makes it difficult to predict how these models for contractility apply. COS-7 cells do express myosin-IIb, which contributes to a relatively small stress fibre population [11]. It therefore remains possible that MT-dependent actin stabilization via Gas2L1 affects contractility also in COS-7 cells. It will be especially interesting to investigate why the SxIP motif appears required for this process, but not for MT-binding.

We made a similar observation regarding contractility in neurons. Axons that mature in the presence of overexpressed Gas2L1 shorten beyond the length predicted for axons that are fixed before overexpression (e.g. the axons of DIV4 neurons expressing high levels of Gas2L1 for 24 hours are shorter than axons of DIV3 neurons; data not shown). This suggests active axon retraction rather than passive inhibition of outgrowth. Axon elongation also involves a retrograde-oriented actomyosin-based contractile force, which is required for elongation but must be overcome at the same time. Changes in F-actin turnover alone are sufficient to alter contractility, with increased actin stability resulting in greater contractile forces and subsequent axon retraction without impacting endogenous myosin activity levels [12]. It seems likely that the putative effects of Gas2L1 on contractility are mediated through actin stability, yet it remains worthwhile to investigate whether Gas2L1 can alter myosin activity alongside.

Obviously, selectivity towards actin subpopulations may primarily arise from the CH domain itself. Gas2L1 belongs to a subclass of proteins that contain a single N-terminal type 3 CH domain. On the other hand, α -actinin contains tandem CH domains of type 1 and 2 [13]. In the latter subclass of actin-binding domains, the type 2 domain typically modulates actin binding of the type 1 domain. By contrast, type 3 domains tend to play regulatory roles in addition to actin binding [13]. We here show that, indeed, the CH domains of Gas2L1 and α -actinin are not equal. Firstly, the Gas2L1 CH domain binds to a different actin subpopulation than the tandem CH domains of α -actinin. Secondly, the CH domain of Gas2L1 affects the actin organization in COS-7 cells, giving rise to numerous filopodia and actin bundles without localizing to all of the structures it induces. This suggests that the Gas2L1 CH domain may possess regulatory functions not relayed via direct binding to actin

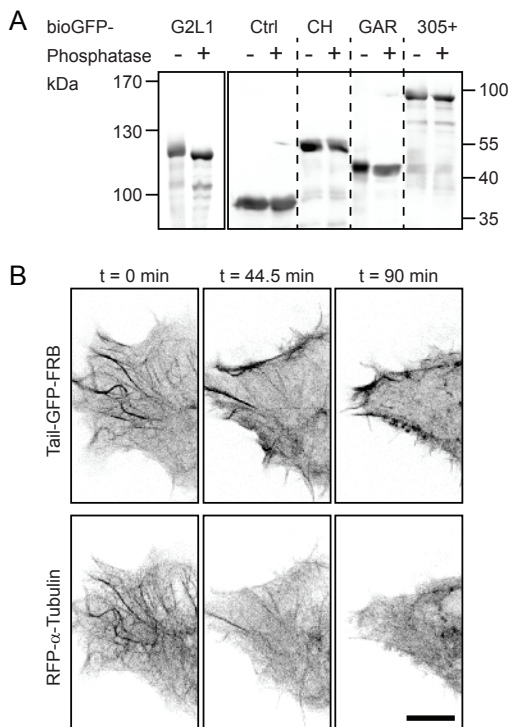


Figure 4. Future prospects for studies addressing Gas2L1.

(A) Electrophoretic mobility of full-length bioGFP-Gas2L1 (G2L1), as well as indicated truncation mutants and bioGFP alone (Ctrl), isolated from HEK cell lysates in the absence and presence of λ protein phosphatase to remove phosphorylation.

(B) Live relocation of Tail-GFP-FRB upon coupling to co-expressed HA-CH-FKBP (invisible), as compared to microtubules visualized by RFP- α -tubulin in COS7 cells. Rapalog heterodimerizer was added 4.5 minutes after the start of imaging. Scale bar: 10 μ m.

filaments. Investigating its potential to control actin organization will shed further light on the function of Gas2L1 in neurodevelopment.

Apart from selective binding, Gas2L1 activity may also be regulated through phosphorylation as Gas2L1 contains a large number of putative phosphorylation sites (curated in PhosphoSite Plus; [14]). Some of these sites are located before the CH domain and on the GAR domain, but the majority is located in its unstructured C-terminus. The latter two regions are required for the intramolecular interaction with the Gas2L1 CH domain as shown in chapter 3. We gauged the extent of Gas2L1 phosphorylation in HEK293 cells by comparing the electrophoretic mobility of bioGFP-Gas2L1 and various truncations in the absence or presence of phosphatases (Fig 4A). Gas2L1 indeed seemed to be mildly phosphorylated, mostly in its SxIP-containing C-terminal region (amino acids 305-681).

Kinase activity may provide an explanation for why Gas2L1 immobilizes EBs only at the cell periphery of COS-7 cells (Figure 1B) and why the immobilization pattern of EBs varies between cell types. Phosphorylation in the vicinity of the SxIP motif controls interactions with EB proteins, and local regulation of EB binding was attributed to GSK3 β -mediated phosphorylation of CLASP proteins [15-17]. Including dephosphorylated Gas2L1 in reconstitution assays as described in chapter 3 can provide insight into how phosphorylation affects autoinhibition, and whether phosphorylation regulates the binding of its individual domains to cytoskeletal filaments and EB proteins.

Finally, we developed additional tools that may help elucidate how Gas2L1 activity is modulated. We describe proximity between a YFP/CFP FRET pair situated at the N-terminus and in the middle of Gas2L1 (YFP-Gas2L1-CFP@304). It remains to be determined whether the FRET signal generated by this Gas2L1 mutant is affected by a change from the active to the autoinhibited conformation, which can be tested by FRET imaging during *in vitro* reconstitution experiments. If so, FRET imaging in live neurons will provide valuable clues on where Gas2L1 is active during neurodevelopment.

Lastly, we also developed a set of CH domains that bind the Gas2L1 tail region via chemically induced heterodimerization of FKBP and FRB domains. This system appears to effectively reconstitute the localization of full-length Gas2L1. Live imaging revealed that in the presence of HA-CH-FKBP and the heterodimerizing component rapalog, Tail-GFP-FRB relocalized from MTs to actin-like structures in COS-

7 cells (Fig 4B). In this experiment, some loss of signal and aggregation is observed for RFP- α -tubulin. Further testing is required to see whether these are structural MT rearrangements caused by rapalog addition, phototoxicity or overexpression, or whether it reflects an issue with MT labelling arising from photobleaching. However, if this system is further validated and placed under optogenetic control, it can be locally induced in neurons. This will allow us to distinguish between the effects of individual Gas2L1 domains and regulatory effects that occur exclusively in the full-length protein, while keeping important parameters such as expression levels and local cytoskeleton composition the same before and after inducing coupling.

Although we identified a regulatory mechanism and neuronal function for Gas2L1 as described in Chapter 3, much remains to be learned about this elusive cytoskeletal crosslinker. Solving the question of its actin- and MT-binding preferences and pinpointing when and where it is active in cells will greatly further our understanding of how Gas2L1 contributes to neurodevelopment.

Tau-tubulin kinases in neurodevelopment

The family of tau-tubulin kinases (TTBKs) consists of two members: TTBK1 and TTBK2. Both proteins share a highly homologous N-terminal kinase domain, contain two functional SxIP motifs at their C-termini (Fig 5A) and have been implicated in various brain disorders [2, 18]. We have extensively reviewed existing TTBK2 literature in Chapter 1, and will therefore provide only a brief introduction to TTBK2 in this chapter.

Premature truncation of TTBK2 causes the neurodevelopmental disorder spinocerebellar ataxia 11 (SCA11) [19], which likely results from the absence of cilia. During ciliogenesis, MTs extend from the basal body after it docks to the membrane. Premature MT extension is inhibited by the centriolar capping protein CP110. CP110 dissociation is thought to occur through TTBK2 phosphorylation and allows extension of the MT-based axoneme [20]. Other interesting targets of TTBK2 kinase activity encompass MAP2, tubulin, TDP-43 and tau, including the sites which have been linked to tauopathies such as Alzheimer's disease (AD) [21-23].

Tau hyperphosphorylation is one of the hallmarks of AD. In healthy neurons, tau decorates axonal MTs, and tau levels increase with distance from the soma.

Pathological hyperphosphorylation triggers tau dissociation from MTs, followed by oligomerization into paired helical filaments (PHF) and eventually PHF aggregation into neurofibrillary tangles. Simultaneously, MTs disassemble and neuronal functions decline, ultimately resulting in neuronal atrophy. Of note, it is still unclear whether MT degradation promotes tau dissociation or vice versa.

Many major kinases have been implicated in pathological tau phosphorylation, and also the absence of phosphatases is thought to play a role [24]. However, +TIP kinases like TTBK1/2 warrant special attention. Treatment with Epothilone D, a MT-targeting agent (MTA) able to cross the blood-brain barrier, reduced pre-existing AD-like pathology of transgenic mice expressing a pathogenic tau P301L mutant [25]. MT-stabilizing agents like Epothilone D are typically hypothesized to counteract MT destabilization in AD [26]. However, at low concentrations, MTAs switch their action from (de)polymerizing MTs to affecting MT plus-end dynamics [27-29]. It is reasonable to assume that the drug dose reaching its target *in vivo* is magnitudes lower than the administered dose, suggesting that the beneficial effect of MTAs may be due to an effect on MT dynamics rather than total polymer mass. As +TIPs and tau kinases, TTBKs are ideally positioned to relay regulatory signals from the MT plus-end to tau.

Confirming a role for TTBK proteins in tau phosphorylation, tau deposits were found in the brain of the only autopsied SCA11 patient to date [20]. However, TTBK1 has been more firmly implicated in tauopathy than TTBK2. Tau phosphorylation sites associated with AD are targets of TTBK1 kinase activity, and mutations in the TTBK1 gene reduced AD risk in different populations [30-32]. Moreover, TTBK1 is more highly expressed in the frontal cortex of AD patients, although no difference was found in TTBK1 mRNA levels in the frontal inferior gyrus [33, 34]. Overexpression of TTBK1 induced tau phosphorylation and aggregation in cultured neurons [30], and transgenic mice overexpressing TTBK1 displayed enhanced levels of tau phosphorylation. These mice suffer from age-dependent memory impairment and an increase of AD-related markers such as enhanced gliosis [33].

TTBK1 was reported to localize to the somatodendritic compartment and to the perinuclear and cytoplasmic regions of neurons by immunohistochemistry on human and murine brain sections [23, 30, 34]. Given the spatial restriction of tau to axons, this is a surprising localization for a tau kinase. However, prior to aggregation, tau is known to mislocalize to the somatodendritic compartment in tauopathies

including AD. This is also apparent in transgenic mice expressing tau P301L, which is associated with frontotemporal dementia with Parkinsonism linked to chromosome 17 (FTDP-17) [35, 36].

It is therefore possible that the contribution of TTBK1 to tau aggregation occurs only later in the pathological cascade, after tau leakage into the somatodendritic compartment. Notably, while tau phosphorylation is enhanced in TTBK1 overexpressing mice, tau aggregation only occurs in double transgenic mice overexpressing both TTBK1 and tau P301L [33, 37], suggesting that tau and TTBK1 may indeed be spatially segregated in healthy neurons. Additionally, increased tau phosphorylation upon TTBK1 overexpression may be in part due to upregulation of other kinases. TTBK1 overexpression also increases the activity of another tau kinase, cdk5, and promotes tau phosphorylation at sites not targeted by TTBK1 itself [33]. Moreover, TTBK1 undergoes post-translational modifications that may affect its subcellular localization and function [33].

Changes in MT plus-end dynamics may interfere with pathological tau phosphorylation

We first investigated the effect of low doses of MT-targeting agents (MTAs) on endogenous tau phosphorylation in primary rat neurons. As mentioned, at such concentrations both stabilizing and destabilizing MTAs affect MT plus-end dynamics rather than induce changes in MT polymer mass. We confirmed these observations by counting the number of comets in the soma of hippocampal neurons treated with 2 nM vinblastine (a destabilizing agent at high doses) or 50 nM taxol (a stabilizing agent at high doses) for 1 or 24 hours. The number of growing MT plus-ends was equally reduced in all conditions, but not nullified (Fig 5B).

Lysates of untreated DIV21-23 cortical neurons showed prominent phosphorylation of tau at Ser202/Thr205 (AT8) sites, which is recognized by a monoclonal antibody raised against PHF-tau from brains of AD patients [38]. Surprisingly, 2 nM vinblastine greatly reduced AT8 phosphorylation already after 1 hour of treatment, yet 50 nM taxol had no effect (Fig 5C). Similar results were obtained using DIV5 cortical neurons (data not shown). These data suggest that pathological tau phosphorylation is linked to MT plus-end dynamics, but that the mechanism through which this occurs is more complex than simply dampening MT dynamics.

To confirm whether TTBK1/2 play a role in tau AT8 phosphorylation, we built upon an experiment by Sato et. al. in which TTBK1 and tau are co-overexpressed in cell lines [30]. We co-expressed GFP-tau0N4R, a tau isoform upregulated during rat development [39], with various HA-tagged TTBK fusions in HEK293T cells and monitored AT8 phosphorylation compared to total tau levels (Figure 5D; S1A). Both wild-type TTBK1 and TTBK2 co-expression increased tau AT8 phosphorylation, and their activity was abolished by respective K63R or K50R mutations in the kinase domains (TTBK-KD for kinase-dead; [2]). In our hands, TTBK1's catalytic domain (TTBK1-cat; amino acids 38-319) was not active, but the truncation mutant of TTBK2 known to cause SCA11 (TTBK2-SCA; amino acids 1-450) caused some increase in tau phosphorylation. We confirm that wild type TTBK1 and TTBK2 have the potential to upregulate tau phosphorylation at sites associated with AD pathology, which are also affected by MTA treatment.

TTBK expression in primary neurons

Next, we looked for TTBK expression in primary neurons. Using TTBK antibodies that exerted reasonable specificity on Western blot (Fig S1B), we probed endogenous TTBK expression in different brain regions of adult rats (Fig 6A) and in cultured cortical neurons at various DIVs (Fig 6B).

A band of 170 kDa corresponding to full-length TTBK1 was observed in all rat brain regions, most prominently in the cortex, and TTBK1-FL expression was weak but upregulated over time in dissociated cortical neurons. Our experiments also revealed a prominent band around 100 kDa, which was previously described and proposed to represent a lysosomal degradation product of TTBK1 [33].

Full-length TTBK2 presented itself as two broad bands around 170 kDa. As the TTBK2-KD mutant is recognized as a single band (Fig S1A), this observation is consistent with reports that TTBK2 auto-phosphorylates itself resulting in differences in electrophoretic mobility [2]. Full-length TTBK2 was most prominently expressed in the brain stem and spinal cord. Similar to TTBK1, TTBK2-FL was weakly expressed and appeared upregulated over time in cortical dissociated neurons. We also detected a stronger band around 100 kDa, although it is unclear whether this corresponded to processed TTBK2 as has been proposed for TTBK1 or whether this band resulted from unspecific reactivity of the antibody.

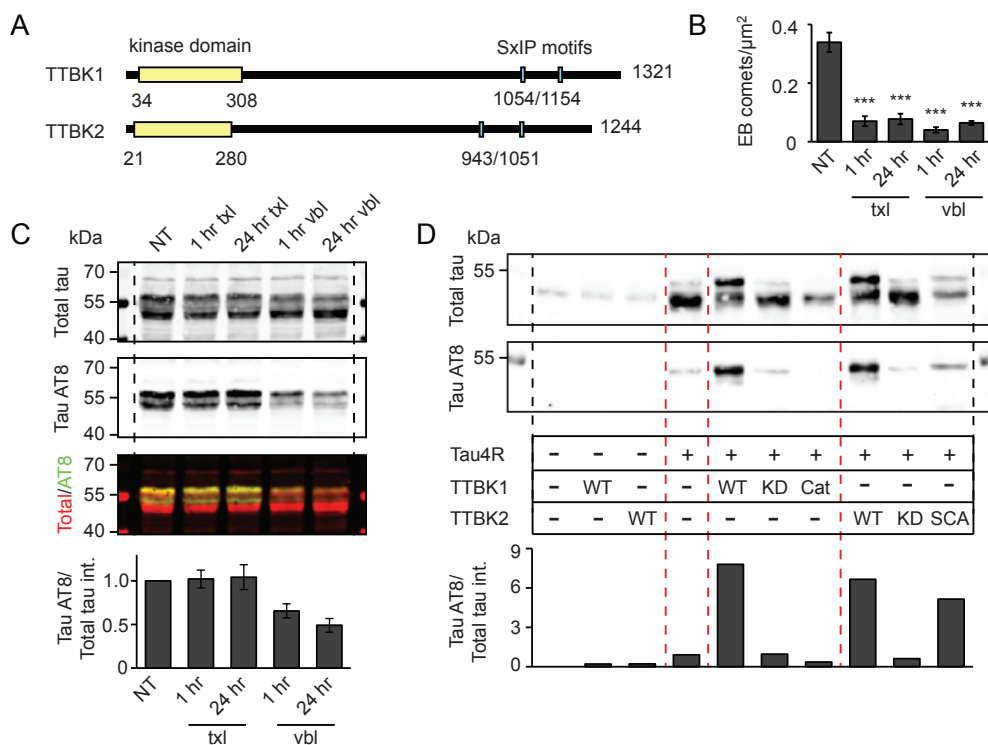


Figure 5. Vinblastine reduces pathological tau phosphorylation at sites targeted by TTBK proteins.

(A) Schematic overview of TTBK1 and TTBK2.

(B) Analysis of the number of EB comets in the soma of fixed DIV5 hippocampal neurons, after treatment with 50 nM taxol (txl) or 2 nM vinblastine (vbl) for the indicated durations.

NT = non-treated; n=9-10 neurons per condition from one experiment.

(C) Western blots probing for endogenous tau AT8-phosphorylation in DIV23 (blot)/DIV21-23 (quantification) cortical neurons, after treatment with 50 nM taxol (txl) or 2 nM vinblastine (vbl) for the indicated durations. Ratios are normalized to control levels. Dashed lines indicate separation between marker lanes. NT = non-treated; quantification based on two independent experiments.

(D) Western blots probing for tau AT8-phosphorylation in HEK cells overexpressing various combinations of GFP-Tau4R and TTBK1/2 fusions. WT = wild type; KD = kinase-dead; cat = TTBK1(38-319); SCA = TTBK2(1-450). Ratios are non-normalized. Dashed lines indicate separation between marker lanes and experimental conditions (black) or groups of experimental conditions (red).

One-way ANOVA with post-hoc Tukey's test (B). ***, $p < 0.001$.

TTBKs localize to the AIS of primary neurons

Knowing that TTBK proteins are expressed in older dissociated neurons, we next studied the localization of TTBK1/2 in DIV14 cortical rat neurons. The TTBK2 antibody used in Fig 6A/B (#1) also recognized low levels of overexpressed TTBK2 in immunofluorescence assays, but TTBK1 antibody #1 did not perform adequately (Fig S1C). We therefore used another antibody against TTBK1 (#2) that recognized overexpressed TTBK1, but not TTBK2, when staining neurons (Fig S1D).

> Figure 6. Expression and localization of TTBK proteins in neurons.

(A, B) Western blots probing endogenous TTBK1/2 expression with antibodies described in Fig S1B in lysates from adult rat brain regions (A) and in lysates from cultured cortical neurons at various DIVs (B). For (B), actin loading controls ran on a separate gel and were published with the experiment shown in Fig 1B of chapter 2, which uses identical lysates to probe protein expression levels. Red arrowheads indicate bands corresponding to full-length TTBK1/2, dashed lines indicate separation between marker lanes and experimental conditions.

(C) TTBK1/2 staining in DIV14 cortical neurons co-stained for Ankyrin-G (AnkG). Red arrowheads indicate the position of the axon initial segment.

(D) Localization of GFP-TTBK1 in DIV4 hippocampal neurons compared to the entire neuron (β -galactosidase co-transfection, fill) and compared to endogenous tau. Arrowheads indicate the path of the transfected axon in tau co-stainings.

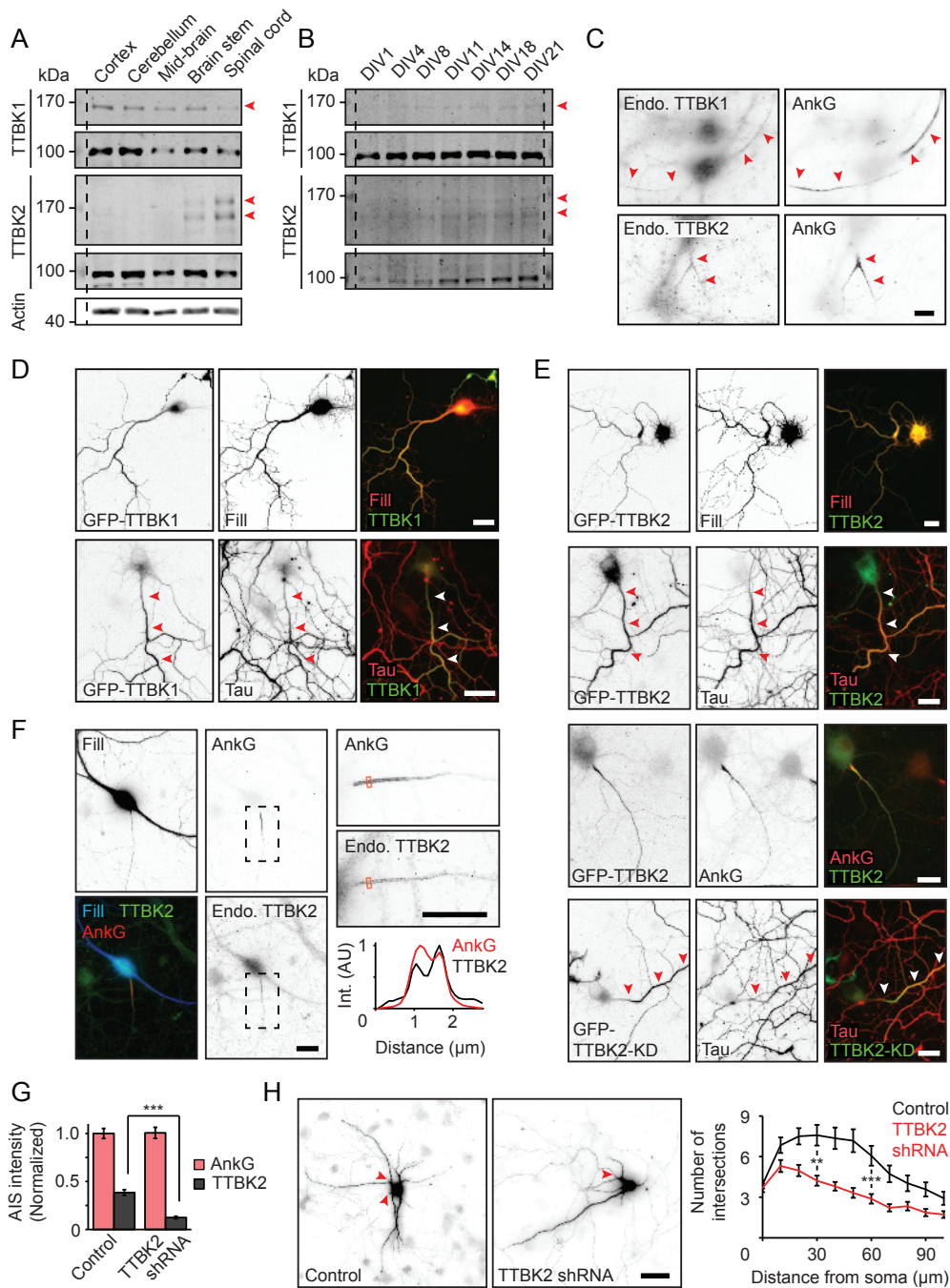
(E) Localization of GFP-TTBK2 (top three panels) and GFP-TTBK2-KD (bottom panels) in hippocampal neurons at DIV4/4/11/4, respectively, compared to the entire neuron (β -galactosidase co-transfection, fill) and compared to endogenous tau or Ankyrin-G (AnkG). Arrowheads indicate the path of the transfected axon in tau co-stainings.

(F) TTBK2 staining in a DIV14 hippocampal neuron, transfected with β -galactosidase (fill, blue) and staining for rabbit-anti-TTBK2 (green) and Ankyrin-G (AnkG, red). Black boxed regions are enlarged to the right of the images, and a linescan of the area boxed in red is shown on the bottom right.

(G) Fluorescence intensities of endogenous Ankyrin-G and TTBK2 in the axon initial segments of DIV12-14 hippocampal neurons transfected with pSuper-empty (control) or pSuper-TTBK2-shRNA. n=36-50 axon initial segments from two independent experiments. All values are normalized to average AnkG intensity in control neurons.

(H) Sholl analysis of dendrite morphology of DIV11 hippocampal neurons transfected for four days with pSuper-empty (control) or pSuper-TTBK2-shRNA. Red arrowheads indicate the axon, which is excluded from analysis. n=31-34 neurons from two independent experiments.

Mann Whitney U test (G, H), ** $p < 0.01$; *** $p < 0.001$. Scale bars: 10 μm in (C), 25 μm in (D), 20 μm in (E, F), 50 μm in (H).



We observed low levels of TTBK1/2 staining in the axon initial segment (AIS) of DIV14 cortical neurons, as evidenced by co-staining with the AIS marker Ankyrin-G (Fig 6C). This is an interesting observation considering that tau is normally excluded from the AIS. However, overexpressed GFP-TTBK1 was enriched in the axons of DIV4 hippocampal neurons, where it did co-localize with the tau gradient along the axon (Fig 6D). The localization of GFP-TTBK2 in DIV4-11 hippocampal neurons was heterogeneous: it varied from diffuse to axonal, where it coincided with the tau gradient, and could indeed also co-localize with Ankyrin-G in the AIS (Fig 6E, top nine panels). The kinase-dead mutant of TTBK2 uniformly and strongly localized to the axon (Fig 6E, bottom three panels), revealing that TTBK2's auto-phosphorylation regulates its subcellular localization in neurons. Furthermore, both TTBK1 and TTBK2 overexpression increased the intensity of endogenous EB protein staining along the axon (Fig S2A). The TTBK2-SCA11 mutant simultaneously localized to both the AIS and along a gradient towards the distal axon (Fig S2B). Finally, GFP-TTBK2 also localized to the base of the cilium, consistent with its function in ciliogenesis (Fig S2C) [20].

As TTBK2 seemed more biased toward the AIS than TTBK1, we further focussed on validating TTBK2's AIS localization. DIV14 hippocampal neurons also showed TTBK2 staining in the AIS (Fig 6F). AIS enrichment varied greatly among individual neurons, reflecting the heterogeneous localization of overexpressed TTBK2. Knockdown of TTBK2 reliably lowered AIS staining levels with TTBK2 antibodies without affecting Ankyrin-G expression (Fig 6G). Our shRNA against TTBK2 simultaneously blocked the formation of cilia associated with TTBK2 depletion (Fig S2C) [20], indicating that this shRNA is specific for TTBK2 and that the observed AIS staining reflects endogenous TTBK2 localization.

Potential functions of tau-tubulin kinases

The AIS localization of TTBK2, and potentially of TTBK1, raises the question what function TTBK proteins exert in the AIS. Unfortunately, preliminary experiments were so far inconclusive: we observed no effect on axon morphology or on polarized cargo trafficking (data not shown). One experiment suggested that the stability of AIS microtubules might be affected in TTBK-depleted neurons (data not shown), but this will need to be addressed further.

We did, however, observe an effect on dendrite outgrowth. Dendrites of

TTBK2-depleted neurons branched less than control neurons (Fig 6H), and the same was seen for multiple shRNAs against TTBK1 (effect of one shRNA is shown in Fig S2E). Although our TTBK1 shRNA lacks proper validation at the time of writing, it did not affect cilium formation in DIV7-11 neurons like TTBK2 shRNA did (Fig S2D), ruling out that it targets TTBK2 instead. Our data suggests that TTBK proteins may be involved in dendrite maturation, which could be a new function independent of TTBK2's role in cilia formation.

TTBK proteins: future directions

We show that low doses of vinblastine, but not taxol, can reduce pathological tau phosphorylation in cortical neurons. It is too early to hypothesize what causes the difference between these MTAs. Instead, this experiment should be repeated with an array of different MTAs and doses, to determine what common ground underlies the effect seen with vinblastine. However, our results do suggest that in addition to MT stabilizing drugs, MT destabilizing agents should be included in screenings for drugs that may relieve pathological changes in tauopathies.

The observation that both TTBK1 and TTBK2 can phosphorylate tau at sites affected by vinblastine prompts the question whether vinblastine relays its effects via TTBKs. To address this, TTBK mutants that cannot bind EBs should be assessed for their potential to phosphorylate tau. Our results indicate that the truncated TTBK2-SCA11 mutant that lacks SxIP motifs is still active, but this contradicts a report by Bouskila et al. [40]. Furthermore, contrary to Sato et al., we observed no activity of the TTBK1 catalytic domain [30]. These experiments, as well as our own, were done using different substrates and in non-neuronal model systems, highlighting the need to re-evaluate and perform future experiments in neurons. Moreover, it is necessary to carefully consider which TTBK substrates best reflect those in healthy and diseased neurons. When evaluating the role of TTBK plus-end tracking, these requirements are further illustrated by substrate-specific effects of EB binding on TTBK2 activity. For example, EB3 promotes TTBK2 activity toward KIF2A by releasing TTBK2 autoinhibition, yet EB-binding is not required for TTBK2 to phosphorylate CP110 during ciliogenesis [41, 42].

Additionally, our results on the endogenous localization of TTBK proteins suggest that the spatial relationship between TTBKs and their substrates should be taken into account. This point is addressed by studies showing TTBK co-localization

with tau aggregates in patient brains [34, 43], but this data resembles late stages of disease. To date, most of the literature on TTBK as a potential cause of tau hyperphosphorylation builds upon overexpression, with the most extreme effects observed in double transgenic animals [37, 43]. Severe overexpression may promote protein mislocalization, and subsequently promote kinase binding to substrates they would not encounter otherwise.

Importantly, since spatial information is not revealed by Western blotting, it will be useful to employ microscopy to observe where in neurons TTBK-induced tau phosphorylation takes place, and how this ties in with endogenous localizations. Recent advances allowing CRISPR/Cas9-mediated gene tagging in neurons [44], as well culturing of patient-sourced iPSC-derived neurons that exhibit tau hyperphosphorylation [45], will provide better understanding of TTBK-tau interplay at expression levels associated with health and disease. Ultimately, such information will help to pinpoint at which stage of disease TTBK activity becomes relevant, and thereby provide information about their utility as therapeutic targets.

With respect to endogenous localization of TTBK proteins, we here show that TTBK2 localizes to the AIS of primary neurons. We also observed TTBK1 AIS staining, although this observation requires further validation. Notably, TTBK2's SCA11 mutant could localize to the AIS, suggesting that the N-terminus of TTBK2 facilitates AIS targeting. The amino acid sequence of TTBK2-SCA11 is 70% identical and 80% similar to that of TTBK1's N-terminus. Furthermore, TTBK1 and TTBK2 are members of the casein kinase family, and casein kinase 2 is native to the AIS [46]. This implies that in addition to TTBK2, TTBK1 may well be capable of targeting the AIS through its kinase domain. Considering the aforementioned relation between protein localization and function, it is tempting to speculate about an AIS-specific role for TTBK proteins.

The AIS maintains neuronal polarity by functioning as a barrier between the somatodendritic and axonal compartments of neurons, and is weakened in transgenic AD mouse models [47, 48]. MAP2 and tau, both substrates of TTBKs, are normally excluded from the AIS and respectively decorate somatodendritic and axonal microtubules. Phosphorylation of microtubule-associated proteins (MAPs) such as MAP2 and tau generally drives their dissociation from MTs [49]. It is therefore possible that TTBK proteins phosphorylate MAP2 and/or tau in the AIS, to locally inhibit their association with the MT lattice and prevent them from invading

other neuronal compartments. In this context, the upregulation of TTBK1 observed in AD patients could be interpreted as a response to rescue tau mislocalization. It will be interesting to see whether neurons depleted of TTBK1/2 are able to maintain MAP polarity.

Alternatively, AIS-localized TTBK proteins may not normally contribute to tau phosphorylation, but instead exert different functions before the onset of tauopathy. We observed that overexpression of TTBK proteins enriched the density of endogenous EB proteins along the axon, whereas this kind of EB immobilization is normally only seen in the AIS. Here, it contributes to AIS assembly and maintenance via a cooperative interaction with Ankyrin-G [50]. Endogenous TTBK2 staining followed the characteristic submembranous staining pattern of Ankyrin-G (Fig 6F, linescan), suggesting that like many AIS proteins, it may be scaffolded by Ankyrin-G. Perhaps TTBKs contribute to the recruitment of a stable pool of AIS EBs.

Lastly, we observed a potential effect of TTBK proteins on dendrite development. This requires further validation via rescue experiments, but if true, would describe a novel function of TTBKs. Potentially interesting targets of TTBK1/2 that contribute to dendrite development include cdk5 and MAP2 [49, 51]. Notably, cdk5's contribution to dendrite development relies on its activity-dependent translocation to the nucleus [51]. The AIS remodels depending on neuronal activity [52], and the cdk5 activator p35 was recently shown to accumulate in the AIS [53]. Although highly speculative, this could put TTBK proteins in a position to influence cdk5-dependent dendrite maturation.

Taken together, TTBKs are exciting +TIPs with a broad range of substrates, including some of the main MAPs and kinases implicated in neuronal development. Many studies have focussed on the role of TTBK proteins in disease. This work can be complemented by further studying the role of TTBK proteins in healthy neurons, their function in the AIS and their relation to tauopathies in suitable model systems.

NCKAP5L in neurodevelopment

NCKAP5L, for Nck-associated protein 5-like, was recently given the alternative name CEP169 for centrosomal protein of 169 kDa. Indeed, current knowledge about NCKAP5L is limited and has thus far focussed on a role for NCKAP5L at the

centrosome.

NCKAP5L interacts with another centrosome-associated +TIP, CDK5RAP2, which promotes centrosomal MT nucleation. CDK5RAP2 is required for the division of neural progenitors and as such, its loss leads to microcephaly [54-56]. NCKAP5L itself seems to affect the stability of centrosomal MTs and to promote cell division in RPE cells [55, 57]. Overexpression of NCKAP5L induces MT bundling, and NCKAP5L interacts with MTs in a second, EB-independent manner, which was mapped to amino acids 746-1152 [58]. During mitosis, NCKAP5L is removed from the centrosome by cdk1-mediated phosphorylation, but its role at the centrosome remains largely unclear [59].

Neurons are post-mitotic cells, and as such the centrosome rapidly loses its function as a MT-organizing center during neurodevelopment [60]. Instead, MT nucleation occurs throughout the neuron, via cytoplasmic γ -tubulin ring complexes and the HAUS/augmin complex, which ensure proper MT polarity, density and bundling [61, 62]. It follows that many centrosomal proteins take on a different role during neurodevelopment, as may be the case for NCKAP5L.

Structurally, human NCKAP5L harbors a predicted N-terminal coiled-coil domain thought to promote its dimerization, and three SxIP motifs of which the C-terminal motif contributes most to its association with EB proteins [55, 58] (Fig 7A). Furthermore, NCKAP5L shares an NCKAP5 domain with NCKAP5. NCKAP5 is also part of the newly identified group of +TIPs [2], although the function of this domain or its namesake is presently unknown. However, NCKAP5 was reported to interact with Src homology 3 (SH3) domains of Nck and Vav2 [63, 64]. SH3 domains

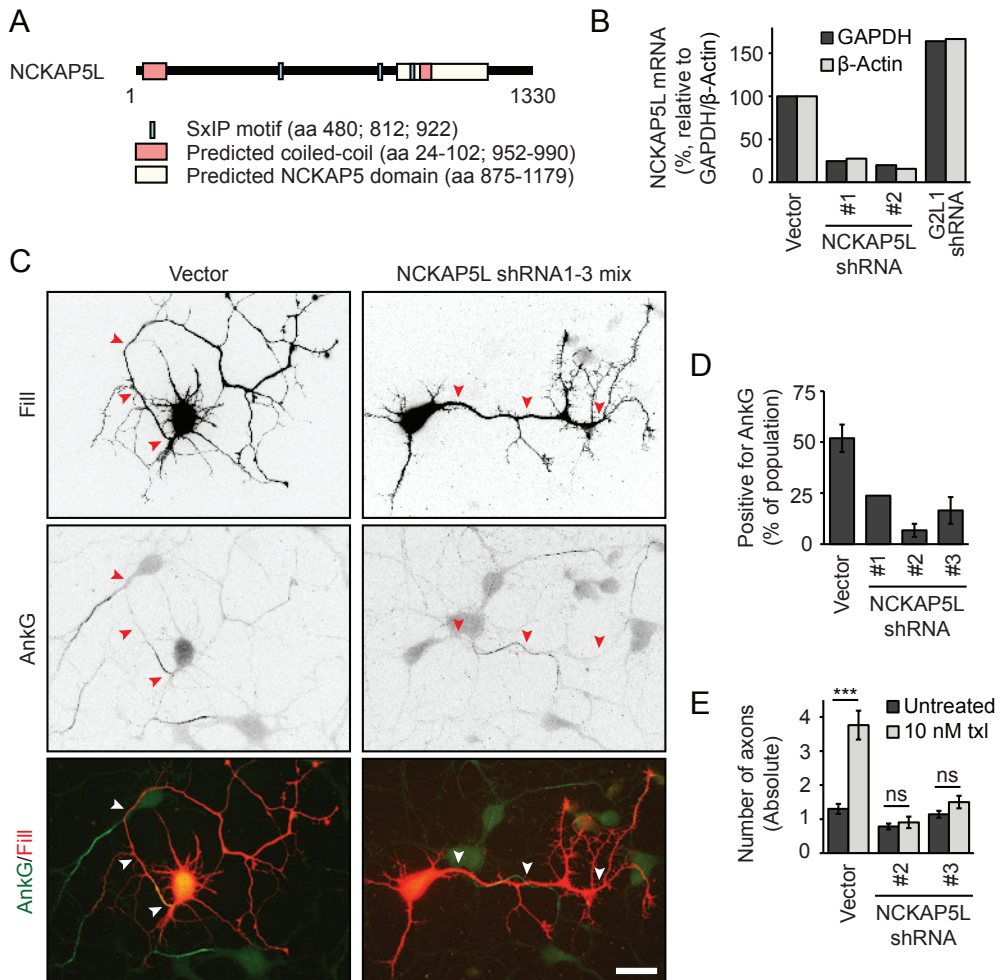
> Figure 7. NCKAP5L depletion impairs early neuronal polarization.

(A) Schematic overview of NCKAP5L.

(B) qPCR experiment showing the change in NCKAP5L mRNA compared to control GAPDH (dark grey bars) or β -actin (light grey bars) mRNA levels, in DIV3 neurons electroporated at DIV0 with empty shRNA plasmid (vector), NCKAP5L shRNA #1/#2 or G2L1 shRNA. All plasmids used in this experiment contained an additional puromycin resistance cassette, and neurons were subjected to 48h puromycin selection prior to mRNA isolation.

(C) Representative DIV4 neurons transfected with empty shRNA control (vector) or a mix of NCKAP5L shRNA #1, #2 and #3 for 4 days, co-transfected with GFP to show outline (Fill) and stained for endogenous Ankyrin-G (AnkG) to show the axon initial segment.

(Legend continues on next page)



(D) Quantification of the percentage of DIV4 neurons with at least one neurite positive for Ankyrin-G (AnkG). Neurons were transfected with empty shRNA control (vector) or NCKAP5L shRNA at DIV0 and analysed at DIV4. For vector, shRNA #2 and shRNA #3, 46-60 neurons were counted in two experiments. For shRNA #1, 21 neurons were counted in one experiment.

(E) Number of neurites positive for both TRIM46 and sodium channel staining, after the induction of axon formation via taxol treatment (light grey bars) or in control DIV6 counterparts (dark grey bars). Neurons were transfected with empty shRNA control (vector) or NCKAP5L shRNA #2/#3 at DIV2, and were left untreated or underwent 48h treatment with 10 nM taxol before analysis at DIV6. $n=20-23$ neurons per condition from one experiment.

Mann-Whitney U test (E), ns; not significant, ***, $p < 0.001$. Scale bars: 30 μm in (C).

typically bind proline-rich sequences and, in case of Nck and Vav2, allow for the scaffolding of multi-protein complexes involved in intracellular signalling [65]. Human NCKAP5 is 1909 amino acids long, of which 8.5% are prolines. Strikingly, the amino acid composition of human NCKAP5L is made up of no less than 16% prolines, suggesting that NCKAP5L may be involved in similar interactions.

Our preliminary data reveals that NCKAP5L could be a key player in establishing the polarity of post-mitotic neurons.

Depletion of NCKAP5L may impair early neuronal polarization

To identify a function for NCKAP5L in primary rat hippocampal neurons, we generated three independent shRNAs against NCKAP5L. Two of those were included in a qPCR experiment detailed in Fig 1A/S1A of Chapter 3, allowing us to compare NCKAP5L mRNA levels upon depletion to those in control neurons as well as in neurons transfected with Gas2L1 shRNA. We found that NCKAP5L shRNA #1 and #2 reduced NCKAP5L mRNA levels by ~74% and ~82%, respectively, while mRNA levels were increased by ~65% in Gas2L1 shRNA-expressing neurons (Fig 7B). We found similar increases in mRNA levels for other proteins when cross-validating samples, indicating that this reflects a global upregulation response not specific to NCKAP5L mRNA or Gas2L1 depletion (data not shown).

DIV4 neurons that expressed a mix of three different NCKAP5L shRNAs after transfection at DIV0 failed to form axons. Axons remained short, occasionally developed excessive filopodia-like structures and lacked an AIS, suggesting that they failed to polarize (Fig 7C). When NCKAP5L shRNAs were separately tested for their effect on polarization, all three shRNAs independently reduced the number of DIV4 neurons with an AIS (Fig 7D). Of note, this phenotype seems limited to NCKAP5L as shRNAs against NCKAP5 did not show an effect on AIS formation; it should be noted, however, that the depletion of NCKAP5 still needs to be validated.

Because dissociated neurons immediately start to form axons upon plating, shRNA-mediated depletion generally takes too long to fully reveal the effects of protein depletion on early events of neurodevelopment. To circumvent this issue and to better understand the contribution of NCKAP5L to polarization, we induced supernumerary axon formation with taxol [66]. Neurons were transfected with NCKAP5L shRNA at DIV2, followed by treatment with 10 nM taxol from DIV4 to DIV6. In one exploratory experiment, this treatment caused control neurons to form four

axons instead of one, whereas the formation of new axons was completely blocked in neurons expressing NCKAP5L shRNA #2 or #3 (Figure 7E).

Although this phenotype and its specificity for NCKAP5L need to be validated more extensively, this data suggests that NCKAP5L may be required for axon formation in developing neurons.

Expression and localization of NCKAP5L in young neurons

Loss of the AIS could be due to a direct, AIS-specific function of NCKAP5L, or due to a more general role in polarization upstream of AIS formation. Following the reasoning that protein localization is closely tied to function, we evaluated the localization of NCKAP5L in developing neurons.

Shintomi et al. briefly mention that NCKAP5L is highly expressed in rat neurons [57]. However, we did not observe endogenous NCKAP5L staining in neurons at DIV4. Instead, glial cells in the same neuron cultures showed prominent staining around centrioles, at MT plus-ends and in the cytosol (Fig 8A, B). This staining pattern matches reports for NCKAP5L localization in cycling cells, and thereby strongly suggests that our antibody recognizes at least one rat isoform of NCKAP5L. We hypothesize that NCKAP5L is either expressed below immunofluorescence detection levels in neurons, or that neurons express one of the other putative NCKAP5L isoforms which is not recognized by our antibodies.

Overexpressed NCKAP5L concentrated around the centrioles of DIV4 neurons, but otherwise presented itself as small, evenly distributed puncta in the soma, axon and neurites (Fig 8C, E). Interestingly, only a fraction of these puncta co-localized with endogenous EB1 at MT plus-ends (Fig 8D), raising the question at which other structures NCKAP5L puncta accumulate.

Additionally, in line with the identification of ciliary proteins in a mass-spectrometry analysis of potential NCKAP5L binding partners [57], we found that overexpressed NCKAP5L occasionally entered the primary cilium of DIV8 neurons (Fig 8E). However, NCKAP5L depletion showed no effect on cilium formation (data not shown). Moreover, a surprisingly large number of +TIPs is able to enter the cilium, yet a preliminary screening suggested that of those, only TTBK2 affects cilium formation (Supplementary Table SI, Figure S3 & data not shown). NCKAP5L's association with cilia may therefore be a general artefact associated with the overexpression of +TIPs, which is an interesting observation deserving of follow-up

research by itself.

Identification of possible NCKAP5L binding partners

We next sought to identify novel, brain-specific interaction partners of NCKAP5L. To this end, we performed pulldown experiments with murine bioGFP-NCKAP5L expressed in, and captured from, HEK293 cell lysates. To allow filtering of brain-specific hits, samples were processed from HEK293 lysates immediately or subsequently incubated with adult rat brain extracts, and we identified proteins that co-precipitated with bioGFP-NCKAP5L in both experiments using mass spectrometry. Pulldowns with only bioGFP were run alongside as a control.

A condensed list of candidate binding partners is presented in Table I. We categorized specific hits according to four distinct, but often overlapping features: proteins with a role in vesicle transport (yellow), proteins involved in the endoplasmic reticulum (ER) and calcium release (blue), cytoskeletal proteins (red) and synaptic proteins (green).

(text continues after Figure 8 and Table I) >

4

> Figure 8. NCKAP5L expression and localization in neurons and glial cells.

(A) Endogenous co-staining of NCKAP5L and centrin in DIV4 neuron cultures. Closed arrowheads point to the soma of neurons, double arrowhead points to a glial cell. Boxed region is enlarged to the right.

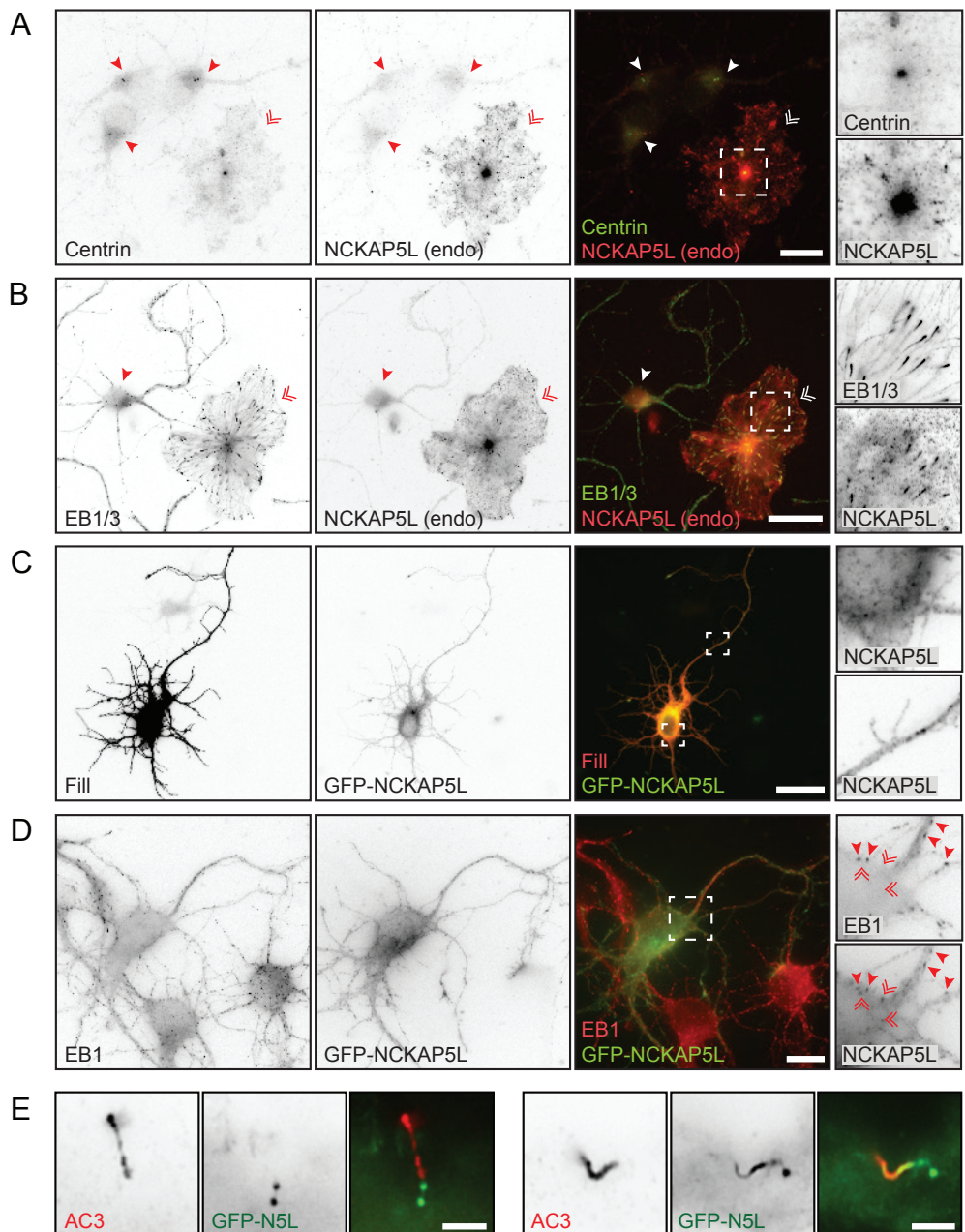
(B) Endogenous co-staining of NCKAP5L and EB1/3 in DIV3 neuron cultures. Closed arrowhead points to the soma of a neuron, double arrowhead points to a glial cell. Boxed region is enlarged to the right.

(C) Localization of overexpressed GFP-NCKAP5L in a DIV4 neuron co-expressing β -galactosidase (Fill). Boxed regions are enlarged to the right with boosted contrast.

(D) Co-localization of overexpressed GFP-NCKAP5L with endogenous EB1 in a DIV4 neuron. Boxed region is enlarged to the right. Closed arrowheads point to examples of GFP-NCKAP5L puncta co-localizing with EB1, double arrowheads point to examples of GFP-NCKAP5L puncta that do not line up with EB1 staining.

(E) Variety in localization of overexpressed GFP-NCKAP5L relative to the primary cilium of DIV8 neurons, visualized by staining the cilium marker Adenylyl Cyclase III (AC3).

Scale bars: 15 μ m in (A, D), 30 μ m in (B, C), 3 μ m in (E).



Cluster	Name	Gene ID	Whole brain lysates		HEK lysates					
			+ GFP	+ GFP- NCKAP5L	+ GFP	+ GFP- NCKAP5L				
			#pep	#psm	#pep	#psm	#pep	#psm		
	NCKAP5L	NCKAP5L	5	5	63	1109			38	348
	Vesicle-associated membrane protein-associated protein A	Vapa	1	1	16	73			19	119
	Vesicle-associated membrane protein-associated protein B	Vapb			12	53			18	90
	Inositol 1,4,5-trisphosphate receptor type 1	Itpr1	5	5	68	119				
	Inositol 1,4,5-trisphosphate receptor type 2	Itpr2	2	2	14	20				
	Phosphatidylinositol 4-kinase alpha	Pi4ka			13	13			4	4
	Phosphatidylinositol 4-phosphatase SAC1	Sacm1l			8	9				
	Neuroplastin	Nptn			6	7				
	AP complex subunit beta	Ap1b1	2	2	21	36			4	4
	AP-2 complex subunit alpha-1	Ap2a1	9	9	39	66			5	6
	AP-2 complex subunit alpha-2	Ap2a2	6	6	37	65			2	3
	AP-2 complex subunit beta	Ap2b1	5	5	31	60			6	7
	AP-2 complex subunit mu	Ap2m1	3	3	27	55			12	16
	AP-2 complex subunit sigma	Ap2s1	1	2	5	10			3	3
	AP-3 complex subunit beta-1	Ap3b1			7	8				
	AP-3 complex subunit beta-2	Ap3b2			14	15				
	Coatomer subunit alpha	Copa			18	19			9	9
	Coatomer subunit beta	Copb1			12	15			2	3
	Coatomer subunit beta'	Copb2			8	8				
	Coatomer subunit delta	Arcn1			6	7			5	6
	Dynammin-1	Dnm1	3	3	22	26				

Dynamitin-like 120 kDa protein	Opal1										1	1	1
Dynamitin-2	Dnm2	1	1								6	9	
Ankrd50	Ankrd50										13	15	
Surf4	Surf4										4	10	4 11
Clathrin coat assembly protein AP180	Snap91										6	8	
Rabconnectin 3- α	Dmxx2										20	21	
Synaptotagmin-1	Syt1	1	1								12	15	
Synaptotagmin II	Syt2										5	6	
Synapsin-1	Syn1	2	2								8	14	
Synaptic vesicle glycoprotein 2A	Sv2a	2	3								7	14	
Synaptotagmin 1	Synj1										8	8	
Endophilin-A2	Sh3gl1										2	4	
Endophilin-A1	Sh3gl2										2	4	
Cytoplasmic dynein 1 heavy chain 1	Dync1h1										64	73	
Microtubule-associated protein 1A	Map1a	3	4								47	80	
Filamin A	Flna	1	1								38	51	45 56
TRIO	Trio	7	7								26	32	
CLIP-associating protein 2	Cksp2										8	8	
ch-TOG	Ckap5										7	8	1 2

Table I. Mass spectrometry analysis of NCKAP5L binding partners identified from HEK cell lysates and/or whole adult rain brain lysates. Results are clustered and color-coded according to the group they belong to: vesicle transport (yellow), proteins involved in the endoplasmic reticulum (ER) and calcium release (blue), cytoskeletal proteins (red) and/or synaptic proteins (green). #pep: number of unique peptides identified; #psm: total number of peptides identified.

Top hits in both HEK293 cells and brain lysates include VAPA and VAPB, which mediate interactions of the ER with other organelles and cytosolic proteins [67]. Inositol 1,4,5-trisphosphate receptors (IP3Rs), particularly IP3R type I, surfaced as strong brain-specific hits. IP3Rs are transmembrane ER-receptors and calcium channels that mediate calcium release from the ER, which underlies synaptic plasticity and other key neuronal processes [68].

Interestingly, the majority of candidate proteins is involved in vesicle trafficking. We identified various subunits of the coatamer and adaptor protein (AP) complexes in both HEK cells and brain extracts. These complexes serve similar functions in different transport pathways: coatamer complexes form COPI- and COPII-coated vesicles that bud from the ER and the cis-Golgi [69], whereas AP complexes 1 through 3 assemble clathrin-coated vesicles in the late secretory and endocytic pathway. AP-2, which was best represented in our candidate list, is specifically involved in endocytosis from the plasma membrane [70]. We also identified dynamins, which pinch off budding vesicles during the final steps of vesicle assembly [71], and Ankrd50, which functions in the retrieval of endosomes to the trans-Golgi network [72].

Of note, a subset of brain-specific hits is associated with synaptic vesicles (SVs). SVs contain neurotransmitters and are docked at the active zone of the presynapse, where they are exocytosed in a calcium-dependent manner. Among candidates is Rabconnectin-3 α , which is thought to scaffold Rab3 on SVs during exocytosis [73]. Synaptotagmins associate with SNARE complexes to fuse SVs with the membrane [74], and Synapsin regulates multiple aspects of SV dynamics, including maintaining a reserve pool of vesicles at the presynapse [75]. Synaptojanin, on the other hand, is required for uncoating endocytosed clathrin-coated vesicles at the presynapse [76], suggesting that the list of potential NCKAP5L-interactors spans the entire synaptic vesicle cycle as well as most other trafficking pathways.

Lastly, we focused on potential cytoskeletal interactors of NCKAP5L. Not surprisingly, some of these candidates are also intimately linked to vesicle transport. The cytoplasmic dynein heavy chain (DHC) is a core component of the motor protein dynein, which drives retrograde cargo transport along MTs [77]. MAP1A is a MT-associated protein with a function at the postsynaptic density, but which also associates with the AP-2 complex and clathrin-coated vesicles [78]. Moreover, Purkinje cells of MAP1A-deficient mice fail to maintain AIS morphology [79].

The actin filament crosslinking protein Filamin A, which was recently reported as a candidate for binding NCKAP5L, also ranked high on our candidate list [57]. Additionally, the +TIP TRIO was found as a potential neuron-specific interactor. TRIO relays signals from the MT plus-end to Rho GTPases, thereby shaping the actin network during neurite outgrowth and axon development [1, 80].

To summarize, potential binding partners of NCKAP5L span a wide range of intracellular functions and pathways. Although further validation is required to confirm NCKAP5L's association with any of these proteins, this preliminary list can direct further research into the function of NCKAP5L.

NCKAP5L: future directions

The preliminary data presented in this chapter suggests that NCKAP5L plays a critical role during axon specification and outgrowth. However, the list of possible binding partners suggests that NCKAP5L could also play a role in mature neurons, as it potentially interacts with a host of presynaptic proteins. This is further illustrated by a genetic study that identified NCKAP5L as a candidate gene for autism [81], which is thought to involve synaptic dysfunction [82].

Indeed, preliminary experiments suggest that dendrites of DIV11 NCKAP5L-depleted neurons also show polarization defects (data not shown). This time point is still too early in neurodevelopment to gauge NCKAP5L's effect on synapse formation and maintenance, and therefore NCKAP5L-associated phenotypes should be carefully catalogued and validated at all stages of neurodevelopment. Combined with the fact that potential interactions between NCKAP5L and the above described proteins also require further biochemical confirmation, the range of pathways that may involve NCKAP5L is too broad to warrant elaborate speculation.

It is, however, difficult to ignore the obvious trend towards vesicle trafficking in our list of potential NCKAP5L interactors. We found that NCKAP5L localizes as puncta throughout neurons, and that only some of these puncta overlap with MT plus-ends. It is possible that these other puncta are vesicles, which can be tested by observing their motility in live neurons. If NCKAP5L indeed appears to associate with vesicles, co-localization studies may reveal the identity of these vesicles. This information should provide further clues on which trafficking pathways involve NCKAP5L and can thereby direct a more targeted search.

A function for NCKAP5L as a regulator of intracellular trafficking could

explain polarization defects in its absence, by mis-sorting of proteins and disruption of membrane supply during axon and dendrite development. Additionally, NCKAP5L may function in MT plus-end-dependent actin remodelling alongside TRIO, or in calcium signalling via an association with the ER. If anything, our preliminary data reveal that NCKAP5L should be considered as a novel and potent modulator of neurodevelopment.

Author contributions

DvdW designed and performed experiments for all projects, analysed results, wrote the manuscript and supervised EvL and MP. JJAH designed and performed experiments, and analysed results for the Gas2L1 project. EvL and MP performed experiments and analysed results for the TTBK project. RRB and RS collected mass spectrometry data for the NCKAP5L project. qPCR experiments were performed in collaboration with OIK. CCH and AA supervised the research and coordinated the study.

4

Acknowledgements

qPCR experiments were performed with the kind assistance of M. de Wit and Prof. Dr. R.J. Pasterkamp. We are also grateful to Dr. K. Jiang, Dr. F.K.C. Au and Prof. Dr. R.Z. Qi for generously sharing constructs and reagents.

This work was supported by the Netherlands Organization for Scientific Research (NWO-ALW-VICI, CCH), the Netherlands Organization for Health Research and Development (ZonMW-TOP, CCH), and the European Research Council (ERC) (ERC-consolidator, CCH).

References

1. Kuijpers, M., et al., Dynein Regulator NDEL1 Controls Polarized Cargo Transport at the Axon Initial Segment. *Neuron*, 2016. 89(3): p. 461-71.
2. Jiang, K., et al., A Proteome-wide screen for mammalian SxIP motif-containing microtubule plus-end tracking proteins. *Curr Biol*, 2012. 22(19): p. 1800-7.
3. Lewis, T.L., Jr., J. Courchet, and F. Polleux, Cell biology in neuroscience: Cellular and molecular mechanisms underlying axon formation, growth, and branching. *J Cell Biol*, 2013. 202(6): p. 837-48.
4. Coles, C.H. and F. Bradke, Coordinating neuronal actin-microtubule dynamics. *Curr Biol*, 2015. 25(15): p. R677-91.
5. Stroud, M.J., et al., GAS2-like proteins mediate communication between microtubules and actin through interactions with end-binding proteins. *J Cell Sci*, 2014. 127(Pt 12): p. 2672-82.
6. Au, F.K., et al., GAS2L1 Is a Centriole-Associated Protein Required for Centrosome Dynamics and Disjunction. *Dev Cell*, 2017. 40(1): p. 81-94.
7. Leterrier, C., The Axon Initial Segment: An Updated Viewpoint. *J Neurosci*, 2018. 38(9): p. 2135-2145.
8. Adikes, R.C., et al., Control of microtubule dynamics using an optogenetic microtubule plus end-F-actin cross-linker. *J Cell Biol*, 2018. 217(2): p. 779-793.
9. Girdler, G.C., et al., The Gas2 family protein Pigs is a microtubule +TIP that affects cytoskeleton organisation. *J Cell Sci*, 2016. 129(1): p. 121-34.
10. Chugh, P., et al., Actin cortex architecture regulates cell surface tension. *Nat Cell Biol*, 2017. 19(6): p. 689-697.
11. Bao, J., S.S. Jana, and R.S. Adelstein, Vertebrate nonmuscle myosin II isoforms rescue small interfering RNA-induced defects in COS-7 cell cytokinesis. *J Biol Chem*, 2005. 280(20): p. 19594-9.
12. Gallo, G., H.F. Yee, and P.C. Letourneau, Actin turnover is required to prevent axon retraction driven by endogenous actomyosin contractility. 2002. 158(7): p. 1219-28.
13. Gimona, M., et al., Functional plasticity of CH domains. *FEBS Lett*, 2002. 513(1): p. 98-106.
14. Hornbeck, P.V., et al., PhosphoSitePlus, 2014: mutations, PTMs and recalibrations. *Nucleic Acids Res*, 2015. 43(Database issue): p. D512-20.
15. Honnappa, S., et al., An EB1-binding motif acts as a microtubule tip localization signal. *Cell*, 2009. 138(2): p. 366-76.
16. Akhmanova, A., et al., Clasps are CLIP-115 and -170 associating proteins involved in the regional regulation of microtubule dynamics in motile fibroblasts. *Cell*, 2001. 104(6): p. 923-35.
17. Kumar, P., et al., GSK3beta phosphorylation modulates CLASP-microtubule association and lamella microtubule attachment. *J Cell Biol*, 2009. 184(6): p. 895-908.
18. Ikezu, S. and T. Ikezu, Tau-tubulin kinase. *Front Mol Neurosci*, 2014. 7: p. 33.
19. Houlden, H., et al., Mutations in TTBK2, encoding a kinase implicated in tau phosphorylation, segregate with spinocerebellar ataxia type 11. *Nat Genet*, 2007. 39(12): p. 1434-6.
20. Goetz, S.C., K.F. Liem, Jr., and K.V. Anderson, The spinocerebellar ataxia-associated gene Tau tubulin kinase 2 controls the initiation of ciliogenesis. *Cell*, 2012. 151(4): p. 847-58.
21. Takahashi, M., et al., A novel tau-tubulin kinase from bovine brain. *FEBS Lett*, 1995. 372(1): p. 59-64.

- 22.** Tomizawa, K., et al., Tau-tubulin kinase phosphorylates tau at Ser-208 and Ser-210, sites found in paired helical filament-tau. *FEBS Lett*, 2001. 492(3): p. 221-7.
- 23.** Liachko, N.F., et al., The tau tubulin kinases TTBK1/2 promote accumulation of pathological TDP-43. *PLoS Genet*, 2014. 10(12): p. e1004803.
- 24.** Chong, F.P., et al., Tau Proteins and Tauopathies in Alzheimer's Disease. *Cell Mol Neurobiol*, 2018. 38(5): p. 965-980.
- 25.** Zhang, B., et al., The microtubule-stabilizing agent, epothilone D, reduces axonal dysfunction, neurotoxicity, cognitive deficits, and Alzheimer-like pathology in an interventional study with aged tau transgenic mice. *J Neurosci*, 2012. 32(11): p. 3601-11.
- 26.** Brunden, K.R., et al., The characterization of microtubule-stabilizing drugs as possible therapeutic agents for Alzheimer's disease and related tauopathies. *Pharmacol Res*, 2011. 63(4): p. 341-51.
- 27.** Mohan, R., et al., End-binding proteins sensitize microtubules to the action of microtubule-targeting agents. *Proc Natl Acad Sci U S A*, 2013. 110(22): p. 8900-5.
- 28.** Panda, D., et al., Differential effects of vinblastine on polymerization and dynamics at opposite microtubule ends. *J Biol Chem*, 1996. 271(47): p. 29807-12.
- 29.** Jordan, M.A., et al., Mechanism of mitotic block and inhibition of cell proliferation by taxol at low concentrations. *Proc Natl Acad Sci U S A*, 1993. 90(20): p. 9552-6.
- 30.** Sato, S., et al., Tau-tubulin kinase 1 (TTBK1), a neuron-specific tau kinase candidate, is involved in tau phosphorylation and aggregation. *J Neurochem*, 2006. 98(5): p. 1573-84.
- 31.** Vazquez-Higuera, J.L., et al., Genetic variations in tau-tubulin kinase-1 are linked to Alzheimer's disease in a Spanish case-control cohort. *Neurobiol Aging*, 2011. 32(3): p. 550.e5-9.
- 32.** Yu, N.N., et al., Tau-tubulin kinase-1 gene variants are associated with Alzheimer's disease in Han Chinese. *Neurosci Lett*, 2011. 491(1): p. 83-6.
- 33.** Sato, S., et al., Spatial learning impairment, enhanced CDK5/p35 activity, and downregulation of NMDA receptor expression in transgenic mice expressing tau-tubulin kinase 1. *J Neurosci*, 2008. 28(53): p. 14511-21.
- 34.** Lund, H., et al., Tau-tubulin kinase 1 expression, phosphorylation and co-localization with phospho-Ser422 tau in the Alzheimer's disease brain. *Brain Pathol*, 2013. 23(4): p. 378-89.
- 35.** Ballatore, C., V.M. Lee, and J.Q. Trojanowski, Tau-mediated neurodegeneration in Alzheimer's disease and related disorders. *Nat Rev Neurosci*, 2007. 8(9): p. 663-72.
- 36.** Hoover, B.R., et al., Tau mislocalization to dendritic spines mediates synaptic dysfunction independently of neurodegeneration. *Neuron*, 2010. 68(6): p. 1067-81.
- 37.** Xu, J., et al., Tau-tubulin kinase 1 enhances prefibrillar tau aggregation and motor neuron degeneration in P301L FTDP-17 tau-mutant mice. *Faseb j*, 2010. 24(8): p. 2904-15.
- 38.** Mercken, M., et al., Monoclonal antibodies with selective specificity for Alzheimer Tau are directed against phosphatase-sensitive epitopes. *Acta Neuropathol*, 1992. 84(3): p. 265-72.
- 39.** Hanes, J., et al., Rat tau proteome consists of six tau isoforms: implication for animal models of human tauopathies. *J Neurochem*, 2009. 108(5): p. 1167-76.
- 40.** Bouskila, M., et al., TTBK2 kinase substrate specificity and the impact of spinocerebellar-ataxia-causing mutations on expression, activity, localization and development. *Biochem J*, 2011. 437(1): p. 157-67.

41. Watanabe, T., et al., TTBK2 with EB1/3 regulates microtubule dynamics in migrating cells through KIF2A phosphorylation. *J Cell Biol*, 2015. 210(5): p. 737-51.
42. Oda, T., et al., Binding to Cep164, but not EB1, is essential for centriolar localization of TTBK2 and its function in ciliogenesis. *Genes Cells*, 2014. 19(12): p. 927-40.
43. Taylor, L.M., et al., Pathological phosphorylation of tau and TDP-43 by TTBK1 and TTBK2 drives neurodegeneration. *Mol Neurodegener*, 2018. 13(1): p. 7.
44. Suzuki, K., et al., In vivo genome editing via CRISPR/Cas9 mediated homology-independent targeted integration. *Nature*, 2016. 540(7631): p. 144-149.
45. Ochalek, A., et al., Neurons derived from sporadic Alzheimer's disease iPSCs reveal elevated TAU hyperphosphorylation, increased amyloid levels, and GSK3B activation. *Alzheimers Res Ther*, 2017. 9(1): p. 90.
46. Sanchez-Ponce, D., A. Munoz, and J.J. Garrido, Casein kinase 2 and microtubules control axon initial segment formation. *Mol Cell Neurosci*, 2011. 46(1): p. 222-34.
47. Sun, X., et al., Selective filtering defect at the axon initial segment in Alzheimer's disease mouse models. *Proc Natl Acad Sci U S A*, 2014. 111(39): p. 14271-6.
48. Jones, S.L. and T.M. Svitkina, Axon Initial Segment Cytoskeleton: Architecture, Development, and Role in Neuron Polarity. *Neural Plast*, 2016. 2016: p. 6808293.
49. Ramkumar, A., B.Y. Jong, and K.M. Ori-McKenney, ReMAPPING the microtubule landscape: How phosphorylation dictates the activities of microtubule-associated proteins. *Dev Dyn*, 2018. 247(1): p. 138-155.
50. Freal, A., et al., Cooperative Interactions between 480 kDa Ankyrin-G and EB Proteins Assemble the Axon Initial Segment. *J Neurosci*, 2016. 36(16): p. 4421-33.
51. Liang, Z., et al., Cdk5 Regulates Activity-Dependent Gene Expression and Dendrite Development. *J Neurosci*, 2015. 35(45): p. 15127-34.
52. Yamada, R. and H. Kuba, Structural and Functional Plasticity at the Axon Initial Segment. *Front Cell Neurosci*, 2016. 10: p. 250.
53. Klinman, E., M. Tokito, and E.L.F. Holzbaur, CDK5-dependent activation of dynein in the axon initial segment regulates polarized cargo transport in neurons. *Traffic*, 2017. 18(12): p. 808-824.
54. Bond, J., et al., A centrosomal mechanism involving CDK5RAP2 and CENPJ controls brain size. *Nat Genet*, 2005. 37(4): p. 353-5.
55. Mori, Y., et al., Cep169, a Novel Microtubule Plus-End-Tracking Centrosomal Protein, Binds to CDK5RAP2 and Regulates Microtubule Stability. *PLoS One*, 2015. 10(10): p. e0140968.
56. Fong, K.W., et al., CDK5RAP2 is a pericentriolar protein that functions in centrosomal attachment of the gamma-tubulin ring complex. *Mol Biol Cell*, 2008. 19(1): p. 115-25.
57. Shintomi, M., et al., Identification of Cep169-interacting proteins and the in vivo modification sites of Cep169 via proteomic analysis. *Biochem Biophys Res Commun*, 2018. 495(3): p. 2275-2281.
58. Mori, Y., et al., Microtubule-bundling activity of the centrosomal protein, Cep169, and its binding to microtubules. *Biochem Biophys Res Commun*, 2015. 467(4): p. 754-9.
59. Mori, Y., et al., Phosphorylation of the centrosomal protein, Cep169, by Cdk1 promotes its dissociation from centrosomes in mitosis. *Biochem Biophys Res Commun*, 2015. 468(4): p. 642-6.
60. Kuijpers, M. and C.C. Hoogenraad, Centrosomes, microtubules and neuronal

- development. *Mol Cell Neurosci*, 2011. 48(4): p. 349-58.
- 61.** Sanchez-Huertas, C., et al., Non-centrosomal nucleation mediated by augmin organizes microtubules in post-mitotic neurons and controls axonal microtubule polarity. *Nat Commun*, 2016. 7: p. 12187.
- 62.** Cunha-Ferreira, I., et al., The HAUS Complex Is a Key Regulator of Non-centrosomal Microtubule Organization during Neuronal Development. *Cell Rep*, 2018. 24(4): p. 791-800.
- 63.** Matuoka, K., et al., A novel ligand for an SH3 domain of the adaptor protein Nck bears an SH2 domain and nuclear signaling motifs. *Biochem Biophys Res Commun*, 1997. 239(2): p. 488-92.
- 64.** Thalappilly, S., et al., Identification of multi-SH3 domain-containing protein interactome in pancreatic cancer: a yeast two-hybrid approach. *Proteomics*, 2008. 8(15): p. 3071-81.
- 65.** Kurochkina, N. and U. Guha, SH3 domains: modules of protein-protein interactions. *Biophys Rev*, 2013. 5(1): p. 29-39.
- 66.** Witte, H., D. Neukirchen, and F. Bradke, Microtubule stabilization specifies initial neuronal polarization. *J Cell Biol*, 2008. 180(3): p. 619-32.
- 67.** Murphy, S.E. and T.P. Levine, VAP, a Versatile Access Point for the Endoplasmic Reticulum: Review and analysis of FFAT-like motifs in the VAPome. *Biochim Biophys Acta*, 2016. 1861(8 Pt B): p. 952-961.
- 68.** Fedorenko, O.A., et al., Intracellular calcium channels: inositol-1,4,5-trisphosphate receptors. *Eur J Pharmacol*, 2014. 739: p. 39-48.
- 69.** Gomez-Navarro, N. and E. Miller, Protein sorting at the ER-Golgi interface. *J Cell Biol*, 2016. 215(6): p. 769-778.
- 70.** Park, S.Y. and X. Guo, Adaptor protein complexes and intracellular transport. *Biosci Rep*, 2014. 34(4).
- 71.** Antonny, B., et al., Membrane fission by dynamin: what we know and what we need to know. *Embo j*, 2016. 35(21): p. 2270-2284.
- 72.** McGough, I.J., et al., Identification of molecular heterogeneity in SNX27-retromer-mediated endosome-to-plasma-membrane recycling. *J Cell Sci*, 2014. 127(Pt 22): p. 4940-53.
- 73.** Nagano, F., et al., Rabconnectin-3, a novel protein that binds both GDP/GTP exchange protein and GTPase-activating protein for Rab3 small G protein family. *J Biol Chem*, 2002. 277(12): p. 9629-32.
- 74.** Sudhof, T.C., Neurotransmitter release: the last millisecond in the life of a synaptic vesicle. *Neuron*, 2013. 80(3): p. 675-90.
- 75.** Song, S.H. and G.J. Augustine, Synapsin Isoforms and Synaptic Vesicle Trafficking. *Mol Cells*, 2015. 38(11): p. 936-40.
- 76.** Harris, T.W., et al., Mutations in synaptojanin disrupt synaptic vesicle recycling. *J Cell Biol*, 2000. 150(3): p. 589-600.
- 77.** Schiavo, G., et al., Cytoplasmic dynein heavy chain: the servant of many masters. *Trends Neurosci*, 2013. 36(11): p. 641-51.
- 78.** Tortosa, E., L.C. Kapitein, and C.C. Hoogenraad, Microtubule Organization and Microtubule-Associated Proteins (MAPs), in *Dendrites: Development and Disease*, K. Emoto, et al., Editors. 2016, Springer Japan: Tokyo. p. 31-75.
- 79.** Liu, Y., J.W. Lee, and S.L. Ackerman, Mutations in the microtubule-associated protein 1A (Map1a) gene cause Purkinje cell degeneration. *J Neurosci*, 2015. 35(11): p. 4587-98.
- 80.** van Haren, J., et al., Dynamic microtubules catalyze formation of navigator-TRIO complexes to regulate neurite extension. *Curr Biol*, 2014. 24(15): p. 1778-85.
- 81.** Chahrouh, M.H., et al., Whole-exome sequencing and homozygosity analysis implicate depolarization-regulated neuronal genes in

autism. *PLoS Genet*, 2012. 8(4): p. e1002635.

82. Ebrahimi-Fakhari, D. and M. Sahin, Autism and the synapse: emerging mechanisms and mechanism-based therapies. *Curr Opin Neurol*, 2015. 28(2): p. 91-102.

83. Kapitein, L.C., K.W. Yau, and C.C. Hoogenraad, Microtubule dynamics in dendritic spines. *Methods Cell Biol*, 2010. 97: p. 111-32.

84. Hoogenraad, C.C., et al., GRIP1 controls dendrite morphogenesis by regulating EphB receptor trafficking. *Nat Neurosci*, 2005. 8(7): p. 906-15.

85. Lansbergen, G., et al., CLASPs attach microtubule plus ends to the cell cortex through a complex with LL5beta. *Dev Cell*, 2006. 11(1): p. 21-32.

86. Lu, M. and K.S. Kosik, Competition for microtubule-binding with dual expression of tau missense and splice isoforms. *Mol Biol Cell*, 2001. 12(1): p. 171-84.

87. Brummelkamp, T.R., R. Bernards, and R. Agami, A system for stable expression of short interfering RNAs in mammalian cells. *Science*, 2002. 296(5567): p. 550-3.

88. van Beuningen, S.F.B., et al., TRIM46 Controls Neuronal Polarity and Axon Specification by Driving the Formation of Parallel Microtubule Arrays. *Neuron*, 2015. 88(6): p. 1208-1226.

89. Kahn, O.I., et al., APC2 controls dendrite development by promoting microtubule dynamics. *Nat Commun*, 2018. 9(1): p. 2773.

90. Ekkebus, R., et al., On terminal alkynes that can react with active-site cysteine nucleophiles in proteases. *J Am Chem Soc*, 2013. 135(8): p. 2867-70.

91. Meijering, E., et al., Design and validation of a tool for neurite tracing and analysis in fluorescence microscopy images. *Cytometry A*, 2004. 58(2): p. 167-76.

92. Ferreira, T.A., et al., Neuronal morphometry directly from bitmap images. *Nat Methods*, 2014. 11(10): p. 982-4.

Materials & methods

Animals, primary neuron cultures and neuron transfections

Experiments involving animals were approved by the Dutch Animal Experiments Committee (DEC) and performed in agreement with guidelines of Utrecht University, Dutch law (Wet op de Dierproeven, 1996) and European regulations (Guideline 86/609/EEC). Adult animals were at least ten weeks old and housed with a companion in a room with a temperature of $22 \pm 1^\circ\text{C}$ and a 12 hour light-dark cycle. Animals had unrestricted access to water and food, and were provided with paper tissue and wood-chip bedding for nest building and cage enrichment.

The procedure for obtaining primary hippocampal dissociated neuron cultures was previously described in detail [83]. Hippocampi or cortices were derived from E18.5 pups from pregnant Wistar rats (Janvier or Charles River), and primary cortical neuron cultures were prepared in the same way as primary hippocampal neuron cultures.

For transfection and imaging, 100k hippocampal neurons were plated per well of a 12-well plate containing 18 mm glass coverslips coated with poly-L-lysine (37.5 $\mu\text{g}/\text{mL}$, Sigma) and laminin (1.25 $\mu\text{g}/\text{mL}$, Roche). For blotting experiments, 600k cortical neurons were plated per well of a 6-well plate (without coverslips) coated as described above. Neurons were maintained at 37°C and 5% CO_2 in full medium (Neurobasal medium (Gibco) supplemented with 2% B27 (Gibco), 0.5 mM glutamine (Gibco), 15.6 μM glutamate (Sigma-Aldrich) and 1% penicillin-streptomycin (Gibco)), although for a subset of experiments penicillin-streptomycin was replaced by Antibiotic Antimycotic Solution (Sigma #A5955). This did not visibly affect culture health.

The neuron transfection procedure using Lipofectamine 2000 (Invitrogen) is described in a previous chapter (chapter 3).

Cell cultures and associated transfections

COS-7 and HEK cells were cultured in 50/50 DMEM/Ham's F10 medium (DMEM: Lonza or Biowest, Ham's F10: Lonza) supplemented with 10% FBS (Sigma) and 1% penicillin-streptomycin (Sigma). COS-7 cells were used for imaging experiments, seeded in 12-well plates and transfected at a confluency of $\sim 40\%$. For transfection, 1 μg DNA was mixed with 2.5 μl Fugene 6 (Promega) in 100 μl Ham's F10 and incubated for 20 minutes. Medium was refreshed, and the DNA/Fugene mix was added dropwise to the cells. Cells were incubated for 12-24 hours at $37^\circ\text{C}/5\% \text{CO}_2$ up until the moment of fixation.

HEK cells were used for biochemical assays, seeded in 10 cm dishes and transfected at a confluency of $\sim 70\%$. For transfection (all experiments except mass spectrometry), 20 μg DNA was mixed with 60 μl MaxPEI (Polysciences) in 1 ml Ham's F10. The DNA/PEI mix was added dropwise to the cells after medium refreshment. Cells were incubated for 24 hours at $37^\circ\text{C}/5\% \text{CO}_2$ up until the moment of lysis. For mass spectrometry experiments, 12 μg DNA was mixed with 36 μl MaxPEI (Polysciences) in 1 ml Ham's F10 and cells were incubated for 48 hours at $37^\circ\text{C}/5\% \text{CO}_2$ up until the moment of lysis.

DNA and shRNA constructs

The following DNA constructs were described before: p β -actin-HA- β -Galactosidase [84]; GW1-GFP/HA-Gas2L1 WT/SxAA, bioGFP-Gas2L1 and all associated truncations, GW1-GFP/HA-ABD and GW1-GFP/HA-ABD-Tail (chapter 3); pCI-Neo-BirA [85]; GFP-TTBK1-KD and GFP-TTBK2-KD as well as all other GFP-tagged +TIPs featured in Fig S3 [2].

GW1-YFP-Gas2L1-CFP was created using standard molecular cloning strategies, by inserting Gas2L1 into *Ascl/Sall* sites of GW1-mYFP-mCFP. GW1-YFP-Gas2L1-CFP@304 was created in two steps; first, by inserting Gas2L1(1-304) into *Ascl/Sall* sites of GW1-mYFP-mCFP, and second, by creating CFP-5xGly-Gas2L1(305-681)-stop using overlap extension PCR and using it to replace CFP in the *Sall/EcoRI* sites of GW1-YFP-Gas2L1(1-304)-CFP.

GW1-GFP/HA-TTBK1/2 and associated truncations were created using PCR with GFP-TTBK1/2 as template, kindly provided by Dr. Kai Jiang [2] and based on human cDNA (TTBK1; HUGE ORK07236/AB058758 restored to full-length by overlap PCR. TTBK2; imaGene IRATp970H0888D/BC071556). TTBK1-cat consisted of amino acids 38-319 based on [30]. TTBK2-SCA11 consisted of amino acids 1-450 based on [18]. GFP-Tau4R was derived from human tau 0N4R cDNA (described in [86]) and cloned into a pEGFP-C1 backbone.

GW1-GFP-NCKAP5L (neuronal expression) and bioGFP-NCKAP5L (mass spectrometry experiment) were created using PCR with GFP-NCKAP5L as template, kindly provided by Dr. Kai Jiang [2] and based on murine cDNA (Riken C230021P08/ NM_001001884).

shRNA sequences were inserted into *HindIII* and *BglIII* sites of the pSuper backbone [87]. The following targeting sequences were used, all based on rat cDNA sequences: TTBK1 shRNA #2 – CAGATGTCAACCGTAACAA, TTBK2 shRNA #1 – GGTATGACCATAGGCTCAT, NCKAP5L shRNA #1 - GACCTCAGAATCCCTAAGT, NCKAP5L shRNA #2 - GAGTTCCTGAATCCCTTGT, NCKAP5L shRNA #3 - CAAGTCGTTTCGTCTGGAT. For qPCR validation of NCKAP5L shRNAs, we inserted the puromycin resistance sequence of pSuper.puro into *EcoRI/BamHI* sites of pSuper-NCKAP5L-shRNA.

Antibodies and reagents

The following antibodies and staining reagents were used for immunofluorescence experiments: chicken-anti- β -galactosidase (1:2500, Aves Labs #BGL-1040); mouse-anti-HA (1:500, Roche 1-666-606, clone 12CA5); mouse-anti-alpha-tubulin (1:1000, Sigma #T-5168, clone #B-5-1-2); mouse-anti-EB1 (1:100, BD Biosciences #610535); mouse-anti-EB3 (1:200, BD Transduction lab #E39120); mouse-anti-AnkyrinG (1:200, Zymed #33-8800, clone #4G3F8); rabbit-anti-TRIM46 serum (1:500, described in [88]); mouse-anti-Sodium Channel (1:2,000, Sigma #S8809); mouse-anti-tau (1:800, Chemicon #MAB3420); mouse-anti-centrin (1:300, Millipore/Merck #04-1624, clone #20H5); rabbit-anti-ACIII (1:500, Santa Cruz #sc-588, clone #C-200); rabbit-anti-NCKAP5L (1:200, Sigma #HPA041034); rabbit-anti-TTBK1 #1 (1:500, Abcam #ab103944); rabbit-anti-TTBK1 #2 (1:200, Absea, custom raised against amino acids 851-1050 of GST-tagged TTBK1); rabbit-anti-TTBK2 #1 (1:100, Proteintech #15072-1-AP); goat-anti-mouse Alexa 405 (1:400, Thermo Fischer Scientific #A31553); goat-anti-mouse Alexa 488 (1:400, Thermo Fischer Scientific #A11029); goat-anti-mouse Alexa 568 (1:400, Thermo Fischer Scientific #A11031); goat-anti-rabbit Alexa 488

(1:400, Thermo Fischer Scientific #A11034); goat-anti-rabbit Alexa 568 (1:400, Thermo Fischer Scientific #A11036); goat-anti-chicken Alexa 568 (1:400, Thermo Fischer Scientific #A11041); Alexa Fluor 594 Phalloidin (1:50, Thermo Fischer Scientific #A12381); CellTracker 488 (C2925, Thermo Fischer Scientific).

The following antibodies and staining reagents were used for Western blotting: rabbit-anti-GFP (1:5,000, Abcam #ab290); mouse-anti-HA (1:2,000, Biolegend/Covance #mms-101p, clone #16B12); mouse-anti-actin (1:10,000, Chemicon #MAB1501R, clone #C4); mouse-anti-tauAT8 (1:5,000, Thermo Scientific #MN1020); rabbit-anti-tau (1:1,000, Abcam #ab64193); rabbit-anti-TTBK1 #1 (1:500, Abcam #ab103944); rabbit-anti-TTBK2 #1 (1:500, Proteintech #15072-1-AP); goat-anti-mouse IRDye680LT (1:20,000, LI-COR #926-68020); goat-anti-mouse IRDye800CW (1:15,000, LI-COR #926-32210); goat-anti-rabbit IRDye680LT (1:20,000, LI-COR #926-68021); goat-anti-rabbit IRDye800CW (1:15,000, LI-COR #926-32211).

The following reagents were used for drug treatments: taxol (Enzo Life Sciences) and vinblastine sulfate (Sigma Aldrich) diluted in DMSO. Stock solutions of 10 mM were stored at -80°C and -20°C, respectively. Rapalog (635056 A/C Heterodimerizer, Takara) was diluted in ethanol. A stock solution of 100 µM was stored at -20°C.

Immunofluorescence microscopy

For co-stainings including mouse-anti-centrin, cells were fixed for 10 minutes at -20°C in MeOH supplemented with 1 mM EGTA. For co-stainings including mouse-anti-EB1/3, cells were fixed for 5 minutes at -20°C in MeOH supplemented with 1 mM EGTA, immediately followed by 5 minutes fixation at room temperature in 4% PFA/4% sucrose. All other stainings were preceded by 10 minutes fixation at room temperature in 4% PFA/4% sucrose. The rest of the immunofluorescence staining protocol for neurons and COS-7 cells follows that described in chapter 3.

Fixed cells were imaged on one of three setups:

- 1) a Nikon Eclipse 80i upright fluorescence microscope (Photometrics CoolSNAP HQ2 CCD camera, Nikon NIS Br Software, Plan Apo VC 100x N.A. 1.40 oil/Plan Apo VC 60x N.A. 1.40 oil/Plan Fluor 40x N.A. 1.30 oil/Plan Fluor 20x N.A. 0.75 oil objectives);
- 2) a Nikon Eclipse Ni-U upright fluorescence microscope (Nikon DS-Qi2 Mono Digital Microscope Camera, Nikon NIS Br software, Plan Apo Lambda 100x N.A. 1.45 oil/Plan Apo Lambda 60x N.A. 1.40 oil/Plan Fluor 40x N.A. 1.30 oil/Plan Fluor 20x N.A. 0.75 oil objectives), or
- 3) a Zeiss LSM 700 confocal laser scanning microscope (Type: Axio Observer Z1, 405/488nm/555nm laserlines, ZEN 2011 software, EC Plan-Neofluar 40x/1.30 Oil DIC/Plan-Apochromat 63x/1.40 Oil DIC objectives).

Live cell imaging, FRAP & rapalog-induced heterodimerization

Live imaging and FRAP was performed on an inverted Nikon Eclipse Ti-E confocal microscope (Nikon perfect focus system, Yokogawa CSU-X1-A1 Spinning Disc unit, Photometrics Evolve 512 EMCCD camera, Roper Scientific ILas FRAP unit, Plan Apo VC 100x N.A.1.40 oil objective or Plan

Apo VC 60x N.A.1.40 oil objective). During imaging, neurons were maintained at 37°C and 5% CO₂ in a stage incubator (Tokai Hit).

To FRAP GFP-Gas2L1 in COS-7 cells (Fig 1D), we chose areas near the cell periphery where GFP-Gas2L1 showed MT-based localization. FRAP regions were scanned 20x using a maximum power Cobolt Calypso 491 nm (100 mW) laser resulting in a FRAP pulse of 720 ms, which was kept identical for all acquisitions. Before the FRAP pulse, we acquired 5 frames at 1 sec/frame that were used to determine baseline fluorescence intensity. After the FRAP pulse, we acquired images at the following intervals: 0.4 sec/frame for 5 seconds, 1 sec/frame for 20 seconds, 5 sec/frame for 30 seconds. Resulting FRAP curves were corrected for bleaching and background signals, and the acquisition sequence was fully automated to prevent inconsistencies in timing of the FRAP pulse.

We followed a similar procedure to FRAP GFP-Gas2L1 in neurons (Fig 1E). FRAP regions were scanned 24x resulting in a 550-600 ms FRAP pulse. We acquired 5 frames at 1 sec/frame pre-FRAP, and imaged at the following intervals post-FRAP: 0.4 sec/frame for 8 seconds, 1 sec/frame for 30 seconds, 5 sec/frame for 60 seconds.

Live imaging of rapalog-induced dimerization was performed on an inverted Nikon Eclipse Ti-E confocal microscope as described above. Images were acquired every 30 seconds to a total of 1.5 hours. Rapalog (1:1000) was added after time point 10.

Lysates for spectrophotometry and Western blotting

For spectrophotometry (Fig 3D, E), transfected HEK cells were collected in pre-chilled PBS supplemented with 5 mM MgCl₂ and 0.5x protease inhibitors (Roche). Cells were then spun down for 5 minutes at 1000 rpm/4°C, after which the supernatant was removed and the cell pellet was resuspended in FRET lysis buffer (20 mM TRIS-HCl pH 7.5, 100 mM NaCl, 1% Triton X-100, 10% glycerol, protease inhibitors (Roche)). The pellet was then homogenized and incubated on ice for 15 minutes, followed by 20 minutes centrifugation at 13,000 rpm/4°C. The supernatant was aliquoted in single-use vials, snap frozen and stored at -80°C. Up until obtaining fluorescence emission spectra, lysates were thawed and kept on ice.

For endogenous tau AT8 phosphorylation experiments in cortical neurons (Fig 5C), lysates were created by washing neurons 1x with pre-warmed PBS (37°C), aspirating the PBS and immediately moving neurons on ice. We then added 100 µl 2x DTT+ sample buffer (20% glycerol, 4% SDS, 200 mM DTT, 100 mM TRIS-HCl pH 6.8, bromophenol blue) per well of a 6-well plate, scraped the neurons and boiled lysates for 10 minutes at 95°C. For one experiment included in the quantification shown in Fig 5C, we supplemented the DTT+ sample buffer with phosphatase and protease inhibitors (both Roche). This did not produce phosphorylation ratios different from experiments performed without inhibitors.

For TTBK tau phosphorylation experiments in HEK cells (Fig 5D), lysates were created in lysis buffer according to Sato et al., 2006 (50 mM TRIS-HCl pH 7.5, 150 mM NaCl, 2 mM EDTA, 10% glycerol, 1% Triton X-100, protease and phosphatase inhibitors [30]). Cells were washed once with pre-warmed PBS (37°C), scraped in 100 µl lysis buffer and centrifuged for 15 minutes at

13.2 krpm at 4°C, after which the supernatant was separated from the pellet. DTT+ sample buffer was then added (to 1x) to supernatants and lysates were boiled for 10 minutes at 95°C.

Whole brain lysates used to detect TTBK expression in various brain regions (Fig 6A) were derived from brains of adult female Wistar rats (Charles River) and kindly provided by Dr. Josta Kevenaar.

Cortical neuron lysates used to detect TTBK expression at different DIVs (Fig 6B) were identical to those used to detect NDE1/NDEL1 expression in Figure 1B of chapter 2 [1]. Prior to probing expression levels, sample loading volumes were calculated to equalize total protein levels based on actin signals on Western blot. Due to the size of TTBK proteins relative to actin, actin loading controls could not be included on the same gel, but are comparable to those shown in Figure 1B of chapter 2.

All lysates were stored at -80°C.

λ protein phosphatase treatment

bioGFP-Gas2L1 fusions were co-expressed with pCl-Neo-BirA (ratio 3:1) in HEK293 cells. Cells were harvested in ice-cold PBS supplemented with 5 mM MgCl₂ and 0.5x protease inhibitor cocktail (Roche), pelleted by centrifuging for 5 minutes at 1000 rpm/4°C and then resuspended in pulldown lysis buffer (50mM Tris-HCl pH 7.5, 233mM NaCl, 0.5% Triton X-100, 5mM MgCl₂, protease inhibitors (Roche)). After 20 minutes incubation on ice, lysates were spun down for 20 minutes at 13.2krpm/4°C. Supernatants were then incubated in the presence of magnetic bioGFP beads (Invitrogen Dynabeads M-280 Streptavidin; pre-blocked by 1 hour incubation with 20 mM Tris-HCl pH 7.5, 150mM KCl, 0.2ug/ul chicken egg albumin at 4°C) for 45 minutes at 4°C, to bind bioGFP to the beads.

Following incubation, beads were washed 5x in wash buffer (20mM Tris-HCl pH 7.5, 150mM KCl, 0.1% Triton X-100). At the last wash step, beads were split in half. Half of the beads was immediately eluted by boiling for 10 minutes in the presence of 2x DTT+ sample buffer (20% glycerol, 4% SDS, 200 mM DTT, 100 mM TRIS-HCl pH 6.8, bromophenol blue), representing phosphorylated samples. The other half of the beads was incubated with λ protein phosphatase (NEB/Bioke) for 1 hour at 4°C, followed by 30 min incubation at RT. Dephosphorylated samples were then eluted as described for phosphorylated samples. All samples were stored at -20°C prior to blotting.

Western blotting

For tau blots, the blotting procedure was identical to that described in chapter 3. For TTBK blots, we employed wet transfer (120 minutes at 300 mA) instead of semi-dry transfer. All other steps were identical to those described in chapter 3.

Spectrophotometry

Emission spectra in Fig 3D were obtained with a Cary Eclipse Fluorescence Spectrophotometer (Agilent Technologies) using the following settings to measure emission per 40 μ l of lysate in a quartz cuvette:

Data mode	Fluorescence	Scan rate (nm/min)	600
Scan mode	Emission	Data interval (nm)	1
X mode	Wavelength (nm)	Averaging time (s)	0.1
Start (nm)	450	Excitation filter	Auto
Stop (nm)	625	Emission filter	Open
Ex. wavelength (nm)	425	PMT Voltage (V)	Medium
Ex. slit (nm)	5	Corrected spectra	Off
Em. slit (nm)	5		

qPCR

NCKAP5L qPCR experiments (Fig 7B) were included alongside Gas2L1 qPCR experiments, for which the methods are detailed in chapter 3 and Kahn et al., 2018 [89]. The following primer pairs were used: NCKAP5L 5'-GCACTTGACAGGCTAATGA and 3'-CCAGGTCAAACACCCTCTTC; GAPDH 5'-TGCCCCATGTTTGTGATG and 3'-TGTGGTCATGAGCCCTCC; β -actin 5'-AGGCCAACCGTAAAAGATG and 3'-CCAGAGGCATACAGGGACAAC.

Mass spectrometry analysis of NCKAP5L binding partners

Murine bioGFP-NCKAP5L was co-expressed with BirA in HEK293 cells transfected as described above. Cell lysis was performed in RIPA buffer (50 mM TrisHCl pH 7.4-7.8, 150 mM NaCl, 1% Triton X-100, 0.1% SDS, 0.5% Sodium Deoxycholate, protease inhibitors) by incubating for 30 minutes on ice. Following lysis, samples were centrifuged for 15 min at 17949 g/rcf at 4°C and supernatants were incubated with pre-blocked magnetic beads (Dynabeads M-280, Invitrogen; blocking with chicken egg albumin) for 1 hour at 4°C. Following incubation, beads were washed five times in wash buffer (20 mM Tris-HCl pH 7.4-7.8, 150 mM KCl, 0.1% Triton X-100) and, in case of identifying binding partners of NCKAP5L from HEK293 cell lysates, immediately processed for mass spectrometry analysis as described below.

In case of identifying brain-specific interactors, magnetic beads pre-incubated with HEK293 cell lysates as described above were washed twice in low salt wash buffer (20 mM Tris-HCl pH 7.4-7.8, 100 mM KCl, 0.1% Triton X-100), twice in high salt wash buffer (20 mM Tris-HCl pH 7.4-7.8, 500 mM KCl, 0.1% Triton X-100) and finally twice in low salt wash buffer in an effort to clear interacting proteins transferred from HEK293 cells. To obtain whole brain lysates, brains were dissected from female adult rats and homogenized in 10x volume/weight in tissue

lysis buffer (50 mM TrisHCl, 150 mM NaCl, 0.1% SDS, 0.2% NP-40, protease inhibitors). Whole brain lysates were centrifuged for 10 minutes at 17494 g/rcf and 4°C and the supernatant was incubated with bioGFP-NCKAP5L-bound magnetic beads for 2 hours at 4°C. Following incubation, beads were washed five times in wash buffer and processed for mass spectrometry analysis.

Following washing steps, proteins bound to beads were eluted in 4x Laemmli sample buffer (Bio-Rad) and loaded on a pre-cast Criterion XT Bis-Tris gradient gel (Bio-Rad). The gel was then fixed in 40% MeOH/10% acetic acid and stained using colloidal coomassie dye G-250 (Thermo Scientific). Gel lanes were sliced up, destained and digested with trypsin according to procedures described in [90]. Following trypsinization, peptides were extracted in acetonitrile, dried and reconstituted in 10% formic acid.

Mass spectrometry analysis was performed on an Orbitrap Q-Exactive mass spectrometer (Thermo Fisher Scientific) coupled to an Agilent 1290 Infinity LC (Agilent Technologies) according to procedures detailed in [62].

Data analysis and statistics

All fluorescence images and Western blots were analysed and processed using ImageJ software. The dynamic range of images was adjusted for display purposes. Conditions that were compared quantitatively were imaged on the same microscope using identical settings between individual conditions. All quantitative measurements of fluorescence intensity, both for microscopy images and Western blots, were performed on raw images and corrected for background levels by subtracting the average fluorescence intensity of a nearby, identically sized background region.

To perform Sholl analyses (Fig 6H, S2E), we first used the NeuronJ plugin [91] to manually trace dendrites. Tracings were then converted to black-and-white images, which were analysed using the Sholl Analysis plugin for ImageJ [92]. We manually selected the center of the soma and calculated the starting radius based on the original image, and manually confined the number of primary dendrites. Finally, two samples were measured per radius, with step sizes of 10 μm .

Statistical analyses were performed in GraphPad 5. Normally distributed data was compared using One-way ANOVA, followed by Tukey's post hoc tests. Datasets that did not satisfy the normality assumption, as determined by Shapiro-Wilk test, were compared using Mann-Whitney U test or Kruskal-Wallis test followed by Dunn's Multiple Comparison post hoc tests. Significance was defined as $p \leq 0.05$; tests were two-tailed. Statistical tests used for each experiment are detailed in the figure legends.

> **Figure S1. Supplement to Figure 5.**

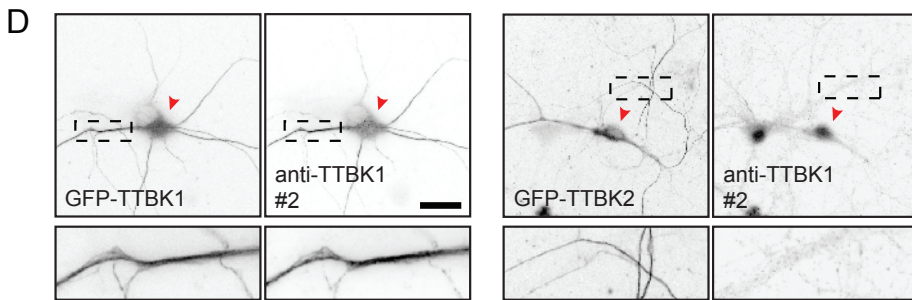
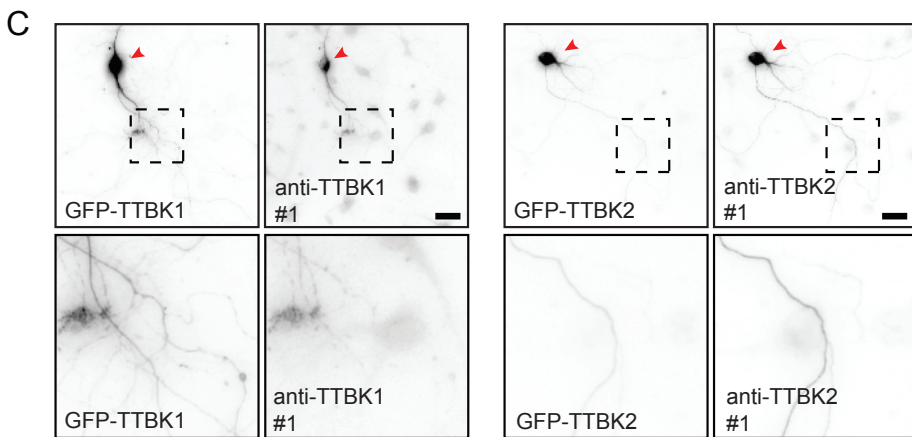
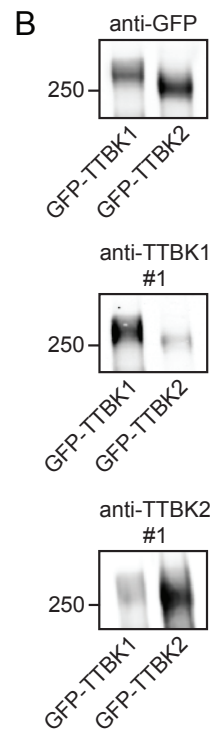
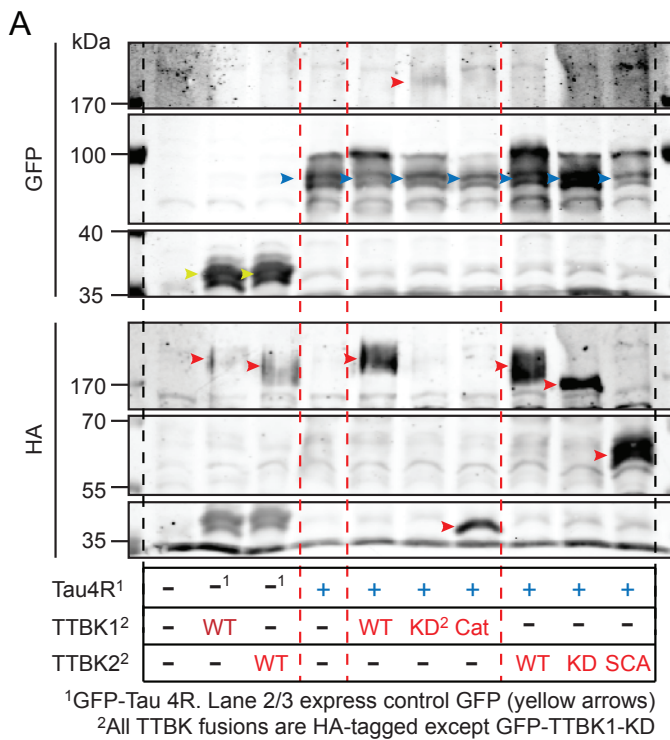
(A) Western blot detection of GFP (yellow arrowheads), GFP-Tau4R (blue arrowheads) and GFP-TTBK1-KD (red arrowhead) using an anti-GFP probe (top) and other HA-TTBK fusions (red arrowheads) using an anti-HA probe (bottom) in HEK cell lysates used for Fig 5D. Dashed lines indicate separation between marker lanes and experimental conditions (black) or groups of experimental conditions (red).

(B) Specificity of TTBK antibodies on western blot: GFP-TTBK1 and GFP-TTBK2 were overexpressed in HEK cells, and lysates were probed with anti-GFP (top), anti-TTBK1 #1 (middle) or anti-TTBK2 #1 (bottom).

(C) Detection of GFP-TTBK fusions with rabbit-anti-TTBK1 antibody #1 in MeOH/PFA fixed DIV11 hippocampal neurons overexpressing GFP-TTBK1 (left), and of TTBK2 using rabbit-anti-TTBK2 antibody #1 in PFA fixed DIV11 hippocampal neurons overexpressing GFP-TTBK2 (right). Red arrowheads indicate the soma of transfected neurons, boxed regions are enlarged below.

(D) Detection and specificity of rabbit-anti-TTBK1 antibody #2 in MeOH/PFA DIV10 neurons overexpressing GFP-TTBK1 (left) or GFP-TTBK2 (right). Red arrowheads indicate the soma of transfected neurons, boxed regions are enlarged below.

Scale bars: 30 μm in (C), 25 μm in (D).



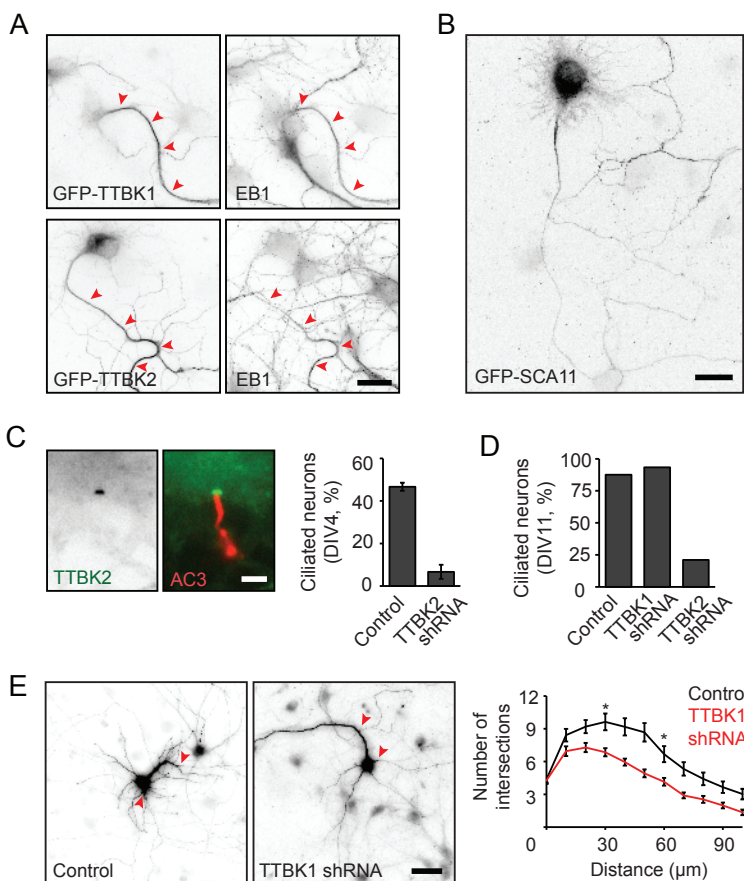


Figure S2. Supplement to Figure 6.

(A) Effect of TTBK1 and TTBK2 overexpression on endogenous EB1 localization in DIV4 hippocampal neurons. Red arrowheads indicate the axon.

(B) Localization of GFP-TTBK2-SCA11 (TTBK2 1-450) in a DIV7 hippocampal neuron.

(C) Left: GFP-TTBK2 localizes to the base of cilia as evident from its position relative to the cilium marker Adenylyl Cyclase III (AC3). Right: Percentage of ciliated DIV4 neurons transfected with control vector (pSuper-empty) or TTBK2 shRNA. 14-15 neurons were counted per condition in two independent experiments.

(D) Effect of TTBK1/2 shRNA on the population of ciliated DIV11 hippocampal neurons, transfected at DIV7. 16-19 neurons were counted that were also included in the Sholl analyses presented in Figure (S2E) and Figure (2H).

(E) Sholl analysis of dendrite morphology of DIV11 hippocampal neurons transfected for four days with pSuper-empty (control) or pSuper-TTBK1-shRNA. Red arrowheads indicate the axon, which is excluded from analysis. $n=23-30$ neurons from two independent experiments. Controls neurons are partially the same as shown in Fig 6H, as TTBK1/2-shRNA conditions were included simultaneously in one experiment.

Mann Whitney U test (E), *; $p < 0.05$. Scale bars: $20 \mu\text{m}$ in (A, B), $2 \mu\text{m}$ in (C), $50 \mu\text{m}$ in (E).

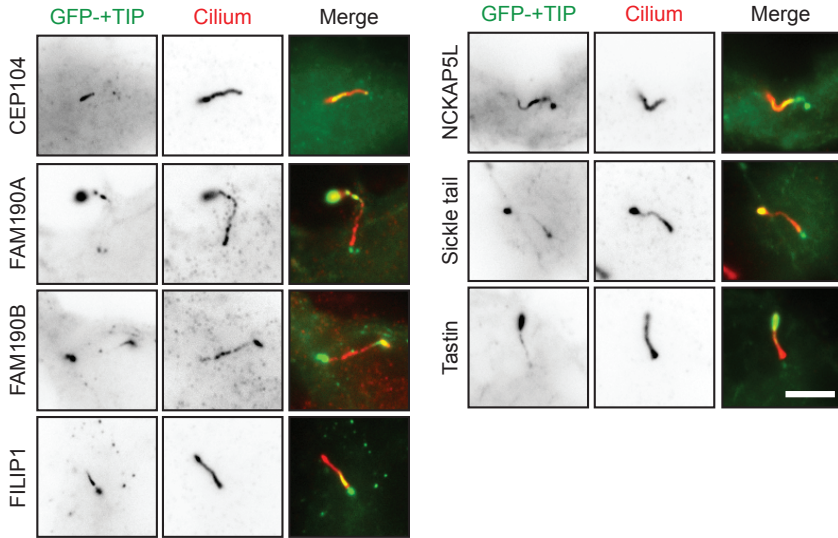


Figure S3. +TIPS and the primary neuronal cilium.

Localization of overexpressed GFP-+TIPs (specified to the left) with respect to cilia as labelled by ACIII staining in DIV8 neurons. Scale bar: 5 μ m.

Supplementary table SI. Localization of various overexpressed +TIPs in young (DIV4-8) primary hippocampal neurons.

+TIP	Subcellular localization	EB1 co-localization	Other confirmed co-localizations	Remarks
Amer2	Somatodendritic membrane	+	F-actin (weak)	Reduced number of EB comets upon overexpression
CEP104	Centriole; Cilium	+++	Pericentrin; ACIII	Only localizes to daughter centriole and cilium tip
CTTNBP2	Centrioles; Granular pattern throughout neuron	+		
CytospinB	Diffuse (low expression); Somatodendritic bundles (high expression)	+		Bundles are mildly positive for EBs
Eg5	Diffuse	-		
Fam190A	Proximal axon; Cilium; Stretches in proximal neurites	+++	Pericentrin; ACIII; Overexpressed NDEL1	Localizations strongly differ among individual neurons; Localizes to tip of cilium; Recruits overexpressed NDEL1
Fam190B	Centrioles; Stretches at most distal tips of growth cones	++		Short isoform is more diffuse
FILIP1	Dots and stretches along neurites (low expression); Somatodendritic bundles (high expression)	+		
Gas2L1	F-actin (medium-low expression); Bundles (high expression)	++	F-actin; Microtubules (weak)	Recruits EBs
Gas2L2	Somatodendritic F-actin (medium-low expression); Bundles (high expression)	+	F-actin	Recruits EBs

Supplementary table SI (continued)

+TIP	Subcellular localization	EB1 co-localization	Other confirmed co-localizations	Remarks
GTSE1	Stretches in tips of neurites (medium-low expression); Microtubules (high expression)	+++		
iASPP	Diffuse	-		
NCKAP5	Axon; Cilium	++	Tau gradient ACIII (weak)	Recruits EBs to tau gradient
NCKAP5L	Centrioles; Cilium (occasional); Granular pattern throughout neuron	+++	ACIII (occasional)	
Ras11b	Diffuse	-		
Skt	Cell-cell junctions; Cilium; Centrioles	+	N-Cadherin; B-catenin; ACIII	Enhances endogenous N-Cadherin and β -catenin intensity
Syntabulin	Mitochondria	+	Cytochrome-C	Recruits EBs (weak)
Tastin	Cilium; Filamentous localization	+++	ACIII	
TTBK1	Microtubules; Axon	++	Tau gradient	Recruits EBs
TTBK2	Diffuse; Proximal axon; Distal axon; Cilium (basal body)	+	Tau gradient; ACIII	Localizations strongly differ among individual neurons and depend on auto-phosphorylation

5



General discussion

General discussion

The question that drove most of the work presented in this thesis was: what are the roles of recently identified microtubule plus-end tracking proteins (+TIPs) in neurodevelopment? In parallel with our results, which primarily concern axon development, a number of other studies have reported interesting observations. We here consider our findings in light of recent developments.

Chapter 1, 3 and 4 prominently feature a number of +TIPs. To summarize, Chapter 1 reviews the state of the neuronal +TIP field as of early 2016. In Chapter 3, we show that the SxIP protein Gas2L1 regulates axon maturation via a complex autoinhibitory mechanism. Gas2L1 does not track growing microtubule (MT) plus-ends, but rather recruits EBs to actin in neurons. We further characterize Gas2L1 in Chapter 4, suggesting that its SxIP motif contributes to binding selectivity, and describe our findings concerning a number of other +TIPs that were screened over the course of this thesis. We explore the putative role of TTBKs in pathological tau phosphorylation and show data which suggests that NCKAP5L is required for axon formation. The implications of these results are extensively discussed in Chapters 3 and 4, and we therefore focus on discussing key findings from other studies and different types of +TIP behaviours here.

5

Ankyrin-G, the master scaffolding protein of the axon initial segment, is a +TIP

A recurring theme in this body of work is the function of the axon initial segment (AIS), where axon potentials are generated. The AIS also maintains neuronal polarity by forming a barrier between the somatodendritic and axonal compartments. Interestingly, formation of the AIS was shown to rely on interactions between EB proteins and the SxIP motifs of Ankyrin-G [1]. The giant isoform of Ankyrin-G (480 kDa) is required for AIS assembly and scaffolds other AIS components [1, 2]. Loss of Ankyrin-G prompts proximal axons to assume dendritic identities [3].

Ankyrin-G was recently re-discovered as a +TIP and found to interact with EB1/3 via twelve C-terminal SxIP motifs, of which ten are exclusively found in the giant isoform [1, 4]. Notably, at the AIS, an immobile subpopulation of EB proteins resides at the MT lattice rather than at the plus-end [4, 5]. This subpopulation is established by Ankyrin-G, but at the same time contributes to the recruitment of

Ankyrin-G in a positive feedback loop [1].

Ankyrin-G is among the most widely studied AIS proteins, and is routinely labelled in immunostainings to mark the AIS. Why, then, has it evaded identification as a +TIP for so long?

Newly emerging behaviours of +TIPs away from the MT plus-end

Classically, EBs are considered to recruit other +TIPs to the MT plus-end via interactions with SxIP motifs or CAP-gly domains (reviewed in [6]). This results in the characteristic comet-like localization patterns associated with +TIPs. In spite of its numerous SxIP motifs, Ankyrin-G does not localize to MT plus-ends during AIS formation and in mature neurons. Surprisingly however, prior to neuronal polarization, Ankyrin-G does behave as a classical +TIP and exogenous Ankyrin-G tracks growing MT plus-ends in COS-7 cells [1]. The change in plus-end tracking behaviour seems to stem from Ankyrin-G's recruitment to the membrane: co-expressing transmembrane ion channels that bind Ankyrin-G results in EB accumulation at the membrane of COS-7 cells instead [1].

Ankyrin-G utilizes immobilized EBs to capture fasciculated MT bundles at the AIS [1]. This model uproots the conventional hierarchy of EB proteins as core scaffolding proteins at the MT plus-end, and suggests that EBs can themselves be scaffolded on different structures. Indeed, in Chapter 3, we report similar behaviour for Gas2L1. The protein tightly binds EBs through its SxIP motif, which results in translocation of EBs onto neuronal actin filaments instead of Gas2L1 accumulation at the MT plus-end. EB recruitment was also observed for Gas2L1 on stress fibres of NIH3T3 cells, where it was proposed to aid MT alignment [7]. Along the same lines, myomegalin was shown to scaffold EB proteins at the Golgi membrane through its SxIP motif [8, 9]. Reminiscent of Ankyrin-G's EB-mediated MT lattice binding, the population of myomegalin-bound EBs mediates attachment of MT minus-ends to the Golgi via weak interactions with the MT lattice [1, 10].

From these studies, it is becoming clear that EBs can also be scaffolded by other +TIPs, which so far seems to correlate with a function for aligning and/or capturing the MT shafts. In this light, it is interesting to take a closer look at the list of candidate SxIP proteins extracted from a computational screening of the mammalian proteome [11]. This study correctly predicted Ankyrin-G as a candidate +TIP. Three other large neuronal scaffolding proteins, the synaptic proteins SHANK1

(post-synaptic; reviewed in [12]) and Piccolo and Bassoon (pre-synaptic; reviewed in [13]), also contain multiple predicted SxIP motifs. Whether they associate with EBs remains to be investigated. Although the presence of MTs at synaptic terminals has historically been challenging to confirm due to their dynamic nature, MTs have since been identified as part of post-synapses [14, 15] and some evidence exists that they may also be part of pre-synapses (reviewed in [16]). It will be interesting to see whether these other familiar neuronal scaffolding proteins will emerge as +TIPs like Ankyrin-G did, and to study the function of their large number of putative SxIP motifs.

A link between primary neuronal cilia and +TIPs

EB1 and EB3 were found to aid primary cilium formation in a number of mammalian cell lines [17, 18]. This function is proposed to rely on a similar, plus-end-independent mechanism, namely the anchoring of MT minus-ends to the basal body by EB proteins [17]. A surprising number of +TIPs examined in Chapter 4 localizes to the primary cilium of neurons upon overexpression (Fig S3 of Chapter 4). Although localization varied between individual neurons, the majority of these +TIPs are seen entering the cilium, rather than just accumulating at the basal body where EBs may reside.

EBs do enter motile cilia of *Chlamydomonas* (green algae) and can do so independently of intraflagellar transport (IFT), which regulates the transport of most proteins into the cilium. *Chlamydomonas* EB proteins also interact with the IFT protein IFT172 at the cilium tip [19-21]. Furthermore, EBs are also found at the tip of motile mammalian cilia [17]. The presence of mammalian EBs seems to depend largely on the type of cilium, however (reviewed in [22]). To our knowledge, neuronal cilia have not been examined in this context, but it is tempting to suggest that there is a link between certain types of cilia and plus-end tracking proteins.

Interestingly, not all tested +TIPs accumulated in neuronal cilia. Neither did overexpressed EB3-tagRFP-T nor short SxIP-containing peptides used to visualize MT plus-ends in cells (MACF18 and MACF43; described in [23]). This suggests that plus-end tracking and/or an SxIP motif is not sufficient to enter the neuronal cilium. It remains possible that the high number of +TIPs seen localizing to cilia is a coincidence, but it is worthwhile to examine whether the SxIP motif contributes to this frequently observed behaviour as it appears to be the only similarity between

this subset of proteins. Following up on these observations may uncover new ways of regulating ciliary protein entry besides IFT pathways.

Before the function of NDEL at the AIS: the pre-axonal exclusion zone and myosins

Chapter 2 describes how the retrograde cytoplasmic dynein motor and its regulators NDEL1 and LIS1 are responsible for transporting mis-sorted dendritic cargoes out of the AIS. NDEL1 is immobilized at the AIS cortex via a direct interaction with the master AIS scaffolding protein Ankyrin-G. We here discuss a number of studies that have since added context to this AIS vesicle filtering mechanism, and reaffirm the possibility of NDEL1 acting as an indirect, immobilized regulator of dynein.

Polarized cargo sorting establishes and maintains the identity of both axons and dendrites. It is therefore essential for neuronal function, and likely to rely on additional safeguarding mechanisms in combination with the AIS pathway described in Chapter 2. Indeed, we show that displacing NDEL1 from the AIS by depleting Ankyrin-G does not lead to complete axonal invasion of somatodendritic cargoes. Rather, reversals spread out over a longer portion of the axon while the distal axon remains free of mis-sorted cargo. This suggests that NDEL1 clustering at the AIS is a way of locally boosting the efficiency of reversals by dynein, instead of an absolute requirement.

Farias and colleagues identified the ‘pre-axonal exclusion zone’ (PAEZ), a region between the soma and the AIS where about half of somatodendritic vesicles are already turned back before reaching the AIS [24]. It seems likely that the PAEZ and AIS work in tandem to ensure complete exclusion of mis-sorted cargoes. One of the questions remaining is how the activity of various motor proteins is coordinated to achieve a reversal at the AIS. Somatodendritic vesicles may pass the PAEZ when they are artificially linked to anterograde kinesin motors [24], suggesting that mis-sorted vesicles arrive at the AIS while being transported by kinesins. The uniform plus-end out orientation of axonal MTs reaffirms the need for anterograde motors.

Janssen et al. showed that there may subsequently be a function for actin-based myosin motors. Myosin-V can stall kinesin-driven vesicles at the AIS by immobilizing them at actin patches, but cannot drive retrograde transport back to the soma [25]. Together, these studies paint a more complete picture of axonal cargo filtering as relying on multiple regions and coordination of all three classes of motor proteins (Fig 1A).

Remote-controlled motor proteins, fact or fiction?

Since publishing the role of AIS-based NDEL1 in polarized cargo transport, the finding was featured in graphical representations of the AIS in a number of reviews (e.g. [26-28]). These depictions all show NDEL1 as associating with dynein on MTs and Ankyrin-G simultaneously, which does not necessarily follow from the data presented in Chapter 2.

Endogenous NDEL1 binds the C-terminus of Ankyrin-G, which is indeed coupled to MTs via EB proteins [1, 29]. The 480 kDa isoform of Ankyrin-G is estimated to extend its C-terminus approximately 150 nm into the AIS cytoplasm [30]. Estimates for the size of the cytoplasmic dynein complex range from ~35-50 nm [31-33], and average vesicle diameters may range from ~20 nm for synaptic vesicles to ~100 nm for dense core vesicles in rat brains [34, 35]. These numbers suggest that the C-terminus of giant Ankyrin-G could in fact extend far enough to scaffold NDEL1 near vesicle-bound dynein motors, which are themselves close enough to MTs to initiate retrograde transport. However, we reported that we could efficiently rescue retrograde transport in NDEL1-depleted neurons by overexpressing chimeric fusions of NDEL1 to the 270 or 480 kDa isoforms of Ankyrin-G, but also by fusing NDEL1 to neurofascin-186 (Fig 1B).

Neurofascin-186 is a transmembrane cell adhesion protein native to the AIS. It harbours a small, C-terminal intracellular domain of only ~120 amino acids which normally binds Ankyrin-G [36, 37]. Therefore, a neurofascin-NDEL1 chimera places NDEL1 much closer to the membrane than the giant isoform of AnkG would. This scenario presumably imposes sterical constraints, which limits the possibility of NDEL1 promoting dynein motility on MTs via a direct interaction with the motors bound to the vesicles. Is it possible that AIS-based NDEL1 affects vesicle-bound dynein indirectly or controls the activity of the local pool of dynein without physically interacting with the moving vesicles? We show that the turnover of NDEL1 in the AIS is low, indicating that NDEL1 is tightly bound to the cortex. The rescue ability of the neurofascin-NDEL chimera also limits options for NDEL1 retrieval from the AIS cortex, considering that the endocytosis of neurofascin is specifically blocked in the AIS [38]. Taken together, our results show that NDEL1 is immobile at the AIS cortex, and suggest that non-direct modes of the regulation of vesicle-associated dynein should be considered.

Uniting models for NDEL1 function at the AIS

A follow-up study showed that NDEL1 requires phosphorylation by cdk5 to promote dynein activity in the AIS, and confirms that it does so together with the +TIP LIS1 [39]. In their model, the authors suggest that NDEL1 dissociates from Ankyrin-G upon phosphorylation and forms a complex with LIS1. The cytoplasmic complex then binds to and activates dynein. However, NDEL1 dissociation is not addressed in the study. A non-phosphorylatable NDEL1 mutant is shown to localize to the AIS,

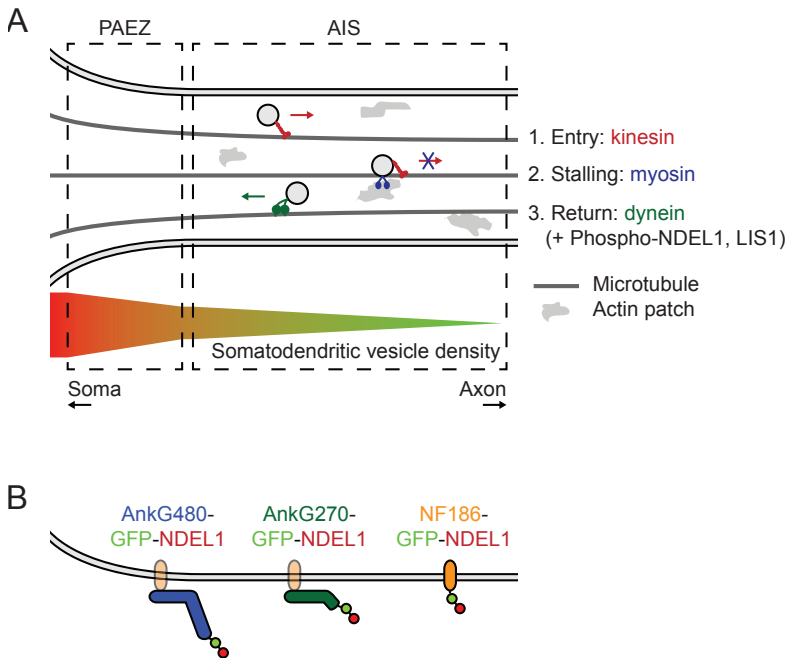


Figure 1. Updated models of neuronal cargo sorting.

(A) Approximately 50% of mis-sorted somatodendritic cargo that enters the axon is filtered at the pre-axonal exclusion zone (PAEZ) located at the axon hillock, just in front of the axon initial segment (AIS). The remainder reverses in the AIS. Prior to reversal, vesicles are stalled by myosin anchoring on actin patches. Reversal is dynein-dependent and relies on NDEL1 (phosphorylated by cdk5) and LIS1.

(B) Overview of NDEL1 chimeric fusion mutants capable of activating dynein in the AIS.

suggesting that phosphorylation is not required for AIS localization of NDEL1 [39]. According to the dissociation model, a phosphomimetic NDEL1-mutant is expected to be diffuse, but was not tested. Furthermore, we found that cortically anchored NDEL1 mutants are functional alternatives to endogenous NDEL1. It therefore remains possible, especially in light of our data, that NDEL1 remains immobile at the AIS cortex in both phosphorylated (active) and dephosphorylated (inactive) states.

In Chapter 2, we entertain the possibility that LIS1 acts as a shuttle between NDEL1 on the AIS cortex and dynein on vesicles. This is based on observations that LIS1 is also enriched at the AIS and required for local dynein activity. However, in contrast to NDEL1, levels of LIS1 enrichment vary greatly between neurons. The protein exhibits fast turnover times, indicating that it remains motile although it can be concentrated at the AIS. Most interestingly, LIS1 depletion results in reduced levels of NDEL1 bound to Ankyrin-G. This suggests that LIS1 contributes to the AIS-bound pool of NDEL1, perhaps by forming a complex with it on the cortex. We propose that a cortical association between NDEL1 and LIS1 may 'prime' the quickly diffusing LIS1, perhaps via phosphorylation or a conformational change, resulting in a local pool of primed LIS1 that can intercept and activate dynein.

While our model remains speculative too, Klinman and colleagues provide evidence for the last step: LIS1 binding to dynein is required for the AIS vesicle filter to function [39]. With respect to NDEL1 phosphorylation by cdk5, it is possible that phospho-NDEL is required for association with LIS1 at the AIS cortex instead of in the cytoplasm or on dynein directly. To reconcile the two models, it will be interesting to see whether phospho-NDEL1 still associates with Ankyrin-G and how NDEL1 phospho-mutants affect the levels of LIS1 enrichment at the AIS. It will be informative to test whether a NDEL1 mutant that can bind LIS1, but not dynein, is able to efficiently activate dynein at the AIS.

Prospects for indirect regulation of motor proteins

It is important not to ignore the possibility of indirect motor protein regulation as it opens up novel therapeutic possibilities. If certain regulators remain potent when immobilized, they may be targeted to restricted areas of the cell where they can locally control vesicle trafficking. A similar principle was recently described for KIF1A-mediated transport of dense core vesicles [40]. Two regulators of KIF1A, TANC2 and liprin- α , localize to dendritic spines where they are proposed to capture

KIF1A and thereby dense core vesicles. This study utilizes the same experiment as we performed for NDEL1 in Chapter 2. In this case, a chimeric fusion of TANC2 to neurofascin-186 immobilizes TANC2 at the AIS, which results in local modulation of KIF1A-based transport [40]. While the mechanisms by which TANC2 and NDEL1 regulate their respective motor protein binding partners are likely dissimilar, these experiments illustrate the potential of immobilized motor protein regulators.

Concluding remarks

During the past five years, both new functions and new working mechanisms have emerged for neuronal +TIPs. It is clear that the body of knowledge about this class of proteins is far from complete. Prominent neuronal proteins maintain their status as candidate +TIPs, and data hint that essentially unstudied +TIPs like NCKAP5L may have key functions in establishing neuronal polarity. The challenge remains in dissecting the contribution of EB binding for each of these proteins. This becomes important especially now that roles for +TIPs away from the MT plus-end are starting to challenge the status quo. The same can be said for the regulation of motor proteins, which may occur not just through cytosolic binding partners, but also through immobilized and potentially distant regulators. It will be exciting to see how the neuronal cytoskeleton field advances in the next years. The ability to modify and label different proteins using CRISPR/Cas-based methodologies is expected to provide exciting advances in this research area, as it allows us to observe the behaviour of proteins at endogenous levels and in their native environment. This will be especially powerful in combination with technical advances in the field of microscopy.

References

1. Freal, A., et al., Cooperative Interactions between 480 kDa Ankyrin-G and EB Proteins Assemble the Axon Initial Segment. *J Neurosci*, 2016. 36(16): p. 4421-33.
2. Jenkins, P.M., et al., Giant ankyrin-G: a critical innovation in vertebrate evolution of fast and integrated neuronal signaling. *Proc Natl Acad Sci U S A*, 2015. 112(4): p. 957-64.
3. Hedstrom, K.L., Y. Ogawa, and M.N. Rasband, AnkyrinG is required for maintenance of the axon initial segment and neuronal polarity. *J Cell Biol*, 2008. 183(4): p. 635-40.
4. Letierrier, C., et al., End-binding proteins EB3 and EB1 link microtubules to ankyrin G in the axon initial segment. *Proc Natl Acad Sci U S A*, 2011. 108(21): p. 8826-31.
5. Nakata, T. and N. Hirokawa, Microtubules provide directional cues for polarized axonal transport through interaction with kinesin motor head. *J Cell Biol*, 2003. 162(6): p. 1045-55.
6. Akhmanova, A. and M.O. Steinmetz, Microtubule +TIPs at a glance. *J Cell Sci*, 2010. 123(Pt 20): p. 3415-9.
7. Stroud, M.J., et al., GAS2-like proteins mediate communication between microtubules and actin through interactions with end-binding proteins. *J Cell Sci*, 2014. 127(Pt 12): p. 2672-82.
8. Wang, Z., C. Zhang, and R.Z. Qi, A newly identified myomegalin isoform functions in Golgi microtubule organization and ER-Golgi transport. *J Cell Sci*, 2014. 127(Pt 22): p. 4904-17.
9. Roubin, R., et al., Myomegalin is necessary for the formation of centrosomal and Golgi-derived microtubules. *Biol Open*, 2013. 2(2): p. 238-50.
10. Yang, C., et al., EB1 and EB3 regulate microtubule minus end organization and Golgi morphology. *J Cell Biol*, 2017. 216(10): p. 3179-3198.
11. Jiang, K., et al., A Proteome-wide screen for mammalian SxIP motif-containing microtubule plus-end tracking proteins. *Curr Biol*, 2012. 22(19): p. 1800-7.
12. Monteiro, P. and G. Feng, SHANK proteins: roles at the synapse and in autism spectrum disorder. *Nat Rev Neurosci*, 2017. 18(3): p. 147-157.
13. Gundelfinger, E.D., C. Reissner, and C.C. Garner, Role of Bassoon and Piccolo in Assembly and Molecular Organization of the Active Zone. *Front Synaptic Neurosci*, 2015. 7: p. 19.
14. Hu, X., et al., Activity-dependent dynamic microtubule invasion of dendritic spines. *J Neurosci*, 2008. 28(49): p. 13094-105.
15. Jaworski, J., et al., Dynamic microtubules regulate dendritic spine morphology and synaptic plasticity. *Neuron*, 2009. 61(1): p. 85-100.
16. Bodaleo, F.J. and C. Gonzalez-Billault, The Presynaptic Microtubule Cytoskeleton in Physiological and Pathological Conditions: Lessons from Drosophila Fragile X Syndrome and Hereditary Spastic Paraplegias. *Front Mol Neurosci*, 2016. 9: p. 60.
17. Schroder, J.M., et al., EB1 and EB3 promote cilia biogenesis by several centrosome-related mechanisms. *J Cell Sci*, 2011. 124(Pt 15): p. 2539-51.
18. Schroder, J.M., et al., EB1 is required for primary cilia assembly in fibroblasts. *Curr Biol*, 2007. 17(13): p. 1134-9.
19. Harris, J.A., et al., Single-particle imaging reveals intraflagellar transport-independent transport and accumulation of EB1 in *Chlamydomonas* flagella. *Mol Biol Cell*, 2016. 27(2): p. 295-307.
20. Pedersen, L.B., et al., The Microtubule plus end-tracking protein EB1 is localized to the flagellar tip and basal bodies in *Chlamydomonas reinhardtii*. *Curr Biol*, 2003. 13(22): p. 1969-74.

21. Pedersen, L.B., et al., Chlamydomonas IFT172 is encoded by FLA11, interacts with CrEB1, and regulates IFT at the flagellar tip. *Curr Biol*, 2005. 15(3): p. 262-6.
22. Larsen, J., et al., Analysis of microtubule plus-end-tracking proteins in cilia. *Methods Enzymol*, 2013. 524: p. 105-22.
23. Honnappa, S., et al., An EB1-binding motif acts as a microtubule tip localization signal. *Cell*, 2009. 138(2): p. 366-76.
24. Farias, G.G., et al., Sorting of Dendritic and Axonal Vesicles at the Pre-axonal Exclusion Zone. *Cell Rep*, 2015. 13(6): p. 1221-1232.
25. Janssen, A.F.J., et al., Myosin-V Induces Cargo Immobilization and Clustering at the Axon Initial Segment. *Front Cell Neurosci*, 2017. 11: p. 260.
26. Zhang, C. and M.N. Rasband, Cytoskeletal control of axon domain assembly and function. *Curr Opin Neurobiol*, 2016. 39: p. 116-21.
27. Nirschl, J.J., A.E. Ghiretti, and E.L.F. Holzbaur, The impact of cytoskeletal organization on the local regulation of neuronal transport. *Nat Rev Neurosci*, 2017. 18(10): p. 585-597.
28. Letierrier, C., The Axon Initial Segment: An Updated Viewpoint. *J Neurosci*, 2018. 38(9): p. 2135-2145.
29. Kuijpers, M., et al., Dynein Regulator NDEL1 Controls Polarized Cargo Transport at the Axon Initial Segment. *Neuron*, 2016. 89(3): p. 461-71.
30. Jones, S.L., F. Korobova, and T. Svitkina, Axon initial segment cytoskeleton comprises a multiprotein submembranous coat containing sparse actin filaments. *J Cell Biol*, 2014. 205(1): p. 67-81.
31. Johnson, K.A. and J.S. Wall, Structure and molecular weight of the dynein ATPase. *J Cell Biol*, 1983. 96(3): p. 669-78.
32. Amos, L.A., Brain dynein crossbridges microtubules into bundles. *J Cell Sci*, 1989. 93 (Pt 1): p. 19-28.
33. Vallee, R.B., et al., Microtubule-associated protein 1C from brain is a two-headed cytosolic dynein. *Nature*, 1988. 332(6164): p. 561-3.
34. Castorph, S., et al., Structure parameters of synaptic vesicles quantified by small-angle x-ray scattering. *Biophys J*, 2010. 98(7): p. 1200-8.
35. May, R.M., et al., Estradiol regulates large dense core vesicles in the hippocampus of adult female rats. *Brain Struct Funct*, 2014. 219(6): p. 1947-54.
36. Davis, J.Q. and V. Bennett, Ankyrin binding activity shared by the neurofascin/L1/NrCAM family of nervous system cell adhesion molecules. *J Biol Chem*, 1994. 269(44): p. 27163-6.
37. Herron, L.R., et al., The intracellular interactions of the L1 family of cell adhesion molecules. *Biochem J*, 2009. 419(3): p. 519-31.
38. Yap, C.C., et al., Doublecortin (DCX) mediates endocytosis of neurofascin independently of microtubule binding. *J Neurosci*, 2012. 32(22): p. 7439-53.
39. Klinman, E., M. Tokito, and E.L.F. Holzbaur, CDK5-dependent activation of dynein in the axon initial segment regulates polarized cargo transport in neurons. *Traffic*, 2017. 18(12): p. 808-824.
40. Stucchi, R., et al., Regulation of KIF1A-Driven Dense Core Vesicle Transport: Ca(2+)/CaM Controls DCV Binding and Liprin-alpha/TANC2 Recruits DCVs to Postsynaptic Sites. *Cell Rep*, 2018. 24(3): p. 685-700.

&



Appendix

Curriculum vitae	220
List of publications	223
English summary	224
Nederlandse samenvatting	230
Acknowledgements	236

Curriculum vitae

Biography

Dieudonné van de Willige was born in Antwerp (Belgium) on October 24, 1990.

In addition to the scientific activities presented in this CV, Dieudonné worked as regional columnist for Dutch newspaper De Telegraaf from 2012 to 2016. Throughout 2012, she took on the role of first 'campus columnist' of Utrecht University.

Apart from column writing and pursuing a PhD, she actively focussed on science communication of both her own research and that of colleagues. Notable examples include over fifteen shows in theatres and high schools across the Netherlands with ScienceBattle.

As of 2018, she is fully committed to science communication of the natural and hard sciences specifically.

Education

- | | |
|-----------|---|
| 2013-2019 | PhD Molecular Neurobiology, Cell Biology Dept., Utrecht University
Promotors: Prof. Dr. Casper Hoogenraad
Prof. Dr. Anna Akhmanova |
| 2011-2013 | MSc Molecular & Cellular Life Sciences, Utrecht University
Minor track 'Science Communication and Education'
Honours track 'Young Leaders League'
<i>Cum laude</i> distinction |
| 2008-2011 | BSc Chemistry, Utrecht University
Honours track for Chemistry students
<i>Cum laude</i> distinction |
| 2007 | Cambridge Certificate in Advanced English (CAE)
Grade A |



Teaching

- 2016 Daily supervisor of master's student nine-month research internship
A potential role for TTBK1 and TTBK2 for microtubule stability in the AIS of hippocampal neurons
by M. A. Post
- 2015 Daily supervisor of master's student nine-month research internship
The relation between microtubules, tau and tau kinases in the context of neurological diseases
by E. van Leeuwen
- 2014 Daily supervisor of bachelor's theses
(1) *The Influence of the +TIP Fam190B on neuronal development*
by V. A. Buijs
(2) *A Possible Role for TTBK2 in Neurodevelopment*
by J. Hanrath

Conference visits & poster presentations

- 2017 EMBO Cell Biology of the Neuron (Heraklion, GR)
- 2016 GRC Cell Biology of the Neuron + poster (Waterville Valley, USA)
- 2015 Science for Life Conference + poster (Utrecht, NL)
- 2014 Dutch BioPhysics Meeting + poster (Veldhoven, NL)
- 2013 Dutch BioPhysics Meeting (Veldhoven, NL)

Prizes & Awards

- 2015 Poster prize Science for Life Conference
- 2012 Erik Hardeman-stipendium (for best column)
- 2011 Wetfil award (for best column)

List of publications on next page >>





List of publications

Van de Willige, D.*, Alkemade, C.*, Hummel, J. J. A.*, Kahn, O.I., Dogterom, M., Koenderink, G. H.#, Hoogenraad, C. C.#, Akhmanova, A.# Cytolinker Gas2L1 regulates axon morphology through microtubule-modulated actin stabilization. In revision.

Freal, A., Rai, D., Tas, R. P., **van de Willige, D.**, Stucchi, R., Aher, A., Yang, C., Altelaar, A. F. M., Vocking, K., Post, J. A., Harterink, M., Kapitein, L. C., Akhmanova, A.#, Hoogenraad, C. C.# Feedback-driven assembly of the axon initial segment. In revision.

Kahn, O. I., Schatzle, P., **van de Willige, D.**, Tas, R. P., Lindhout, F. W., Portegies, S., Kapitein, L. C., Hoogenraad, C. C. (2018). APC2 controls dendrite development by promoting microtubule dynamics. **Nature Communications**, 9(1), 2773. doi:10.1038/s41467-018-05124-5

Bouchet, B. P., Gough, R. E., Ammon, Y. C., **van de Willige, D.**, Post, H., Jacquemet, G., Altelaar, A. M., Heck, A. J., Goult, B. T.#, Akhmanova, A.# (2016). Talin-KANK1 interaction controls the recruitment of cortical microtubule stabilizing complexes to focal adhesions. **eLife**, 5. doi:10.7554/eLife.18124

Van de Willige, D., Hoogenraad, C. C.#, & Akhmanova, A.# (2016). Microtubule plus-end tracking proteins in neuronal development. **Cellular and Molecular Life Sciences**, 73(10), 2053-2077. doi:10.1007/s00018-016-2168-3

Kuijpers, M.*, **van de Willige, D.***, Freal, A., Chazeau, A., Franker, M. A., Hofenk, J., Kapitein, L. C., Akhmanova, A., Jaarsma, D., Hoogenraad, C. C. (2016). Dynein Regulator NDEL1 Controls Polarized Cargo Transport at the Axon Initial Segment. **Neuron**, 89(3), 461-471. doi:10.1016/j.neuron.2016.01.022

* Co-first author

Co-corresponding author



English summary for non-experts

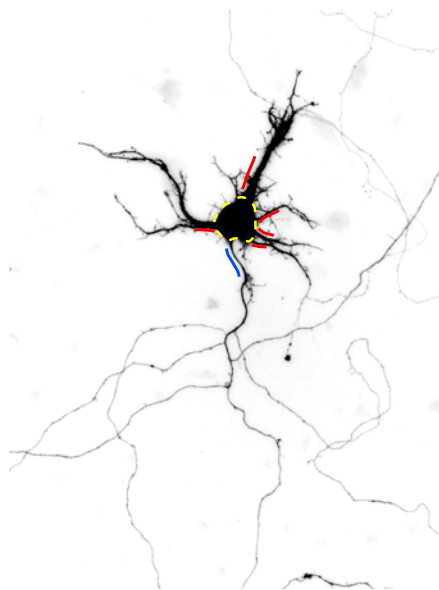
Brain cells – neurons – are the most complex cells in our body. Their function is complex, but so is their physical shape. This is not a coincidence: the shape of a neuron is closely related to how it does its job in the brain. The brain consists of billions of neurons, which are all connected and exchange signals with each other. Neurons therefore have roughly two functions, the sending and receiving of signals, which take place in two distinct areas of the cell.

Anatomy of a brain cell

Consider the silhouette of the neuron on the right. One of the two separate areas of the neuron is the somatodendritic compartment: this encompasses the neuron's *soma* or cell body (designated with the yellow dotted line), where genetic information is stored, and the *dendrites*, which are the thick extensions labelled in red. The dendrites receive information from other neurons by connecting to their *axons*. In case of the neuron pictured, the axon is labelled in blue.

The axon is the second sub-compartment of the neuron, and it is responsible for sending out signals to the other neurons by physically touching them.

The axon is a thin and highly branched structure that can reach lengths of a meter in humans. If the dendrites and axons of neurons are shaped the wrong way, they can't properly interconnect and the brain can't function.



So many shapes, so many questions

The fascinating shape of neurons poses some interesting questions. First of all, how does a neuron turn into something that elaborate over the course of its development? Neurons start out as small spheres, roughly the size of their cell body,

that somehow shapeshift into their mature form. Secondly, how can a single neuron maintain two different compartments without mixing up the components of each? Cells are essentially bags filled with molecules, and unless something keeps those molecules separated, they will mix.

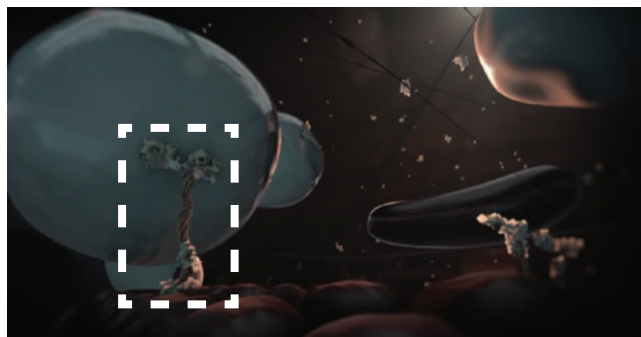
It is crucial for neurons to separate different molecules. Getting things mixed up would be like putting postage stamps on your mailbox: you need the stamp to send mail, not to receive it, and stamps become completely useless when you make them part of the receiving mechanism. A neuron, too, cannot send or receive signals when its specialized molecular building blocks are mis-sorted.

The cytoskeleton

Part of the answer to both of those questions lies in the so-called *cytoskeleton*. Like a human skeleton, one of the functions of the cytoskeleton is to provide structural support to the cell. However, the cell's skeleton is much more dynamic. By changing continuously, the cytoskeleton allows cells to quickly adapt their shape to the circumstances. The cytoskeleton controls the neuron's changing shape by stabilizing and destabilizing in specific places.

A second, crucial function of the cytoskeleton is to allow the transport of nutrients and other building blocks within the cell. In addition to providing structural support, the cytoskeleton serves as rails on which *motor proteins* walk. These motor proteins carry molecules around the cell. They provide the right nutrients in the right places at the right times, allowing neurons to grow. However, how this works is far from clear.

Computer animation of a motor protein (marked by the white dotted box) walking inside a cell, carrying encapsulated building blocks along the cytoskeleton which serves as cargo rails in addition to providing structural support.



Still taken from the Youtube movie 'Transport inside the brain: The basic mechanisms of neuronal trafficking' by the Hoogenraad Lab



Cytoskeletons and motor proteins are not unique to brain cells, but the large size and complexity of neurons does add unique challenges that these mechanisms must overcome. Not surprisingly, issues with the cytoskeleton and motor proteins cause a myriad of diseases, including diseases of the brain.

The contribution of this work

The work in this thesis sheds some light on the regulation of motor protein-based transport in neurons, as well as how the cytoskeleton controls the changing shape during the neuron's development. Understanding how a healthy neuron works may help the medical field come up with an informed strategy on how to treat neurological disorders.

Most of the work in this thesis focuses on the development of the axon, the long extension that sends out signals to other neurons. On the cytoskeleton-side of things, this thesis focuses mainly on *microtubules*: a subcomponent of the cytoskeleton that is used for long-range transport by motor proteins. Microtubules are microscopically small tubes that continuously shrink and grow.

Chapter 1 contains a review (an overview and discussion of scientific literature on a specific topic) about proteins that bind to the dynamic ends of microtubules ('+TIPs'). By binding there, they are able to control most of the properties of a microtubule: for example whether it grows or shrinks, how stable it is and whether the tube is anchored somewhere in the cell. In 2015, our lab discovered twenty new +TIPs. My PhD time started with a project to see which of those have important functions in neurons, as a lot of the previously identified +TIPs are involved in various brain diseases.

Chapter 2 looks into how the two neuronal subcompartments are kept separate. At the beginning of the axon, there is a small structure where motor proteins that carry the wrong type of building blocks turn around and head back out of the axon. For a long time, we knew that it happened, but not how.

In **Chapter 2**, we show which motor protein carries mis-sorted building blocks out of the axon. We also show that the reversal – and thus the separation of sending and receiving components – is controlled by a small protein that is immobilized at the beginning of the axon. Normally, this protein can touch the



motor protein itself as the motor protein travels. However, we prove that in this part of the axon, the protein does not leave its location on the axon's 'wall' the entire time. Both microtubules and the motor protein may be out of reach from that spot. Thus, we might have identified a new way of controlling motor proteins remotely. If true, it opens up interesting perspectives on how we can treat diseases that involve motor protein malfunction.

Chapter 3 deals with a protein called Gas2L1. Gas2L1 is one of the newly discovered proteins on the dynamic ends of microtubules, but it is also part of a family of proteins that connects different parts of the cytoskeleton to each other. For this particular protein, it had been shown that it can act as a cytoskeleton linker, but it didn't have a reported purpose in neurons. This is actually surprising: cooperation between various parts of the cytoskeleton is well-known to be required for neurons to mature, and another research group showed that there should be relatively large amounts of Gas2L1 in the brain.

We saw that removing Gas2L1 from young neurons causes their axons to develop the wrong way. That was to be expected, but in some ways Gas2L1 had the opposite effect from other, better-studied cytoskeleton linkers. We therefore needed to know more about how Gas2L1 works.

Fortunately, **Chapter 3** features a collaboration with a group that specializes in taking proteins outside of the cell. We literally took Gas2L1 out of the cell and brought it together with a cytoskeleton, which had also been built outside of cells. This is a powerful way of studying protein behaviour, because researchers control all the variables. You never know what else is influencing your result in the hyper-complex environment of a real cell. In this isolated context, we saw that Gas2L1 did not associate with either type of cytoskeleton, unless they were both present.

We eventually found that Gas2L1 folds on itself and keeps itself inactive until it encounters all parts of the cytoskeleton. Back in neurons, we saw that Gas2L1 controls axon development by stabilizing one part of the cytoskeleton. Because it's most active when not one, but two parts of the cytoskeleton are present, the other part of the cytoskeleton – the microtubules – determine where in the neuron Gas2L1 is active. Via Gas2L1, microtubules instruct other components of the cytoskeleton on how to collectively shape the axon.



Chapter 4 contains preliminary data: bits and pieces of information, which unfortunately don't paint a complete picture yet and/or need to be validated further. **Chapter 4** collects the most exciting preliminary results from looking at all the new proteins that associate with dynamic microtubule ends.

Chapter 4 contains more information about Gas2L1, which suggests that it is highly sensitive to its local environment. We also try to pinpoint the role of Gas2L1's association with the dynamic ends of microtubules, which appears to have something to do with this sensitivity, but unfortunately this largely remains unclear.

We further explore a family of proteins linked to Alzheimer's Disease. They associate with the dynamic plus-ends of microtubules, but they also modify *tau*, a protein central to Alzheimer's Disease, in a way that is mis-regulated in patients. Strangely, these proteins don't seem to be present in the same space as tau in healthy neurons. How can they modify it, then? This question is currently not considered in scientific literature. However, it will need to be addressed in order to evaluate how these proteins are linked to Alzheimer's Disease.

Lastly, we discuss NCKAP5L: a protein that hardly makes any appearance in scientific literature. We saw that neurons without NCKAP5L can't form an axon to begin with. It is clearly an extremely important protein, but unfortunately we didn't yet discover how or why.

Finally, **Chapter 5** discusses the above chapters in light of the newest scientific developments.

It makes two arguments: firstly, we should be aware that proteins that can associate with the dynamic ends of microtubules don't always do that, which has important consequences for how we consider this family of molecules.

Secondly, it makes the case for the existence of remote-controlled motor proteins as Chapter 2 seems to suggest, which is so far overlooked in scientific literature that discusses our study.



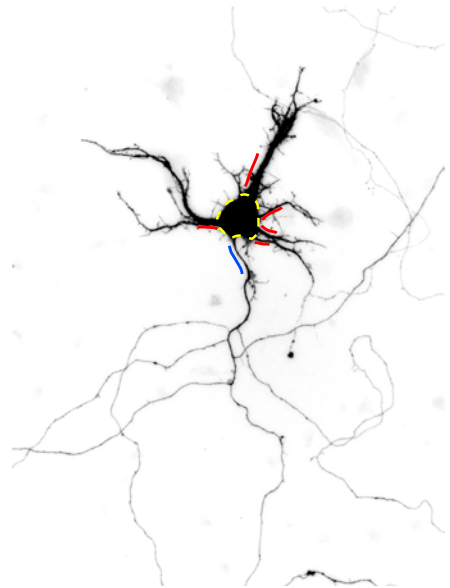


Nederlandse samenvatting voor non-experts

Hersencellen – zogenaamde neuronen – zijn de meest complexe cellen in ons lichaam. Hun functie is complex, maar hun fysieke vorm is dat ook. Dit is geen toeval: de vorm van een neuron is direct verbonden met de manier waarop hersencellen hun functie uitoefenen in het brein. Het brein bestaat uit miljarden neuronen, die met elkaar in verbinding staan om signalen uit te wisselen. Hersencellen hebben dus grofweg twee functies, het versturen en ontvangen van signalen, die zich afspelen in twee afzonderlijke gedeeltes van de cel.

De anatomie van een hersencel

Kijk naar het silhouet van de neuron rechts. Eén van de twee gedeeltes van hersencellen is het somatodendritische compartiment: dit bestaat uit het *soma* of cellichaam (aangegeven met de gele stippellijn), waar de genetische informatie opgeslagen is, en uit *dendrieten*, de dikke vertakkingen die met rood gemarkeerd zijn. De dendrieten ontvangen informatie van andere hersencellen, door verbinding te maken met de *axonen* van vele andere neuronen tegelijk. De axon van deze neuron is met blauw gemarkeerd.



De axon is tevens het tweede subcompartiment van de neuron. Axonen zijn verantwoordelijk voor het versturen van signalen naar andere hersencellen door fysiek contact met ze te maken. De axon is een dunne en sterk vertakte uitloper, die tot wel een meter lang kan worden in mensen. Als de axonen en dendrieten van neuronen de verkeerde vorm hebben, kunnen ze onderling niet de juiste verbindingen maken en kunnen de hersenen niet functioneren.



Zoveel vormen, zoveel vragen

De fascinerende vorm van neuronen roept een aantal vragen op. Ten eerste: hoe ontwikkelt een neuron zich tot zo'n uitgebreide en complexe cel? Neuronen beginnen als klein bolletje, ongeveer ter grootte van het cellichaam, die op een of andere manier van gedaante wisselen tot ze hun volwassen vorm bereikt hebben. Ten tweede: hoe kan een enkele hersencel twee verschillende compartimenten onderhouden, zonder dat de onderdelen van elk compartiment door elkaar raken? Cellen zijn in essentie niks meer dan zakken vol moleculen, en tenzij iets de moleculen actief uit elkaar houdt, zal alles vanzelf door de war raken.

Het uit elkaar houden van de moleculen is van cruciaal belang. Wanneer dat fout gaat, ontstaat een situatie vergelijkbaar het plakken van een postzegel op een brievenbus: postzegels zijn nodig om een brief te versturen, en door ze onderdeel te maken van het ontvangende systeem worden ze opeens nutteloos. Ook een hersencel kan geen signalen meer verzenden of ontvangen als er iets mis gaat met het sorteren van de gespecialiseerde moleculaire bouwstenen.

Het cytoskelet

Een deel van het antwoord op beide vragen schuilt in het zogenaamde *cytoskelet*. Eén van de functies van het cytoskelet is om, net als het menselijke skelet, fysieke ondersteuning te bieden aan de cel. Het cytoskelet is echter veel beweeglijker. Doordat het continu verandert, kunnen cellen hun vorm snel aanpassen aan de omstandigheden. Het cytoskelet stuurt de vormverandering van hersencellen door zich op bepaalde plekken te stabiliseren of juist te destabiliseren.

Een tweede, cruciale functie van het cytoskelet is het faciliteren van transport van voedingsstoffen en bouwstenen. Behalve voor fysieke ondersteuning, wordt het cytoskelet ook gebruikt als transportrails waarop *motoreiwitten* lopen. Motoreiwitten vervoeren moleculen binnen de cel. Ze zorgen ervoor dat de juiste bouwstenen op de juiste tijd en plaats aanwezig zijn, zodat de neuron kan groeien. Hoe dit precies werkt is echter nog lang niet duidelijk.

Cytoskeletten en motoreiwitten zijn aanwezig in veel meer soorten cellen dan hersencellen alleen, maar de ingewikkelde vorm van neuronen en vooral de grootte van de cellen maakt dat er unieke uitdagingen zijn die deze transportmechanismen moeten trotseren. Het is dan ook geen verrassing dat problemen met het cytoskelet en motoreiwitten verschillende aandoeningen veroorzaken, waaronder hersenziekten.



Computeranimatie van een motoreiwit (gemarkeerd met witte stippellijn) dat door een cel loopt, en daarbij moleculaire bouwstenen vervoert. Het motoreiwit loopt op het cytoskelet.



Fragment uit het Youtubefilmje 'Transport inside the brain: The basic mechanisms of neuronal trafficking' van het Hoogenraadlab

De bijdrage van dit werk

Het werk in deze thesis geeft enerzijds meer inzicht in de regulatie van bouwsteentransport binnen neuronen, en draagt anderzijds bij aan kennis over de manier waarop het cytoskelet de vorm van neuronen stuurt tijdens hun ontwikkeling. Begrijpen hoe een gezonde neuron functioneert, kan het medische veld helpen bij het ontwikkelen van een gerichte therapieën tegen hersenziekten.

Het grootste deel van het werk in dit boek richt zich op de ontwikkeling van de axon, de lange uitloper die signalen naar andere neuronen stuurt. Op het gebied van het cytoskelet richt deze thesis zich voornamelijk op *microtubuli*: een van de hoofdonderdelen van het cytoskelet, dat onder andere gebruikt wordt voor transport van bouwstenen over lange afstanden. Microtubuli zijn microscopisch kleine buisjes waarvan de uiteinden continu groeien en krimpen.

Hoofdstuk 1 bevat een zogenaamde review (een overzicht en bespreking van wetenschappelijke literatuur over een bepaald onderwerp) over eiwitten die aan de dynamische uiteinden van microtubuli binden ('+TIPs'). Door daar te binden, kunnen ze de meeste eigenschappen van microtubuli beïnvloeden: bijvoorbeeld of de microtubulus groeit of krimpt, hoe stabiel hij is en of het buisje ergens in de cel verankerd is. Ons lab ontdekte in 2015 twintig nieuwe +TIPs. Mijn PhD-tijd begon met een project om te zien welk van deze nieuwe eiwitten belangrijk zijn in neuronen, aangezien veel van de eerder ontdekte +TIPs betrokken zijn bij hersenziekten.



Hoofdstuk 2 bekijkt hoe de twee verschillende gedeeltes in neuronen gescheiden worden en blijven. In het begin van de axon zit een kleine structuur waar we zien dat motoreiwitten die de verkeerde bouwstenen dragen, omdraaien en de axon weer uit gaan. Lange tijd was bekend dát dit gebeurt, maar niet hoe.

In **Hoofdstuk 2** laten we zien welk motoreiwit verantwoordelijk is voor het terugbrengen van verkeerde gesorteerde moleculen. We laten daarnaast zien dat het omkeren – en dus de scheiding tussen verzend- en ontvangonderdelen – afhankelijk is van een klein eiwit dat in het begin van de axon vastzit. Normaal gesproken kan dit kleine eiwit fysiek binden aan het motoreiwit terwijl het motoreiwit op weg is. Wij bewijzen echter dat het eiwit in dit stuk van de axon niet van de ‘muren’ afkomt. Het is goed mogelijk dat zowel microtubuli als motoreiwitten vanaf die plek buiten bereik zijn. Mogelijk hebben we dus een nieuwe manier ontdekt waarop motoreiwitten gestuurd worden, namelijk op afstand. Als dat klopt, ontstaan nieuwe ideeën over hoe we ziektes kunnen behandelen die worden veroorzaakt door een verkeerde aansturing van motoreiwitten.

Hoofdstuk 3 gaat over een eiwit met de naam Gas2L1. Gas2L1 is één van de nieuw gevonden eiwitten die kan binden aan de dynamische uiteinden van microtubuli, maar het is ook onderdeel van een familie eiwitten die verschillende onderdelen van het cytoskelet met elkaar verbindt. Van dit betreffende eiwit was al bekend dat het dat doet, maar er was nog geen functie in neuronen beschreven. Dat is verrassend: we weten dat zulke verbinders ontzettend belangrijk zijn voor de ontwikkeling van neuronen. Een andere onderzoeksgroep heeft bovendien laten zien dat er relatief veel Gas2L1 in het brein aanwezig zou moeten zijn.

Wanneer we Gas2L1 uit jonge neuronen verwijderden, zagen we dat de axon misvormd raakte. Dat resultaat was te verwachten, maar op sommige punten had Gas2L1 juist het *tegenovergestelde* effect van andere, beter bestudeerde verbinders. We moesten daarom beter bekijken hoe Gas2L1 werkt.

Gelukkig is **Hoofdstuk 3** een samenwerking met een groep die zich specialiseert in het bestuderen van eiwitten buiten de cel. We haalden Gas2L1 letterlijk uit de cel en brachten het samen met een cytoskelet, dat ook buiten de cel was gebouwd. Dit is een bijzonder krachtige manier om eiwitten te bestuderen, omdat onderzoekers controle hebben over alle variabelen. In de hypercomplexe omgeving van een cel weet je nooit zeker weet wat je meetresultaten nog meer



beïnvloedt. In deze geïsoleerde context zagen we dat Gas2L1 aan geen enkel afzonderlijk onderdeel van het cytoskelet bindt, tenzij alletwee de onderdelen samen aanwezig zijn.

Uiteindelijk ontdekten we dat Gas2L1 zichzelf in elkaar vouwt en zo inactief houdt, tot alle onderdelen van het cytoskelet aanwezig zijn. In neuronen zagen we vervolgens dat Gas2L1 één van de twee cytoskelet-onderdelen stabiliseert. Omdat het eiwit het meest actief is wanneer beide onderdelen van het celskelet aanwezig zijn, kan het andere onderdeel – de microtubuli – bepalen waar in de hersencel Gas2L1 actief is. Via Gas2L1 kunnen microtubuli dus andere onderdelen van het cytoskelet aansturen zodat ze samen de axon kunnen ontwikkelen.

Hoofdstuk 4 bevat zogenaamde *preliminary data*: losse stukjes informatie, die helaas nog geen compleet verhaal vormen of proeven die nog vaker herhaald moeten worden. **Hoofdstuk 4** verzamelt de meest spannende resultaten naar aanleiding van het bestuderen van de twintig nieuwe +TIPs.

Hoofdstuk 4 bevat extra informatie over Gas2L1, waaruit we kunnen afleiden dat het eiwit heel gevoelig is voor de omgeving waarin het zich bevindt. We proberen ook te kijken waarom Gas2L1 kan binden aan de dynamische uiteinden van microtubuli, wat iets te maken lijkt te hebben met die gevoeligheid, maar helaas blijft dit vooral onduidelijk.

We kijken daarnaast naar een familie eiwitten die gelinkt is aan de ziekte van Alzheimer. Deze eiwitten gaan interactie aan met het dynamische uiteinde van microtubuli, maar ze modificieren ook het eiwit *tau*, op een manier die op hol slaat in de hersencellen van Alzheimerpatiënten. Wij beschrijven dat deze eiwitten, gek genoeg, niet fysiek op dezelfde plek aanwezig zijn als tau. Hoe kunnen ze het dan modificieren? De huidige wetenschappelijke literatuur neemt dit gegeven niet in overweging. Dit zal wel moeten, als we willen weten welke rol deze eiwitten spelen bij de ziekte van Alzheimer.

Tenslotte hebben we het over NCKAP5L: een eiwit dat amper terug te vinden is in de wetenschappelijke literatuur. Wij zagen dat jonge neuronen zonder NCKAP5L helemaal geen axon kunnen maken. Het is duidelijk een extreem belangrijk eiwit, maar we hebben helaas nog niet ontdekt waarom.



Als sluitstuk bespreekt **Hoofdstuk 5** de voorgaande hoofdstukken in de context van de nieuwste wetenschappelijke ontwikkelingen.

Dit hoofdstuk maakt zich sterk voor twee dingen: ten eerste moeten we ons beter bewust zijn van het feit dat eiwitten die aan de dynamische einden van microtubuli *kunnen* binden, dat niet altijd *doen*. Dit heeft gevolgen voor de manier waarop we naar deze eiwitten kijken.

Ten tweede besteedt dit hoofdstuk meer aandacht aan het concept van 'op-afstand-bestuurbare-motoreiwitten', dat door de resultaten in **Hoofdstuk 2** aannemelijk wordt gemaakt. Tot nu toe wordt dit over het hoofd gezien in wetenschappelijke publicaties die onze studie bespreken.



Acknowledgements

Well, I'm glad I didn't have to do this alone!

If you helped me or kept me company along the way: thank you, please turn the page for a more personal note. I'll keep the printed part short to save mutually embarrassing anecdotes from being distributed and archived forever (you'll thank me later). So, here goes:

Thanks to my promotors, Anna and Casper, for placing your trust in me and letting me experience science up close in your labs. Your mentorship has been very complimentary.

Thanks to my PhD committee: Prof. Lukas Kapitein, Prof. Maarten Kole, Prof. Jeroen Pasterkamp, Prof. Bernd Helms, Prof. Gijsje Koenderink and Prof. Joost Holthuis.

Thanks to my paranympths, Joep and Antoinette, for all the good times – past, present and future!

Thanks to everyone who mentored me since I first set foot in Utrecht ten years ago, in order of arrival: Joep, Joost, Anna, Ben, Casper, Marijn, Maarten. I learned so many skills, technical and otherwise, from all of you.

Thanks to all co-authors on my chapters and list of publications. I'm very happy to have worked with all of you.



Thanks to the neuron culture club: Bart, Casper, Josta, Elena, Marta, Xingxiu, Eliana, Eitan, Ginny, Feline, Amélie, Lisa, Klara, Nicky, Anna, Lena and Esther. Since hardly anyone says it, I will: you all deserve(d) to wear little hero capes around the lab on culture mornings (it's never too late to start this tradition).

Thanks to N503: Petra, Marta, Elena, Joanna, Xingxiu, Jessica, Feline and Lisa. It's been a pleasure! Sorry for the organized chaos, glad to see order has returned following my departure.

Thanks to those lab mates who didn't flinch when I e-mailed something (ok, maybe one incriminating anecdote then) along the lines of *guys guys let's dress up as Rembrandt characters and do a secret photoshoot yes YES!!*: Martin, Lena, Feline, Sybren, Jessica, Yujie and Bart. Amélie, Xingxiu and Robin, you are there in spirit. Jasper, you knocked this one out of the park.

Of course, thanks to all other lab mates too - most of you have saved the day at one point or another.

Thanks to all who kept me grounded outside of my PhD, notably Bob, Joep, Antoinette, Mex and Tim.

Thanks to my parents; I couldn't think of enough superlatives to put here if my life depended on it. Instead, this book is for you.

Dieudonné







